UNIVERSITY OF SOUTHAMPTON

FACULTY OF ENGINEERING, SCIENCE AND MATHEMATICS

OPTOELECTRONICS RESEARCH CENTRE

A NANOTECHNOLOGY APPROACH TO DNA ANALYSIS

by Katrin Pechstedt

A thesis submitted for the degree of Doctor of Philosophy

May 2011

UNIVERSITY OF SOUTHAMPTON

ABSTRACT

FACULTY OF ENGINEERING, SCIENCE AND MATHEMATICS

OPTOELECTRONICS RESEARCH CENTRE

Doctor of Philosophy

A NANOTECHNOLOGY APPROACH TO DNA ANALYIS

by Katrin Pechstedt

This thesis describes the investigation of quantum dots and nano-structured metallic films for use in single genomic DNA analysis. The fluorescence of continuously illuminated core/shell CdSe/ZnS quantum dots (QDs) under various atmospheric conditions is investigated experimentally. Initial enhancement in fluorescence intensity is observed followed by degradation; both are highly dependent on the atmospheric conditions. Following a series of studies theories are put forward to explain these observations.

Solution mixtures of DNA strands and QDs are imaged with Atomic Force Microscopy and Fluorescence Microscopy to investigate the binding properties of DNA strands with QDs.

Gold nanovoids are fabricated for use as a substrate to provide localised enhanced fluorescence intensity of fluorescently labelled regions of DNA strands stretched and located over nanovoids as a result of resonant coupling with localised surface plasmon polariton modes. The energy and electric field distribution of localised surface plasmon polaritons is considered for various void geometries for use with fluorescently labelled DNA. The experimental fluorescence intensity profile along fluorescently labelled DNA strands stretched over glass, electrochemically grown gold and gold nanovoid substrates is compared and the fluorescence lifetime is measured. Short fluorescence lifetimes and increased intensities over gold nanovoids and a constant lifetime over glass are observed.

The results of these biophysical studies are discussed with a view for application as methods for distinguishing different DNA sequences on the nanoscale.

Contents

List of Figures

List of Tables

Declaration of Authorship

I, Katrin Pechstedt,

declare that the thesis entitled

A Nanotechnology Approach to DNA Analysis

and the work presented in the thesis are both my own, and have been generated by me as the result of my own original research. I confirm that:

- this work was done wholly or mainly while in candidature for a research degree at this University;
- where any part of this thesis has previously been submitted for a degree or any other qualification at this University or any other institution, this has been clearly stated;
- where I have consulted the published work of others, this is always clearly attributed;
- where I have quoted from the work of others, the source is always given. With the exception of such quotations, this thesis is entirely my own work;
- I have acknowledged all main sources of help;
- where the thesis is based on work done by myself jointly with others, I have made clear exactly what was done by others and what I have contributed myself;
- parts of this work have been published as in **Publications**.

Signed:……..

Date: May 2011

Acknowledgements

Firstly of all would like to thank my supervisors Dr. Tracy Melvin and Professor Jeremy Baumberg, for giving me the opportunity to pursue the research project described in this thesis. I am deeply indebted to them as their hard work helped me in all aspects that the project touched upon in the past few years. I would like to thank Dr. Tracy Whittle and Professor Graham Leggett from the department of Chemistry, University of Sheffield, for assisting with the XPS, and Dr. Sumeet Mahajan, University of Cambridge, for assisting with the fluorescence lifetime measurements. I extend my gratitude to Becky Pennington for providing useful and helpful discussions about the fabrication of gold nanovoids. My gratitude also goes to Dr. Phillip Thurner for allowing me to use his AFM machine, to James Richardson and Professor Tom Brown for demonstrating the ligand exchange procedure of quantum dots and other chemistry related issues, and to Zondy Webber for technical support and assistance in the nanofabrication cleanroom. Thanks also goes to Garcia deAbajo for providing the BEM model, aswell as to all the members of Dr. Melvin`s group, the past post-docs Nic, Samson, Lucy, Matt, Suzanne, Liquin and Patrick, and PhD student Chien for demonstrating the sphere deposition techniques, as well as Tim, Daniel, Chris, Mukhzeer, all of whom who have provided helpful discussions, assistance and motivation. In addition, I would also like to thank EPSRC for providing the funding for the research.

I would also like to give my special thanks to my parents for their encouragement and patience.

Chapter 1

1 Introduction

1.1 Background and Motivation

Cancer poses one of the major health issues facing modern medicine today. In cancer cells, the genome sequence is altered, and the specific DNA sequences present can be analysed to provide a diagnosis for the type of cancer. In the past, chromosomal painting and fluorescence *in situ* hybridisation (FISH) approaches, in which chromosomes are fluorescently labelled, have been able to detect cytogenetic alterations in chromosomes. Recently, approaches have been developed to increase the spatial resolution on naturally coiled-up genomic DNA by decondensing and extending the genomic DNA into a linearised configuration. One of the approaches includes fibre-FISH, which uses a receding meniscus to stretch DNA strands in a uniform and controlled manner.[1] Extended DNA allows facilitated analysis of DNA sequences using fluorescence and quantitative analysis of the chromosomal alterations present in genomic DNA.[2] The optical resolution achievable for DNA analysis is limited by the optical resolution limit. Various optical approaches have been developed to circumvent this limit, such as tip enhanced Raman spectroscopy of single DNA strands.[3] However, the slow sequencing speed of near-field optical techniques is a major limitation.

Evidence suggests that cancerous cells release low copy numbers of their aberrant DNA into the patient`s blood serum.[4] For a non-invasive DNA detection approach, the aberrant DNA present in the serum could be amplified using polymerisation chain reaction (PCR) or analysed using fluorescence *in situ* hybridisation. However, high labour costs are associated with PCR and FISH is a slow analysis method as it relies on surface-attached DNA strands. Microfluidic devices, on the other hand, could provide a faster DNA analysis method. Microfluidic devices can be designed such that laminar fluid flow itself stretches and elongates a

coiled-up DNA strand, which would allow more rapid and high-throughput screening. It has been shown that genomic DNA strands can be stretched by laminar microfluidic flow, as first demonstrated by Yamashita *et al.*[5] who used microfluidic flow in a capillary tube. Chan *et al.*[6] have demonstrated controlled stretching of long DNA strands using accelerated fluid flow in a microfluidic device induced by a tapered region, and demonstrated the feasibility of this technique for subsequent DNA mapping (Figure 1.1). Cipriany *et al.*[7] have recently used fluidic nanochannels for DNA analysis. Direct DNA sequencing on single stranded DNA a few kb long has been shown with biological nanopores,[8] and relies on the detection of an unique electrical current for each individual nucleotide base within the pore. The fabrication of lipid bilayers suspended across a quartz nanopore membrane may in future provide an increased signal to noise ratio, and thus faster data acquisition rates.[9]

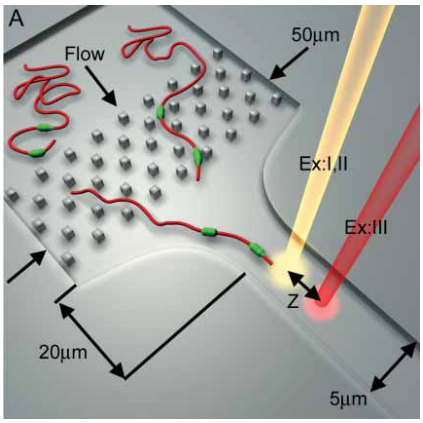

Figure 1.1: Illustration of DNA elongation using accelerated flow: coiled DNA molecules enter a post region for DNA uncoiling, followed by a tapered region in the microfluidic channel which provides DNA elongation by accelerated fluid flow. Elongated DNA can then be mapped using fluorescence excitation and detection of fluorescent tags.[6]

The major limiting factor when detecting DNA sequences tagged with fluorescent probes is obtaining spatial resolutions that allow the detection of DNA sequences separated by up to the optical resolution limit, which is equal to a few hundred nanometres. In this thesis, the aim is to develop a novel technique for high resolution analysis of genomic DNA sequences directly from double stranded DNA, by exploiting the use of fluorescent semiconductor quantum dots (QDs) and gold nanostructures. QD nanoparticles, such as CdSe capped with a ZnS shell, have been

suggested by many to provide better alternatives to fluorophores[10-15] because (a) photobleaching, as seen for fluorophores, does not occur (b) QDs have a narrow fluorescence spectrum, and (c) the excitation of a number of differently sized QDs with a single excitation wavelength is possible.[16, 17] However, as shown in the following chapters, the potential of quantum dots for quantitative DNA analysis was found to be problematic. The studies reported in this thesis will demonstrate that the QD fluorescence is highly sensitive to the illumination time and the atmospheric conditions surrounding the QDs, and furthermore, illumination under oxygen and water containing atmospheres leads to the degradation of QDs.

Randomly patterned metal nanostructures have been shown to increase the quantum yield of nearby excited-state fluorescent emitters by reducing their radiative decay lifetime.[18-20] The gold nanovoids have been shown to support strong localised surface plasmon modes within the void volume,[21, 22] which could be exploited for the fluorescent enhancement of fluorescently tagged DNA strands stretched over the gold nanovoid substrate (figure 1.2(ii)).

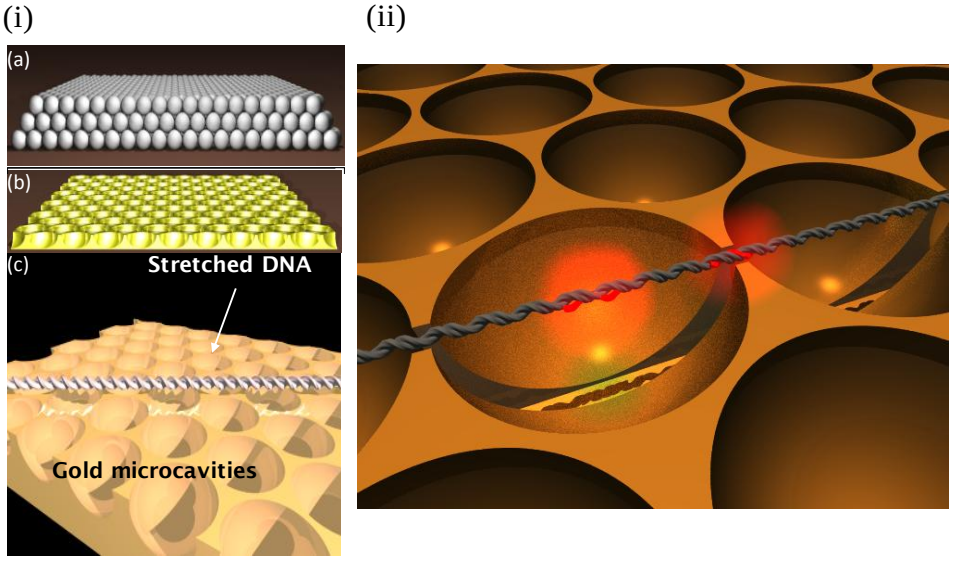

Figure 1.2: Illustration of (i) the fabrication of a regular array of gold nanovoids by (a) the deposition of a regular array of polystyrene spheres, and (b) the electrochemical growth of gold around the sphere template and subsequent removal of the spheres (c) DNA strand stretched over the nanovoid substrate (ii) conceptual fluorescence enhancement strategy by the spatial overlap between fluorescently labelled DNA strand stretched over a gold nanovoid and a resonant surface plasmon mode localised within the gold nanovoid.

In this thesis, a novel fluorescence enhancement strategy for fluorescent emitters attached to a stretched DNA strand, using gold nanovoids, is investigated, which relies on resonant coupling between the excited emitter and localised surface plasmon polariton modes within the nanovoids. A method for facile fabrication of ordered gold micro and nanovoids has already been developed,[22, 23] by electrochemically growing gold around a template of polystyrene spheres (Figure 1.2(i)). Due to the localised surface plasmon modes within the nanovoids, gold nanovoids, unlike randomly rough or corrugated metal surfaces, would allow fluorescence enhancement at larger distances from the substrate surface, providing a more effective route for sensitive detection of fluorescently labelled DNA strands in solution.

1.2 Current DNA Sequencing and DNA Mapping Technologies-an Overview

Most current approaches used to detect a specific DNA sequence within target DNA employ a fluorescently labelled DNA probe that is complementary in sequence to the target sequence. Probe-target hybridisation is then be detected by fluorescence microscopy. Naturally, the DNA molecule is in a random coiled up state, so that DNA stretching into a linearised form can greatly facilitate analysis and enhance resolution in most fluorescence based DNA sequencing/mapping approaches. Also, human chromosomes range in size from 50 Mbp to 250 Mbp,[24] which, with current sequencing/mapping techniques, need to be fragmented into smaller pieces before analysing.

1.2.1 Polymerase Chain Reaction

The polymerase chain reaction (PCR) is a technique to amplify DNA that has been adapted for the detection of DNA mutations.[25, 26] For PCR, double stranded (ds) target DNA is denatured into single stranded (ss) DNA by heating. After cooling, a primer, a short oligonucleotide sequence that serves as a starting point for DNA replication, anneals to a nucleotide sequence within the single-stranded DNA. DNA polymerase enzymes extend the primer, base by base, along the single-stranded DNA by adding nucleotides complimentary to the target strand. Subsequent cycles of denaturing and extension exponentially amplify the copy numbers of the original DNA strand. A mutation can be detected as changes in the DNA melting curve shape compared to the melting curve of non-mutated sequences. [187, 226, 321]. Polymerase can extend DNA fragments of up to 40 kb long.[27] However, polymerase can introduce single nucleotide errors at a rate per nucleotide between 2.0×10^{-5} and 1.6×10^{-6}, introducing artificial errors.[28]

1.2.2 Fluorescent Sanger Sequencing

One of the earliest DNA sequencing techniques was that published by Sanger *et al.* in 1977, which employed radioactive phosphorous labels that are detected by autoradiography.[29] By 1990, the hazardous radioactive detection has been replaced by fluorescent labelling. The Sanger technique comprises 4 separate reactions that extend a DNA template, one reaction for each of the 4 nucleotide bases, adenine (A), thymine (T), cytosine (C) and guanine (G). In each reaction, a primer is annealed to the single-stranded DNA template and polymerase extend the DNA base by base by adding the complementary nucleotide dNTP (2`-deoxynucleotidetriphosphate), of which all four bases, A, T, C and G are present in each reaction. The novel aspect about the Sanger reaction is that each reaction also contains one of the four bases ddNTP (2`, 3`-dideoxynucleotide triposphate), which terminates the extension when inserted into the DNA strand, because it fails to form a phosphodiester bond with the next nucleotide. The result is that each reaction contains extended strands of different lengths that all terminate with the same terminating base ddNTP in each reaction. For instance, the reaction containing ddATP will contain extended DNA strands of different lengths all ending with the base A. The products are separated out according to length by electrophoresis. Each of the four ddNTPs is labelled with a fluorescent dye emitting at a unique colour, so that the sequence of fluorescence colours and thus nucleotides of the DNA products can be read off by fluorescence. To reduce the cost of sequencing, techniques have been developed that increase the throughput. Today, automated sequencing using the Sanger method can sequence about 1.6 million base pairs (bp) a day.[30] Despite the highly automated approach, the Sanger method has limitations, such as high cost, and the strand length that can be sequenced is limited to less than about 1 kb.[31] Sanger sequencing also requires high copy numbers of DNA templates to allow DNA strand extension to many different lengths. Amplified DNA templates can be obtained by isolating the target DNA, fragmenting it and cloning it into vectors for DNA

amplification in bacterial cells. After the amplified DNA is isolated from the bacterial colonies, they can be sequenced. The problem with bacterial amplification is that some parts of the chromosomes, such as centromers, cannot be cloned.[29] Instead, other amplification methods, such as PCR, have to be used, but PCR, compared to bacterial amplification, is a slow throughput method.[29]

1.2.3 Restriction Mapping

Restriction enzymes are enzymes isolated from bacteria that recognize specific nucleotide base sequences in single or double stranded DNA and cut (digest) DNA at those restriction sites into smaller fragments (DNA digestion). For instance, the enzyme EcoRI, which is isolated from E.Coli, recognises the sequence GAATTC.[32] Restriction mapping can detect mutations: a mutation in a restriction sites would make this site unrecognisable by restriction enzymes and thus result in an abnormally long fragment, while a mutation that creates a new restriction site would be detectable as abnormally short fragments. The fragment size of digested DNA is usually analysed by agarose gel electrophoresis, in which the digested DNA is loaded (pipetted) into a well in the agarose gel. Under the influence of an electric field, the negatively charged DNA fragments will migrate through the gel towards the positive anode located at the other end of the gel. The migration rate depends on the net charge and mass (size) of the fragment. As the different sizes of DNA fragments have the same charge to mass ratio, the main separation factor is the fragment size, with smaller (lighter mass) fragments migrating faster than larger (heavier mass) fragments. The different fragment sizes form bands on the gel, which can be made visible by staining the DNA fragments with the fluorescence marker ethidium bromide and fluorescence imaging. Restriction mapping avoids the use of DNA clones by working with genomic DNA fragments directly. However, there are limitations associated with restriction mapping. DNA digestion removes the information of the order of the fragments within the original intact DNA molecule, requiring the use of multiple enzymes to reconstruct the fragment order of the original DNA.[6]

Gel electrophoresis is also a slow process, especially for larger DNA molecules, where the analysis can take up to several hours.[6] Also, large amounts of DNA are needed for digestion and in the electrophoresis step, requiring an additional DNA amplification step, such as PCR, when only a small amount of DNA sample is available. Also, restriction mapping can only be applied to short DNA molecules with an upper limit of DNA length equal to about 50 kbp.[33] Also, gel-electrophoresis poorly separates fragment longer than about 50 kb long, reducing the resolution for DNA molecules longer than 50 kb.[33]

1.2.4 Fluorescence *in situ* Hybridisation

Fluorescence *in situ* Hybridisation (FISH) is a fluorescence imaging technique that can be used to detect aberrations in genomic DNA, such as duplications,[34-36] deletions,[37, 38] translocations[36, 39] and amplifications. For FISH, target DNA strands are first denatured by heating, followed by in situ addition of fluorescently labelled DNA probes for probe-target hybridisation. The location of the probe, and hence specific nucleotide sequence, on the DNA strand is visualised by fluorescence microscopy. FISH can be done on target DNA that is chromosomal DNA, or on stretched, isolated DNA fibres, which yields higher resolution (minimum resolvable spatial separation between two probes) due to its extended, linearised form. Chromosomal DNA structure varies with cell cycle, which affects the maximum resolution attainable. During cell division (metaphase), DNA is very condensed, yielding a maximum resolution of 1 and 5 Mbp, while non-dividing (interphase) DNA is least condensed, which increases the resolution to up to 50 kbp (Figure 1.3).

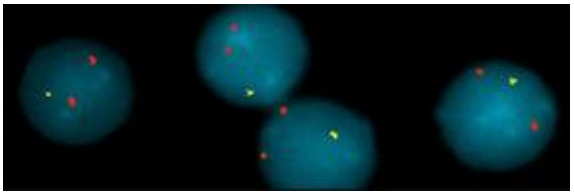

Figure 1.3: FISH on interphase nuclei of chronic lymphatic leukaemia cells (LLC), showing the normal two red signals per nuclei (a region in chromosome 7), but only one green signal per nuclei for the tumour suppressor gene RB-1 in chromosome 13, showing that one RB-1 copy is deleted.[40]

The resolution can be increased to 5 kbp by a method called DIRVISH (Direct VIsual Hybridisation), in which interphase chromosomal DNA is freed from the cell membrane by lysing interphase cells with detergent, so that the DNA can slide down a tilted coverslip to become linearly extended.[41] Fibre-FISH takes this further by removing the proteins present in chromosomal DNA (such as histones and scaffolding proteins), and stretching the protein-free DNA to 340 nm per 1 kbp [42] by molecular combing (Figure 1.4(a)). In molecular combing, one end of the DNA strand is anchored to the surface of a silanised glass cover slip, and the glass coverslip is pulled at a constant speed out of DNA solution, so that a moving meniscus at the air-water interface applies hydrodynamic forces on the DNA molecule, stretching DNA into a linearly extended form (Figure 1.4(b)).

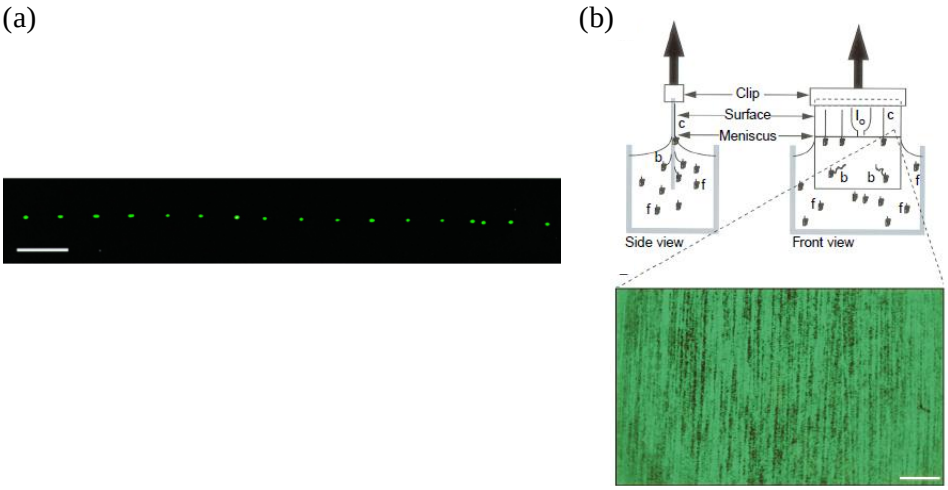

Figure 1.4: Fibre-FISH (a) showing the 18eRNA gene in the fungus C. heterostrophus using a probe 0.7 kb long, the fluorescence signal was amplified by using antibodies, bar is equal to 5 µm[43] (b) DNA stretching method by a receding meniscus.[1]

The theoretical resolution limit of optical microscopy (r) is about 230 nm or 0.68 kbp (assuming diffraction limited optical detection in which case $r=0.61\lambda/NA$, with an objective of numerical aperture $NA=1.4$, fluorescence wavelength $\lambda=532$ *nm*, and *340 nm=1 kbp*), and resolution limits of up to 1 kbp have been demonstrated with fibre-FISH.[42] An increase in the optical resolution limit by the use of Fibre- FISH in

combination with Scanning Near Field Optical Microscopy (SNOM) has been demonstrated,[44, 45] although SNOM has longer read-times in analytical methods. Deletions can also be detected as the absence of a specific sequence compared to its presence in intact DNA.[36] Probes are usually labelled directly with fluorophores, which means that the probe contains modified nucleotides which each can hold one fluorophore (Figure 1.5(a)). The fluorescence intensity then depends on the probe length/target length, with shorter probes, which contain fewer fluorophores, lower in intensity (lower signal to noise ratio). The minimum probe length (for deletions, duplications) that can be detected is then limited by the light gathering power of the microscope (sensitivity). FISH has thus been limited to the detection of larger sequences, such as micro-deletions.[36]

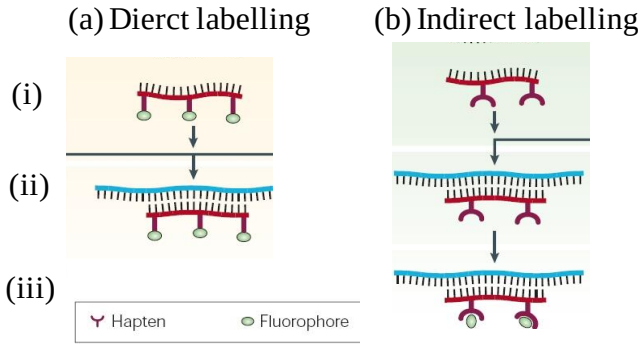

Figure 1.5: Labelling strategies in FISH (a) Direct labelling (b) indirect labelling (probe/target DNA is red/blue strand (i) probe containing nucleotides modified with (a) a fluorophore (direct) or (b) a hapten (indirect) (ii) probe-target hybridisation (iii) in indirect labelling, fluorescent antibodies bind to the hapten.[46]

To maintain detection sensitivity with shorter probes (a few bases long), the probe fluorescence intensity can be amplified using indirect labelling approaches, in which probes contain modified nucleotides that contain an antigen (hapten). A fluorescently labelled antibody can bind to the antigen (Figure 1.5(b)). Fluorescence intensity can be increased by (i) attaching several fluorophores onto one antibody or (ii) adding additional layers of fluorescently labelled molecules that have high affinity to the antibody.[47]

It has also been suggested that low hybridisation efficiencies limit the FISH sensitivity.[48, 49] In summary, limitations of FISH are limited resolution and slow speed due to low throughput of the DNA stretching

method (combing). Also, although the molecular combing DNA linearisation technique does not require high sample volumes, strands longer than about 150 kbp fragment under the moving meniscus,[24] limiting the DNA size that can be linearised.

1.2.5 Fluid Flow Stretching

DNA stretching methods in fluid flow for use in single molecule DNA mapping have been developed.[50-52] One such method is Direct Linear Analysis (DLA), which relies on accelerated fluid flow to stretch DNA (Figure 1.6(a)) and which has demonstrated high throughputs of up to several thousand DNA molecules per minute.[6] The optimal DNA length for DLA is between 100 and 250 kbp,[53] with longer DNA requiring prior fragmentation to the desired length by restriction enzymes.[53]

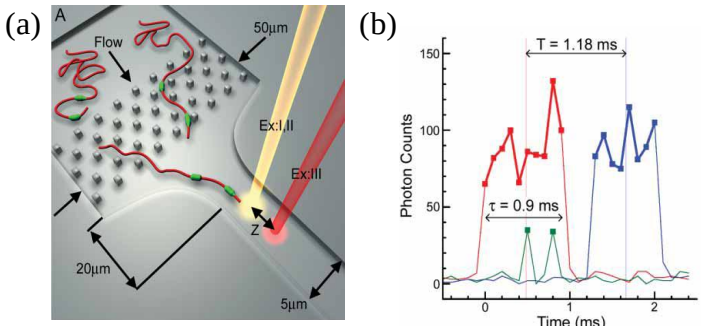

Figure 1.6: DLA method for DNA stretching in fluidic flow for single molecule DNA mapping, (a) setup of DLA (b) length measurements of DNA molecule, fluorescence signal from backbone staining detected in detection spot (red) EXII and (blue) ExIII, (green) fluorescence from site specific fluorescent tag when passing through excitation spot ExI.[6]

In DLA, naturally coiled up DNA follows the laminar fluid flow through a post region, uncoiling the DNA strand (Figure 1.6(a)). The subsequent tapered region results in flow speed acceleration, so that the DNA strand in this region experiences extension along the molecule, and is stretched to its contour length (Figure 1.6(a)). The linearised DNA molecule, its backbone stained with intercalating dye and specific sequences fluorescently labelled with sequence specific tags, is then interrogated optically at two different positions (ExI,II and ExIII) along the flow channel to create a map and deduce its stretched length (Figure 1.6(a)). Only DNA stretched to within a certain range of its contour length is mapped. The DNA length X is

determined by measuring using the backbone staining dye the time it takes for a molecule to pass through the ExII excitation spot (the residence time τ) at a constant flow velocity v, so that $X=v*\tau$ (Figure 1.6(b)). The flow velocity is determined by the spatial separation between the two interrogation spots ExII and ExIII (z) and the time for the molecule to travel between these two spots (transit time T) (Figure 1.6(b)). Maps are built up by locating the fluorescently labelled tag along the DNA strand as it passes the excitation spot ExI. The tag is a 7-8 bp long peptide-nucleic-acid (PNA) which can form very stable bonds with DNA motif due to being electrically neutral.[6] Map building involves the location of the centre of the molecules (CM) via the transit time T of backbone-stained DNA when passing excitation spot ExII, detecting the fluorescent bursts from the tags when passing ExI and converting the time domain into length (μm) via the calculated velocity (Figure 1.7(A) and (B)).

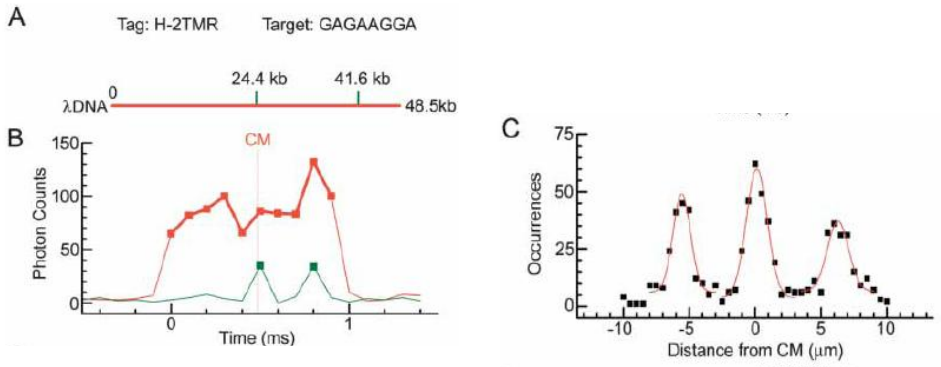

Figure 1.7: DLA-based single molecule DNA mapping using different tags (A)theoretical location along a Lambda-phage DNA strand of (red) dye intercalated into the DNA backbone and (green) two sequence specific tags, of PNA sequence TCCTTCTC and which use TMR dye (B) experimental fluorescence signals from the (red) intercalated DNA backbone and (green) fluorescent tags (C) occurrence of fluorescence peaks from tags a as function of distance from the centre of the DNA molecule (black) experimental data (red)Gaussian fits.[6]

With a large number of identically tagged and identical DNA molecules, a histogram of occurrence of fluorescence peaks versus distance can be built up, and Gaussian fits can be made to the peaks, for more accurate tag location along the DNA strand (Figure 1.7(C)), with limiting resolution equal to the full width at half maximum of the Gaussian peaks. DLA allows high throughput stretching and mapping sensitivity at a single DNA

molecule level, with no need for DNA amplification, but the resolution is limited by the optical resolution limit of the microscope.

1.2.6 DNA Linearisation by Confinement in Nanochannels

DNA is a continuously semi-flexible, self-avoiding polymer.[54] An unconfined DNA molecule in solution has an associated radius of gyration, R_G, which is a theoretical measure of the DNA dimension, and is equal to

$$R_G^2 = \frac{1}{N+1}\sum_{i=0}^{N}(r_i - r_{cm})^2 \qquad (1.1)$$

where r_i is the coordinate vector of segment i, and $r_{cm} = \sum_j m_j r_j$ is the molecule`s centre of mass coordinate vector, where $r_j$ and $m_j$ are the coordinate vector and mass, respectively, of segment $j$. $R_G$ depends on the root mean square distance of all DNA segments $N$ from the molecule`s centre of mass and thus depends on the number of base pairs the DNA molecule consists of. According to DeGennes, a DNA molecule inside a cylindrical channel of diameter D, where $D<<R_G$, is confined and cannot retain its naturally coiled up configuration.[55] Due to self-avoidance, the confined DNA molecule then elongates into a series of non-interpenetrating particles along the confining channel (Figure 1.8(a)).[55] DeGennes` theory predicts an even DNA mass distribution along the channel with a uniform DNA density along the channel length resulting in a stretched end-to-end DNA length, L_Z, that scales linearly with the DNA contour length L according to[55, 56]

$$L_Z \approx L\frac{(pw)^{1/3}}{D^{2/3}} \qquad (1.2)$$

where p is the DNA persistence length, a measure of the DNA`s rigidity (about 50-60 nm under physiological conditions),[24] and w is the DNA width (about 2 nm).[24] The self-avoidance introduces a L_Z-dependence on DNA width w, while confinement, which prevents DNA backfolding, increases the L_Z-dependence in the DNA contour length L.[56] As a result, an increased stretching length, L_Z, occurs for smaller confining channels.

For instance, a 100 nm diameter channel extends DNA to an extension factor equal to $L_z/L = 0.2$ i.e. 20% of its contour length L, while a 400 nm diameter channel achieves an extension factor of 15%, assuming $p=50nm$.[24, 56]

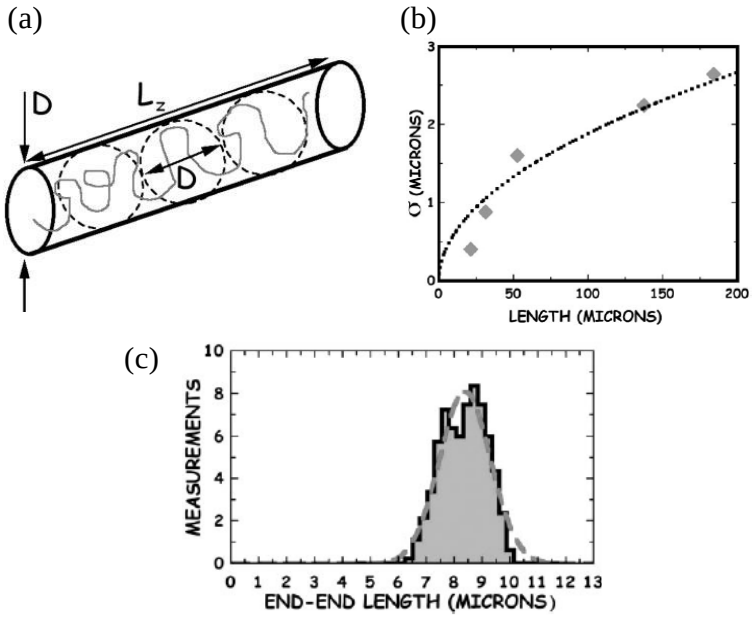

Figure 1.8: DNA elongation in a nanochannel (a) in a confining tube of diameter D, DNA elongates as a series of non-interpenetrating particles, resulting in elongated DNA length of end-to-end distance L_Z (D) (b) measured dependence of the standard deviation in the extension length L_Z on the DNA contour length L for a nanochannel width D=100 nm, dashed line is a fit to the experimental data (c) Measured extended length L_Z of a DNA monomer inside a 100 nm wide nanochannel, dashed line is a Gaussian fit, with mean value of 8.38 µm ± 0.15 µm.[56]

Other ways to influence the stretching is by variations in p and w: the persistence length (DNA stiffness) increases with decreasing ionic strength and DNA staining.[24] The DNA width w varies inversely with salt concentration, due to repulsion between like-charged DNA segments.[24] The contour length L is the fully stretched DNA length, and increases with staining.[24] DeGennes regime is valid for channel diameters in the range of $p<<D<<R_G$.[24, 56] The dependence of the stretched DNA length L_Z on the channel diameter and the DNA contour length L has been experimentally verified by Guo *et al.*[57] and Tegenfeldt *et al.*,[56] respectively. Thermal fluctuations introduces variation around the mean value of the extended length L_Z, which have been measured[54, 56] and theoretically scale as

$$\left\langle \delta L_Z^2 \right\rangle = \frac{k_B T}{k} = \frac{4L}{15}(pwD)^{-1/3} \qquad (1.3)$$

where δL_Z^2 is the rms variance in the mean extension length L_Z and k is the effective DNA spring constant. The standard deviation from L_Z at any one measurement, defined as $\sigma=\sqrt{<\delta L_z^2>}$, thus varies with the square root of the contour length L, as has been experimentally verified (Figure 1.8(b)).[56] The standard deviation scales inversely with the number of independent measurements M as $\sigma_M=\sigma/\sqrt{M}$, so that the more precise length measurements are possible with an increase in the number of length measurements. Tegenfeldt *et al.* have been able to measure DNA with a precision of ±400 bp within 1 minute (20 measurements) of an DNA molecule extended to 8.36 μm (Figure 1.8(c)).[56] The main advantage of DNA extension by nanochannel confinement is the possibility of stretching longer DNA molecules than is possible with molecular combing, as Tegenfeldt *et al.* have demonstrated DNA extension $>10^6$ bp in length.[56] However, constant extension lengths are not achieved.

1.2.7 Direct DNA Sequencing Using Nanopores

This technique promises, compared to Sanger sequencing, high speed sequencing without the need for DNA cloning (amplification by enzymes) or labelling. In the nanopore sequencing approach, a nanopore a few nanometers in diameter, either biological (protein pore in a lipid bilayer) or solid-state, separates two electrolyte filled chambers.[58] A voltage applied across the nanopore creates an electric field that causes ions to flow through the pore. Negatively charged, coiled up DNA present in one of the chambers can be uncoiled and passed through the nanopore by the action of the electric field. During translocation through the pore, the DNA partially blocks the ion flow through the pore, modulating the ion current. The narrowness of the pore, typically less than 5 nm, ensures base by base, sequential translocation of the DNA strand, potentially allowing direct read out of the base sequence. However, while this approach can clearly distinguish between an open and a blocked pore by means of the

modulated blockage current, it cannot attribute the modulated current to a single nucleotide, because the blocking current is the result of at least 10 nucleotides inside the pore at any one time, even for the shortest nanopore of 5 nm.[8] Even an infinitely thin nanopore has a readout region of 3 nm, much more than the required 0.4 nm that separate two successive bases.[8] Various alterations have been shown to overcome this resolution limit. One ensures the presence of only one nucleotide inside the pore at any one time. Exonuclease that is attached to the top of a α-hemolysin pore cleaves off individual nucleotides from the end of the target strand.[8] An aminocyclodextrin adaptor fitted within the nanopore then measures the blocking current of each nucleotide.[8] The blocking current of a pore filled with nucleotides was shown to differ from that of a free pore, and the blocking current was shown to be dependent on the nucleotide within the pore.[8] However, the single file translocation, as in an intact DNA strand is lost, so that for sequencing it has to be made sure that each cleaved off base is translocated and expelled at the other side that mirrors the actual DNA sequence.[8]

Another potential limitation is the high translocation speed of DNA through the pore. A typical bias of 150 mV gives a speed of 1 nucleotide per microsecond, which would have to be slowed down to at least 1 nucleotide per millisecond to resolve pA modulations in the current.[8] Processive enzymes have been shown to reduce the DNA translocation rate to a few milliseconds per base, which is achieved as the enzyme binds to the DNA and prevents the DNA strand from moving into the pore quicker than the processing rate of the enzyme.[8]

These nanopore sequencing methods are still in their infancy, but provide potential advantages over concurrent sequencing methods. The main challenge at present is how to increase the rate of sequencing.

1.2.8 Direct DNA sequencing via Tip-Enhanced Raman Spectroscopy

Tip-Enhanced Raman Spectroscopy (TERS) allows direct analysis of the DNA by detection of unique vibrational spectroscopic fingerprint for each nucleotide base (Figure 1.9(ii) and (iii)). In TERS, the DNA molecule, located on an atomically flat surface, is placed within the strong optical near-field of a sharp metal tip[3] or a metal nanoparticle attached to an AFM tip[59] (Figure 1.9(i)), providing enhancements in the Raman intensities for improved sensitivity.

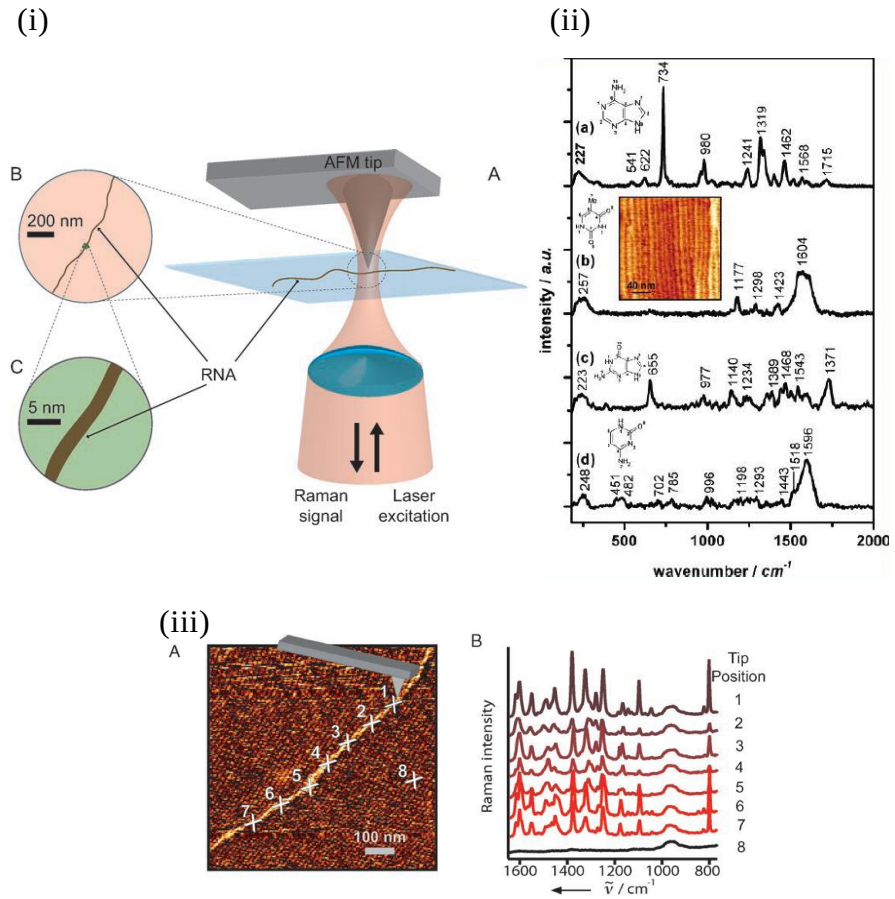

Figure 1.9: Tip-Enhanced Raman-Scattering on RNA (i) Schematic view of the experimental setup[3] (ii)TERS signal of a monolayer of the nucleotide bases (a) adenine (b) thymine (c) guanine (d)cytosine[59] (iii)TERS on a single stranded cytosine RNA strand (A) topography obtained by AFM (B) TERS spectra at sample locations indicated in figure 1.9(iii)(A).[3]

Enhancements of about 10^4 on a single-stranded RNA polymer have been demonstrated, as well as single nucleotide base sensitivity.[3] The use of the AFM tip also provides topographic information. The spatial (lateral) resolution is limited by the AFM tip or particle diameter, ranging between

5 and 20 nm, so that the interaction area between the tip and the sample spans several nucleotide bases, which will all be visible in the TERS spectrum obtained from this region.[3] Conceptually, single nucleotide base resolution can still be achieved by determining the TERS spectrum at lateral locations on the DNA strand separated by the base-to-base separation, with differences in TERS spectra revealing differences in base content and composition.[3] However, the effectiveness of this concept has not yet been experimentally verified. The advantages of TERS are direct analysis of the DNA strand without the need of labelling, single molecule analysis and single base sensitivity. However, the high lateral resolution relies on linearised DNA strands. Bailo *et al*. have not stretched strands, but looked for appropriate linearised strands, which is time consuming.[3]

1.3 The Thesis Outline

The thesis outline is as follows:

Chapter 2 presents a literature overview of pervious experimental results and theoretical models about the evolution of quantum dot fluorescence under continuous illumination under various atmospheric conditions. The experimental setup for QD illumination and XPS experiments is detailed, and the experimental results on the investigation of the effect of oxygen and water on the QD fluorescence are presented.

Chapter 3 is an experimental investigation into possible DNA wrapping around quantum dots. A literature overview about experimental results and theoretical models of DNA strand wrapping around nanostructures is presented. The sample preparation procedures and experimental setup are detailed, followed by the presentation of experimental results on imaging of mixtures of DNA and QDs.

Chapter 4 introduces the theoretical and experimental background regarding surface plasmon polaritons and fluorescence enhancement. The fabrication techniques of gold nanovoids are detailed and the theoretical localised surface plasmon modes for various nanovoid geometries are modelled. Experimental results of fluorescently labelled DNA stretched over glass, gold and nanovoid substrates are compared, and fluorescent lifetime measurement results of fluorescently labelled DNA stretched over glass and nanovoids are presented.

Chapter 5 presents a summary of the experimental results of the previous chapters and gives suggestions for future work.

Chapter 2

2 Influence of the Atmosphere on Quantum Dot Fluorescence

Colloidal semiconductor quantum dots (QDs) potentially lend themselves as attractive biomarkers for single DNA analysis due to their high quantum yield, high photo-stability, and the possibility of facilitated colour multiplexing compared to traditional organic fluorophores.[16] There are, however in part, contradictory reports on the effect of the presence of oxygen and water molecules on QD fluorescence under continuous QD illumination.[60-68] Hence, this chapter investigates, in detail, the effect of oxygen and water molecules on the fluorescence of core/shell CdSe/ZnS QDs.

2.1 Optical Properties of Quantum Dots

This section details the optical properties of colloidal semiconductor quantum dots, which includes theoretical models and experimental observations typically found in the literature, as well as a comparison of the optical properties of quantum dots and organic dyes.

2.1.1 Energy States

Quantum Dots are semiconductor nanocrytsals of a few nanometres in diameter, in which an electron is confined in all three spatial dimensions, leading to quantum effects. We first consider the case of a bulk semiconductor in 1 dimension of length *L*. Neglecting the ionic potential from the core ions of the lattice, the energy of an electron is equal to the kinetic energy, which is equal to (appendix A.1)

$$E = \frac{\hbar^2 k^2}{2m_e} = \frac{\hbar^2 n^2 \pi^2}{2m_e L^2} \tag{2.1}$$

where $k=n\pi/L$ is the wavevector, $n>0$ is a positive integer, m_e is the electron mass and $\hbar$ is the reduced Planck`s constant. Neighbouring states in k-space are separated by (appendix A.1)

$$\Delta k = \pi / L \tag{2.2}$$

For macroscopic values of L, Δk is small, so that the energy levels merge into a continuous energy band (Figure 2.1(a)). In a periodic lattice of period a, the periodic ionic potential due to the core ions can be assumed to be sinusoidal (appendix A.1), and electrons in a periodic lattice diffract off the periodic lattice potential, leading to energy bands separated by an energy gap (Figure 2.1(a)). The size of the energy gap is material dependent. In a semiconductor, the valence band is completely filled with electrons while the conduction band is empty. An electron excited from the valence band into the conduction band leaves behind a hole in the conduction band. Due to their electrostatic attraction, the hole and electron can form a bound state, an exciton, which has an average size equal to the Bohr radius (R_B). A quantum dot is smaller than the Bohr radius and thus is a zero-dimensional structure which confines the exciton in all three dimensions, leading to quantum effects.

There exist two confinement regimes: depending on the relative size of the QD radius (R) and the Bohr radius (R_B), the exciton can be either weakly or strongly confined. If $R>R_B$, the exciton is weakly confined and the electron and hole can be considered as a single particle (the exciton) held together by the coulombic attraction between the oppositely charged electron and hole, and weak quantum effects already occur. If $R<R_B$, the electron and hole are strongly confined, resulting in an increase in the kinetic energy to a value much greater than the coulombic attraction, so that the electron and hole are unbound from each other and can be considered as individual particles. The exciton Bohr radius is equal to[69]

$$R_B = \frac{4\pi\varepsilon\hbar^2}{m_r e^2} \tag{2.3}$$

where $\varepsilon=\varepsilon_0\varepsilon_r$ and $\varepsilon_0/\varepsilon_r$ is the dielectric constant of free space/the crystal, m_r is the exciton reduced mass, which is defined as $\frac{1}{m_r}=\left(\frac{1}{m_e*}+\frac{1}{m_h*}\right)$, where $m_{e/h}*$ is the effective mass of the electron/hole in a semiconductor due to interaction with the lattice, and e is the electron charge. Thus, $R_B(\varepsilon)$ depends on the material, and is typically a few nm in size. For instance, CdSe has a Bohr radius equal to 5.4 nm.[70]

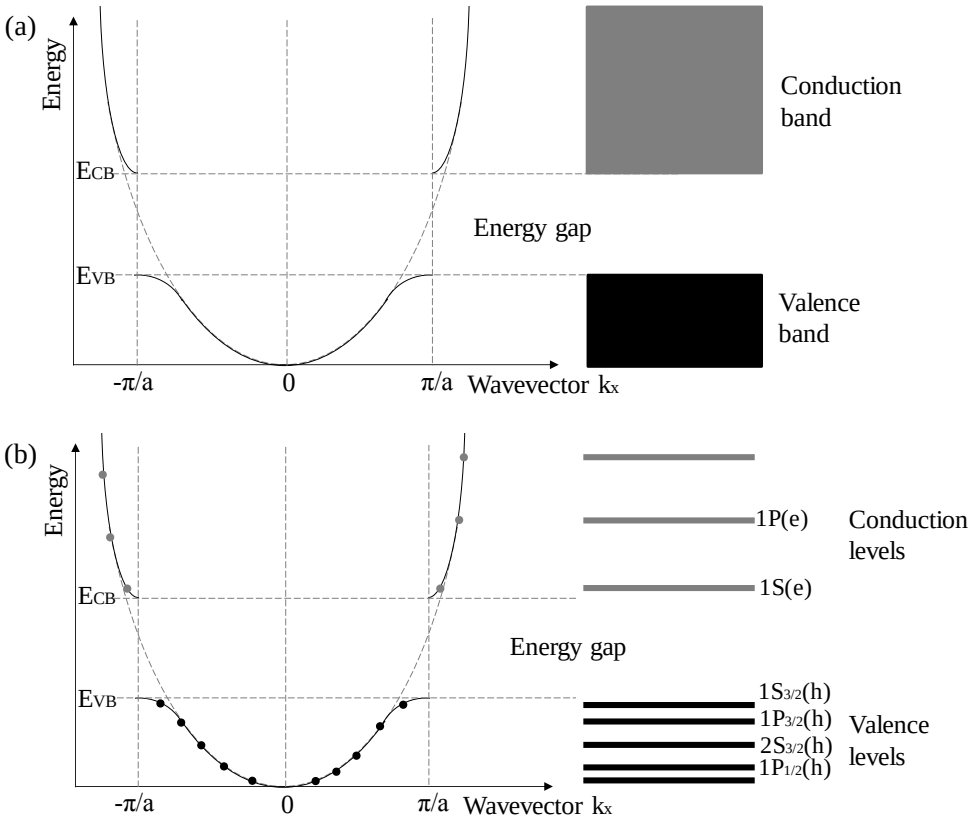

Figure 2.1:Dispersion curve of an electron inside (a) a bulk semiconductor and (b) a semiconductor quantum dot (adapted from[69]). The discrete energy levels in a QD can be labelled with quantum numbers n, L and F (as shown for a CdSe QD[71] in figure 2.1(b)).

The reduction in material size increases the separation between states in k-space (Figure 2.1(b) and equation 2.2), so that the energy spacing between neighbouring states increases (equation 2.1), leading to the formation of discrete energy levels (figure 2.1(b)). The energy levels of a strongly confined electron and hole in a QD can be labelled like atomic orbitals with the principle quantum number *n=1, 2, 3,...* and the orbital angular quantum number *L=0, 1, 2,...= S, P, D,...*The hole states are additionally

labelled with the subscript *F*, which is the total angular momentum quantum number $\vec{F} = \vec{L} + \vec{J}$, and takes into account the Bloch function angular momentum *J* due to confinement-induced mixing between different valence subbands.[71]

The increase in kinetic energy with reduced dimensionality (equation 2.1) leads to an increased energy gap in QDs compared to in bulk ($E_g(bulk)$) (Figure 2.2(a) in section 2.1.2). The energy gap in a spherical QD in the strong confinement regime is equal to [72-74]

$$E_g(QD) = E_g(bulk) + \frac{\hbar^2 \pi^2}{2m_r R^2} - \frac{1.8e^2}{\varepsilon R} \qquad (2.4)$$

The first term of equation 2.4 is the bulk crystal band gap, the second term is the lowest kinetic energy of the excited electron and excited hole, while the third term describes the attractive Coulomb interaction between the excited electron and the excited hole, and is negligible relative to the kinetic energy in the strong confinement regime. As can be seen from equation 2.4, unlike in bulk, the energy gap in a QD is not constant, but varies with QD size, with a reduced QDs radius yielding an increased energy gap.

2.1.2 Fluorescence and Absorption Spectrum

In the QD ground state, the valence band is filled with electrons, and the conduction band is filled with holes. Light of energy equal to or higher than the energy gap can excite an electron into the conduction band, leaving behind a hole in the valence band. Both excited charge carriers non-radiatively relax to the energy gap edge within a few picoseconds. Radiative electron-hole recombination, across the energy gap, occurs within nanoseconds, releasing a photon of energy equal the energy gap (equation 2.4 in section 2.1.1).

Due to quantisation, the density of states in a QD consists of well-separated delta-like states (Figure 2.2(b)), whereas the density of states of a bulk semiconductor scales as the square-root of the energy (Figure 2.2(b)). Figure 2.2(a) shows the allowed optical transitions in a QD, which should

be clearly identifiable in the QD absorption spectrum. While the first absorption peak is clearly identifiable, higher energy excitation peaks merge into a continuous absorption spectrum (Figure 2.3(i)). This is due to two reasons (1) the energy spacing between energy levels decreases with increasing energy, and (2) broadening in the individual energy peaks (see below). Beyond the first excitation peak, the absorbance increases with increasing excitation energy (Figure 2.3(i)), due to a higher density of states at higher energies. The absorption onset and fluorescence peak is blue-shifted in QDs relative to the same bulk crystal, and the energy gap increases with smaller QD size (Figure 2.3(i) and 2.3(ii)) as the energy gap in QDs is strongly dependent on QD size (equation 2.4 in section 2.1.1).

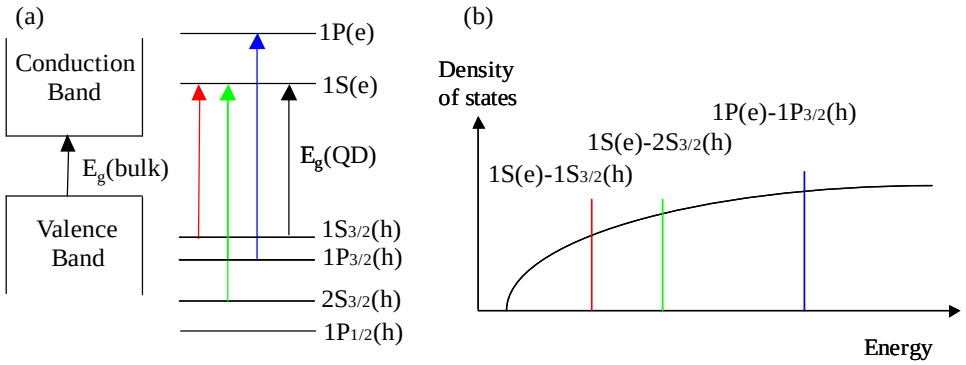

Figure 2.2: (a) Energy levels in a bulk CdSe semiconductor (left) and a CdSe QD (right),[71] arrows show allowed optical transitions (b) Density of states versus energy for bulk CdSe (black line) and a CdSe QD (coloured).[71]

The absorption and fluorescence peaks are broadened homogeneously and inhomogeneously: Homogeneous (intrinsic) broadening occurs in single QDs and is caused mainly by electron-phonon interactions. According to the Heisenberg uncertainty principle $\Delta E \Delta t \geq \hbar$, where ΔE represents the uncertainty in fluorescence energy and Δt the fluorescence lifetime, phonon interactions shorten the fluorescence lifetime, broadening the fluorescence peak. Phonon-interactions and thus the width of the fluorescence peak can be reduced with decreasing temperature.[75, 76] In a QD ensemble, additional broadening due to a distribution of sizes and shapes in QDs, and a distribution of localised charges on the QD surface, occurs (inhomogeneous or extrinsic broadening). Charges on the QD surface can induce a local electric field,

thus altering the separation between excited electron and hole, modifying the fluorescence energy (Stark effect).[77, 78] Temporal fluctuations in the local electric field can thus broaden the fluorescence peak for QD ensembles.[77]

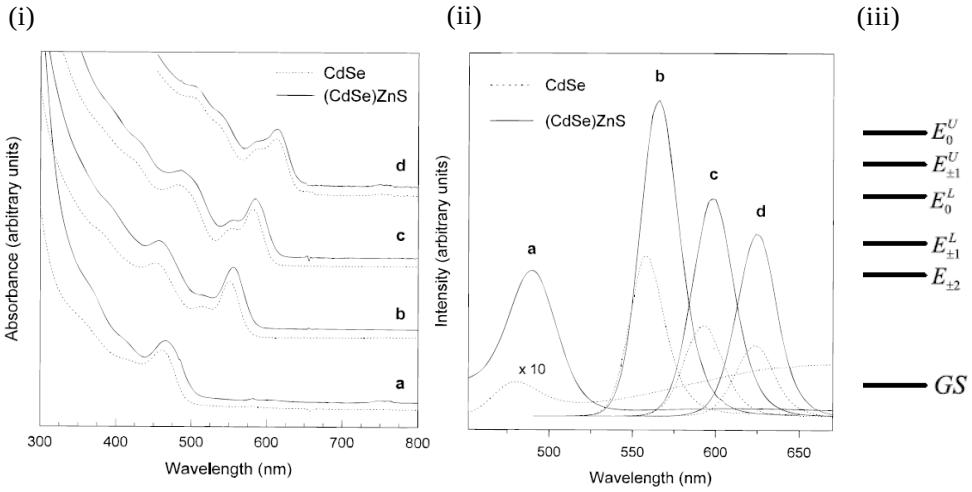

Figure 2.3: (i) Absorption spectrum and (ii) fluorescence spectrum of core CdSe (dashed line) and core/shell CdSe/ZnS QDs (continuous line) of core diameters of (a) 2.3 (b) 4.2 (c) 4.8 (d) 5.5 nm[17]; (iii) Energy level diagram of the lowest exciton state and the ground state (GS) in a CdSe QD. States are labelled according to the total angular momentum projection along the wurtzite hexagonal axis.[80]

The fluorescence peak is experimentally observed to be red-shifted relative to the absorption onset (Stokes shift), which cannot be explained by equation 2.4 in section 2.1.1. The Stokes shift is equal to a few milli-electron-Volts (meV), and increases with increasing confinement.[79] To explain the Stokes shift, equation 2.4 must be extended to include the electron-hole exchange interaction, and an asymmetric crystal field.[79, 80] The effect of this is to lift the degeneracy of the lowest excited state 1s(e)-$1s_{3/2}$(h), splitting it into five separate states[79, 80] (Figure 2.3(iii)). All of these states are optically active, except the first and third lowest in energy, $E_{\pm2}$ and E^L_0, which are optically dark.[80] Absorption is to the lowest bright state, from where thermal relaxation to the lowest dark state occurs. [79] Emission is from the dark state and is mediated by longitudinal-optical phonons, to conserve momentum.[79] Thus, the Stokes shift is equal to the energy difference between the two lowest states, which increases with increasing confinement.[79]

2.1.2.1 Surface Trap States

A surface trap state is a site on the QD surface that can trap a photo-generated charge carrier from the QD core. The trapped, localised charge carrier decays via a route other than fluorescence, so that surface traps have the effect of reducing the fluorescence quantum yield. As the surface to volume ratio is large in QDs, the limitation of surface trap states is crucial to obtaining high quantum yields. Surface trap sites include dangling (unpassivated) surface atoms, surface defects, and unbonded (free) electrons, and their occurrence can be minimised by coating the QD core with ligand molecules or a few monolayers of wide-gap inorganic semiconductor.

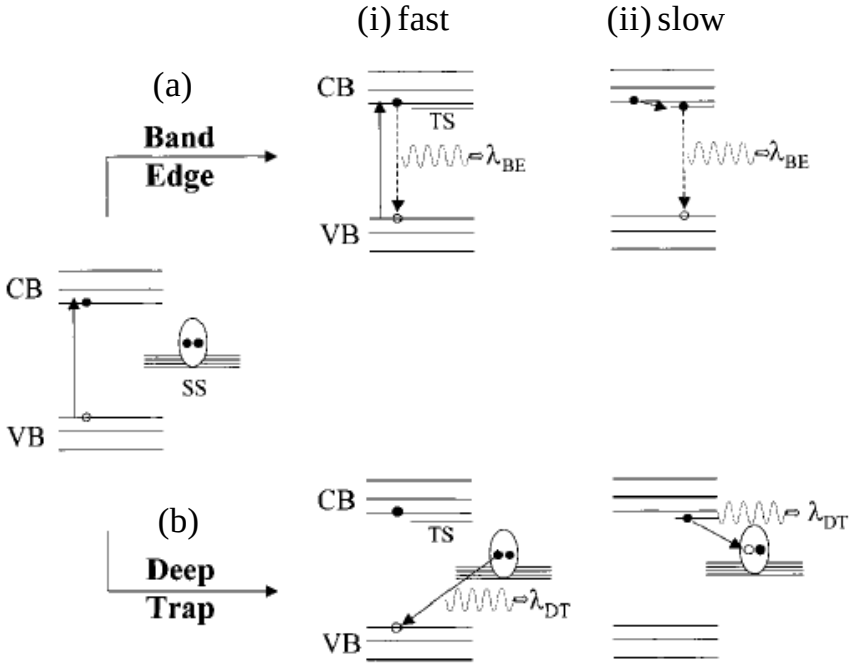

Figure 2.4: Illustration of the proposed (i)fast radiative and (ii) slow radiative de-excitation routes via (a) the bandedge or (b) deep trap states due to surface selenium (SS) dangling bonds in CdSe QDs. The excited electron either(a)(i)quickly recombines radiatively with the hole in the valence band via the energy gap , or(a)(ii) or relaxes into a long-lived triplet state (TS), which lies a few meV below the singlet state, before radiatively decaying via the energy gap. Both radiative decay mechanisms in (a) yield bandedge emission (λ_{BE}). (b)(i) an electron trapped in the SS state can quickly recombine with a hole in the valence energy levels, resulting in NIR deep trap emission, or (b)(ii)an electron slowly migrates towards a hole trapped in the SS site, before radiatively recombining with each other.[81]

We now consider core QDs in more detail. Carrier loss to surface trap states yields quantum yields as low as 5%[17] and a broad emission peak that is red-shifted relative to the narrow fluorescence peak (Figure

2.3(ii)(10x dashed line) in section 2.1.2). The red-shifted broad emission band is attributed to emission from surface trap sites. As an example, in cadmium-selenide (CdSe) QDs the main trap sites for holes are selenium (Se) dangling bonds on the QD surface, which have energy levels within the energy gap[82] (Figure 2.4 left). Radiative recombination of a photo-generated hole trapped within the surface Se dangling site can occur with the photo-generated electron in the QD core that slowly migrates to the QD surface[81] (Figure 2.4(ii)(b)). This yields long-lived, near-infra-red (NIR), deep-trap (DT) emission.[81] Experiments have also revealed a short-lived NIR emission component, which is attributed to radiative recombination of an electron in the Se dangling bond with a photo-generated hole in the valence band[81] (Figure 2.4(i)(b)). Furthermore, the effect of surface trapping of one charge carrier is that a single delocalised charge carrier within the QD core is left behind, which induces non-radiative decay of subsequently photo-generated excitons, resulting in a non-fluorescent QD (section 2.2.1).

By coating tri-n-octylphosphine oxide (TOPO)-ligands around a CdSe QD core Se surface sites are passivated by lifting the energy levels from the dangling atoms out of the energy gap with the ligand potential, leaving the energy gap free of dangling orbital states.[83] A few monolayers of ZnS around the CdSe QD core, on the other hand, passivates both Se and Cd surface sites. The energy gap of the ZnS shell exceeds that of the CdSe core, ensuring that photo-excited carriers stay confined within the QD core, further reducing carrier trapping into any remaining surface traps. The addition of a passivating semiconductor shell around a QD core slightly red-shifts the absorption onset and the fluorescence peak (Figure 2.3(i) and (ii) in section 2.1.2), as the electron wavefunction is less confined and thus extends partially into the QD shell.[17] Core/shell QDs, such as CdSe/ZnS, can reach quantum yields in excess of 50%[17] or even up to 85%.[84]

2.1.3 Inorganic Quantum Dots and Organic Fluorophores

Quantum dots have several advantages as fluorescent labels compared to organic fluorophores, such as rhodamine, fluorescein or cyanine dyes, and this is leading to their increased use in biological analytical applications.[85-88]

First, the energy of the fluorescence peak of fluorophores is specific to the fluorophore composition. In contrast, in QDs, the fluorescence peak can be tuned with QD size. For instance, a 2.3 nm diameter CdSe QD emits at 480 nm, while a 5.5 nm diameter CdSe QDs emits at 650 nm; QDs spanning the whole of the visible spectrum can be fabricated.[17] Figure 2.5 shows the absorption and fluorescence spectrum of a typical quantum dots (Figure 2.5(a)) and fluorophore (Figure 2.5(b)).

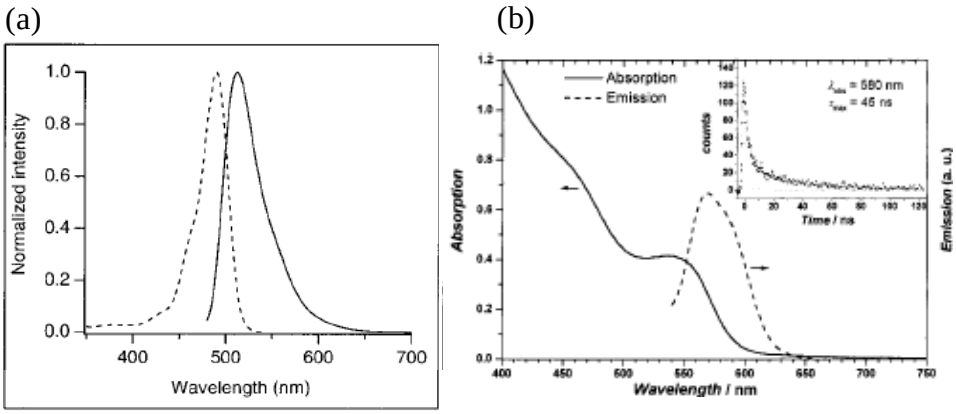

Figure 2.5: Absorption (dashed)and emission (solid) spectrum of (a) fluorescein[91] (b)CdSe QDs.[92]

It can be seen that while fluorophores have a red-tailed fluorescence peak, QDs have a narrow, symmetric fluorescence peak. The full-width-half-maximum (FWHM) of the fluorescence peak ranges between 35 to 100 nm for fluorophores,[16] and is equal to only 30 nm for QDs with a 5% size-variation.[89] The absorption spectrum of QD is broader than that of fluorophores (Figure 2.5(a) and 2.5(b)). The narrow symmetric fluorescence peak and broad absorption spectrum of QDs, compared to a broad fluorescence peak and narrow absorption spectrum of fluorophores, makes QDs suitable for multiplexing applications, yielding more fluorescence colours with a single excitation wavelength. For instance, up

to five different fluorescence colours can be used simultaneously with a single excitation wavelength using QDs, while this number is reduced to three with fluorophores.[16]

QDs can absorb and fluoresce more efficiently than fluorophores, yielding higher fluorescence intensities from QDs compared to from fluorophores. For instance, the extinction coefficient at the first absorption peak in QDs can range from 10^5 to 10^6 $M^{-1}cm^{-1}$, while extinction coefficient of fluorophores at the absorption peak is equal to only (0.25 to 2.5)x10^5 M^{-1} cm^{-1}.[16] The quantum yield of organic fluorophores in the visible can vary considerably depending of the dye, equalling for example 3% for Cy3 in ethanol and 97% Fluorescein in ethanol.[16] Quantum yields of 50%[17] and up to 85%[90] have been reported for core/shell QDs.

Also, core/shell QDs are more resistant to photobleaching than fluorophores, owing to the shell: the semiconductor shell around the QD core protects the fluorescing QD core from photo-induced reaction with surrounding oxygen (photo-oxidation), which can result in photo-bleaching.[17] This makes QDs more suited for observations over longer timescales, such as dynamic and quantitative measurements. For instance, QDs resist photo-oxidative bleaching for more than 6 times longer than Alexa fluorophores when excited at 485 nm with a 100 W mercury lamp.[11]

2.2 Blinking and Photo-induced Fluorescence Enhancement

Blinking and photo-induced fluorescence enhancement (PFE) are two phenomena observed for quantum dots (QDs) when continuously illuminated. In contrast, fluorophores only blink when illuminated, albeit by a different mechanism, as compared to QDs. This chapter looks into the proposed origin of blinking and PFE in quantum dots, as well as reported atmospheric effects on PFE.

2.2.1 Blinking

The random switching between an emitting (bright) and non-emitting (dark) state of a continuously excited emitter is called blinking or fluorescence intermittency (FI) (Figure 2.6). The uncorrelated FI between single emitters means FI is averaged out in ensembles and thus observable in single emitters only.

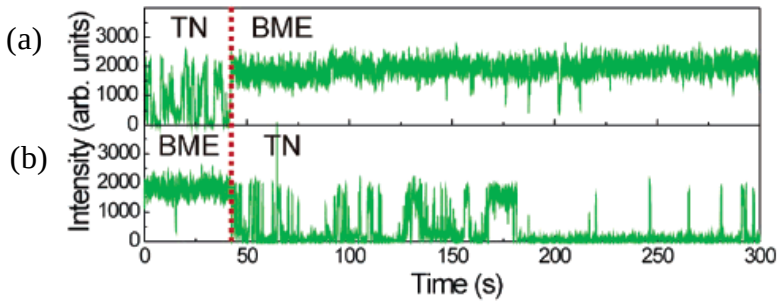

Figure 2.6: Intensity timetrace of a single QDs CdSe QD in Tris-HCl, NaCl (TN buffer) in the (a) presence or (b) absence of electron-donating β-mercaptoethanol (BME).[93]

Fluorophores blink because of photo-induced fluorophore isomerisation. Photo-induced reorientation of the π-electrons from the anti-bonding orbital about the sigma bond[94] results in a change in the absorption resonance of the fluorophore isomer compared to the fluorophore. Thus, the excitation energy for the fluorophore cannot excite the fluorophore isomer which is now in a dark state. In contrast, the blinking in QDs is believed to be due to switching between a neutral (bright) and charged (dark) QD state.[95, 96] Gooding *et al.* have shown that injection of holes into CdSe/ZnS QDs results in complete emission quenching.[97] An exciton in a neutral QD, within nanoseconds of excitation, radiatively

recombines across the energy gap, emitting a photon. A charged QD is one that has a single delocalised charge carrier, either a hole or an electron, inside its core. Any subsequently photo-induced exciton non-radiatively transfers its energy to any extra charge carrier present in the core (non-radiative Auger process), instead of emitting a photon.[98] In QDs, unlike in bulk, the non-radiative Auger process occurs on a faster timescale than fluorescence (picoseconds and nanoseconds, respectively), as it is mediated by the Coulomb interaction, which is increased in QDs compared to in bulk.[99]

QD charging (darkening) is a result of trapping of a hole or electron, leaving behind a single delocalised charge carrier inside the QD core (QD ionisation). The QD returns to a bright state when the core is neutralised, which occurs via the (thermal) return of the trapped charge to the QD core, the capture of an electron from the surrounding into the QD core[100] or an additional Auger ionisation event. The trap states are proposed to be those on the QD surface or in the QD environment (such as deep traps in the surrounding matrix[101]). Ionisation events have been experimentally shown to become more frequent with increasing excitation intensity, due to an additional Auger process involving a neutral QD that contains two excitons simultaneously inside the core.[103]. Auger-assisted tunnelling is the main ionisation route to capping and substrate traps for excitation intensities in excess of 0.1 kW/cm^2 (emission peak at 575 nm, excitation at 488 nm).[102] In this regime, a second exciton can be excited before the first had time to radiatively relax via the energy gap. The recombination energy of one exciton is then given non-radiatively to a charge carrier in the second exciton, transferring that charge carrier to a higher energy state, from where it can either relax non radiatively or scatter to a surface trap or an external trap state, ionising the QD.[103]

Blinking has been experimentally suppressed by coating the core QD with a semiconductor shell[95] or by coating with electron-donating molecules.[93] For instance, ZnS coated CdSe QDs showed longer on states and fewer off states than bare CdSe QDs, which is attributed a reduced likelihood of charging events due to passivated surface trap

sites.[95] As another example, the addition of thiols to aqueous solution of CdSe/ZnS/streptavidin QDs has been experimentally shown to considerably prolong the duration of the QD on-state (Figure 2.6), which is due to the filling of vacant electron surface trap states on the QD surface by electron donating thiols, reducing the capturing frequency of core electrons.[93] A similar charge transport hypothesis has been suggested to explain reduced blinking of CdSe QDs surface functionalised with oligonucleotides.[104] An indium tin oxide (ITO) substrate has also been shown to suppress blinking, by donating electrons to traps below the CdSe QD conduction band edge, which can then quickly recombine with any single delocalised hole inside the core.[105]

The absence of oxygen has also been experimentally been shown to increase the mean on-time duration in CdSe/ZnS QDs, but does not change the mean off-time duration.[65] This is attributed to a photo-induced reaction of the QD with the electro-negative oxygen, such as transfer of an Auger electron from the QD core to surface adsorbed oxygen, leaving behind a positively charged dark QD and oxygen radical anion (superoxide).[65]

Jin *et al.*[105] have suggested that only positively charged QDs are dark, as derived from observations that blinking is suppressed by the presence of electron donors[93, 104] and enhanced by the presence of electron scavengers,[65] and that negatively charged QDs have a fluorescence yield of up to 15% of that of neutral QDs, which might be bright enough to be considered an on state.[94] However, experimental results that show a reduced duration of the dark state in the presence of electronegative oxygen suggest that the dark state is depopulated by electron transfer to adsorbed oxygen,[64] implying that negatively charged QDs are also dark. However, there is no consensus on this in the literature.

Experiments have revealed occasional shifts in emission energy following an off-period.[106] These Stark shifts are attributed to a permanent redistribution of charges localised on the QD surface during a trapping and de-trapping event, which changes the local electric field on the QD surface.[106] It has been shown that a QD have a permanent

internal dipole moment due to charges localised on the QD surface,[107] and that a change in surface charge causes spectral shifts in the fluorescence peak.[77]

A power law dependence on the blinking decay (number of on/off times versus on/off duration) is observed experimentally, and various models have been suggested to explain this, such as a distribution of many trap states[108] and a fluctuating barrier model.[109]

2.2.2 Photo-induced Fluorescence Enhancement Models

Photo-induced fluorescence enhancement (PFE) has been observed in continuously excited CdSe/ZnS core/shell QD ensembles under various conditions, such as dissolved in solution, on substrates prepared as mono- or multilayers,[110] on various substrates[67, 110] under dry and humid gaseous atmospheres,[67] and various capping agents.[67, 111] Accordingly, various theories have been put forward to explain the origin of PFE, such as (i) photo-induced passivation or neutralisation of trap sites on the QD surface by photo-induced adsorption of water molecules[64, 112] (ii) photo-induced re-arrangement of capping agents on the QD surface[66] (iii) photo-ionisation of QDs and ejected electrons suppressing the photo-ionisation of nearby QDs (photo-electrification)[110, 112-115] and (iv) photo-neutralisation of charged sites in and outside the QDs. Furthermore, the fluorescence yield of QD has been found to depend upon the presence of oxygen (as an electron acceptor and by energy transfer),[64, 92] electron donors or acceptors,[116-119] as well as the properties of the substrate[120] and QD density (mono-or multilayers).[110] This section aims to summarize the main PFE theories suggested in the literature.

2.2.2.1 Photo-electrification

According to the photo-electrification model, in addition to radiative recombination across the energy gap, there exist trap states in the glass substrate and the QD capping agent to which an excited electron in the QD core can tunnel.[110] Trapped carriers in the capping agent can quickly

return to the QD core followed by radiative recombination across the energy gap, resulting in no overall loss of fluorescence, but carriers trapped in the substrate are lost, as they either thermally relax to the QD ground state (if trapped in a near substrate trap state), or stay trapped in the long-lived, far trap state (Figure 2.7).[110]

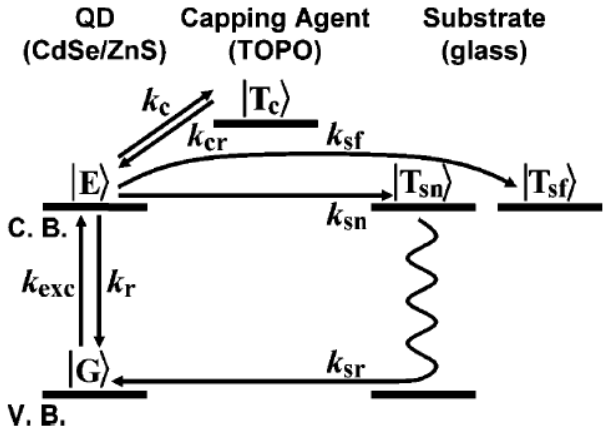

Figure 2.7: Illustration of the Photo-electrification model: allowed transitions for a monolayer of TOPO capped core/shell CdSe/ZnS QDs on glass: electrons in the excited QD state IE> can auger-tunnel to substrate trap states T_{sn} and T_{sf} (near and far substrate traps, respectively) at a rate of k_{sn} and k_{sf}, respectively. Electrons in T_{sn} can return to the QD ground state (IG>) at a rate of k_{sr} via thermal relaxation through trap sites with various energy levels existing in the substrate, while electrons in the capping traps return to the excited QD state at a rate of k_c. CdSe/ZnS QDs were illuminated on glass under a dry nitrogen atmosphere.[110]

The electrostatic potential due to electrons trapped in far substrate trap states in the substrate suppresses electron tunnelling from the core of nearby neutral QDs to the substrate, and as a result, increases trapping to the capping agent, reducing carrier loss.[110] The capping agent is assumed to be far enough away from the far substrate traps as not to be affected by the electrostatic blockage.[110] Continuous excitation builds up the electron population in the far substrate trap state, with a consequently increased electrostatic blockage reducing carrier loss to the substrate, which increases the QY of the QD ensemble.[110] Stabilisation of the population in the substrate and capping trap states after prolonged illumination saturates the quantum yield.[110] Although at the saturation point more ionised QDs exist in the ensemble than before illumination, the quantum yield of the still neutral, emissive QDs is higher than before saturation, yielding an overall PFE effect.[110] Auger-assisted tunnelling

is suggested to be the main ionisation route for excitation intensities in excess of 0.1 kW/cm^2 (emission peak at 575 nm, excitation at 488 nm).[102]

2.2.2.2 Photo-transformation Model and Fluorescence Quenching by Surface Ligands

PFE has been experimentally observed for continuously excited CdSe/ZnS QDs capped with various surface ligands.[66] It is suggested that an electron or hole trapped in a QD surface trap state either non-radiatively decays to lower-lying traps, eventually producing lower energy emission, or thermalises back to the QD core, where subsequent, delayed radiative decay via the energy gap occurs (Figure 2.8(a)). The PFE is then attributed to the stabilisation of those surface traps, increasing the likelihood of trapped charges returning to the QD core (Figure 2.8(a)), effectively reducing carrier loss and increasing the fluorescence yield.

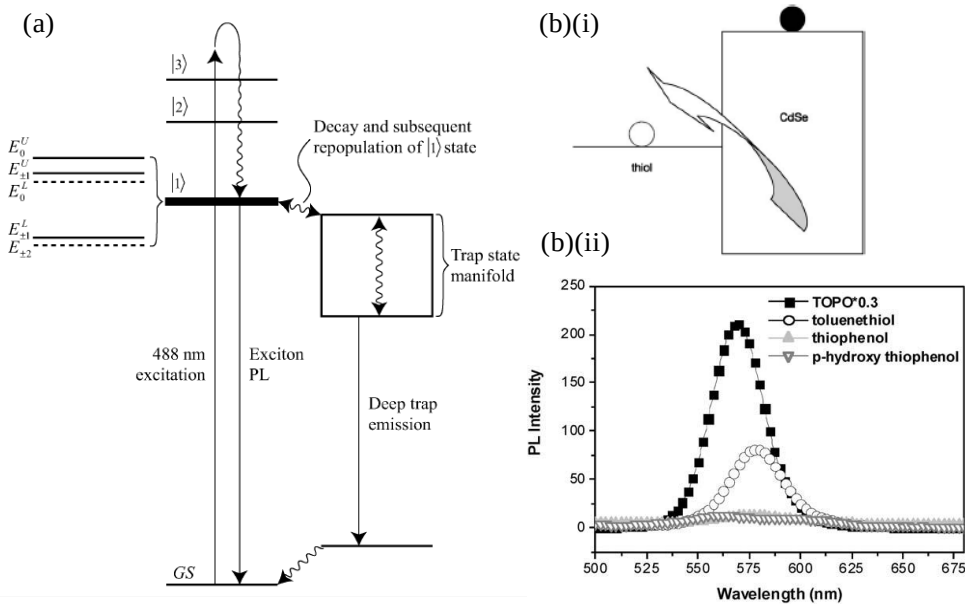

Figure 2.8: Effect of surface ligands (a) PFE model of photo-transformation[66] (b) fluorescence quenching: different surface ligands on CdSe surface (b)(i) Schematic of energy levels of excitons at the surface of thiol capped CdSe QD. QDs are dissolved in water[121] (b)(ii) fluorescence spectrum with surface ligands thiophenol, p-hydroxy thiophenol, toluenethiol, TOPO.[121]

The stabilisation of surface traps is attributed to the photo-induced re-arrangement of ligands on the QD surface. Stabilisation by water, either through coordination through oxygen or due to the water dipole moment, has also been suggested to occur.[66] Experimental evidence for the

stabilisation of surface traps is an increase in fluorescence lifetime that accompanies PFE with illumination.[66]

Various hole-accepting (electron-donating) ligands on the QD surface have been experimentally shown to quench QD fluorescence[121](Figure 2.8(b)(ii)). This is attributed to quick charge separation of an exciton in the QD, as observed in a reduced fluorescence lifetime with hole-accepting compared to non-hole accepting ligands on the QD surface.[121] It is suggested that surface ligands scavenge a photo-excited hole from the valence band edge if the redox potential of the ligand lies within the QD energy gap[121] (Figure 2.8(b)(i)). Electron acceptors, such as benzoquinone, can also quench QD fluorescence.[119] Furthermore, the photo-excited hole scavenged by a surface- thiol can be a precursor to QD oxidation (section 2.2.2.4).

2.2.2.3 Effect of Water

Two main theories exist as to the role of atmospheric water in PFE: (i) photo-activation[115, 122] and (ii) photo-neutralisation.[68] Water is also suggested to facilitate QD dark state depopulation in the presence of oxygen[64] (section 2.2.2.4).

2.2.2.3.1. Photo-activation

According to the Photo-activation model, under illumination, atmospheric water molecules adsorb onto the CdSe QD surface where they photo-passivate surface trap states, causing PFE[122] (Figure 2.9, path A). There are two examples of evidence supporting this theory: (i) PFE occurs under humid atmospheres (oxygen (O_2) and nitrogen (N_2)), but not under dry atmospheres, for illuminated CdSe QDs-this suggests water is central to PFE, and (ii) cycling from vacuum to ambient air increases the fluorescence bandedge peak, and decreases the deep trap emission peak, suggesting trap state passivation occurs. The non-complete reversibility of the bandedge fluorescence intensity upon return from air to vacuum has lead Cordero *et al.* to suggest the incomplete removal of all surface adsorbates, i.e. photo-dissociative adsorption: the presence of chemisorbed

OH groups and H atoms, in addition to the physisorbed H_2O molecules, on the QD surface.[122]

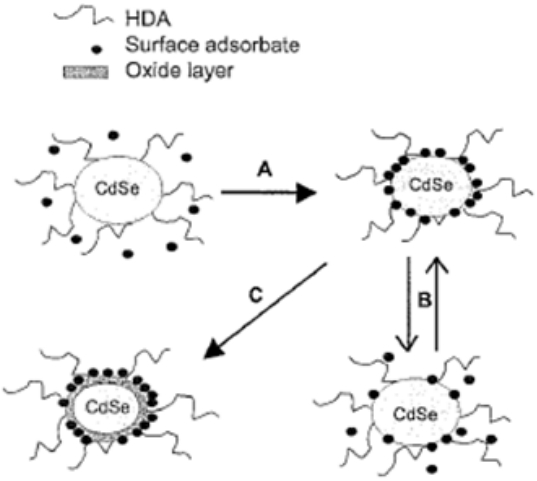

Figure 2.9: Photo-activation model: Light induces adsorption of water molecules onto QD surface (path A); water adsorbates oxidise QD surface (path C), quasi-reversible adsorption under return from air to vacuum (path B), or under dark conditions. Samples were monolayers of CdSe QDs and CdSe/ZnS QDs on glass.[122]

Signs of QD photo-oxidation, i.e. fluorescence decay, fluorescence peak blue-shift and broadening of the fluorescence peak (section 2.2.2.4.1), occur under prolonged illumination of CdSe QDs under ambient air, and is assigned to water oxidising the QD surface (Figure 2.9, path C). However, ambient air does contain oxygen molecules, so that under ambient air photo-oxidation by oxygen cannot be excluded. Furthermore, a faster PFE is observed for core CdSe QDs compared to core/shell CdSe/ZnS QDs illuminated under air.

2.2.2.3.2. Photo-neutralisation

It is assumed that some traps on or near the QD surface are charged, creating a local electric field that increases the exciton size, and hence induces a Stark fluorescence red-shift, and induces carrier trapping into charged traps.[68] Trapping switches the QD from an "on" to an "off" state, with the switch back to the "on" state occurring after the trapped charge returns into the QD core. According to the photo-neutralisation model, illumination photo-induces the adsorption of ambient water molecules onto the QD surface, and the polar water adsorbates electrostatically shield the charges in trap sites, neutralising, and thus

inactivating, charged traps.[67, 68, 123] As a result, trapping events are less frequent and the emission yield is increased.[68]

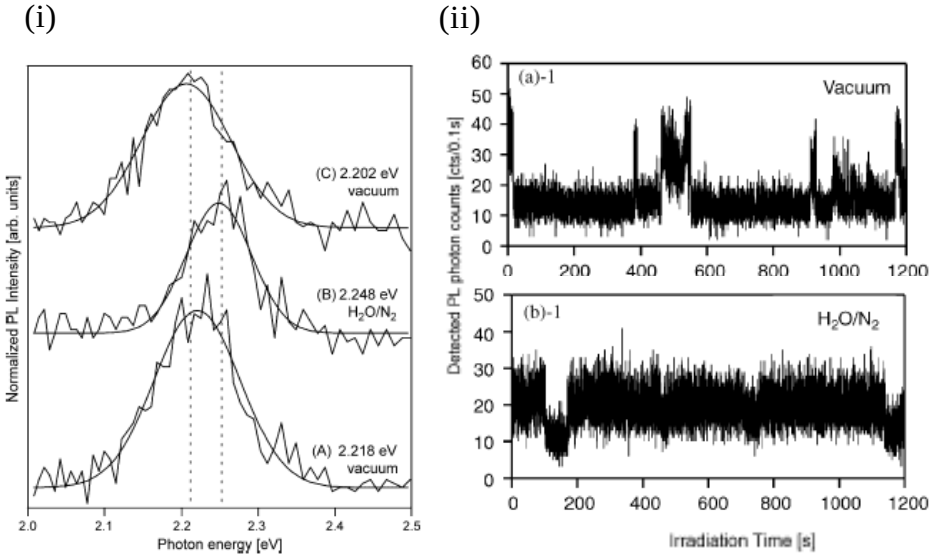

Figure 2.10: The Photo-neutralisation model:(a) reversible fluorescence peak blue-shift and peak sharpening of single QD when atmosphere is cycled between vacuum (A,C) and H_2O/N_2 atmosphere[68] (b) fluorescence timetrace of single QD in (ii)(a) vacuum and (ii)(b) under an H_2O/N_2 atmosphere.[67] Samples were CdSe/ZnS/TOPO QDs.[67, 68]

Experimental evidence for the photo-neutralisation model are (i) longer "on" times in single QDs in the presence compared to in the absence of water molecules[67] (Figure 2.10(ii)), suggesting that water adsorbates suppress the occurrence of carrier trapping[67] and (ii) upon transfer of a single QD from vacuum into humid nitrogen atmosphere (a) a reversible blue-shift occurs[68] (figure 2.10(i)), indicating a reduced stark red-shift due to water adsorbates shielding the charged surface traps[68] and (b) the fluorescence peak width narrows[68] (Figure 2.10(i)) suggesting reduced fluctuations in charged surface traps and thus internal electric field, which otherwise broaden the fluorescence peak.[68]

It should be noted that the PFE behaviour of core/shell CdSe/ZnS QDs[67] (TOPO capped) differs from those of core CdSe QDs (HDA capped).[122] In the absence of water, PFE does not occur for core QDs,[122] but an increase in quantum yield by about 40% is seen within 20 minutes of illumination does occur for core/shell QDs[67, 123] (excitation at 488 nm, 66.7W/cm^2 and 610 nm fluorescence peak).[68]

2.2.2.4 Effects of Oxygen

Various reports, some conflicting, describing the effects of oxygen on the QD fluorescence yield and PFE effect, exist.[61, 64, 122, 124] One of the earliest of these studies was that of van Sark *et al.* where a reduction in the fluorescence of CdSe/ZnS QDs in air was observed along with a fluorescence spectral shift to the blue.[61] It was suggested that the QDs were photo-oxidised and this resulted in both a reduction in the core size as well as a possible degradation of the ZnS shell. On the other hand, and initial PFE has been observed to precede photo-oxidation in CdSe/CdS and CdSe QDs, which is attributed to photo-corrosion.[125] Also, reversible fluorescence reduction under oxygen has been observed for CdSe/ZnS QDs, which is attributed to shortening in the "on" time duration of blinking QDs.[65] The "on"-time shortening is explained by oxygen charging the QD by transfer of an Auger electron from a neutral QD core to surface adsorbed oxygen, creating a positively charged, dark QD and superoxide. This is in contrast to Muller *et al.*,[64] who, have observed a shortening in the "off" time duration under ambient air, compared to under vacuum, for CdSe/ZnS QDs, and as a result, an increase in the fluorescence yield under air. This is attributed to the de-charging of dark QDs by the direct transfer of a single electron from the QD core at the conduction band to surface adsorbed oxygen, creating a neutral, bright QD and superoxide.[64] In contrast to oxygen (which is assumed to be dry), air also contains water molecules, which may facilitate the electron transfer process from QD core to oxygen adsorbates.[64]

This section summarises the main theories on the effect of oxygen on the QD fluorescence yield and PFE effect.

2.2.2.4.1 Photo-oxidation

Photo-induced oxidation (photo-oxidation) of the QD core creates new surface trap states and shrinks the QD core, resulting in an irreversible reduction in fluorescence quantum yield, an irreversible blue-shift and broadening of the fluorescence peak under continuous excitation[61] (Figure 2.11). Broadening of the fluorescence peak is suggested to be due

to fluctuations in exciton-size as the local electric field fluctuates with redistributing surface charge during a trapping and de-trapping event. Broadening may be assigned to fluctuations in exciton size due to fluctuations in the local electric field arising from surface charge redistribution during a trapping and de-trapping event.[106]

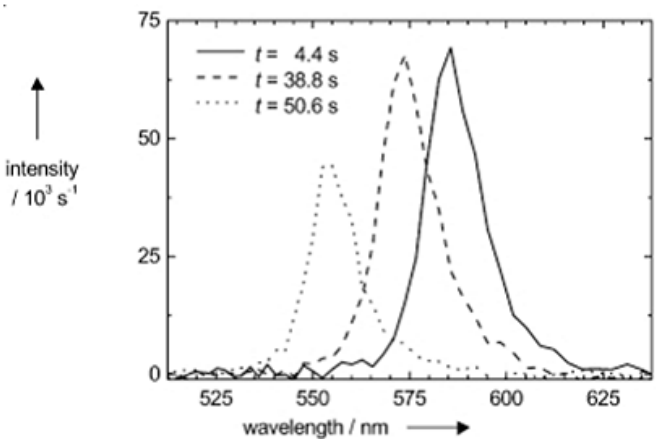

Figure 2.11: Effect of photo-oxidation: fluorescence spectrum of a single CdSe/ZnS core/shell QD at various illumination times excited under ambient air. The non-epitaxial ZnS shell is 4 monolayers thick.[61]

CdSe QDs are usually coated with a ZnS shell, which is structurally similar to and has a higher band gap than CdSe, which passivates surface trap states[118] and hence increases the fluorescence yield. The ZnS shell is also suggested to prevent photo-oxidation of the QD core in air (CdSe/ZnS, TOP/TOPO QDs under air[122]). However, photo-oxidation of CdSe/ZnS core/shell QDs has been observed under ambient air.[126] This is attributed to partial exposure of the core to oxygen due to incomplete core coverage by the ZnS shell or a too low a ZnS thickness (< 1.3 monolayers). [17] However even, a thick (4 monolayer) ZnS shell can be permeable to oxygen, as oxygen is suggested to diffuse through grain boundaries, which exist in non-epitaxially grown shell, to the CdSe core.[61, 126] Suggested photo-oxidation products for core/shell QD oxidation include the formation of $CdSeO_x$, where x=2 or 3, at the core/shell boundary for a thick, non-epitaxially grown shell,[126] or SeO_2 if the CdSe core is only partially/sparsely covered by ZnS shell.[17] For core CdSe QDs, either SeO_2 forms via the reaction $CdSe+O_2 \rightarrow Cd^{2+}+SeO_2$, if a Cd-passivating TOPO coating is present that leaves

unpassivated surface Se atoms free to react with adsorbed oxygen, or a compound oxide forms, such as $CdSeO_3$ via the reaction[127] $CdSe+3/2\,O_2 \rightarrow CdSeO_3$, if no coating is present, leaving both Cd and Se unpassivated surface sites.[127] Photo-induced oxidation is suggested to be the result a reaction of the QD with reactive oxygen species such as singlet oxygen[128] which is formed on the QD surface.

Unlike most molecules, oxygen is a triplet in its ground state ($^3O_2$), as it contains two unpaired electrons of the same spin in its outer most orbital. Spin reversal of one of the unpaired electrons generates singlet oxygen ($^1O_2$), an excited state of $^3O_2$, with the lowest $^1O_2$ state being 0.98 eV (1270 nm) above the $^3O_2$ ground state.[129, 130] The presence of $^1O_2$ is usually detected by the 1270 nm emission given off during the decay of $^1O_2$ back to $^3O_2$.[131] The lifetime of $^1O_2$ varies with the environment, and is equal to 2 to 4 µs in H_2O and 53 ± 5 µs in D_2O.[132] The $^1O_2$ lifetime is influenced by the O-H vibrational energy in the infra-red near 1270 nm, the excitation energy of $^1O_2$.[133] This is because $^1O_2$ can non-radiatively decay to the $^3O_2$ ground state via energy transfer from the $^1O_2$ to vibrational levels of the solvent molecule H_2O.[133] An isotope effect is expected because of the mass of D is larger than that of H, and therefore D-O has a different vibrational resonances to H-O. The $^1O_2$ lifetime is also influenced by reduction-oxidation reactions in the solution.[134] The increased singlet oxygen lifetime in D_2O compared to in H_2O is expected to result in accelerated photo-oxidation under D_2O compared to in H_2O.

Superoxide (or oxygen radical anion, $O_2^{\cdot-}$), on the other hand, is an oxygen molecule with an extra unpaired electron, and can be formed by electron transfer. Reports in the literature indicate that irradiated QDs are able to generate reactive oxygen species. A summary on the relevant literature is given in section 2.2.2.4.1.1.

2.2.2.4.1.1. Reactive Oxygen Species Generation by Irradiated Quantum Dots

There are conflicting reports about the potential of CdSe/ZnS QDs generating oxygen radical anions ($O_2^{\cdot-}$). The oxygen radical anion has an extra unpaired electron, and is generated via electron transfer to a sufficiently reducing species, such as oxygen (Figure 2.12(i)). The presence of $O_2^{\cdot-}$ can be detected by electron paramagnetic resonance (EPR). Experimental evidence suggests that irradiated dry CdSe/ZnS and CdSe QDs do not generate $O_2^{\cdot-}$,[135] in agreement with theory according to which the redox potential of the reaction $O_2 \rightarrow O_2^{\cdot-}$ does not lie within the energy gap of CdSe.[64, 135] Furthermore, a ZnS shell in excess of two monolayers (ML) confines both the hole and the electron within the QD core, further increasing the energy barrier.[135] In contrast, superoxide has been suggested to form on the surface of CdSe/ZnS QDs in an air environment via electron transfer from the QD core to surface adsorbed oxygen molecules,[64, 65] even with a 4.2 ML thick ZnS shell.[64] Specifically, Koberling *et al.*[65] and Mueller *et al.*[64] have suggested excited CdSe/ZnS QDs generate superoxide, via electron transfer to adsorbed oxygen molecules, either via direct electron transfer from a negatively charged QD core[64] (section 2.2.2.4.4), or by ejection of an Auger electron from a neutral QD core[65] (section 2.2.2.4.3). Direct electron transfer from the conduction band edge is suggested to be facilitated by the presence of polar water molecules in the air, which broaden the O_2 LUMO state of surface-adsorbed oxygen (Figure 2.12(iii)).

In addition to electron transfer from the QD core, surface trapped charges are also suggested to chemically react with surface adsorbed oxygen molecules. For instance, the reaction of oxygen with holes trapped in surface Se dangling bonds[136] oxidizes surface Se to SeO_2. An equivalent oxidation mechanism, involving electrons instead, has also been proposed, whereby a transfer of electron density from Se^{2-} surface sites to adsorbed oxygen yields SeO_2.[137]

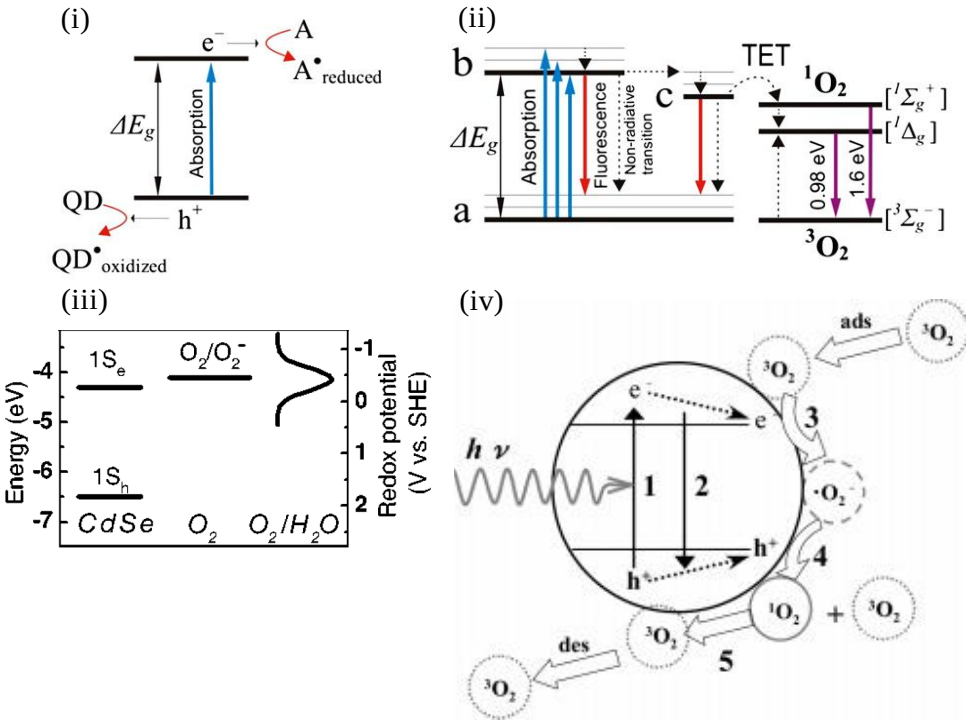

Figure 2.12: (i) formation of oxygen radial anion by electron transfer to oxygen[138] (ii) formation of singlet oxygen via energy transfer to triplet oxygen,[138] a is the electronic ground state, b is the excited electronic state (singlet) and c is a triplet state (iii) Energy level diagram of the CdSe QD core and the O_2 LUMO state of dry oxygen ($O2/O2^-$) and hydrated oxygen (O_2/H_2O) and the redox potential of the O_2/ $O_2^{\cdot-}$ couple. The redox potential lies above the conduction bandedge and poses an energy barrier. Polar water molecules broaden the LUMO state[64] (iv) Proposed route of singlet oxygen formation from superoxide by an excited titanium dioxide (TiO_2) nanoparticle: (1)light creates an exciton within a TiO_2 nanoparticle (2) the exciton recombines, or (3) the electron transfers to surface adsorbed $^3O_2$, (reduction of $^3O_2$) forming the oxygen radical anion $O_2^{\cdot-}$, followed b (4) oxidation of $O_2^{\cdot-}$ with the photo-induced hole which partly forms singlet oxygen $^1O_2$.[139]

Samia *et al.*[92] and Zhang *et al.*[128] have experimentally shown that CdSe and CdTe QDs, respectively, generate singlet oxygen at low yield (~5% for CdSe).[92] Generally, singlet oxygen can be created by energy transfer from an excited state molecule in a triplet state to an oxygen molecule initially in the ground state (triplet energy transfer or TET)[138] (Figure 2.12(ii)). For TET to occur, also the energy transferred must be equal to at least 0.98 eV (1267 nm), which is the minimum energy difference between $^1O_2$ and $^3O_2$ (Figure 2.12(ii)), and the excited state molecule must be in contact with $^3O_2$.[138]

The lowest excited state of a CdSe QD is a triplet state, and thus direct $^1O_2$ generation via TET is allowed.[138] CdSe QDs have been shown to generate $^1O_2$, via two routes (1) directly via TET, when in

oxygen saturated toluene (the QDs were capped with TOPO),[92] or (2) indirectly in water, via energy transfer from an excited singlet state CdSe QD to a singlet state photosensitiser molecule, which transfers to its triplet state, followed by energy transfer to the triplet ground state oxygen.[92] CdSe/CdS/ZnS QDs were shown to generate $^1O_2$ indirectly via energy transfer from the QD to a photosensitiser molecule.[140] In contrast, CdSe/CdS/ZnS QDs in the absence of a photosensitiser were shown not produce detectable amounts of singlet oxygen,[140] and CdSe/ZnS were shown not to generate free radicals,[135] although the generation of singlet oxygen has been implied by DNA nicking in the presence of CdSe/ZnS QDs.[141]

The formation of singlet oxygen from the superoxide radical has also been proposed to occur on the surface of excited titanium dioxide (TiO_2) nanoparticles via the formation of superoxide (Figure 2.12(iv)): a $^3O_2$ molecule adsorbed onto the TiO_2 surface converts into a oxygen radial anion ($O_2^{\cdot -}$) via electron transfer from the excited state TiO_2 nanoparticle, followed by the oxidation of $O_2^{\cdot -}$ with the excited hole in the TiO_2 nanoparticle, forming singlet oxygen ($^1O_2$).[139]

It is known that, in aqueous solution, an oxygen radical anion can be converted into hydrogen peroxide (H_2O_2), via spontaneous dismutation of the oxygen radical anion: various such dismutation routes have been suggested to occur:[142, 143]

$$O_2^{\cdot -} + H^+ + HO_2^{\cdot} \rightarrow H_2O_2 + O_2 \qquad \text{(i)}$$

$$O_2^{\cdot -} + HO_2^{\cdot} \rightarrow H_2O_2 + O_2 \qquad \text{(ii)}$$

$$O_2^{\cdot -} + 2H_2O \rightarrow 2H_2O_2 + e^- \qquad \text{(iii)}$$

The rate of spontaneous dismutation via reaction (i) is equal to 5×10^{-5} $M^{-1}s^{-1}$,[142] so that hydrogen peroxide is present in significant amounts when oxygen radical anions are formed.[142]

Alternatively, heat-induced H_2O_2 formation in oxygen saturated water has also been suggested to occur.[144, 145] Bruskov *et al.*[144] observed higher H_2O_2 formation rates, across a pH range from 6 to 12, if water was additionally saturated with oxygen, compared to just with air, at 40°C. For example, at pH 7.0, the amount of H_2O_2 produced, after 3 hours

of heating at 40°C, was about 5 nM and 15 nM, in water saturated with just air or additionally with oxygen, respectively.[144] Based on these observations, Bruskov *et al.*[144] have suggested an additional H_2O_2 formation route, which is heat induced and is the dismutation of a pair of hydroxyl radicals into hydrogen peroxide. In effect, it was proposed that a hydroxyl ion (OH^-) looses an electron, forming a hydroxyl radical ($OH^\cdot$) and a solvated electron, according to $OH^- \rightarrow OH^\cdot + e^-_{aq}$; the dismutation of two hydroxyl radicals forms a hydrogen peroxide molecule, according to[144]

$$OH^- \rightarrow OH^\cdot \rightarrow H_2O_2 \qquad \text{(iv)}$$

This reaction is made possible by the presence of an electron acceptor, such as singlet oxygen, in water, as it captures the solvated electron lost by the hydroxyl ion, facilitating hydrogen peroxide formation via reaction (iv). In effect, the mechanism proposed is that ground state oxygen ($^3O_2$) forms singlet oxygen ($^1O_2$) when heated (to 40°C).[144] The singlet oxygen ($^1O_2$) accepts an electron from the hydroxyl anion (OH^-), resulting in the formation of an oxygen radial anion ($O_2^{\cdot -}$) and a hydroxyl radical ($OH^\cdot$), respectively.[144] Two hydroxyl radicals then dismutate to hydrogen peroxide via reaction (iv).[144] The oxygen radical anion ($O_2^{\cdot -}$) is suggested to also dismutate, forming the electron acceptor singlet oxygen ($^1O_2$) and hydrogen peroxide via[144]

$$O_2^{\cdot -} + H^+ + HO^\cdot_2 \rightarrow H_2O_2 + {}^1O_2 \qquad \text{(v)}$$

Reactions (iv) and (v) are summarised in Figure 2.13.

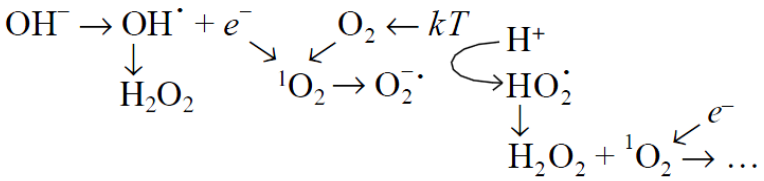

Figure 2.13: Proposed route to heat-induced hydrogen peroxide (H_2O_2) formation via the dismutation of hydroxyl radical ($OH^\cdot$) and oxygen radical anion ($O_2^{\cdot -}$) in water (reactions (iii) and (iv) in the text): OH^- looses an electron, forming $OH^\cdot$ and a solvated electron (e^-). The dismutation of two $OH^\cdot$ forms H_2O_2 (reaction (iii) in the text). $^3O_2$ forms $^1O_2$ through 40°C heat (kT). The solvated electron (e^-) is accepted by $^1O_2$, forming an oxygen radical anion. The dismutation of the oxygen radical anion, H^+ and $HO^\cdot_2$ forms H_2O_2 and $^1O_2$ (reaction (iv) in the text).[144]

Similarly, ZnS powder irradiated with an electron beam forms ZnO and volatile SO_2.[146, 147] It has been suggested that the electron-beam induces the dissociation of molecular O_2 and oxygen containing H_2O (water vapour) adsorbed onto the ZnS surface, resulting in their conversion into reactive atomic species, and subsequent chemical reaction with the ZnS, forming volatile H_2S or SO_x, and ZnO or $ZnSO_4$.[147]

It has been shown via XPS analysis that H_2O_2 exposure to oleic acid-coated CdSe nanocrytsals yields SeO_2, while the XPS peak of Cd shows no shift.[148]

The photo-oxidation of CdSe QDs in water following the disintegration of hole-scavenging surface thiols has been reported.[149] It is suggested that photo-excited hole scavenged from the CdSe core by surface thiols induces thiol oxidation, turning the thiols into disulfides, which form a structure that is permeable by oxygen present in water.[149]

2.2.2.4.2. Photo-corrosion

In the photo-corrosion model, atomic scale roughness on the QD surface forms surface defects that can act as carrier traps.[125] It is assumed that these "roughness states" are removed by smoothing out the surface roughness during the initial stages of photo-oxidation (Figure 2.14), and as a result the emission yield is enhanced and blue-shifted i.e. reducing the QD size, when exposed to ambient air and light. Photo-corrosion has been experimentally observed with CdSe core QDs and CdSe/CdS core/shell QDs.[125] The photo-corrosion in core/shell QDs, however, has been attributed to an incomplete CdS shell.

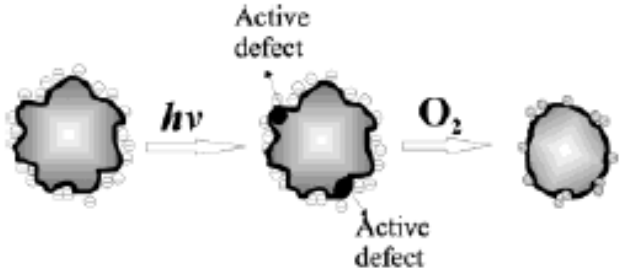

Figure 2.14: Illustration of the photo-corrosion model.[125]

2.2.2.4.3. Bright State Depopulation

Koberling *et al.*,[65] who studied the oxygen-induced blinking of CdSe/ZnS QDs under normal oxygen pressures, suggested that the adsorbed oxygen can provide extra trap states where the Auger electrons from the QD core are trapped. The Auger electron from a QD core can now not only be transferred to the surrounding matrix or nearby QD environment, but can now also be transferred to the adsorbed oxygen, creating a positively charged, non-emitting QD and a negatively charged oxygen radical.

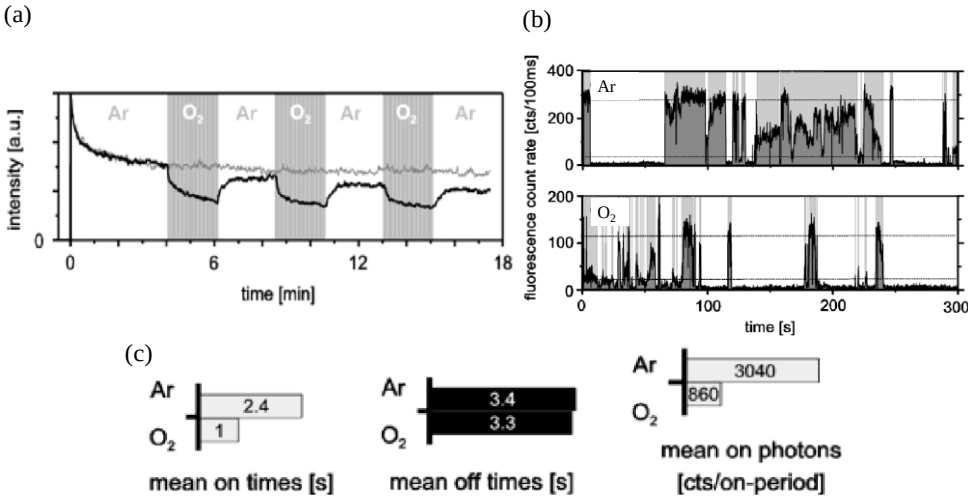

Figure 2.15: Experimental results for the bright-state-depopulation model under oxygen: (a) ensemble CdSe/ZnS QD fluorescence under illumination under argon (grey line) and when switched between argon and oxygen (black line). QDs were spin-cast onto a glass slide (b) Fluorescence time trace of a single CdSe/ZnS QD under argon and oxygen (c) mean "on", "off" time durations and mean number of photons emitted during the on-time period, under argon and oxygen for single CdSe/ZnS QDs. The ZnS shell thickness of CdSe/ZnS QDs was equal to a few monolayers.[65]

QD neutralisation is suggested to occur via subsequent ionisation of the remaining hole in the QD core to the negatively charged oxygen. Oxygen-induced QD charging reversibly quenches the QD fluorescence of CdSe/ZnS QDs when illuminated under oxygen (Figure 2.15(a)), and reduces the mean time a single QD spends in the emitting state compared to under argon (Figure 2.15(b) and 2.15(c)), suggesting oxygen provides an additional charge trapping route.

2.2.2.4.4. Dark State Depopulation

Müller *et al.*[64] observed that CdSe/ZnS QDs illuminated in air compared to in vacuum spend on average less time in the charged, non-emitting state (Figure 2.16(b)). They suggested that rapid de-charging of QDs due to electron transfer from the QD core to adsorbed oxygen can lead to a fluorescence rise for samples irradiated in air.[64] It was also suggested that the low number of water molecules in the air facilitate the electron transfer by broadening the O_2 LUMO state of surface-adsorbed oxygen, and this then results in a reduction of the energy barrier that must be overcome during electron transfer (Figure 2.16(a)). This effect was reversible under evacuation to vacuum. Müller *et al.* also observed a fluorescence increase by a factor of 2 upon purging in dry oxygen, further suggesting an additional de-charging mechanism induced by oxygen.

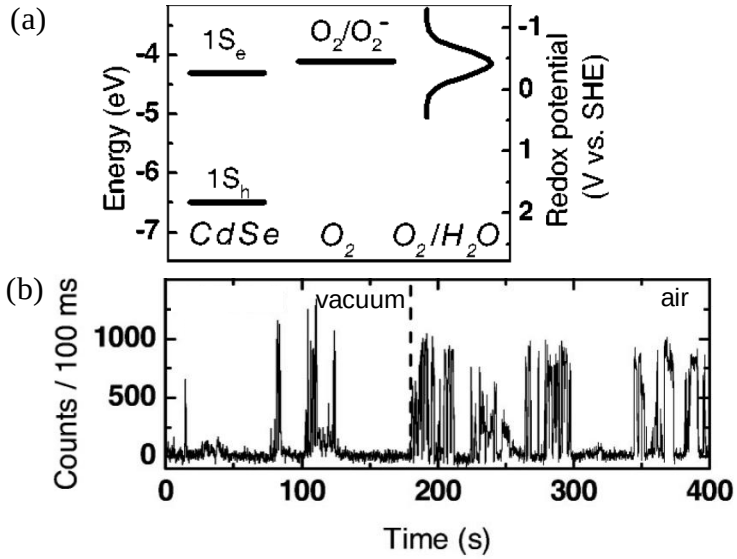

Figure 2.16: (a) Energy level diagram of the CdSe QD core and the O_2 LUMO state of dry oxygen (O2/O2$^-$) and hydrated oxygen (O_2/H_2O) and the redox potential of the O_2/O_2^- couple. The redox potential lies above the conduction bandedge and poses an energy barrier. Polar water molecules broaden the LUMO state[64] (b) Fluorescence time trace of a single CdSe/ZnS QD illuminated under vacuum or air. The ZnS shell thickness was equal to between 1.2 and 4.2 monolayers.[64]

The reduction of the mean time spent in the non-emitting state under air compared to under vacuum observed by Müller *et al.*[64] contrasts with the reduction in the mean time spent in the emitting state under dry oxygen compared to under dry argon observed by Koberling *et al.*,[65] although both samples were CdSe/ZnS QDs.

2.2.2.4.5. Surface-Trap-State- Passivation

According to the surface-passivation model, surface-adsorbed oxygen molecules passivate surface trap states on the surface of CdSe/ZnS core/shell QDs, reducing carrier loss via surface traps.[62] This yields higher fluorescence yields in the presence of oxygen. This is interpreted from the experimental observations that show (i) an increased fluorescence intensity (or quantum yield) and narrowing of the fluorescence peak with increasing oxygen pressure, as more surface traps get passivated, reducing carrier loss (Figure 2.17), and (ii) an increasing fluorescence peak red-shift with oxygen pressure, which is attributed to electronegative oxygen extending the wavefunction of the electron confined inside the QD more towards the ZnS shell, increasing the electron hole separation.

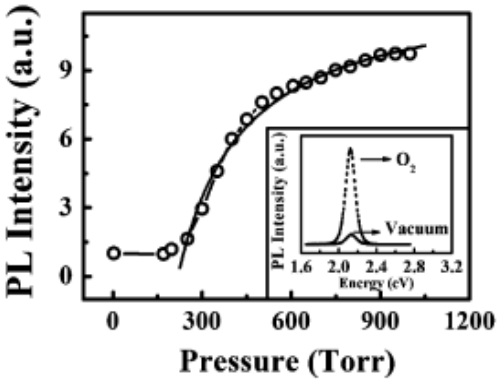

Figure 2.17: Increase in experimental fluorescence yields of CdSe/ZnS QDs with increasing oxygen pressure.[62]

2.3 Materials and Methods

All experiments in this section employed quantum dots (QDs) that were 602 nm fluorescence peak CdSe/ZnS core/shell QDs (QDs) dissolved in toluene supplied by Evident Technologies.

2.3.1 Quantum Dot Illumination Experiments

Under clean-room conditions, QDs dissolved in toluene were diluted to a concentration of 2 µM using dry toluene (Analar grade), and drop-cast (5 µL) onto the glass substrate. The drop-cast QD solution was left to dry, which took less than one minute. The dried drop-cast QDs covered a spot of radius equal to 4.0±0.5 mm, as measured by a ruler. Drop-cast QD samples to be illuminated under ambient air were placed onto a reflective silver mirror in ambient air, while drop-cast QD samples to be illuminated under specific atmospheric conditions were placed, immediately after having dried, onto a reflective silver mirror inside a purpose-built sample chamber and purged with the appropriate gas with appropriate humidity content. The fluorescence experiment setup was calibrated by focussing the excitation laser onto the sample. This was followed by a dark period of at least 50 minutes to allow the QDs to return to their pre-illumination state, before illumination experiments were started. During this dark period, drop-cast samples to be illuminated under specific atmospheric conditions were purged with either argon or oxygen (BOC, 99.998% minimum purity). Gas humidification occurred by flow through water (Millipore) or deuterated water ((99.999%, Aldrich) of a certain volume inside a bubbler. The gas humidity was measured with an Omega RS-232 HH310 Series humidity-temperature meter, which is based upon a semiconductor and polymer capacitive sensor: a polymer between the capacitor plates absorbs moisture from the environment in which it is placed. The absorbed moisture affects the capacitance, which is used to calculate the relative humidity.

The substrate onto which QDs were drop-cast was a glass slide and was prepared as follows. The glass sides were cleaned by sonication in acetone, isopropanol and ultrapure de-ionised water (18MΩ resistivity), in this order, for 20 minutes each, followed by drying under a dry nitrogen gas flow.

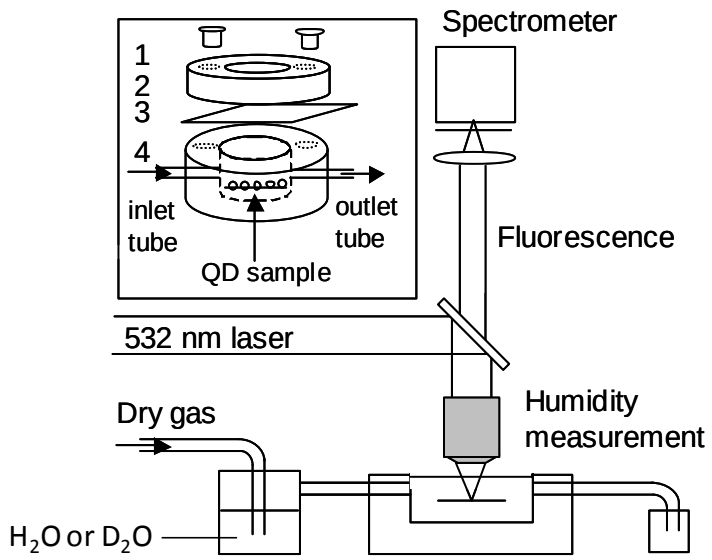

Figure 2.18: Illustration of the experimental setup for illumination experiments under argon or oxygen at various humidities Dry gas passes through a bubbler, which contains a certain volume of H_2O or D_2O, and enters and exits the sample chamber after which it is collected inside a sealed container. Excitation light (532 nm) is focussed by a lens onto the QD sample inside the chamber. QD fluorescence is collected by the same lens. Inset: configuration of the purpose-built sample flow chamber, made of Teflon, which consists of a cylindrical Teflon wall inside which the sample was placed, on top of which was placed an optically transparent quartz window to allow sample excitation and fluorescence detection. The sample was made airtight by sealing with a cylindrical top using screws; Inlet and outlet tubes were fitted to the sample chamber side walls to allow the sample chamber to be purged with gas.

The illumination setup is shown in Figure 2.18. During illumination, excitation was with a 532 nm V5 Verdi laser (Coherent Inc) focussed onto the sample to a 590 nm waist (assumed diffraction limited spot)) with a x50 objective lens (*NA=0.55* (Nikon)). The excitation power was equal to 80 μW (7.32 kW/cm^2) under ambient air, dry oxygen and dry argon, and equal to 60 μW (5.49 kW/cm^2) for humidity studies under oxygen, and equal to 45 μW (4.12 kW/cm^2) for humidity studies under argon and for QD solutions. QD fluorescence was collected with the same lens as used for excitation and passed through a 2" visible beamsplitter (Newport) and 570nm long pass filter (E570lP, Chroma) before being detected by a

spectrometer and CCD camera. The spectrograph was a SpectraPro 2300i spectrograph with a 300 g/mm=500 nm grating, and the CCD was a PIXIS 1024 CCD, both supplied by Acton Scientific. The fluorescence on the CCD was integrated over 191 pixels, with a theoretical saturation level of $1.27x10^7$ counts. All accumulated data was less than or equal to 12% (1.46×10^6) of the saturation level. The CCD was connected to a computer, and in-house software was used to collect fluorescence spectra at regular time intervals and at an integration time of 5 seconds per spectrum. The first set of data (fluorescence spectrum) taken (i.e. t=0 mins) is the moment the sample is first illuminated with the 532 nm laser light; the laser is left illuminated throughout the experiment and further spectra are obtained at various times during the continued illumination.

2.3.2 X-Ray Photoelectron Spectroscopy Experiments

QDs were prepared for illumination by slowly drop-casting QDs dissolved in toluene (1.5 mg/mL, 4.94 μL) onto a pre-cleaned microscope slide under clean-room conditions. The microscope slide was previously cut to an area of 2.5 mm x 2.5 mm in size, and then pre-cleaned by sonication in acetone, isopropanol and de-ionised water, in this order, for 20 minutes each. Once dried, the QD sample was transferred to a purpose-built sample chamber (Figure 2.18 in section 2.3.1), and the excitation laser (20 mW, 1 mm beam diameter, 532 nm, Power Technology Inc.) was focused onto the sample area, resulting in an excitation intensity of 2.5×10^{-3} kW/cm^2. The sample was then kept in the dark for a minimum of time of 40 minutes, during which time the sample chamber was purged with humid oxygen (1.47 mole/m^3). Using the known dimensions of the glass substrate, the illumination process was automated using an x-y stage: the excitation laser was scanned across the QD sample with multiple x and y steps, with a single step in the x or y direction being 0.8 mm in magnitude, and a parking time on each illumination spot of 18 minutes. Once the illumination of the whole drop-cast QD sample was completed, the QDs were carefully washed off the glass substrate into a pre-cleaned glass jar using a minimal amount of toluene. The illuminated QD solution was

stored under inside a pre-cleaned glass jar under dry argon inside a fridge at 2°C, during which the jar was covered with aluminium foil to minimise light exposure. This illumination-wash process was repeated 12 times until a total sample volume of 59.28 µL was reached. The total quantity of illuminated QDs was thus 1.5 mg/mL x 59.28 µL = 88.9 µg. The resulting total QD solution was slowly drop-cast into the well of a pre-cleaned aluminium sheet. Non-illuminated QDs were drop-cast into the well of a different pre-cleaned aluminium sheet. QD drop-casting and drying was done under clean room conditions under a fume-cupboard with lights switched off, so that only some ambient light was present. Aluminium sheets (purity of 99.999%, 0.5 mm thick, from Sigma-Aldrich) were prepared by cutting to a size of 10 mm x 10 mm and stamping to form a well of diameter of roughly 2.9 mm and height of roughly 0.9 mm. The so-formed aluminium sample holders were then cleaned by sonication in acetone (for 20 mins) and then methanol (for 10 mins) and immediately dried under dry nitrogen gas flow. The aluminium substrate was then rinsed 6 times with acetonitrile and then swept through acetonitrile solution several times to remove any residue, followed by drying under dry nitrogen gas flow (all solvents used were dry and highest purity). The aluminium substrates were stored under dry argon until QD samples were drop-cast into the aluminium well. The QD samples drop-cast into the aluminium well were stored under dry argon inside a pre-cleaned glass jar, which is covered in aluminium foil to minimise light exposure, and stored inside a fridge, until XPS analysis.

X-ray photoelectron spectra were acquired on a Kratos Axis Ultra X-ray photoelectron spectrometer (Kratos Ltd, Manchester). All samples were run as insulators, requiring use of the electron flood gun. The X-ray source was a monochromated Al source operated with an X-ray emission current of 10 mA and an anode high throughput (acceleration voltage) of 15 kV. Survey scans were acquired with a pass energy of 160 eV and a step size of 1.0 eV, whilst high resolution spectra were collected at a pass energy of 20 eV and a step size of 0.1 eV. All spectra were charge corrected to saturated hydrocarbon at 285.0 eV. XPS data were corrected

for transmission using the NPL system. Calculation of the transmission function for each operating mode and pass energy allowed the use of a theoretical Scofield relative sensitivity factor library to generate quantitative data.

2.4 Experimental Results

The evolution of the fluorescence spectrum of continuously illuminated CdSe/ZnS quantum dot samples under various atmospheric conditions was investigated to better understand the effects of atmospheric gases and water molecules.

2.4.1 Sample Characterisation

Figure 2.19 shows a fluorescence image of a typical QD sample drop-cast onto a glass substrate.

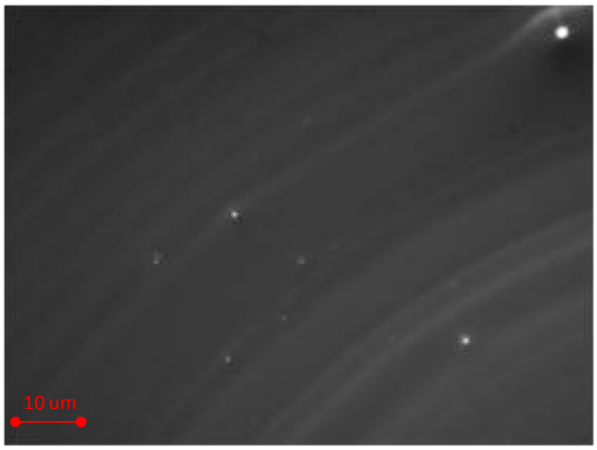

Figure 2.19: Fluorescence images of CdSe/ZnS QDs drop-cast onto a glass substrate x range=895 µm, y range=671 µm, 50 ms exposure, 10x objective, filters: BP 546/12 (excitation), FT 560 (beam splitter), BP 575-640 (emission).

The QD distribution is not uniform across the drop-cast sample area. Successive concentric, higher intensity fluorescence rings are seen, which can be attributed to the coffee ring effect, in which, during evaporation of a drop-cast drop of colloidal solution, a higher evaporation rate of the solution occurs at the drop rim that is in contact with the substrate, creating an outward flow of particles and depositing the particles at the outer rim of the droplet.[150, 151] Consequently, the fluorescence intensity depends on the QD density at the illumination spot.

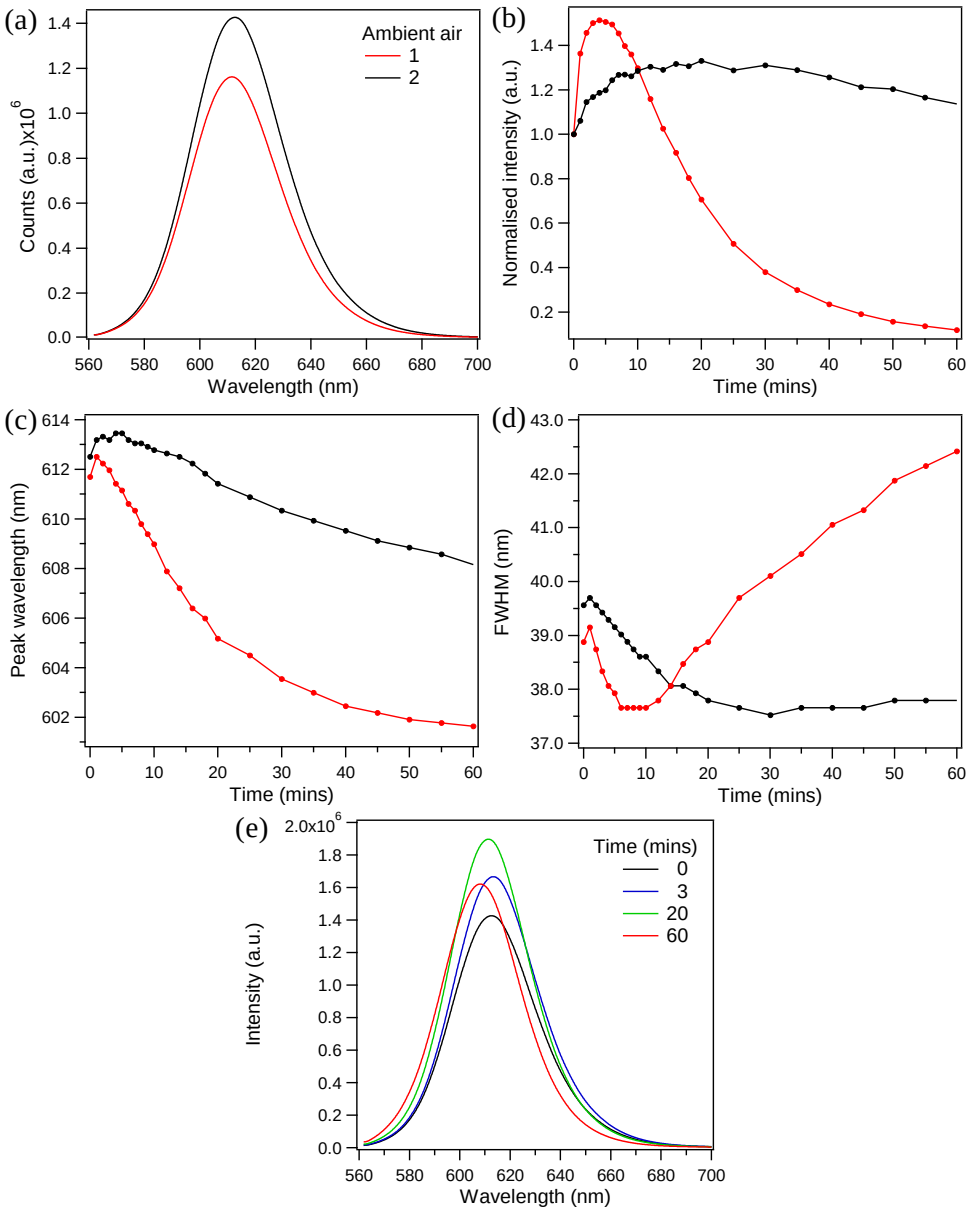

Figure 2.20: The time evolution of the fluorescence spectrum excited under ambient air at an area on the QD sample with initially (1) low or (2) high fluorescence intensity (a) fluorescence spectra at illumination time =0 mins; evolution under illumination of (b) the normalised fluorescence intensity peak height (c) the emission peak wavelength and (d) the emission peak width (FWHM) (e) the fluorescence spectrum of spot 2 after 0, 3, 20 and 60 minutes of illumination. Excitation was at 532 nm, 80 µW.

Two areas on the QD sample of different fluorescence intensities are investigated in more detail. At zero illumination time, the brighter sample spot, compared to the dimmer sample spot, has a 23% higher fluorescence peak intensity (Figure 2.20(a)), with a fluorescence peak that is red-shifted (Figure 2.20(c)) and broader (Figure 2.20(d)) than that of the dimmer spot. In particular, the initial peak wavelength of the

brighter/dimmer spot is equal to 612.5/611.7 nm, a difference of 0.8 nm (Figure 2.20(c)), and the initial FWHM of the peak is equal to 39.6/38.9 nm, a difference of 0.7 nm (Figure 2.20(d)). The fluorescence peak of the QD sample is expected to be centred at 602 nm. A red-shift in the fluorescence peak has previously been attributed to (i) non-radiative inter-dot energy transfer from smaller to larger QDs (Förster Resonant Energy Transfer or FRET), which results in a red-shift of the emission peak with a narrower FWHM, as observed for close-packed CdSe QDs;[152] (ii) quantum-mechanical coupling between adjacent QDs in contact with each other, as reported for aggregated CdSe QDs.[153, 154] Coupling results in the exciton wavefunction being spread/localised over more than one QD, splitting the single exciton transition into two peaks, broadening the FWHM and red-shifting the fluorescence peak and absorption onset;[153, 154] (iii) dipole-dipole interaction, as observed for close-packed CdS QD layers, in which a photo-induced electron-hole pair in one QD induces a dipole in a neighbouring QD, lowering the exciton energy.[155] All of these mechanisms (i, ii, iii) are results of a close-packed QD configuration. In our samples, a ZnS shell and surrounding ligand molecules separate neighbouring QDs and are thus expected to reduce dipole-dipole and quantum-mechanical coupling interactions compared to core QDs that are in direct contact with each other. The initially brighter illumination sample spot, compared to the initially dimmer sample spot, shows a larger red-shift relative to the expected 602 nm fluorescence peak and its fluorescence spectrum is broader, consistent with observations of quantum-mechanical coupling between neighbouring core QDs.[153, 154] It is thus reasonable to assume that the initially higher fluorescence intensity sample spots are areas of increased QD density.

For both QD sample spots, constant illumination induces changes in the fluorescence intensity and spectrum (Figure 2.20(e)), with the less dense QD distribution showing faster and more pronounced spectral changes (Figure 2.20(b), (c), and (d)). Oxygen and water molecules have been suggested to profoundly affect the recombination dynamics of excited

charge carriers within a QD. Thus, the next step is to investigate in detail the effects of oxygen and water molecules. In all subsequent illumination experiments, low fluorescence intensity spots are chosen for illumination experiments on drop-cast QD samples.

2.4.2 Variations in Atmospheric Conditions

In this section, the influence of oxygen and water molecules on the quantum dot fluorescence spectrum is investigated in detail.

2.4.2.1 Illumination under Dry Argon and Dry Oxygen Atmospheres

The initial fluorescence spectra under dry oxygen and dry argon are very similar. The initial fluorescence intensity of QDs under dry oxygen, however, is slightly higher (by 11%), broader (by 3.0 nm) and red-shifted (by 1.5 nm) compared to under dry argon (Figure 2.21(a)). An initially higher fluorescence intensity of CdSe/ZnS QDs under ambient air compared to under dry nitrogen has been attributed to the quenching of trap state emission by oxygen.[126] Also, a progressive red-shift, fluorescence intensity increase and narrowing of the fluorescence peak has also been observed with increasing oxygen pressure by Shu *et al.*,[62] which is attributed to passivation of surface trap states and extension of the electron wavefunction towards the ZnS shell by (electronegative) oxygen adsorbed onto the surface of CdSe/ZnS QDs. However, here an initially broader fluorescence peak is observed under dry oxygen compared to under dry argon (Figure 2.21(a)). Under dry argon, within 60 minutes of illumination the fluorescence peak slightly increases (by roughly 15 %), broadens (a FWHM change from 37.9 nm to 39.0 nm) and red-shifts (from 612.1 to 613.1 nm) (Figure 2.21(b-d)).

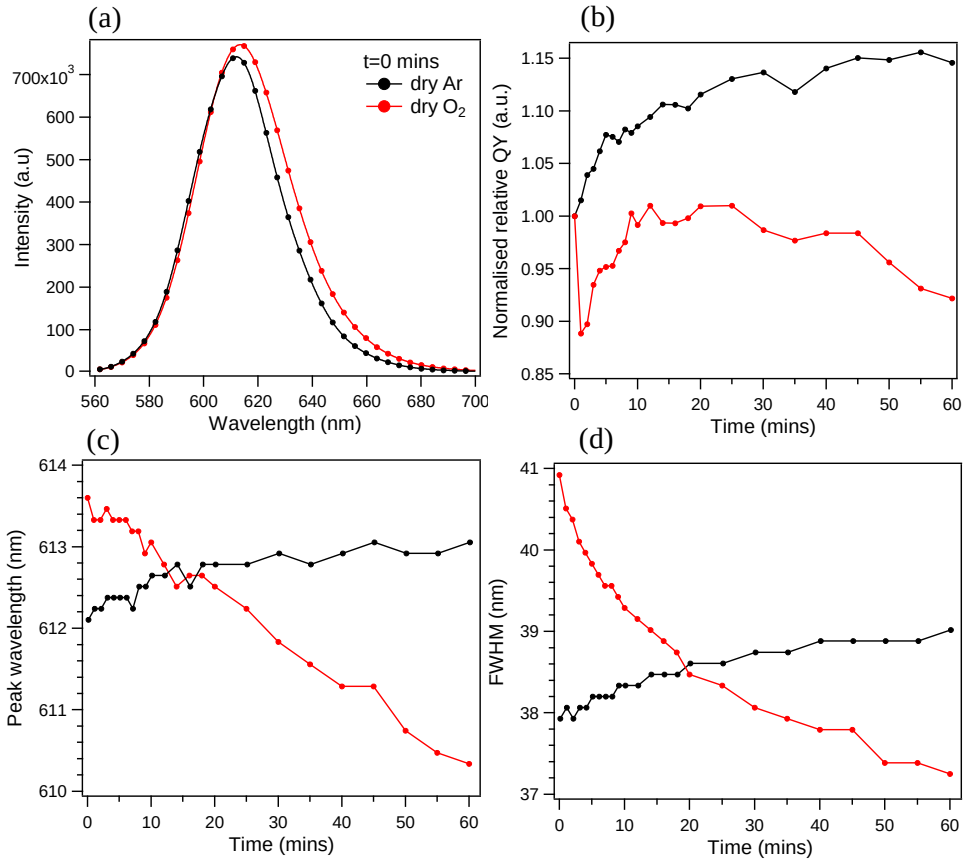

Figure 2.21: CdSe/ZnS QD illumination under dry argon (black) or dry oxygen (red) atmospheres (a) fluorescence spectrum at illumination time t=0 minutes; evolution under illumination of the (b) normalised relative quantum yield (c) emission peak wavelength (d) emission peak width (FWHM). Excitation was at 80 µW, 532 nm.

While PFE has previously been observed for CdSe/ZnS core/shell QDs illuminated under dry nitrogen,[67, 110] no significant PFE has been reported for CdSe QD monolayers illuminated under dry oxygen or dry nitrogen on glass.[122] In the cases where a PFE effect was observed, the excitation intensities were much higher (67x 10^{-3} kW/cm^2 and 0.4-173 kW/cm^2) [67, 110, 123] than in the case were no PFE effect was observed (3x10^{-3} kW/cm^2).[122] The PFE signal of CdSe/ZnS/TOPO QDs illuminated under an inert dry atmosphere has previously been attributed to photo-electrification.[110] Photo-electrification attributes PFE to an increased probability of radiative recombination of photo-generated charge carriers via the energy gap due to the inhibition of QD ionisation by the electrostatic potential of Auger-ejected electrons trapped in surface trap states (section 2.2.2.1).[110, 115] It is suggested that photo-electrification

is effective only at excitation intensities exceeding about 100 x 10^{-3} kW/cm^2, when Auger ejection of excited electrons is the dominant ionisation process.[102, 110] Thus, these different observations may be related to the excitation intensities. Here, an excitation power exceeding 100 x 10^{-3} kW/cm^2 is used and a small PFE effect is observed under dry argon, in agreement with experimental observations from Uematsu *et al.*[110] and Oda *et al.*[67, 123] Thus, it is reasonable to assume that the small PFE effect observed here under dry argon is due to photo-electrification.

The continuous red-shift observed under dry argon is consistent with previous observations for monolayers of illuminated CdSe/ZnS core/shell QDs,[68, 110, 113, 114, 156] and is attributed to the Stark effect induced by the presence of trapped charges on the QD surface or core/shell interface,[66, 77, 110, 113, 114, 156] while broadening of the fluorescence peak has been attributed to trapped carriers near the QD or in shallow traps,[75] or fluctuations in the charge of charged surface trap states.[67] Thus, the slight fluorescence peak broadening and red-shift indicate surface charging of illuminated QDs under dry argon.

The change in the fluorescence yield of QDs continuously illuminated under dry oxygen differs compared to that of QDs illuminated under dry argon. Under dry oxygen, a rapid 10% drop in fluorescence yield is observed within the first minute of illumination (Figure 2.21(b)). This is followed by a gradual fluorescence recovery (PFE) to near the pre-illumination fluorescence yield (after 25 mins of illumination and subsequent slight gradual fluorescence loss, by 8% after 60 mins of illumination (see Figure 2.21(b)). In contrast to illumination under dry argon, illumination under dry oxygen slightly blue-shifts and narrows the fluorescence peak (Figure 2.21(c) and (d)). After 60 mins of illumination, the blue-shift equals 3.3 nm (a shift from 613.6 nm at t=0 mins to 610.3 nm at t=60 mins) and the fluorescence peak at FWHM is narrower by 3.7 nm (a change from 40.9 nm at t=0 mins to 37.2 nm at t=60 mins) (Figure 2.21(c) and (d)).

The initial drop in fluorescence yield suggests the fluorescence yield under dry oxygen is initially quenched, suggesting there is a photo-induced reaction with oxygen. Oxygen is a good electron-acceptor, and other electron acceptors, for instance benzoquinone, have been shown to quench the fluorescence emission of CdSe QDs.[119] Consistent with this, Gooding *et al.*, show that injection of holes into CdSe/ZnS QDs results in complete fluorescence quenching.[97] Koberling *et al.* have experimentally observed a drop in fluorescence intensity under oxygen of illuminated CdSe/ZnS QDs, which was attributed to electron transfer from a neutral QD core to oxygen adsorbates, resulting in a positively charged QD (QD core charging) and a oxygen radical anion.[65] In light of these reports, the initial drop in fluorescence intensity observed here under dry oxygen might be attributed to oxygen-induced charge-separation in the QD core.

Under a dry oxygen atmosphere, a continuous photo-induced shift in the fluorescence peak to the blue and narrowing of the emission peak occurs (Figure 2.21(c) and (d)). In the presence of oxygen, a blue-shift in the emission is usually attributed to shrinkage of the QD core due to photo-oxidation.[61, 126] In the context of photo-oxidation, narrowing of the fluorescence peak has been attributed to (i) a higher photo-oxidation rate of smaller QDs compared to larger QDs in a QD ensemble,[122] as a narrowing followed by a broadening was observed previously for CdSe QDs,[122] or (ii) photo-corrosion initially removing surface trap states, by smoothing out surface roughness states in the early stage of photo-oxidation.

In summary, a small PFE effect of similar magnitude occurs under both dry argon and dry oxygen atmospheres, and is consistent with previous results under dry nitrogen[67, 115, 123] and might be attributed to photo-electrification. Evidence of photo-induced QD surface-charging under dry argon is seen, while an initial drop in the fluorescence yield with illumination for samples under dry oxygen indicates initial charging of the QD core under dry oxygen. These results show that there is a small difference in the fluorescence spectrum and a minimal difference in yield

for CdSe/ZnS QDs illuminated under a dry oxygen or argon environment and are inconsistent with a number of studies where PFE has been evaluated for CdSe/ZnS QDs under 'air'.[122] Since such environments (i.e. air) contain both oxygen and water molecules, our next step was to establish the effect of humidity under an inert (argon) and oxygen environment on the fluorescence properties of CdSe/ZnS QDs using similar conditions to those used in our experiments described above.

2.4.2.2 Illumination under Humid Argon

Prior to illumination, drop-cast CdSe/ZnS QDs were purged under argon, at various humidities, for at least 50 minutes, in the dark. The humidity content does not influence the initial (t=0 mins) fluorescence yield or spectrum of QDs under argon (Figure 2.22(a)). However, the humidity content does appear to enhance a process that accelerates the PFE effect (Figure 2.22(b)). For instance, within 10 minutes of irradiation, the relative quantum yield is increased by 55%/43% at 1.19/0.61 mole/m^3 H_2O humidity (Figure 2.22(b)). High humidity levels (1.19 mole/m^3 H_2O) under argon also accelerate the broadening and red-shift of the fluorescence peak compared to under dry argon (Figure 2.22(c)). As a result, after 20 minutes of illumination, the spectrum looks different under dry, compared to under humid, argon (Figure 2.22(a)). These spectral changes cannot be clearly interpreted, but what is certain is that the presence of water molecules results in a photoproduct that is different to the starting CdSe/ZnS QDs and this is crucial to the PFE effect. In short the initial emission yield is independent of the humidity, but the PFE is highly dependent on the humidity content.

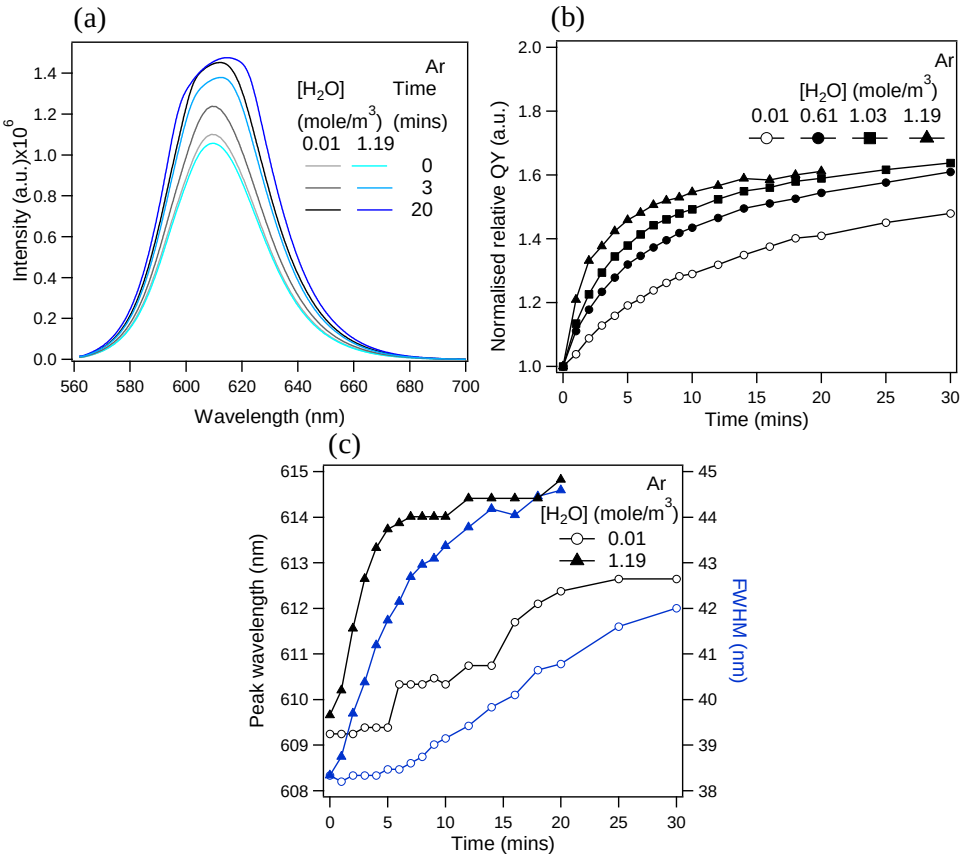

Figure 2.22: Humidity dependence on the fluorescence spectrum evolution of CdSe/ZnS QDs excited under argon: (a) fluorescence spectra after 0, 3 and 20 minutes of illumination, evolution under illumination of the (b) normalised relative quantum yield (c) emission peak wavelength (black) and emission peak width (FWHM) (blue). Excitation was at 45 µW, 532 nm.

Water-induced PFE in QDs has previously been observed experimentally, and have been attributed to (i) photo-induced passivation of surface traps by water-adsorbates,[122] (ii) photo-induced neutralisation of charged surface traps[67, 68, 123] (iii) stabilisation of surface trap states by photo-induced re-arrangements of surfactant molecules on the QD surface for CdSe/ZnS QDs in solution.[66] To further investigate the effect of water molecules on the PFE, the effect of deuterated water (D_2O) at various humidities was compared to similar humidities of H_2O. The H_2O/D_2O solvent isotope effects have been seen in the past to probe for electron solvation processes[157] and electron-transfer processes.[158] The data obtained from these experiments is shown in Figure 2.23.

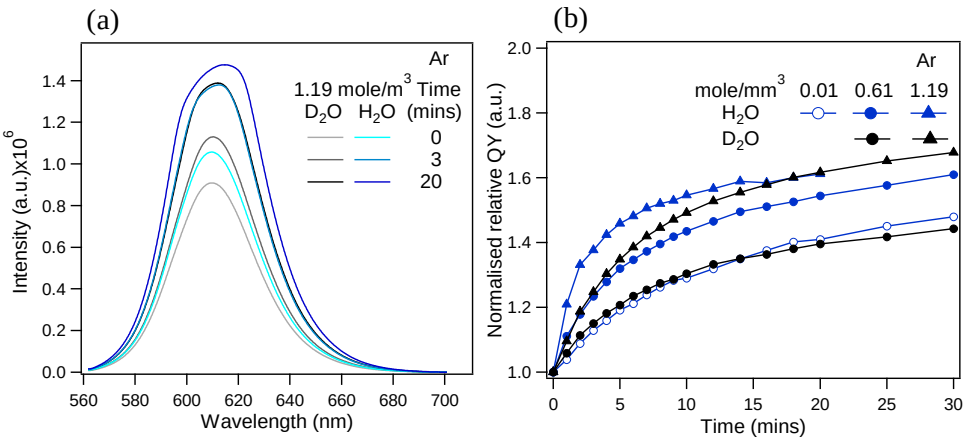

Figure 2.23: D_2O versus H_2O humidity dependence of the fluorescence spectrum evolution of CdSe/ZnS QDs excited under argon: (a) fluorescence spectra after 0, 3 and 20 minutes of illumination (b) evolution under illumination of the normalised relative quantum yield. Excitation was at 45µW, 532 nm.

The initial (t=0 mins) fluorescence intensity is lower under D_2O humidities compared to under H_2O humidities. For example, the initial intensity at 1.19 mole/m^3 under D_2O is 14 % lower than under H_2O (Figure 2.23(a)). Also, the rate of fluorescence enhancement is slower under D_2O compared to under H_2O. For example, the normalised relative quantum yield at 0.61 mole/m^3 D_2O/H_2O has increased by 44%/68% after 30 mins illumination (Figure 2.23(b)). At 1.19 mole/m^3, the rate of PFE is lower under D_2O compared to H_2O, but they reach the same enhancement value after about 15 minutes of illumination (Figure 2.23(b)). Deuterium oxide has a molecular structure and physical properties similar to water, but deuterium has twice the mass of hydrogen; The isotope effect is due to differences in the solvent reorganisation of H_2O and D_2O, with different solvent reorganisation energy in H_2O and D_2O, a result of a difference in the strength and structural order of intermolecular hydrogen bonds formed by H_2O and D_2O.[159] The differences in the fluorescence properties of QDs illuminated in the presence of H_2O or D_2O under argon can thus only be explained by the isotope effect. The isotope effect observed under argon suggests that water is involved in the solvation process that leads to a photoproduct responsible for the PFE effect. The PFE is facilitated by the solvation of a charged state that is more favoured by H_2O than in D_2O. Negative isotope effects have previously been observed in other electron

solvation processes.[160] The most probable process is stabilisation of a surface trap state of the CdSe/ZnS QDs by water molecules.

The humidity content does not affect the initial fluorescence yield under argon but increases the PFE effect. The most reasonable explanation of the effect of water is that water molecules play an important role in stabilising photo-induced charge-separated states, providing a route to preferred radiative as compared to non-radiative decay (see discussion at the end of section 2.4.2.4).

2.4.2.3 Illumination under a Humid Oxygen Atmosphere

Prior to illumination, drop-cast CdSe/ZnS QDs were purged under oxygen, at various humidities, for at least 50 minutes, in the dark. Unlike under argon, the initial fluorescence yield of QDs illuminated under oxygen is highly dependent upon humidity (Figure 2.24(a)). For example the initial (t=0 mins) peak height is about 60% lower at 0.01 mole/m^3 compared to similar QD samples at 1.47 mole/m^3 (Figure 2.24(a)). During illumination at low oxygen humidity (0.01 moles/m^3) the fluorescence intensity sharply drops (by 12% within 1 minute), followed by a slight fluorescence increase to only 90 % of the original value within 10 minutes of illumination, and subsequent decay in the fluorescence yield by 9% after 45 minutes of illumination (relative to the value at 10 mins)(Figure 2.24(b)). Samples illuminated at a slightly higher humidity (0.15 moles/m^3) show a lower level of decay in the initial fluorescence yield (a decay by 9% within 1 minute), and a higher PFE (a recovery to approx. 98% of initial fluorescence yield within 10 minutes), as well as a slightly quicker drop in fluorescence yield with further illumination (the fluorescence is quenched by 15% after 45 minutes of illumination, relative to the yield at 10 minutes) (Figure 2.24(b)). At even higher humidity levels (1.47 moles/m^3) no initial reduction in fluorescence yield is observed, but instead, a PFE effect occurs initially (Figure 2.24(b)), and this then drops (the fluorescence yield is reduced by 30% after 45 minutes of illumination, relative to the value at 10 minutes).

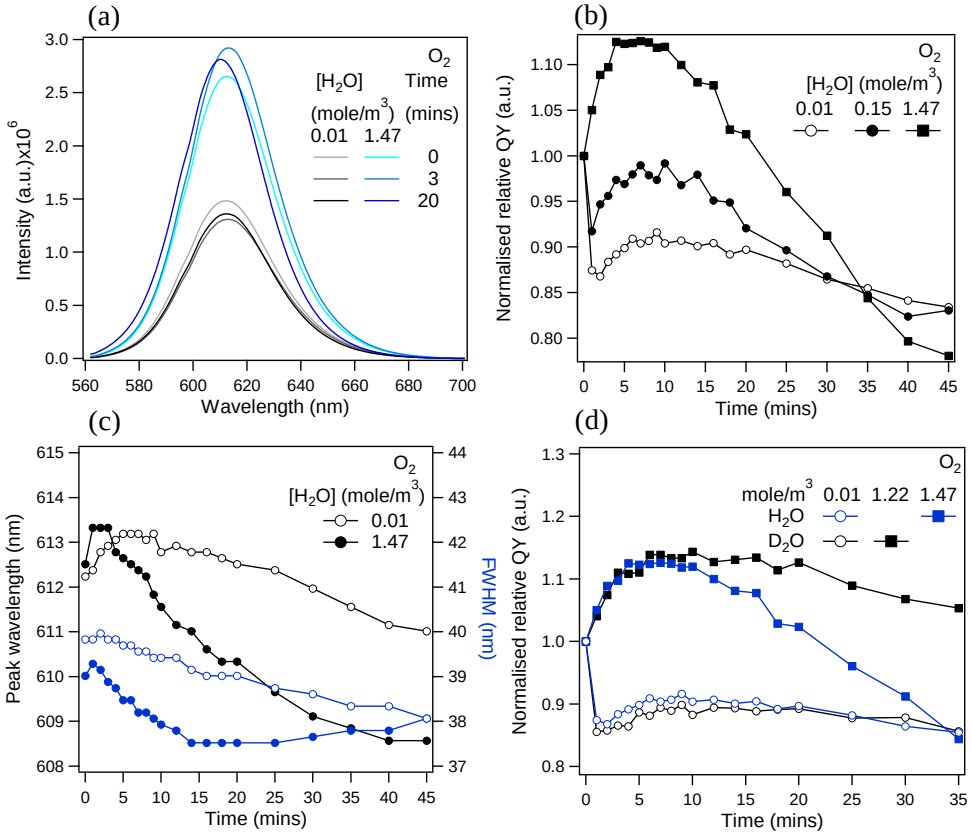

Figure 2.24: H_2O and D_2O humidity dependence of the fluorescence spectrum evolution of CdSe/ZnS QDs excited under O_2 atmosphere: (a) fluorescence spectra at illumination times 0, 3 and 20 mins under H_2O; evolution under illumination of the (b) normalised relative quantum yields under H_2O (c) emission peak wavelength (black) and emission peak width (blue) under H_2O (d) normalised relative quantum yields under H_2O or D_2O. Excitation was at 60 µW, 532 nm.

The evolution of the fluorescence spectra of the QDs is also affected by the humidity content: at low humidity (0.01 moles/m^3) a small red-shift in the spectrum (from 612.2 nm to 613.2 nm within 5 minutes) is followed by a gradual blue-shift in the spectrum, reaching a difference by 1 nm after 45 minutes (Figure 2.24(c)). The fluorescence peak broadens slightly within 1 minute, and narrows upon further illumination, yielding a 1.7 nm narrower fluorescence peak after 45 minutes of illumination (Figure 2.24(c)). At higher humidity content, the blue-shift is accelerated and starts earlier compared to under dry oxygen: at a humidity content of 0.01/1.47 mole/mm^3, the blue-shift starts after roughly 8 minutes/3 minutes of illumination, and shifts from 612.2 nm (t=0 mins) to 611.0 nm (t=45 mins)/ from 612.5 nm (t=0 mins) to 608.6 nm (t=45 mins)(Figure 2.24(c)). Accelerated narrowing of the fluorescence peak is observed under

increased humidities, with illumination at 1.47 mole/mm^3 H_2O also yielding an eventual broadening in the fluorescence peak after 14 minutes of illumination, which is not observed at lower humidities (Figure 2.24(c)).

The initial drop in fluorescence yield with illumination observed under dry oxygen was previously attributed to be due to QD charging via electron-transfer from the neutral QD core to oxygen adsorbates (section 2.4.2.1), as previously suggested by Koberling *et al.*[65] Our results under oxygen of a reduced initial drop in fluorescence yield with illumination and increased PFE effect under increased humidties (Figure 2.24(b)) suggest that at increased humidities under oxygen charging of the QDs becomes less dominant and that instead the PFE effect dominates.

The fluorescence spectrum of CdSe/ZnS QD samples under oxygen was also studied under various humidity levels of D_2O and compared to those of similar samples under various H_2O humidity levels. Two potential effects of using deuterated, versus non-deuterated water, under oxygen might be expected:

(i) The fluorescence yield is dependent on the same water dependent process (solvation of a charged state), as seen for the CdSe/ZnS QDs illuminated under a humid argon atmosphere, as described in section 2.4.2.2.

(ii) The singlet oxygen ($^1O_2$) lifetime is fifteen times longer in D_2O compared to in H_2O,[132, 134] which could lead to greater oxidation of potential photoproducts.

At a low humidity (0.01 mole/m^3) no difference is detected irrespective of whether D_2O or H_2O was used (Figure 2.24(d)). Very similar results within the error of measurement at a low humidity under oxygen, irrespective of whether H_2O or D_2O was used, suggest that under oxygen, compared to under argon, water molecules are less important in defining the fluorescence properties of CdSe/ZnS QDs at low humidity. It is only at the higher humidity level (1.19 moles/m^3) that there is a significant difference after longer illumination times (Figure 2.24(d)).

One possible reason as to why the humidity content under oxygen plays such a significant role in the fluorescence properties is a photo-induced reaction with oxygen. We suggest that there are two competing processes occurring in the presence of oxygen and humidity (Figure 2.25(b)). At low humidity levels the major process is an electron transfer from a neutral QD core to oxygen molecules, resulting in quenching of the emission of CdSe/ZnS QDs (by an Auger process). At high humidity levels the process that is responsible for the PFE predominates, which results from photo-induced interactions of the CdSe/ZnS QDs with water molecules. We suggest that this site could be a surface trap state.

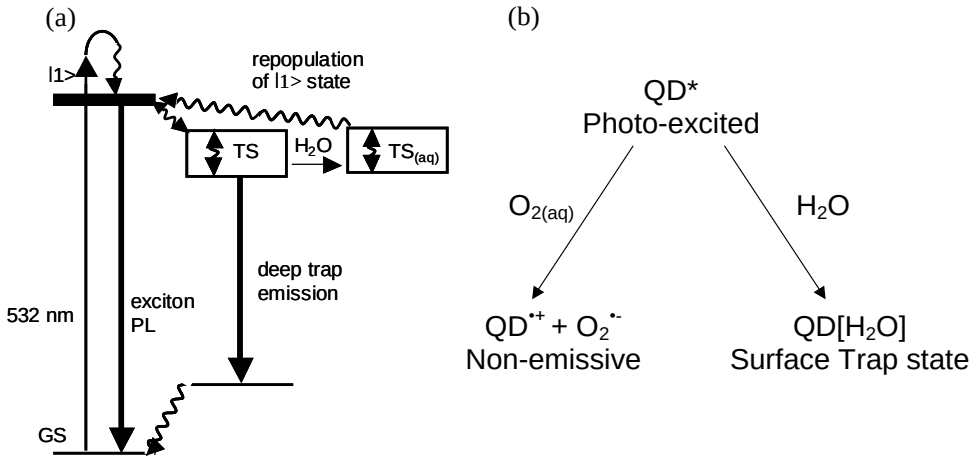

Figure 2.25: (a) Illustration of the proposed effect of water: a QD is excited from the ground state (GS) to the lowest emitting exciton state (I1>), followed by fluorescence or trapping into a surface trap state (TS) of either the electron of hole in an exciton, followed either by return of the trapped charge to the QD core, or by deep trap emission. Water stabilises the solvated surface trap state (TS_{aq}), resulting in a higher likelihood of solvated surface trapped charges returning to the lowest emitting QD state, where radiative decay via the energy gap occurs (b) suggested processes occurring under a humid oxygen atmosphere in excited CdSe/ZnS QDs: electron transfer from an excited state QD core to adsorbed oxygen creates a positively charged, non-emitting QD core, and an oxygen radical anion (left), whereas water stabilises a solvated surface trap state (right).

We explain the PFE effect by adapting the schemes suggested by Jones *et al.*,[66] where a trap state manifold is suggested (Figure 2.25(a)). We suggest that water can stabilise a surface trap state and that trap state stabilisation involves reorganisation of the water environment, as suggested by the isotope effect under argon. Our studies suggest that solvation of a charged surface trap leads to a rise of the fluorescence of CdSe/ZnS QDs.

Figure 2.25(a) summarises the proposed effect of atmospheric humidity on QD recombination dynamics. We suggest that the lowest exciton state (|1> state) either relaxes radiatively to the ground state, producing fluorescence, or undergoes rapid decay to a charge-separated trap state (TS). In the presence of water molecules, the trap state is rapidly solvated, forming a solvated trap state (TS_{aq}) that is more stable than TS. The enhanced PFE under a more humid argon atmosphere and the isotope effect, suggest that, similar to the process suggested by Jones *et al.*,[66] water-stabilised charge-separated trap states (TS_{aq}) repopulate the lowest emitting state in the QD core more efficiently, resulting in radiative decay via the energy gap, rather than non-radiative decay processes.

In the presence of hydrated oxygen, the charge separated trap state (TS) (and possibly the lowest exciton state (|1> state)) are quenched by a reaction, which is most likely to be by electron transfer, yielding the non-emissive ionised QD and the oxygen radical anion (Figure 2.25(b)). The hydration of the charge-separated state (TS) to yield the solvated trap state ($TS_{(aq)}$) occurs in competition with the reaction with hydrated oxygen (Figure 2.25), and thus at high humidity levels, higher fluorescence yields are seen (see Figure 2.24(b)).

2.4.2.4 X-Ray Photoelectron Spectroscopy Analysis

To establish the chemical processes involved in photo-degradation of the QD under a humid oxygen atmosphere, and to verify the proposal of van Sark *et al.* that both the CdSe core and the ZnS shell are degraded by oxidation,[61] we evaluate the photoproducts using X-ray photoelectron spectroscopy (XPS)(appendix A.2). XPS spectra of CdSe/ZnS QD samples illuminated under humid oxygen (1.47 mole/m^3) were analysed and compared to those not illuminated. As can be seen in Figure 2.26(i), the XPS spectra contain a number of lines, which can be assigned to elements of the non-illuminated CdSe/ZnS QDs and photoproducts of illuminated CdSe/ZnS QDs, which are shown in detail in Figure 2.26(ii-v) and are discussed below. The samples also contains lines at 282 eV, 529 eV and 399.8 eV (Figure 2.26(i)), which can be assigned to C_{1S}, O_{1S} and NO_3,

respectively, and these are most likely from the capping layer of hexadecylamine (whose structure is $CH_3(CH_2)_{15}NH_2$). The photoproducts also contain silicon 2s and 2p lines from adventitious silicon.

The amounts of Cd, Se, Zn and S are drastically reduced in the illuminated compared to the non-illuminated QD sample (Table 2.1).

The XPS spectra of cadmium consist of the doublet Cd $3d_{5/2}$ and Cd $3d_{3/2}$ lines, due to spin-orbit coupling, and reveal a slight shift to higher binding energies with photo-illumination (Cd $3d_{5/2}$ peak at 404.4eV/409.4 eV for non-illuminated/illuminated sample) (Figure 2.26(ii)). In both cases, the position of the $Cd3d_{5/2}$ line is between that previously recorded for cadmium selenide (405.0 eV to 405.3 eV), cadmium (404.6 eV to 404.9 eV) and cadmium oxide (404.0 eV to 404.2 eV),[161, 162] and so both peaks could represent either compound. Thus, it is not possible to state definitively that the photo-illuminated sample is entirely composed of either Cd, CdSe or CdO.

The XPS spectrum of selenium is shown in Figure 2.26(iii) and consists of the Se 3d peak. The Se 3d peak is made up of two peaks, Se $3d_{5/2}$ and Se $3d_{3/2}$, separated by 0.85 eV, due to spin-orbit coupling. The Se $3d_{5/2}$ peak of the non-illuminated sample is located at 53.8 eV, consistent with quoted values of 53.89 eV for CdSe,[163] while no selenium is detected for the illuminated sample. The absence of Se after illumination is most likely a result of photo-oxidation and evaporation of selenium dioxide in the vacuum pump during XPS sample analysis.

Figure 2.26(iv) shows the XPS spectrum of zinc. The Zn 2p signal is a doublet, with a separation of 23 eV, but only the Zn $2p_{3/2}$ peak is shown here for clarity. The non-illuminated sample has a Zn $2p_{3/2}$ peak at binding energy 1020.0 eV, consistent with metallic zinc, while the 2p3/2 peak of the illuminated sample has shifted to higher binding energy of 1021.6 eV, consistent with zinc oxide.[164]

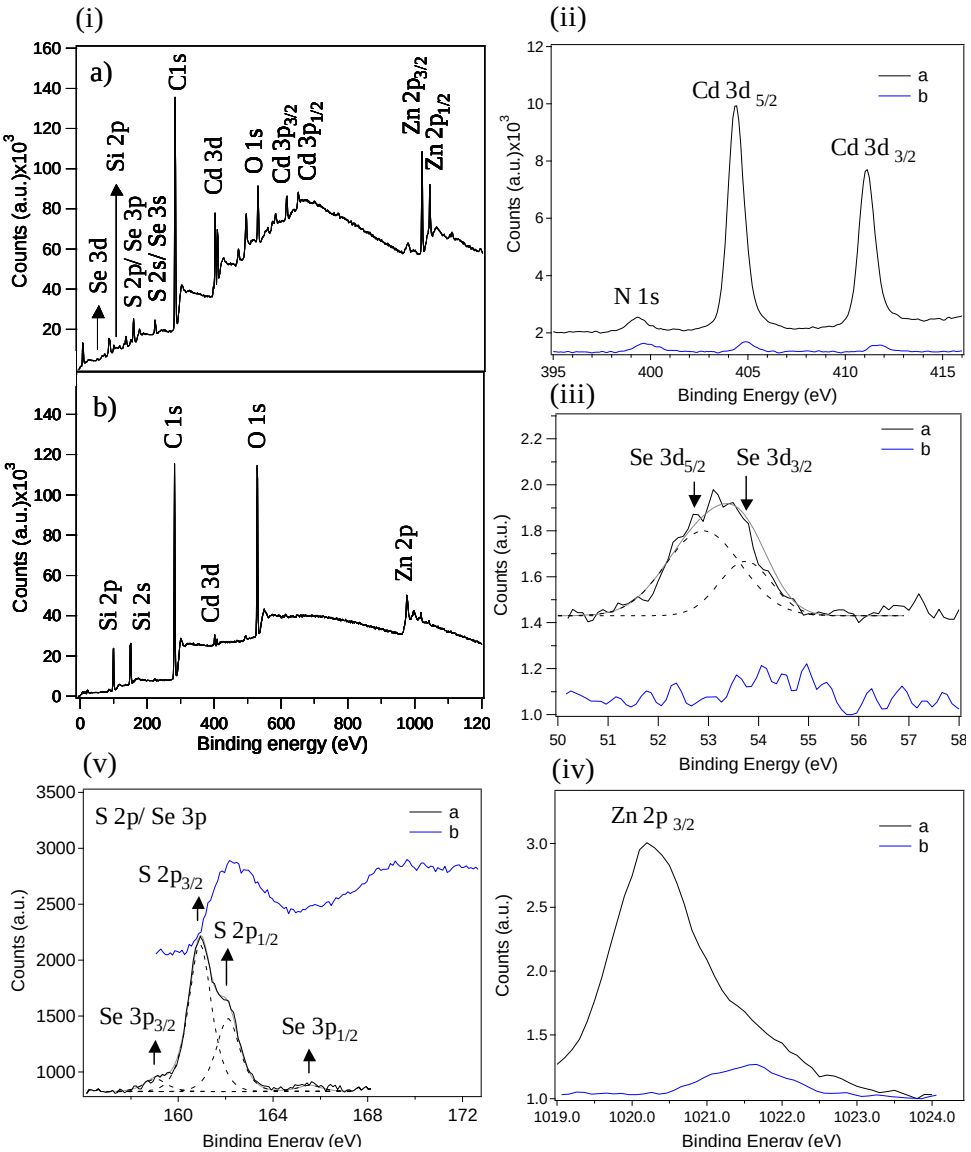

Figure 2.26: XPS spectra of CdSe/ZnS QDs (a) not illuminated and (b) illuminated under humid oxygen atmosphere s (i) full XPS spectrum; expanded view of (ii) Cd peaks (iii) Se 3d peaks (iv) Zn peak and (v) S and Se 3p peaks.

The XPS signal of sulphur and selenide is shown in Figure 2.26(v) and is in the region of 157 to 167 eV. The non-illuminated sample shows a peak at 161 eV consisting of 4 lines, namely Se $3p_{5/2}$, Se $3p_{3/2}$, S $2p_{5/2}$ and S $2p_{3/2}$. The S $2p_{3/2}$ peak observed at 161 eV is indicative of bound, unoxidised sulphur. The illuminated sample showed two peaks, one at 162 eV, indicating sulphur, and a second peak at 168 eV, indicating some oxidised sulphur (SO_3 moieties). However, the illuminated sample contained much less sulphur than the illuminated sample, although the detection in the illuminated sample was complicated due to low levels of

silicon contamination. Volatile oxidation products of sulphur and selenide will be lost from the sample.

Sample	C 1s	Cd 3d	N 1s	O 1s	Se 3d	Zn 2p	S 2p
(a) non-illuminated	85.6	0.92	0.51	7.5	0.2	2.8	2.6
(b) illuminated	77.1	0.1	0.1	21.4	0	0.2	1

Table 2.1:Calculated amounts (%) of elements in CdSe/ZnS QDs that were (a) not illuminated, and (b) illuminated under humid oxygen.

A reasonable explanation of the XPS results of cadmium and selenium suggest that the CdSe core is oxidised. More surprisingly, the XPS results for zinc indicate that the ZnS shell is also oxidised, producing ZnO when illuminated under a humid oxygen atmosphere. It has been shown that a colloidal dispersion of ZnS particles exposed to hydrogen peroxide (H_2O_2) is oxidised to ZnO.[165] The oxidation of the ZnS shell as a result of photo-oxidation is unlikely, so that it is suggested that the ZnO forms as a result of ZnS exposure to hydrogen peroxide. Hydrogen peroxide is known to be formed via the spontaneous dismutation of an oxygen radical anion in water via the route[142, 166]

$$O_2^{\cdot -} + H^+ + HO^{\cdot}{}_2 \rightarrow H_2O_2 + O_2 \qquad \text{(vi) or}$$

$$O_2^{\cdot -} + 2H_2O \rightarrow 2H_2O_2 + e^- \qquad \text{(vii)}$$

The oxygen radical anion itself may be formed by the transfer of an Auger electron from the QD core to surface adsorbed oxygen, as suggested by Koberling *et al.*[65]

In summary, we suggest that at low humidity levels the major process is an electron transfer to surface-adsorbed oxygen molecules and quenching of the emission of CdSe/ZnS QDs (by an Auger process), whereas at high humidity levels the process that is responsible for the PFE predominates and this results from photo-induced interactions of the CdSe/ZnS QDs with water molecules. We suggest that this site could be a surface trap state. At high humidity levels in oxygen, the solvated-trapped charge from the QD is effectively stabilised by water and returns to the QD core, where it radiatively recombines across the energy gap, which results in PFE. This stabilisation of trapped surface charge, which results in PFE, relies on the presence of water, so that it is very effective at high humidities. The electron transfer to adsorbed oxygen molecules creates an oxygen radical

anion, which, in the presence of water, can convert into hydrogen peroxide, as suggested by Aust[142] and Chen *et al.*[166] Hydrogen peroxide oxidizes the ZnS shell of photo-excited CdSe/ZnS core/shell QDs, resulting in the photo-oxidation of the CdSe core and thus QD degradation,

2.5 Conclusion

The fluorescence properties of CdSe/ZnS QDs are significantly affected by the presence of water molecules. Under inert environments (i.e. argon), increasing water humidity accelerates the photo-induced fluorescence (PFE) effect, but there is no difference in the initial fluorescence yield irrespective of humidity. It is suggested that the PFE is a result of a solvation of a charged state, a 'solvated' surface trap state; as implied by the different PFE rates under comparable D_2O humidity levels. Under oxygen environments, the initial fluorescence yields increases with water humidity. The PFE is highly dependent upon the humidity. At low humidity levels there is a reduction of fluorescence yield with illumination, but at high humidity there is a significant PFE effect and no initial fluorescence yield reduction. We assign this effect to two competing processes (i) photo-induced electron transfer (via the Auger process) of the CdSe/ZnS QDs to generate a non-emissive QD and generation of oxygen radical anion and (ii) water stabilisation of a highly emissive surface trap state, as seen for samples illuminated under argon. With high humidity under oxygen, the PFE effect is predominant, and under low humidity levels the photo-induced electron transfer process is predominant (see Figure 2.25 in section 2.4.2.3). The eventual reduction in PFE of CdSe/ZnS QDs illuminated for longer timescales under a humid oxygen environment is suggested to be a result of chemical degradation of the ZnS shell by peroxide products and the core, as confirmed by XPS analysis.

The suitability of QDs as quantitative fluorescent labels in bio-analytical applications, as initially planned in this thesis, is not ideal as QD fluorescence is highly sensitive to the illumination time and is greatly affected by the atmospheric conditions.

Chapter 3

3 Investigation into DNA Quantum Dot Interactions

This chapter aims to establish whether long genomic DNA strands associate with colloidal quantum dots. Presented are absorption and fluorescence studies, as well as atomic force and fluorescence microscopy studies

3.1 Literature Review- DNA Adsorption onto Nanoparticle Surfaces

DNA adsorption onto various nanometre-sized surfaces, such as carbon-nanotubes, gold colloids, semiconductor quantum dots (QDs) and silica nanoparticles, has been experimentally observed. This section aims to summarize the DNA absorption processes onto surfaces reported in the literature

3.1.1 DNA Structure in Chromosomes

In human cells the DNA strands associate with proteins (histones) forming a chromatin fibre (DNA-protein complex) that is compacted into a highly condensed structure (a chromosome) inside the cell nucleus. The smallest repeatable unit of chromatin is the nucleosome,[167] which consists of (i) 8 histones (a histone octamer), 2 each of the core histone proteins H2A, H2B, H3 and H4[168, 169] (Figure 3.1(a)), which takes the form of a flattened cylindrical shape, about 10 nm in diameter and 5 nm high[170]

(Figure 3.1(c)), (ii) ~146 base pairs of DNA strand wrapped by ~1.65 times, as a left-handed superhelix, around the histone octamer[168] (Figure 3.1(a- c)). The (i) histone octamer and the (ii) 146 bp DNA winding constitute the nucleosome core.[171] The nucleosome also contains (iii) a 5th histone, H1, which stabilises the nucleosome core by associating to the 10 bp of extended DNA present at the entrance and exit sites of the nucleososome[172] (Figure 3.1(b)).

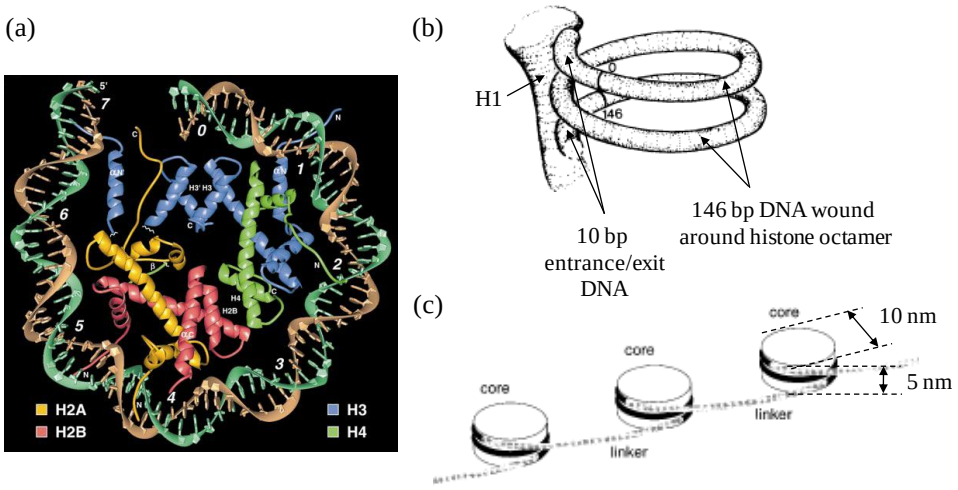

Figure 3.1: (a) structure of nucleosome viewed from above as probed by X-ray diffraction, showing half of the nucleosome core, split between the 1.65 turns of DNA strand around the histone octamer, thus containing 4 histones (H2A, H2B, H3 and H4) and 73 DNA base pairs.[168, 173] (b) schematic of histone H1 "sealing off" the nucleosome core: 146 bp DNA (marked by the markers 0 and 146) is wound around the histone octamer and is extended by 10 bp at each end to form a full 2 turn winding that is 166 bp long. Histone H1 is attached to the extended DNA strand at the side of the nucleosome core (adapted from[172])(c) schematic representation of the nucleosome, consisting of a core, where DNA (dark) wraps around a histone octamer (represented as a disk), and a DNA linker region (light), which connects nucleosome cores (adapted from[173]).

Adjacent nucleosomes are linked together by a stretch of 15-100 base pairs of linker DNA strand[174] (Figure 3.1(c)). This 10 nm diameter chromatin fibre has previously been compared to beads on a string.[173] The 10 nm chromatin fibre is compacted into a higher order structure, a chromatin fibre of about 30 nm in diameter (Figure 3.2),[171] which is stabilised by the fifth histone protein, H1.[172, 175] These 30 nm chromatin fibres in turn are folded into further levels of compactness, eventually resulting in the formation of chromosomes.[176] The histones in the histone octamer are highly positively charged, while the DNA strands are negatively

charged, due to the sugar-phosphate backbone, resulting in tight binding between the histones and the DNA strand.[176]

The DNA folding into a 30 nm diameter chromatin fibre occurs at high concentrations of monovalent or divalent salt concentrations.[171] In general, the formation of higher order structures depends on the ionic strength: while at low ionic strength the chromatin is in an unfolded state, increasingly high ionic strengths yield increasingly condensed chromatin structures[171, 172] (Figure 3.2). The presence of histone H1 is crucial for the formation of higher order chromatin structures, as chromatin depleted of H1 does not form ordered fibres with increasing ionic strengths.[172]

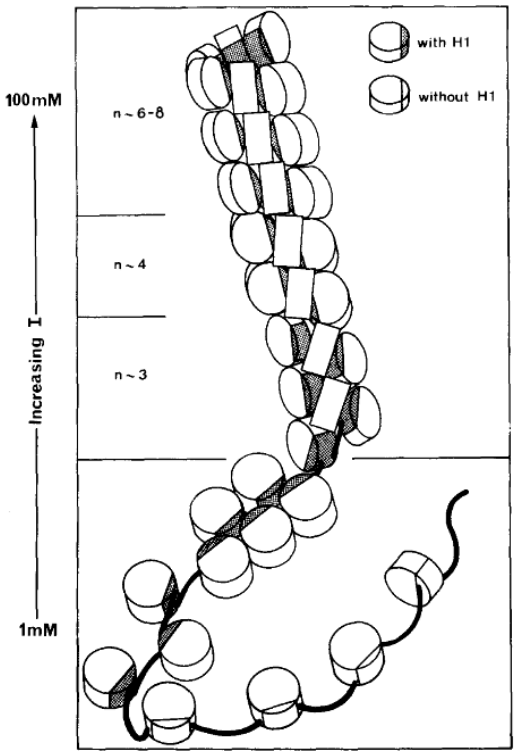

Figure 3.2: Schematic of effect of ionic strength (I) on the chromatin structure: in the absence of H1, the DNA entrance and exit sites from the nucleosome do not coincide with each other (bottom right) and there is no higher order structure; in the presence of H1, the exit/entrance sites coincide with each other and a zigzag structure forms (bottom left); with increasing salt concentration (I), the chromatin forms higher ordered helical structures with increasing number of nucleosomes per turn (n), which are held together by histone H1.Salt was NaCl between 0 and 100 mM.[172]

3.1.2 DNA Adsorption onto Carbon Nanotubes

Carbon nanotubes (CNT) are manufactured carbon cylinders a few nanometers in diameter and up to a few centimetres long,[177] and made of a single rolled-up carbon sheet.

Guo *et al.*[178] have used Transmission Electron Microscopy (TEM) to image double-stranded (ds) DNA immobilised on the surface of carbon nanotubes (Figure 3.3), although no details are given on how the nanotubes were treated with DNA. An even coverage of DNA strand on the nanotube surface was observed, indicating a strong, but at the time unclear, interaction mechanism between double-stranded DNA and carbon nanotube.

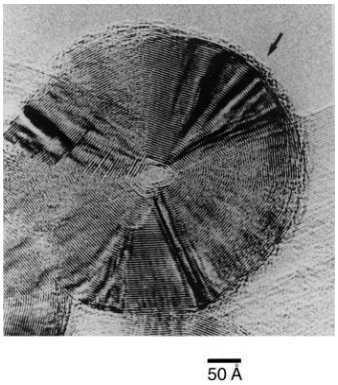

Figure 3.3: TEM image of iodinated and platinated double-stranded DNA (arrow) on a carbon nanotube surface. DNA was self complementary 5`-ATG GTA GCT ACC AT-3` double-stranded DNA.[178]

Binding of single-stranded (ss) DNA,[179] short double-stranded DNA[179] and Calf-thymus DNA[180] onto single-walled carbon-nanotubes (SWCNT) has been experimentally observed. Nepal *et al.*[181] have also observed wrapping of double-stranded DNA from herring testes around multi-walled carbon nanotubes, accomplished by milling of a solid state mixture of multi-walled carbon nanotubes and DNA.

The binding efficiency of DNA onto nanotubes was found to depend on whether it was single or double-stranded DNA[179] and on the base sequence in the case of single-stranded DNA.[179, 182] While single-stranded DNA binds readily to nanotubes after mild sonication of a solution mixture of DNA and nanotubes, short double-stranded DNA requires vigorous sonication in order to bind to nanotubes, suggesting

single-stranded DNA binds more readily with nanotubes as compared to double-stranded DNA.[179] However, with single-stranded DNA, hybridisation must be eliminated either by using homopolymers, or by adding a denaturant that disrupts base pairing.[179] The different binding efficiencies to nanotubes of single and double-stranded DNA is suggested to be due to different binding geometries to nanotubes of single-stranded DNA compared to double-stranded DNA.[180] A change in Calf-thymus DNA conformation upon binding to SWCNTs from A-DNA to B-DNA (appendix B.10) is proposed by Dovbeshko *et al.*[180]

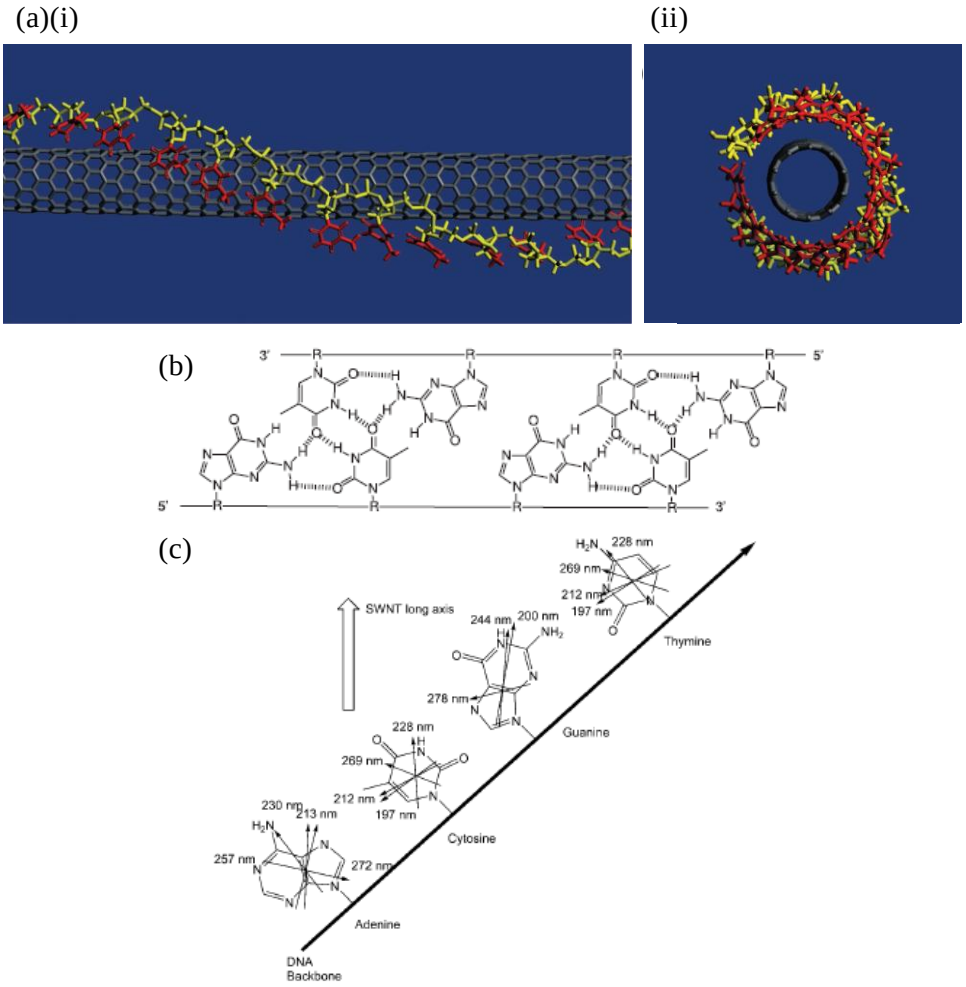

Figure 3.4: Model for single-stranded DNA association onto carbon nanotubes illustrated with (a) the poly-T sequence in (i) side-view and (ii) top view,[179] showing right-handed helical wrapping, with the nucleotide bases (red) attached to the nanotube surface by π-stacking, and the sugar-phosphate backbone (yellow) oriented away from the bases,[179] and (b) the $d(GT)_n$ sequence, where n=10-45, where antiparallel $d(GT)_n$ strands interact by hydrogen binding to form a double-strand that wraps around the nanotube in a highly periodic helical manner,[182] (c) proposed orientation of single-stranded DNA bases on a SWCT. The bases lie flat on the nanotube surface at an oblique angle of about 45°.[183]

In the case of single-stranded DNA, DNA sequence and length depend studies have shown that 30mer poly-T binds most efficiently to carbon nanotubes out of a length selection of 15 to 60 bases and the bases A, T, C and G.[179] Other single-stranded DNA sequences that bind efficiently to nanotubes were alternating sequence repeats of G and T, that is $d(GT)_n$, where n=10-45 nucleotides.[182] Rajendra *et al.* have experimentally shown that single-stranded DNA binds to SWCNTs differently than observed with double-stranded DNA, suggesting that the nucleic acid bases of single-stranded DNA lie flat on the nanotube surface with the DNA wrapping around the nanotube at an oblique angle of about 45°(Figure 3.4(c)).[183]

Molecular modelling suggests that in general, single-stranded DNA binds to nanotubes by π-π-stacking interactions (appendix B.9) between aromatic nucleotide bases and the CNT surface.[179] It was suggested that in single-stranded DNA the highly flexible bond torsion within the sugar-phosphate backbone allows single-stranded DNA to adapt to a low-energy conformation that maximizes the π-π interaction between the DNA bases and nanotube surface.[179]

In general, molecular modelling suggests that within a range of preferred torsion angles, there are a number of single-stranded DNA conformations that allow DNA binding to nanotubes, all with similar binding free energies, such as right or left handed helical structures with different pitches or a linear conformation on the nanotube surface.[179] For instance, poly-T (single-stranded DNA) forms a right-handed helical structure around the nanotube surface, with the bases bound to the nanotube surface by π-π interactions, while the sugar-phosphate backbone is extended away from the nucleic acid bases, making otherwise water-insoluble nanotubes hydrophilic[179] (Figure 3.4(a)). In contrast, Zheng *et al.*[182] suggest, based on observations of AFM images, that antiparallel strands of the sequence $d(GT)_n$, where n=10-45 nucleotides, interact by hydrogen bonding, forming a double strand (Figure 3.4(b)), which self-assembles into a highly ordered helix around a nanotube, with regular pitch of 18 nm.[182] It is suggested that the single-stranded DNA sequence and

structure determines the exposure of the DNA bases to the nanotube surface.[179]

3.1.3 DNA Adsorption onto Quantum Dots

3.1.3.1 Quantum Dots- Oligonucleotide Conjugation

The surface chemistry of colloidal CdSe/ZnS core/shell quantum dots (QDs) and CdS core QDs has been developed to allow formation of QD-DNA conjugates. QD-DNA conjugates are applied for detecting specific target DNA using DNA hybridisation and FRET.[184] Most QD-DNA conjugate formation methods involve two steps, ligand exchange to make QDs water soluble, and QD-DNA conjugation.

3.1.2.1.1. QD Water Solubility

QD water solubility is achieved by ligand exchange with ligands that contain both (a) a thiol (SH), (for linkage to the ZnS QD-shell or CdS QD surface,[185, 186] making use of the high reaction between ZnS shell surface and thiols), and (b) a hydrophilic carboxylic acid end group (COOH),[188, 189, 190] or hydrophilic hydroxyl (OH)[185, 186] end-group for water solubility. For example, 3-Mercaptopropionic acid (MPA)($HSCH_2CH_2COOH$)[190, 191] or 2-Mercaptoacetic acid (MAA) ($HSCH_2COOH$)[188] have been attached to CdSe/ZnS QDs, while 2-Mercaptoethanol ($HSCH_2CH_2OH$) –capped CdS QDs yielded water soluble CdSe QDs.[185] Instead of mono-thiol-terminated ligands such as MAA or MPA, ligands with two thiol-end groups, such as dihydrolipoic acid (DHLA), have been used as a coating for CdSe/ZnS QDs, which increased the QD stability in buffer solutions.[192] However, both DHLA and MAA/MPA contain a COOH-end group for water solubility. CdSe/ZnS QDs have also been COOH-functionalised by coating in a amphiphilic triblock copolymer, consisting of polybutylacrylate ($C_7H_{12}O_2$), polyethylacrylate ($C_5H_8O_2$) and poly(methacrylic acid)($C_4H_6O_2$).[184]

3.1.2.1.2. QD-DNA Conjugation

QD-Oligonucleotide conjugates have been formed in various ways using different chemistries. MAA-capped CdSe/ZnS QDs rely on amine-modified DNA to form QD-DNA conjugates, via the formation of an amide bond between the COOH-end group of the MAA ligand and the carbon-amine linker (NH_2C_6 or NH_2C_{12}) of modified DNA.[188] The DNA was a 19mer, mixed base single-stranded (ss) oligonucleotide.[188] Similarly, DNA conjugation to CdSe/ZnS QDs coated by EG_3COOH and EG_3OH was achieved by the formation of an amide link between the C_6-amide-modified 30mer mixed base DNA and the carboxylate surface-groups of the QD surface.[186] Single-stranded RNA has also been attached to a COOH-functionalised CdSe/ZnS QD surface using amino (NH_2)-modified 21-23mer ssRNA and 1-Ethyl-3-(3-dimethylaminopropyl) carbodiimide hydrochloride (EDAC)($C_8H_{18}N_3Cl$) as a cross-linker.[184]

On the other hand, conjugation between MPA-capped CdSe/ZnS QDs and 30mer mixed-base double-stranded DNA[190] or 26mer mixed base single-stranded DNA[191] was achieved via a thiol linker.

Whereas DHLA coated CdSe/ZnS QDs formed QD-DNA conjugates with DNA modified with a polyhistidine –peptide linker (His_n-Cys(ac)-S-S-Py):[193] the thiol-reactive polyhistidine-peptide-linker attaches to thiolated DNA via disulfide exchange, and the metal-histidine interaction drives the self-assembly of histidine-modified DNA to CdSe/ZnS QDs.[193] It was shown that histidine-metal interaction promotes the DNA self-assembly onto CdSe/ZnS/HDLA QDs, and that the internal disulfide-bond (-S-S-) between the linker and the DNA played no role in the DNA self-assembly onto QDs. The DNA sequence used was mixed base 29mer oligonucleotides.[193]

Wang *et al.*[194] have developed a one-step method to prepare water soluble QD-DNA conjugates, which involves mixing oleylamine-capped CdSe QDs with Zn^{2+}, S^{2-} and thiolated DNA in DMSO (dimethyl sulfoxide) to produce water soluble CdSe/ZnS core/shell QDs capped with a high density of mixed-base 34mer single-stranded DNA. Also, association of biotinylated 100mer DNA to streptavidin coated CdSe/ZnS

QDs has been experimentally demonstrated,[195] with the QD-DNA conjugates forming within 3-4 hours.[195]

3.1.2.1.3. Conformation of QD-DNA Conjugates

Using FRET between QD donor and dye attached to a complementary hybridising strand, the conformation of DNA linked to a QD surface was found to be dependent on the QD surface chemistry. For instance, while DNA covalently attached to MAA-capped CdSe/ZnS QDs lies across the QD surface[188] (Figure 3.5), thiolated DNA conjugated directly to CdSe/ZnS surface had a fully extended conformation away from the QD surface.[194]

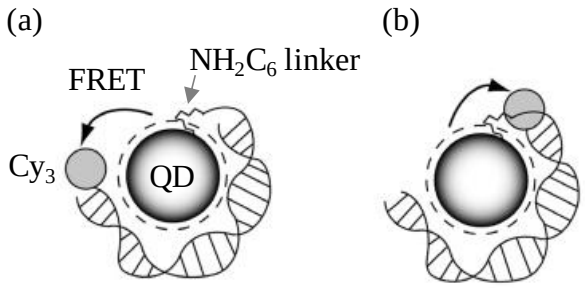

Figure 3.5: Model of double-stranded DNA configuration of mixed-base 19mer oligonucleotide conjugated to MAA-capped CdSe/ZnS QD. Similar FRET efficiencies of the QD-Cy3 dye donor-acceptor system for when the Cy3 dye is attached to the (a) far-end (b) near-end of the double-stranded DNA indicate double-stranded DNA lies across the QD surface of MAA-capped QDs.[188]

DNA is also fully extended for conjugates of hexahistidine-modified DNA (29mer, mixed base) and CdSe/ZnS/HDLA QDs.[193] The fully extended DNA conformation of hexahistidine-DNA in DNA-QD conjugates is attributed to DNA being prevented from folding on the QD surface due electrostatic repulsion between (i) negatively charged oligonucleotides attached to the same QD (up to 12 oligonucleotides per QD), and (ii) negatively charged COOH–end group (COO^-) of the DHLA QD coating and the negatively charged oligonucleotide.[193]

In contrast, mixed-base DNA (19mer) conjugated to a COOH-containing MAA-capped QD was shown to lie across the QD surface.[188] The conformation of conjugated oligonucleotides lying across the surface of MAA-capped QDs was explained with a hydrogen bonding model, according to which hydrogen bonding between nucleotide bases and

protonated carboxyl group (-COOH) of the MAA capping drives conjugated double-stranded mixed-base DNA to lie across the QD surface. Furthermore, it was found that hydrogen-bonding interactions not only drives ds-conjugated, but also free ss-oligonucleotides, to adsorb onto the surface of MAA-capped QDs, and that the DNA conformation on the QD surface depended on the DNA sequence. Specifically, polyA/polyT double-stranded DNA conjugated to MAA-capped QDs was found to adopt a conformation that is more upright than that of mixed-base conjugated DNA.[188]

3.1.3.2 Non-specific DNA Adsorption onto QD Surfaces

Some experimental abnormalities of QDs directly linked to a DNA strand have been suggested to be due to non-specific DNA adsorption onto the QD surface.[190, 191] For instance, aggregation of QD-DNA conjugates, consisting of MPA-capped CdSe/ZnS QDs directly linked to 30mer mixed base double-stranded DNA via a C_6-thiol linker, was experimentally observed at low QD: DNA ratios, and attributed to direct binding between Zn^{2+} ions on the QD surface and the negatively charged DNA phosphate backbone.[190] Also, Gill *et al.*[191] have experimentally observed efficient QD fluorescence quenching due to FRET from a QD donor to a nearby dye acceptor that is attached to DNA linked to the QD surface (Figure 3.6(i)(a), (i)(b) and (ii)(a), (ii)(b)), but only partial recovery of QD fluorescence occurred after cleavage of dye-labelled DNA from the QD surface (Figure 3.6(ii)(a) and (ii)(c)). The residual QD fluorescence quenching was attributed to non-specific adsorption of dye-labelled DNA onto the non-protected vacancies on the QD surface. The QD was a 3.8 nm diameter 3-mercapto-propionic acid (MPA)-capped CdSe/ZnS QD and the DNA was 26mer mixed-base duplex DNA.

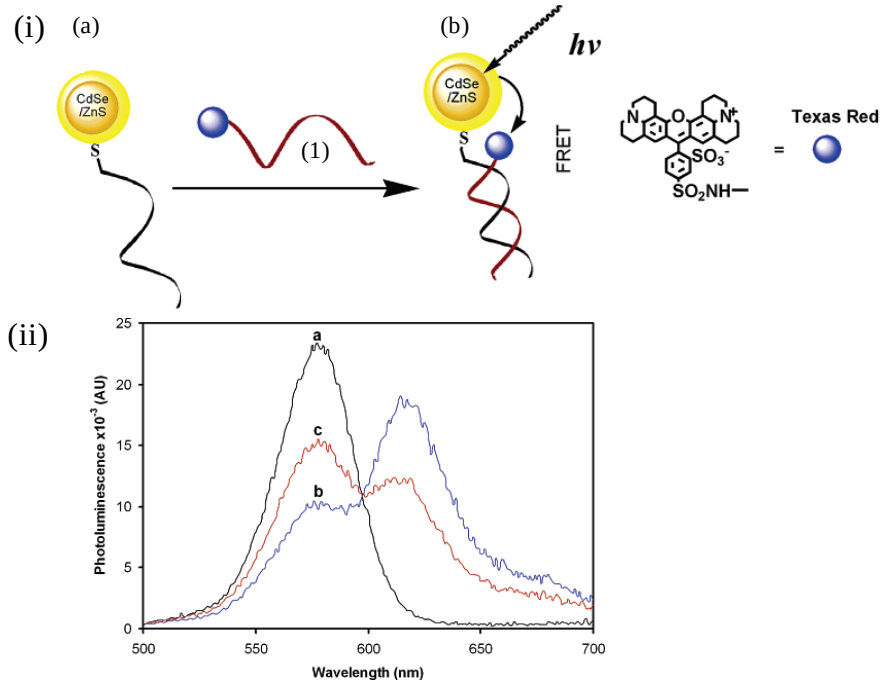

Figure 3.6: (i) (a) a CdSe/ZnS QD functionalised with a single-stranded DNA strand (i)(1) a dye-functionalised complementary single-stranded DNA strand (i)(b) QD/dye functionalised DNA duplex; (ii) Fluorescence spectra of (a) CdSe/ZnS QD functionalised with a single-stranded DNA strand (b) QD/dye functionalised DNA duplex, and (c) after reaction of QD/dye duplex DNA with the enzyme DNase 1, which cleaves the DNA from the QD. QD was CdSe/ZnS QDs, dye was Texas-Red.[191]

However, there has been more direct experimental evidence for non-specific DNA association to QD surfaces, explained by the hydrogen bonding model (section 3.1.3.2.1) and counter-ion exchange model (section 3.1.3.2.2).

3.1.3.2.1. Hydrogen Bonding Model

According to the hydrogen bonding model, hydrogen-interaction between the nucleotide bases of oligonucleotides and the protonated COOH-end group of the MAA ligand drives non-specific oligonucleotide adsorption onto the surface of MAA-capped QDs.[188] The adsorption efficiency was found to depend on various factors, such as buffer pH, presence of formamide, free single-stranded DNA or double-stranded DNA, and presence of conjugated DNA on the QD surface.[188] Specifically, experimental results showed that the adsorption efficiency (i) increases with decreasing pH, explained by protonation/deprotonation of most COOH-groups of the MAA-ligands at low/high buffer pH, (ii) reduces in the presence of hydrogen-bonding disturbing formamide, (iii) was higher

for single-stranded compared to double-stranded oligonucleotide, because the nucleotide bases are more available in single-stranded compared to in double-stranded DNA (iv) was reduced by the presences of already conjugated DNA, due to (a) reduced availability of the QD surface, and (b) added negative charge and thus increased electrostatic inter-strand repulsion destabilizing the adsorption.[188] FRET experiments have shown that the conjugated mixed-base oligonucleotides lie across the QD surface, while oligonucleotides with weaker adsorptive interaction, such as a polyA/polyT duplex, adopt a more upright configuration. All oligonucleotides were 19 bases long.[188]

3.1.3.2.2. Counter-ion Exchange Model

Mahtab *et al*. have shown that with QDs that have a net negative surface charge, a QD-DNA adduct formation can be driven by the exchange and expulsion of solvent ions and counter-ions from the QD-DNA interface,[196] and that the counter-ion exchange induces a change in the DNA structure that more closely matches the QD surface curvature, which further facilitates QD-DNA adduct formation.[192] It is proposed that a metal hydroxide layer forms around CdS QDs upon addition of metal cations in solution, with divalent metal cations Cd^{2+},[192, 197] Mg^{2+} and Zn^{2+} to yield a stable hydroxide layer.[192] The effective surface charge of QD surface-activated with divalent cations was measured to be more negative compared to unactivated QDs,[192] and a loosely bound cloud of divalent cationic counter-ions is suggested to form around QDs surface-activated with divalent cations (Figure 3.7(a)).[192] In contrast, negatively charged DNA is surrounded by a monovalent counter-ion cloud when in sodium containing buffer (Figure 3.7(a)).[192] It is suggested that non-specific adsorption of DNA onto surface-activated QD is driven by exchange of counter-ions between DNA and QD (Figure 3.7(b)). Divalent cations are thought to bind more tightly to the DNA than to the QD (Figure 3.7(b)), and after binding, counter-ions are expelled from the interface (Figure 3.7(b)).

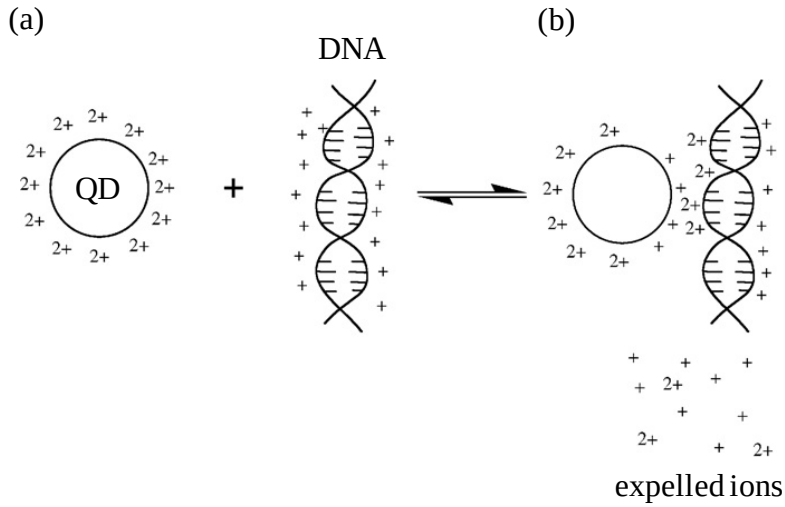

Figure 3.7: Model of ion-mediated interaction between Calf-thymus DNA and cationic CdS nanoparticle[192]: (a) in solution the QD is surrounded by loosely-bound divalent counter-ions (2+), and the DNA strand by sodium counter-ions (+), (b) QD-DNA binding is counter-ion exchange between QD and DNA.[192]

For all DNA shapes investigated, that is kinked, bent and straight DNA, experiments suggest a higher QD-DNA association efficiency for harder Zn^{2+} and Mg^{2+} ions compared to softer Cd^{2+} cations, suggesting that harder ions have a higher affinity to the DNA backbone than softer ions. Also, the divalent cations on the DNA surface are suggested to "pre-bend" the DNA strand, resulting in a DNA shape that more closely matches the QD curvature, facilitating QD-DNA adsorption.[192] The pre-kinking suggestion stems from the experimental observation that differences in binding efficiencies due to differences in DNA shape (kinked, bent, straight) were smallest in the presence of Zn^{2+} as it most efficiently induces DNA bending and thus best eliminates differences in DNA shape.[192] The pre-bending theory is supported by previous reports that divalent metal cations cause changes in the DNA structure, and divalent cations divalent cations[198] Zn^{2+} and Mg^{2+} introduce sharp kinks[199, 200] and smooth bends,[200-203] respectively, in DNA strands. In these experiments, DNA was double-stranded, 16 bases long, with sequence induced DNA shapes being straight, bent or kinked, while QDs were 4.5 nm diameter CdS QDs capped by 2-mercaptoethanol.[192]

Mahtab *et al.* have also experimentally shown that the release of counter-ions from the QD-DNA interface is the major mechanism that

drives binding of long (10,000 base pairs) Calf-thymus DNA strands to Cd^{2+} rich (cationic) CdS QDs.[196]

3.1.3.2.3. Base-Sequence/Structure Dependent Adsorption onto a Neutral QD Surface

Mahtab *et al.* have proposed that sequence-directed DNA structure and/or DNA flexibility affects the QD-DNA binding efficiency.[185] It is well documented that DNA sequence can alter the DNA structure and flexibility.[204, 205] For instance, DNA containing the sequence 5`-GGCC-3` has a 23° kink across the GGCC,[185] which is believed to be due to the presence of Mg^{2+}, while polyA/polyT is conformationally bent but stiff,[185] with the bend increasing in the presence of Mg^{2+} ions.[192] Mahtab *et al.* have experimentally shown that the DNA sequence and hence DNA conformation or DNA flexibility does affect the non-specific binding efficiency onto a QD surface.[185] Specifically, it was found that only kinked DNA, containing the GGCC sequence, binds to a 4 nm diameter, neutral, CdS QD surface, while stiff and bent DNA, containing AAAAAA, and straight DNA, do not adsorb onto the QD surface.[185] It is suggested that the intrinsically kinked DNA binds stronger or faster to the QD because its shape more closely matches that of the QD surface, reducing the energy cost associated with DNA binding to a curved QD surface, or because the kinked DNA is intrinsically more flexible, allowing it to wrap around the QD many more times than other DNA shapes upon collision with a QD in solution.[185] The mechanism that drives DNA association to a neutral QD surface was suggested to be (i) hydrogen bonding (section 3.1.2.2.1) (ii) van der Waals hydrophobic interactions[206, 207] or (iii) the release of counter-ions from the DNA and /or the QD surface.[192, 208] The QDs were 4 nm diameter CdSe QDs capped with 2-mercaptoethanol, with a neutral surface charge,[185] while DNA was 16 base, mixed base double-stranded oligonucleotides in Tris, 5mM NaCl buffer.[185] However, experimental evidence suggests that in the presence of the divalent metal cations Mg^{2+}, Zn^{2+} and Cd^{2+}, various DNA structures, kinked, bent and straight, can bind to negatively charged DNA believed to be due to divalent cation induced DNA bending.[192]

3.1.4 DNA Adsorption onto Gold Surfaces

Specific DNA adsorption onto gold surfaces through a thiol linker, and non-specific DNA adsorption through gold-nucleotide bases interactions, have been experimentally observed.

3.1.4.1 Specific DNA –Gold Binding

Gold has a high affinity to thiol-modified molecules allowing specific binding of thiol-modified oligonucleotides to gold surfaces[209] through spontaneous reaction of the thiolated DNA with the gold surface.

Gold nanoparticles have previously been functionalised with thiol-terminated[210, 211] and dithiol-terminated[212] oligonucleotides. In the case of planar gold surfaces, instead of a thiol modification at one end of a DNA strand, poly(dG)-poly(dC) oligonucleotides have been synthesised where the backbone of the G-strand contains phosphorothioate groups (Figure 3.8) which can bind to gold through the sulphur-gold interaction, creating multiple points through which DNA and the gold surface can interact.[209]

Figure 3.8: Schematic representation of a poly(dG)-poly(dC) oligonucleotide showing the phosphorothioate groups added into the backbone of the G-strand (red).[209]

Although the Au-S bond is one of the strongest bonds available for Au-DNA conjugation, thiol-terminated DNA has been experimentally shown to desorb from a 5 nm Au-NP surface upon exposure to temperatures exceeding 70°C.[210]

3.1.4.2 Non-specific Adsorption of DNA onto Gold Surfaces

It has been experimentally shown that due to non-specific interactions between nucleotide bases and a gold surface, thiolated single-stranded DNA non-specifically adsorbs onto a flat gold surface, resulting in a DNA strand configuration that is not perpendicular to the planar gold surface but rather lies flat on the surface[213, 214](Figure 3.9(a)).

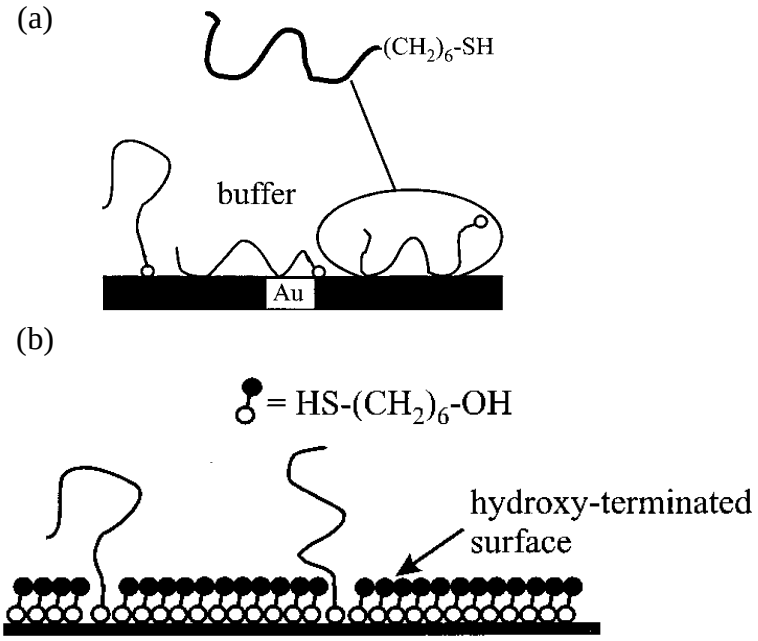

Figure 3.9: Schematic representation of adsorption states of alkanethiol-functionalised oligonucleotides (HS-$(CH_2)_6$-single-stranded DNA 49mer) onto a flat Au surface (a) Specific adsorption via the sulphide-gold interaction as well as non-specific adsorption via nucleotide base-gold interaction occurs on a flat Au surface, leading to DNA strand orientation that is not perpendicular to the planar Au surface[214] (b) addition of a monolayer of mercaptohexanol (MCH) on the Au surface after DNA adsorption prevents contact between backbone and gold surface, eliminating non-specific adsorption.[214]

While a parallel orientation of single-stranded DNA (49mer) on a flat gold surface has been experimentally verified;[213, 214] it has been proposed that single-stranded DNA (12mer) also lies flat on the NP surface due to the nucleotide-gold interaction.[215] Gold nanoparticles are frequently modified such that a net positive charge is present in order to induce electrostatic interparticle repulsion and thus prevent NP aggregation by coating in a citrate layer,[215] but positively charged NPs are also likely to attract negatively charged DNA.[215]

The non-specific adsorption of DNA onto a flat gold surface has been eliminated by (i) growth of a molecular monolayer either (a) before DNA adsorption (Figure 3.10) or (b) after DNA adsorption onto a flat gold surface (Figure 3.9(b)), or (ii) increase of the DNA surface coverage on a gold nanoparticle by increasing the ionic buffer concentration (section 3.1.4.3.1).

Once nonspecific DNA adsorption has already occurred, it can be eliminated by growing a monolayer of the thiol spacer mercaptohexanol (MCH) onto the gold surface, which displaces non-specifically adsorbed DNA and DNA does not adsorb onto the hydroxyl-terminated MCH (Figure 3.9(b)).

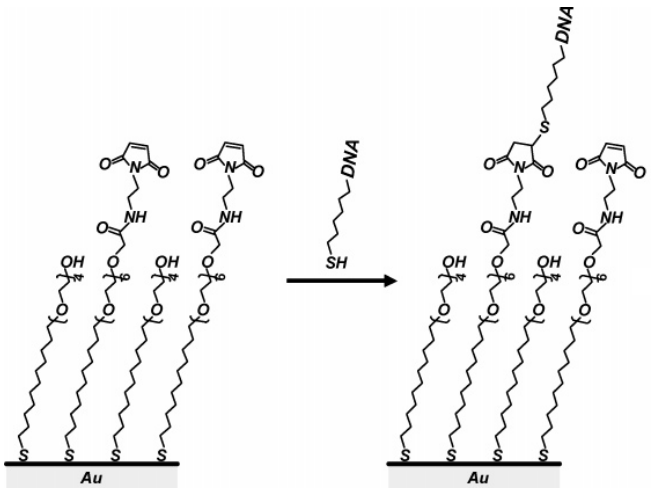

Figure 3.10: Schematic representation of adsorption of thiolated 20mer single-stranded DNA (SH-single-stranded DNA) onto a MEG monolayer onto of a gold surface: thiolated single-stranded DNA specifically binds to the maleimide (M), while the ethylene glycol (EG) layer prevents non-specific adsorption of DNA onto the gold surface.[216]

Lee *et al.* [216] have developed an alternative monolayer for preventing non-specific DNA adsorption which is deposited before DNA adsorption: a maleimide ethylene glycol disulfide (MEG) monolayer on a flat gold surface (i) allows specific adsorption of thiolated single-stranded DNA to the maleimide through the formation of a thiol bond, but (ii) prevents nonspecific DNA adsorption onto gold due to the non-reactive ethylene glycol layer (Figure 3.10).[216]

3.1.4.3 Configuration of DNA linked to Gold Surfaces

The orientation of thiolated DNA (HS-DNA) linked to a gold surface has been found to depend on (i) the presence of non-specific adsorption via nucleobases-gold interaction[213-215] (ii) the surface density of adsorbed DNA[216] (iii) at which end of the DNA strand (the 3` or 5`-end) the DNA strand is linked to the gold surface[217] and (iv) whether the DNA is single and double-stranded.[218, 219]

3.1.4.3.1. Effect of DNA Surface Coverage

Lee *et al.*[216] have found that the orientation of the thiolated adsorbed single-stranded DNA on a MEG-covered gold surface (Figure 3.10 in section 3.1.4.2) depends on the surface density of the adsorbed DNA: at low surface densities the DNA bases are aligned parallel to the gold surface, as low electrostatic inter-strand repulsion increases the disorder among DNA strands, while at higher surface densities the DNA strand orientation is more upright.

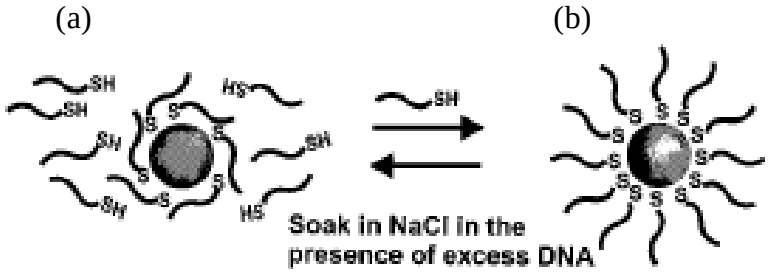

Figure 3.11: Effect of ionic buffer concentration of DNA coverage and DNA configuration: At low ionic strength (a) DNA lies flat on the gold NP surface due to nonspecific interaction between nucleotide bases and gold and attraction between negatively charged DNA and positively charged (citrate stabilised) gold NPs, while at increased ionic strength (b) the inter-strand electrostatic repulsion decreases, increasing the DNA surface coverage.[215]

It has been experimentally shown that surface coverage and DNA strand configuration can be manipulated with ionic buffer strength for thiolated single-stranded-DNA (12mer) and gold nanoparticles, with increasing ionic strength leading to reduced interstrand repulsion and thus higher surface coverages.[215] It was found likely that at low ionic strengths, the DNA lie flat on the NP surface due to (1) nonspecific nucleotide base-gold interaction and (2) electrostatic attraction between negatively charged

DNA and positively charged (citrate stabilised) gold NPs (Figure 3.11(a)), while at higher ionic strengths, the electrostatic attraction between NP and DNA and the electrostatic inter-strand repulsion is screened, and thus reduced, and the reduced inter-strand repulsion leads to a higher DNA surface coverage at higher ionic strength (Figure 3.11(b)).

3.1.4.3.2 Effect of DNA Linker Position

Experiments have shown that the end at which DNA is linked to a flat gold surface determines the DNA orientation: while thiolated double-stranded DNA (15mer) linked to the gold surface via the 3`-carbon lie down flat on the surface, double-stranded DNA linked to the surface via the 5`-carbon take a more upright configuration.[220]

3.1.4.3.3 Effect of Single or Double-stranded DNA

It has also been suggested that unmodified (no thiols) 16mer oligonucleotides adsorb onto a 14nm Au NP surface when double-stranded, but not when single-stranded, as seen in an increase in the Raman signal of the double-stranded DNA bases, with the double-stranded-oligonucleotides lying down flat on the surface of the Au NP, while the bases A and G are aligned perpendicularly to the Au surface.[218] In contrast, an enhanced Raman signal has been observed for single-stranded compared to double-stranded Calf-thymus DNA when adsorbed onto silver colloids.[219]

3.1.4.4 DNA Surface Coverage

The DNA surface depends on whether the gold surface is flat or a nanoparticle (section 3.1.3.4.1), and on the buffer ionic strength (section 3.1.2.4.1).

3.1.4.4.1 Flat Gold Surface versus Gold Nanoparticle

Experimental results suggest that the surface coverage of dithiol-terminated oligonucleotide (i) is higher[212] on a NP-surface compared to a flat surface, reaching up to 220 strands per NP,[212] as the surface curvature of the NP reduces steric interference between DNA strands,[212] and (ii) unlike on a flat gold surface, the DNA surface coverage on a Au

NP does not significantly decrease with increasing oligonucleotide length.[212] However, increased oligonucleotide length by the insertion of a 20-dA spacer between the alkanethiol group ($(SH(CH_2)_6\text{-}N_{12})$) and the original single-stranded 12-base sequence was experimentally shown to decrease the oligonucleotide surface coverage on a 15.7 nm Au NP-surface by half.[215]

3.1.4.4.2. Buffer Ionic Strength

The ionic strength has been shown to affect the surface coverage of thiol-terminated oligonucleotides to (i) a Au NPs[213, 215] and (ii) a flat gold surface covered by a monolayer of MEG.[216] Specifically, the surface coverage (adsorption) of single-stranded thiol functionalised oligonucleotide[213, 215, 216] on gold surfaces has been experimentally shown to increase with increasing salt concentration of the buffer.[213, 215, 216] It is believed that with increasing ionic buffer conditions, the electrostatic charge of the negatively charged DNA strands is more effectively screened, reducing inter-strand repulsion and thus increasing the DNA surface coverage.[213]

3.1.5 Additives Preventing DNA –Nanoparticle Interaction

It has been experimentally shown that incorporation of the spacer ethylene glycol into the nanoparticle coating eliminates non-specific DNA adsorption onto the nanoparticle surface for both gold nanoparticles,[221] CdSe/ZnS QDs[189] and paramagnetic beads.[222] Specifically, Zheng *et al.*[221] have shown that a monolayer of di,-tri-or tetra(ethylene glycol) thiols, EG_n-SH, where n=2,3 and 4, respectively, attached to a gold nanoparticle surface via a thiol bond, yielded gold NPs EG_n-S-Au, that are stable in aqueous solution and shielded from non-specific binding to chromosomal DNA.[221] The DNA-adsorption resistant surface coating of CdSe/ZnS QDs was EG_3COOH (11-Mercaptoundecyl tri(ethylene glycol) alcohol) and EG_3OH (11-Mercaptoundecyl tri(ethylene glycol) acetic acid), with the EG_3 spacing out the hydrophilic hydroxyl (OH) and carboxylic acid (COOH) functional groups from the QD surface.[186]

Also, DNA adsorption onto a bead surface via disulphide bond decreased by incubation in 0.2% SDS.[222] The oligonucleotides contained a 5`-terminal thiol groups and immobilize onto a thiol-terminated paramagnetic Biomag beads via a disulphide bond.[222]

3.1.6 DNA binding to Silica Nanoparticles

Amino-surface functionalised silica nanoparticles, consisting of a dye core encapsulated by a silica coating, have been grown with a water-in-oil microemulsion method and[223] and range in size between 5 to 400 nm.[223-225] It has been experimentally shown that negatively charged DNA (green fluorescence protein (GFP) plasmid DNA,[223] plasmid and genomic DNA[224]) electrostatically bind to positively charged amino-modified silica NP to form NP-DNA complexes.[223, 224] The positive charge on the silica NP stems from the protonation of the amino groups at the NP surface at neutral pH.[223]

3.2 Materials and Methods

Colloidal CdSe/ZnS core/shell quantum dots (QDs) of various sizes were obtained dissolved in toluene solution (Evident Technologies). The QDs are not soluble in aqueous solution due to a hydrophobic coating, but were made water soluble by in-house ligand exchange with designed peptide polymers (section 3.2.1). QDs were then used for the absorption and emission studies of mixtures of QDs and oligonucleotides (section 3.2.2), AFM studies of QD-DNA mixtures (section 3.2.3) or Fluorescence Microscopy of QD-DNA mixtures (section 3.2.4).

3.2.1 Ligand Exchange of Quantum Dots

As-delivered QDs are coated in either long-chain-amine-molecules (Evident Technologies), and precipitate in aqueous solution. For example, hexadecylamine (HDA), a surfactant molecule, consists of (a) a polar head group (NH_2) which attaches to the CdSe shell via formation of a N-Zn bond (Figure 3.12(i)), and (b) a hydrophobic chain (Figure 3.12(i)).

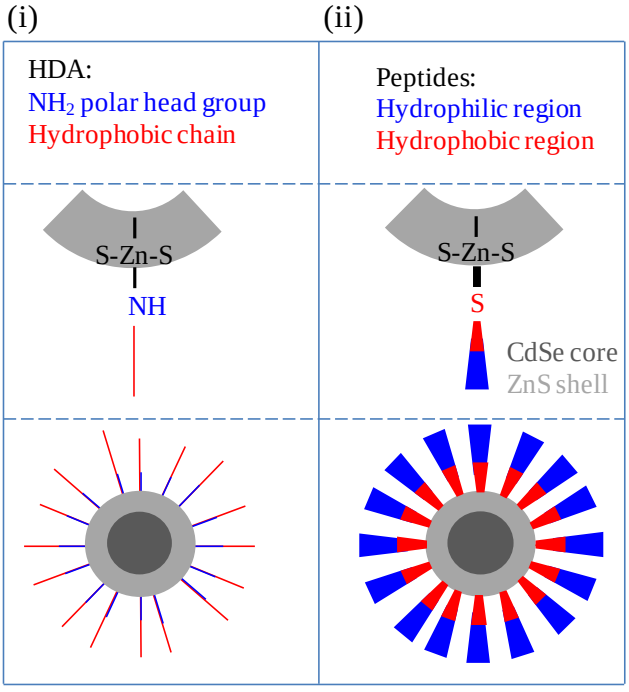

Figure 3.12: Schematic representation of (a) QDs coated in (i) HDA or (ii) peptides.

QDs are made water soluble by ligand-exchange with designed peptide polymers (Table 3.1(a)). A peptide is a chain of amino acids, which can either be hydrophobic, hydrophilic, acidic or basic (appendix B.4).

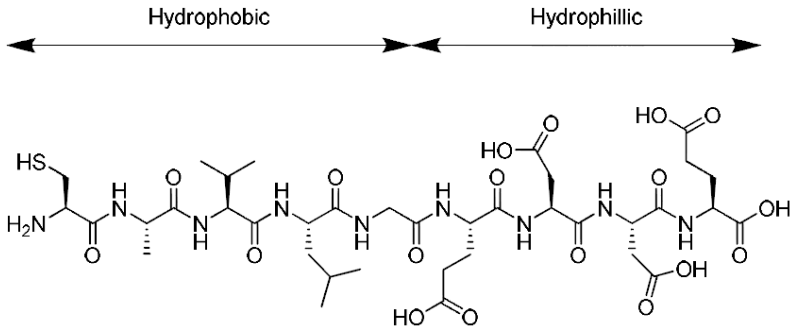

Figure 3.13: Schematic representation of the molecular structure of a designed peptide, consisting of one hydrophobic end with a SH group, and one hydrophilic end.[227]

The structure of all designed peptides is listed in appendix B.5, and that of typical designed peptide is shown in Figure 3.13, which, by the choice of the appropriate amino acid sequence, consists of a hydrophobic region and hydrophilic region (Table 3.1(a) and (b)). The hydrophobic chain is always terminated by a cysteine amino acid to allow peptide attachment to the CdSe/ZnS QD surface (appendix B.4 and see below). The cysteine is followed by a chain of hydrophobic amino acids with increasing side chain extend/size (Figure 3.12(ii), Figure 3.13 and appendix B.5) to prevent water reaching the QD surface. At the other end of the peptide, the peptide is terminated with a hydrophilic amino acid chain for increased QD stability in aqueous solution.

The cysteine amino acid, which terminates the hydrophobic end of the designed peptides, is conjugated to the ZnS shell of a CdSe/ZnS QD as it contains a thiol group (SH) in its side chain. The thiol group deprotonates (looses the H^+) under neutral pH (pH 7.0), allowing a strong bond between the sulphur of the cysteine and the zinc of the ZnS QD shell to be formed (Figure 3.12(ii)). Specifically, in the ligand exchange reaction (section 3.2.1.1), the weak N-Zn bond between HDA and ZnS QD shell is cleaved and replaced by the stronger S-Zn bond between the Zn and the cysteine amino acid (Figure 3.12(ii)). Peptide ligand exchange of the initially long

chain amine molecules coated CdSe/ZnS QDs (Evident Technologies) maintains the optical properties of the QDs except for a red-shift in the fluorescence spectrum by a few nanometers.[227] The hydrophilic end region of the designed peptides contains the amino acids "aspartic acid" (D) and "glutamic acid" (E) (Table 3.1(a) and (b)), which both contain carboxylate groups (-COOH) in their side chain (Figure 3.13). The pk_a value of COOH group is about 4.0, so that at physiological pH, most of the COOH is deprotonated (negatively charged), so that the designed peptides are negatively charged at physiological pH.

(a)

Peptide	Amino acid sequence
1	CAL GGE DDE
2	CLL GGE DDE
3	CAV LGE DDE
4	CAV FLG EDD E
5	CAV VLG EDD E
6	CDV LGE DDE

(b)

Amino acid	Letter	Side chain polarity
Alanine	A	non-ploar
Cysteine	C	non-polar
Aspartic acid	D	polar
Glutamic acid	E	polar
Phenylalanine	F	non-polar
Glycine	G	non-polar
Leucine	L	non-polar
Valine	V	non-polar

Table 3.1: Designed peptides (a) Amino acid sequence of designed peptides (b) polarity of amino-acids used.[228]

3.2.1.1 Ligand Exchange Procedure

For long-amine-chain molecule-coated QDs dissolved in toluene (536nm fluorescence peak, 1.3 mg/mL, 80.03 nmol/mL, Evident Technologies), 19.2 µL of QD solution and 480.8 µL of pyridine is mixed by vortexing, and separately from this 2.1 mg of peptides and 48 µL of dimethylsulphoxide (DMSO) is mixed by vortexing. The QD-pyridine and peptide-DMSO solutions are then mixed together by vortexing, followed by the addition of 9 µL of tetramethylammoniumhydroxide (TMAOH) which raises the pH. The resulting mixture is vortexed and then centrifuged at 4,000 rpm for 30 minutes. The QD-peptide conjugates are then at the

bottom of the Eppendorf tube. The supernatant is removed with a pipette and any excess peptides and unmodified QDs are removed by washing several times with DMSO using a pipette. The QDs can then be re-suspended into aqueous solution.

3.2.2 Absorption and Emission Studies of Quantum-Dots Mixed with Oligonucleotides

Free oligonucleotides, synthesised and purified by ADTBio, were added to aqueous solution of peptide-coated QDs. The base sequence of the added oligonucleotides is listed in Table 3.2. The QD-oligonucleotide solution was mixed by gentle pipetting several times and left to stand for several minutes, and diluted to an optical density of less than 0.1 at the excitation wavelength, before taking fluorescence and PLE spectra of the incubated QD-oligonucleotide mixture with a fluorimeter (Perkin, Elmer EM 50B). Fluorescence spectra were measured with 350 nm or 395 nm excitation, while PLE spectra were measured by detecting the fluorescence intensity as a function of the excitation wavelength, noting that the fluorescence intensity scales with the absorption efficiency, and scanning over a range of excitation wavelengths to yield a PLE spectrum.

oligonucleotide	nucleotide base sequence
r0336	gca gca aat tgc act gga gtg cga g
O1	gca gca aat tgc act gga gtg cga g
O2	gca gca aat agc act cta gtg cga t
O3	gca gcg ggt agc act cta gtg cga t

Table 3.2: Oligonucleotide sequences

The fluorimeter setup for fluorescence intensity detection is shown in Figure 3.14. Monochromatic excitation light is obtained by passing a high intensity white light source through a monochromator, which selects a specific wavelength for excitation by spatially separating the wavelength components of the white light (appendix B.1). The selected wavelength passes through an entrance slit into the sample chamber. The slit width determines the spectral resolution and the amount of light passing through[229] (appendix B.1). The fluorescence of fluorophores within the

sample chamber is detected through an exit slit that is aligned 90° to the path of the monochromatic excitation light (Figure 3.14).

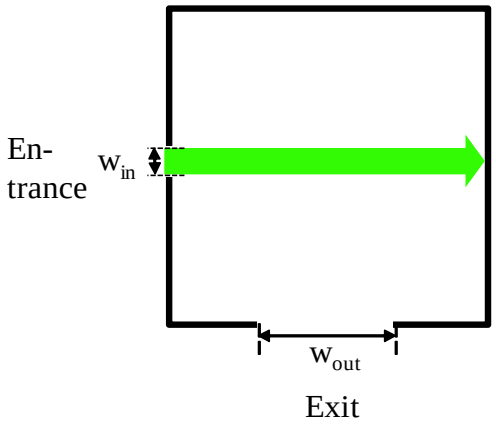

Figure 3.14: Schematic of the fluorimeter cuvette configuration of the exit and entrance slits of widths w_{in} and w_{out}, respectively. The green arrow denotes the excitation light path.

The fluorescence light then passes through a scanning monochromator before passing to a PMT. The relative alignment between excitation light path and fluorescence detection of 90° prevents direct exposure of the excitation light onto the detector, allowing facile separation of the excitation and fluorescence light. The slit widths determine the spectral resolution, with smaller slit widths yielding a higher spectral resolution. The signal to noise ratio can be increased by adjusting the narrow slit width,[230] but also depends on both the relative width of the exit slit to entrance slit, as well as the sample concentration. A high signal to noise ratio is obtained with an entrance slit that is narrower than the exit slit, as a narrow entrances slit minimizes the amount of scattered excitation light, while a wider exit slit increases the amount of detected fluorescence signal (appendix B.1). A high signal to noise ratio is also obtained for optical densities of the sample of less than 0.1 at the excitation wavelength, as a higher optical density results in quick absorption of most of the excitation light and thus a reduced signal to noise ratio. On the other hand, the minimum sample concentration is set by the detection limit of the fluorimeter, as a too low sample concentration yields a reduced signal to noise ratio.

3.2.3 AFM Studies

3.2.3.1 Sample Preparation

AFM samples of DNA, QDs and QD-DNA mixtures were prepared. DNA was polymerised Calf-thymus DNA with sodium salt (Sigma, 300 to 3,000 bp, DNA is double and single-stranded, but mostly double-stranded). Quantum Dots were 536 nm fluorescence peak CdSe/ZnS core/shell QDs coated in long-chain amine molecules (Evident Technologies). The QDs were made water-soluble by ligand exchange with peptide polymers (peptide 4) (section 3.2.1). Sample buffer solutions were prepared containing 10 mM Tris and 1 mM EDTA at pH 8.0. DNA solutions were prepared to a final DNA concentration of 0.2 µg/mL in sample buffer and various concentrations of the divalent salt $MgCl_2$ was added to the DNA sample solution. Mixtures of QD and DNA in solution were prepared to a final concentration of 0.2 µg/mL DNA and 100 nM or 10 nM QDs in sample buffer, and various concentrations of the divalent salt $MgCl_2$ was added to the QD-DNA sample solution, followed by sample mixing by gentle pipetting and subsequent incubation for one day or two weeks inside a fridge at 2°C.

For sample deposition, freshly cleaved muscovite mica was treated with Mg^{2+} cations by drop-casting buffer solution (20 µL, 10 mM Tris, 1mM EDTA, ph 8.0) containing various concentrations of $MgCl_2$ onto freshly cleaved mica and incubating for 2 minutes, except where otherwise stated, followed by washing under a stream of de-ionised, ultrapure water (15 mL, Millipore, 18 MΩ) and drying under a gentle dry argon flow. The QD, DNA or QD-DNA sample solution were then deposited onto the Mg^{2+} pre-treated mica substrate by drop-casting sample solution (6 µL) onto the mica surface and leaving to incubate for 3 minutes, followed by gently sweeping the mica substrate in ultrapure, de-ionised water (Millipore, 18 MΩ) to remove excess salt and unbound DNA/QDs, and subsequently the sample was dried first with filter paper (Whatman) and then under a gentle dry argon flow. The presence of divalent cations Mg^{2+} in the mica pre-

treatment step and the sample buffer help DNA and QD adhesion onto the like charged mica surface (appendix B.8).

For DNA extraction, DNA and peptide coated QDs were prepared to a final concentration of 0.2 µg/mL DNA and 500 nM QDs in sample buffer. To precipitate out the DNA from the sample solution, ethanol was added to a final concentration of 70% volume and sodium acetate (pH 5.2) was added to a final concentration of 0.3 M. The resulting mixture was incubated overnight in a fridge at 2°C, followed by centrifugation at 13,000 rpm for 30 minutes in a minifuge to collect the DNA. In a modified extraction method, the same procedure as above was repeated, but without the addition of ethanol.

3.2.3.2 AFM Imaging

Dry AFM imaging was performed in air in the tapping mode with an AFM (Asylum Research, MFP-3D-SA) and an AFM tip. The AFM tip was either a Tap300AI tip (10 nm radius of curvature (ROC), 300 kHz resonant frequency, 40N/m force constant, 125 µm cantilever length, Budget Sensors**)** or a SSS-NCHR tip (2 nm ROC, 330 kHz, 42 N/m, 125 µm, Nanosensors). The sample images (excluding the DNA or QDs in the imaging area) were flattened using algorithms provided by Asylum Research, and then analysed using processing software (IGOR).

3.2.4 Fluorescence Microscopy Studies

Samples of DNA, QDs and QDs mixed with DNA, on a glass substrate were fluorescently imaged. DNA was either (i) Calf-thymus DNA with sodium salt (Sigma), contains both single-stranded (ss) and double-stranded (ds), but predominantly ds DNA), (ii) ds Lambda-phage DNA (Promega, 48,502 bp, double-stranded), or (iii) single-stranded Lambda-phage DNA**.** QDs were 536 nm fluorescence peak CdSe/ZnS QDs coated in long chain amine molecules (Evident Technologies). QDs were made water soluble by ligand exchange with peptides (peptide 4) (section 3.2.1).

Samples for fluorescence imaging were prepared as follows. Peptide-coated QDs in sample buffer were prepared at a QD concentration

of 10 nM, and drop-cast onto mica. Mixtures of QD and ds Calf-thymus DNA were prepared in sample buffer at a concentration of 200 µg/mL DNA and 50 nM QDs and mixed by gentle pipetting and incubated for one day in a fridge at 2°C, followed by drop-casting onto mica. Mixtures of QD and ds Lambda-phage DNA were prepared in the same way as mixtures of QD and ds Calf-thymus DNA, except at concentrations of 23 pM (750 ng/mL) ds Lambda-phage DNA and 190 nM QDs, and except instead of drop-casting the sample, the sample was stretched over a pre-cleaned glass slide using capillary action (section 4.4.3). The mixture of QD and ss Lambda-phage DNA was prepared by first denaturing ds Lambda-phage DNA, which involves heating double-stranded DNA in sample buffer at 98°C for 8 minutes, followed immediately by the addition of QD-sample buffer solution and 2-Mercaptoethanol (MetOH), yielding a solution of 20% MetOH and 80% sample buffer, and mixing by gentle pipetting. The mixed QD-single-stranded DNA solution was subsequently incubated in an ice-bath which was kept inside a fridge (2°C) for more than 24 hours. The final sample concentration was 750 ng/mL (23 pM) single-stranded DNA and 200 nM QDs. Following incubation of the QD-single-stranded DNA mixture, the sample was stretched over a pre-cleaned glass slide using capillary action (section 4.4.3)

The glass substrate was pre-cleaned by sonication in acetone, isopropanol and high purity de-ionised water, in this order and for 20 minutes each, and subsequently dried under a dry argon flow. The samples were imaged with an inverted fluorescence microscope (Zeiss), fitted with a broadband Mercury Xenon lamp as the excitation source. Various excitation and emission filter sets were used for fluorescence imaging (appendix B.2).

The quantum yield of peptide functionalised quantum dots was measured by measuring the fluorescence spectra of quinine sulphate in solution and QDs in solution at optical density of 0.01 and excitation wavelength of 350 nm, and comparing the area under the fluorescence spectrum of QDs and quinine sulphate. Sample TE buffer containing 10 mM Tris, 1 mM EDTA at pH 8.0 was prepared.

3.3 Experimental Results

3.3.1 Emission Studies of QDs in the Presence of Oligonucleotides

The quantum yield of long-chain-amine molecule-coated CdSe/ZnS QDs from Evident Technologies was measured to equal up to 0.22, by comparison with the emission yield of fluorescein in 0.1 M sodium hydroxide.

3.3.1.1 Effect of Peptide Ligand Exchange on QD Fluorescence Spectrum

Figure 3.15 shows the fluorescence spectrum of CdSe/ZnS core/shell QDs functionalised with long-chain amine molecules and dissolved in toluene or functionalised with peptide 2 and dissolved in aqueous solution, as obtained by James Richardson.[227] Upon ligand exchange, the fluorescence peak red-shifts by 14.0 ±0.5 nm, from 532.0 nm in toluene to 546.0 nm in water, and the fluorescence quantum yield falls by several tens of percent.[227] A red shift in fluorescence peak and reduced fluorescence efficiency has been experimentally observed before upon ligand exchange from TOPO to MPA on colloidal CdSe/ZnS QD solutions drop-cast onto glass.[231] The fluorescence peak red shift has been attributed the extension of the electron-wavefunction to the MPA ligand that is covalently attached to the QD surface, reducing electron confinement of the electron-wavefunction within a QD,[231] while a reduction in quantum yield was attributed to an increase in the number of surface trap states after ligand exchange.[231] The polarity of the environment surrounding the QD can also influence QD fluorescence (solvent effect)[232] (appendix B.6). For instance, a blue-shift in fluorescence peak, with no change in the absorption onset, occurred in mercapto-coated QDs in aqueous solution

after conjugation with the low-polarity protein, trichosanthin (TCS), attributed to a reduced polarisibility of the TCS compared to water.[232]

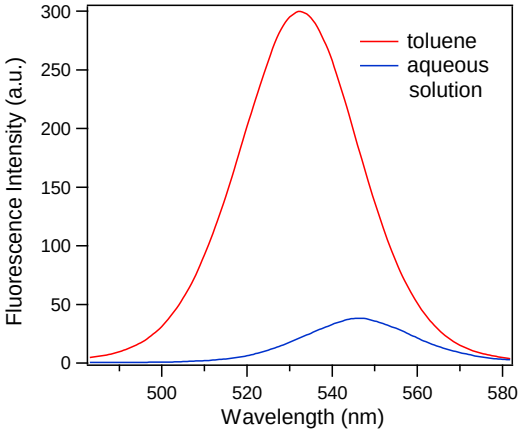

Figure 3.15: Fluorescence Spectra of CdSe/ZnS QDs from Evident Technologies in toluene (red) or aqueous solution coated in peptide 2 (blue), excitation was at 400 nm, optical density at 400 nm was 0.019 in toluene and 0.009 in water.[227]

3.3.1.2 Quantum Yield Measurement of Peptide Functionalised QDs

The fluorescence quantum yield of peptide functionalised CdSe/ZnS core/shell QDs can be established using quinine sulphate as a reference, by measuring the relative area under the fluorescence spectrum of QDs compared to the fluorescence spectrum for quinine sulphate (quantum yield=54%)[233](Figure 3.16). The emission spectrum of both samples in solution, at optical density 0.01 and 350 nm excitation, was measured with a fluorimeter.

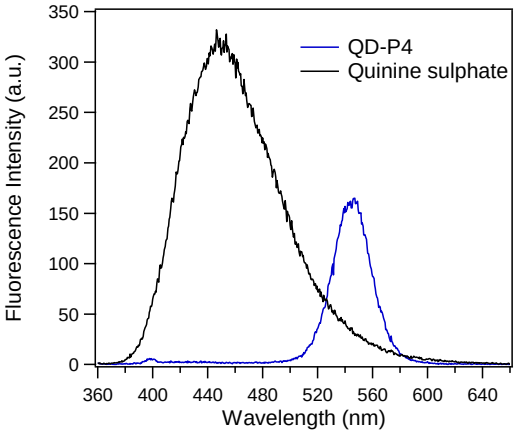

Figure 3.16: Fluorescence spectra of quinine sulphate (black) and CdSe/ZnS QDs coated in peptide 4.

For instance, the total area under the fluorescence graph was equal to 59865.9 and 19854.1 for quinine sulphate and peptide 4 functionalised

QDs, respectively, (Figure 3.16) so that the quantum yield of the functionalised QDs is equal to 54%*19854.1 /59865.9=18%.

Multiple peptide sequences were conjugated to CdSe/ZnS QDs (Figure 3.17). Peptide-functionalised QDs show a variation in fluorescence quantum yield as a function of peptide sequence (Table 3.3). The highest yields are obtained with peptide 2 and peptide 4 (Table 3.3), which is due to the high steric hindrance from the large non-polar peptide sequence near the QDs (the sequence CL LGG and CAV FLG in peptide 2 and peptide 4, respectively (Table 3.3)).

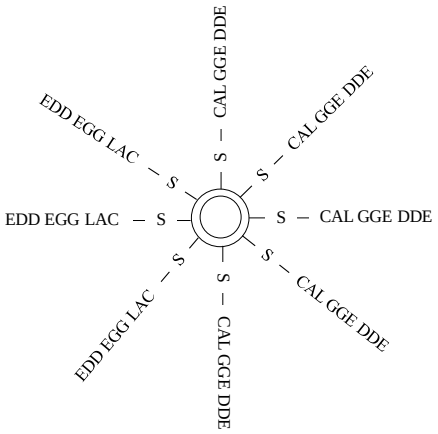

Figure 3.17: Illustration of CdSe/ZnS core/shell QD functionalised with peptide 1 (see Table 3.1 in section 3.2.1).

Peptide		QY (%)
	Quinine Sulphate	54
CAL GGE DDE	QD-P1	10
CLL GGE DDE	QD-P2	22
CAV LGE DDE	QD-P3	9
CAV FLG EDD E	QD-P4	18
CAV VLG EDD E	QD-P5	18
CDV LGE DDE	QD-P6	14

Table 3.3: Fluorescence Quantum Yield of CdSe/ZnS QDs coated in designed peptides.[227]

3.3.1.3 Effect of the Adduct of DNA Oligonucleotides to QDs on the Fluorescence Quantum Yield and Spectrum

Figure 3.18 shows the fluorescence spectrum of (i) various mixed base free oligonucleotides in solution in the absence and presence of high quantum yield QDs from Evident Technologies and (ii) oligonucleotides in solution in the absence of QDs. The QDs were functionalised with peptide 3.

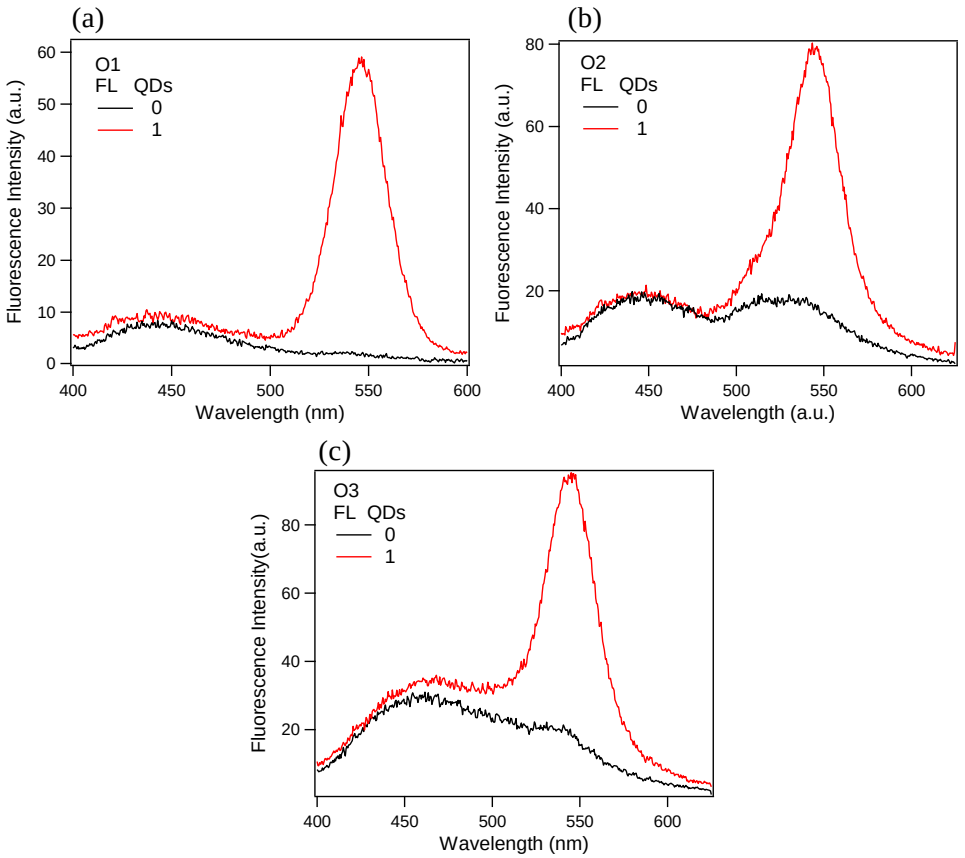

Figure 3.18: Fluorescence (FL) spectra of various mixed base oligonucleotides in the presence and absence of peptide-functionalised CdSe/ZnS QDs (Evident Technologies), oligonucleotide were (a) O1 (b)O2 (c) O3 (see Table 3.2 in section 3.2.2); 350 nm excitation, oligonucleotide concentration equals 250 µM, QD concentration equals 5µM. QDs were 530 nm fluorescence peak QDs coated in peptide 3 (see Table 3.1 in section 3.2.1) in water.

Compared to QD solution (not shown), for solution mixtures of oligonucleotides and QDs a new emission peak centred at about 450 nm peak appears (Figure 3.18(a)(1), (b)(1) and (c)(1)). In solutions of oligonucleotides only the 450 nm emission peak is also present, and for oligonucleotides in solution the intensity of the 450 nm peak is unchanged whether the QDs are present or not (Figure 3.18(a)(0), (b)(0) and (c)(0)), suggesting that the 450 nm emission peak does not originate from an interaction between oligonucleotides and QDs, but might be due to some artefact in the oligonucleotide, either from the oligonucleotides themselves or from the oligonucleotide synthesis. Spectral ovelap between the QD absorption spectrum and the 450 nm emission peak, and the same intensity of the 450 nm peak for oligonucleotides and for mixtures of QDs and oligonucleotides suggests the QDs and the species from which the 450 nm

emission originates are spatially separated by a distance exceeding the Foerster radius.

Core/shell CdSe/ZnS QDs coated in long chain amine molecules have been ligand exchanged with peptide 4 (see Table 3.1 in section 3.2.1) to make QDs water soluble. Peptide 4 was chosen of all the designed peptides as it yields QDs with one of the highest quantum yields of 18% (Table 3.3 in section 3.3.1.2). The fluorescence and PLE spectra of peptide 4-functionalised QDs is shown in Figure 3.19.

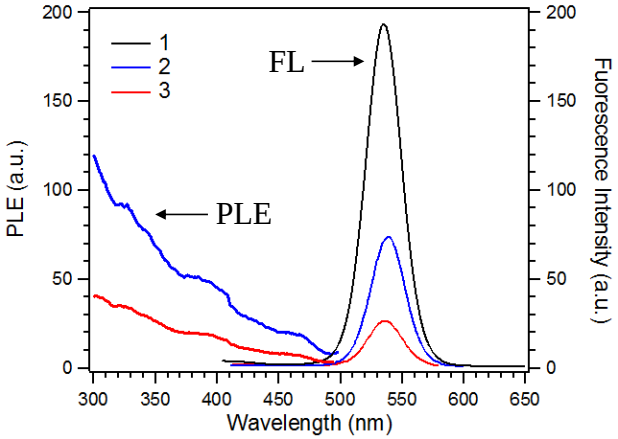

Figure 3.19: Fluorescence (FL) and photoluminescence excitation (PLE) spectra of 536 nm fluorescence peak CdSe/ZnS QDs (1) as delivered (Evident Technologies) in toluene (2) functionalised with peptide 4 (Table 3.1 in section 3.2.1) in water (3) functionalised with peptide 4, mixed with double-stranded Calf-thymus DNA (200 µg/mL) in water. Excitation (for the fluorescence spectrum) was at 350 nm and detection (for the PLE spectrum) was at 539 nm. QD-DNA incubation time was 24 hours.

Upon ligand exchange, the QD fluorescence peak maximum is seen to red-shift by 4 nm from 536 nm to 540 nm (Figure 3.19(1) and (2)). The red-shift upon ligand exchange could be due to the solvent effect, in which the higher polarisibility of water, compared to toluene, reduces the exciton energy (appendix B.6). However, other batches of peptide 4-coated QDs have shown a larger red-shift of the fluorescence spectrum to 545 nm (Figure 3.16 in section 3.3.1.2), indicating that the amount of red-shift can vary for different batches, which might be due to a variation in the surface coverage of peptides on the QD surface from batch to batch. Each peptide-functionalised QD sample was checked for good QD water solubility by leaving freshly peptide-functionalised QDs in water for at least overnight, and checking, with a UV lamp, that no QD precipitation has occurred. The

addition of ds Calf-thymus DNA to peptide-4 coated QD solution does not significantly change the QD fluorescence or PLE spectrum (Figure 3.19(3)).

3.3.1.4 Fluorescence Imaging of Quantum Dots

Although fluorescence spectroscopy studies showed no evidence for an interaction between the DNA sequences and QD-peptide 4 conjugates (section 3.3.1.3), further investigations were considered necessary. This was especially important as QD-DNA structures may not be formed in the majority- so a series of fluorescence microscopy studies were done. By using different excitation and emission filtersets in conjunction with microscopy, it was possible to image and probe the samples for different QD species. The co-association of QDs with DNA strands was considered possible to image, if this occurred.

As shown in Figure 3.16 in section 3.3.1.2, the emission spectrum of peptide functionalised QDs falls between 495 nm and 585 nm with a maximum at 540 nm. Fluorescence images of peptide-4-coated CdSe/ZnS QDs drop-cast onto a cleaved mica substrate are shown in Figure 3.20. Well-separated fluorescing spots are visible when excited with 450-490 nm and emission is detected at wavelengths > 515 nm (Figure 3.20(i)), but not when excited with 536-558 nm and emission is detected at wavelengths > 590 nm (Figure 3.20(ii)), so that the fluorescent spots can be attributed to fluorescence from QDs. Larger assemblies are also visible when excited with 536-558 nm and emission detected at > 590 nm (Figure 3.20(ii)), which might be attributed to coagulated QDs: a red-shift in QD fluorescence peak has previously been observed for close-packed and coagulated QD, and has been attributed to non-radiative fluorescence resonant energy transfer (FRET) from smaller to larger QDs.[152] A red-shift in the QD fluorescence spectral peak has also been attributed to dipole-dipole interaction between an exciton within a QD core that was optically excited and its induced dipole in an adjacent QD.[155, 234] A red-shift in the absorption onset induced by dipole-dipole interaction, however, is small, for instance only 3.6 meV for 4 nm diameter CdSe

QDs,[155] whereas a much larger shift, from at least 490 nm to 536 nm (a shift by 46 nm or 238 meV) would be required before excitation at 536-558 nm would excite the QDs used here.

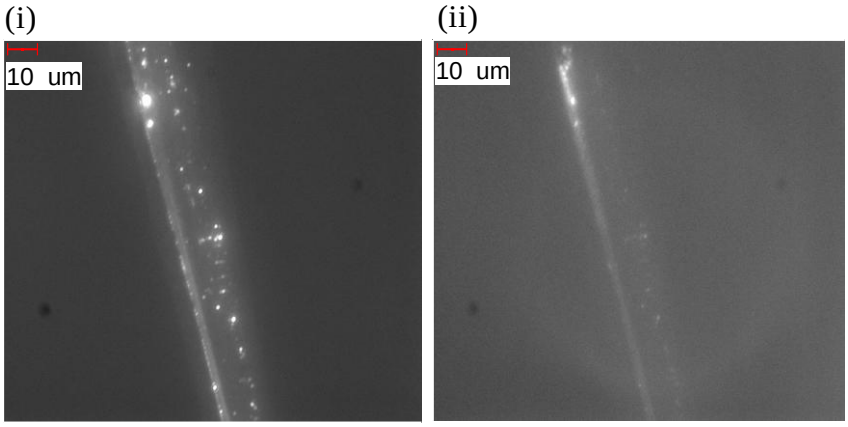

Figure 3.20: Fluorescence images of CdSe/ZnS QDs drop-cast onto mica (i) excitation between 450-490 nm, emission >515 nm (ii) excitation between 436-558 nm, emission > 590 nm. The QD concentration in sample buffer was equal to 10 nM. Integration times were (i) 10.6248 s and (ii) 14.9608 s. Magnification was equal to x63, 1.0 optovar. QDs were coated on peptide 4 (see Table 3.1 in section 3.2.1).

3.3.1.5 Fluorescence Imaging of Drop-Cast QD-Double-Stranded DNA Mixtures

Figure 3.21 shows fluorescence images of QDs incubated overnight with ds Calf-thymus DNA (CT-DNA) and drop-cast onto mica.

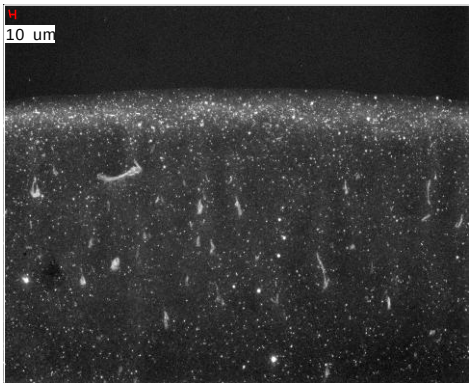

Figure 3.21: Fluorescence image of a mixture of Calf-thymus double-stranded DNA and QDs drop-cast onto mica with excitation at 450-490 nm and detection at >515 nm. The sample concentration in sample buffer was equal to 50 nM QDs and 200 µg/mL DNA. The integration time was equal to 2.8736 s. The magnification was equal to x10, 1.0 optovar. QDs were coated in peptide 4 (see Table 3.1 in section 3.2.1). DNA-QD incubation time was 24 hours.

Fluorescence from spots and strand-like-structures is clearly visible with excitation at 450-490 nm and an emission detected at >515 nm (Figure 3.21) but not with excitation at 536-558 nm and emission detected at > 590

nm (not shown), as previously seen for drop-cast QD solution. It can be seen that the fluorescence originates from strand-like structures (Figure 3.21). The next step was look at single-stranded DNA interaction with QDs.

3.3.1.6 Fluorescence Imaging of Stretched QD-Single-stranded DNA Mixtures

Single-stranded Lambda-phage DNA was incubated with peptide-4 functionalised QDs for about 24 hours before being stretched over a glass slide by capillary action. The single-stranded Lambda DNA-peptide 4 assemblies were examined by fluorescence microscopy. By the use of different emission and excitation filter sets it was possible to evaluate whether the QDs were associated in either mono QD or assemblies. While no emitting structures are visible when QD-DNA mixtures are absent (not shown), emission from linear strands can be clearly seen in the presence of QD-DNA mixtures (Figure 3.22). The images shown in Figure 3.22(i), (ii) and (iii) are for samples where the filter sets are appropriate for the detection of single QD-peptide 4 samples (individual QDs separated far enough for FRET not to occur) (see Figure 3.20(ii) in section 3.3.1.4) (see filter sets in Appendix B.2), whereas images shown in Figure 3.22(iv) are by excitation with light of 536-558 nm and emission collected at wavelengths greater than 590 nm. This emission, detected in Figure 3.22(iv), is not observed for single QDs (see Figure 3.20(ii) in section 3.3.1.4).

The results can be understood by assuming that QDs associate at high densities to the structures seen. The linear strands are on average 5.3 μm long, with a range of 3 to 10 μm, consistent with previous measured lengths of double-stranded Lambda-phage DNA stretched by capillary action (chapter 4.4.3). Thus, the results can be rationalised by assuming that DNA strands wrap around QDs at the end of the DNA strands, resulting in a low QD density which is spectrally detectible at the same excitation and emission range as that observed for single, well-separated QDs (Figure 3.23(a)). Regions where QDs associate in high densities to the

DNA strand are visible at longer wavelengths i.e. with excitation at 536-558 nm and with emission detected at >590 nm (Figure 3.23(b)), as previously observed for QD assemblies in drop-cast QD samples (Figure 3.20(ii) in section 3.3.1.4).

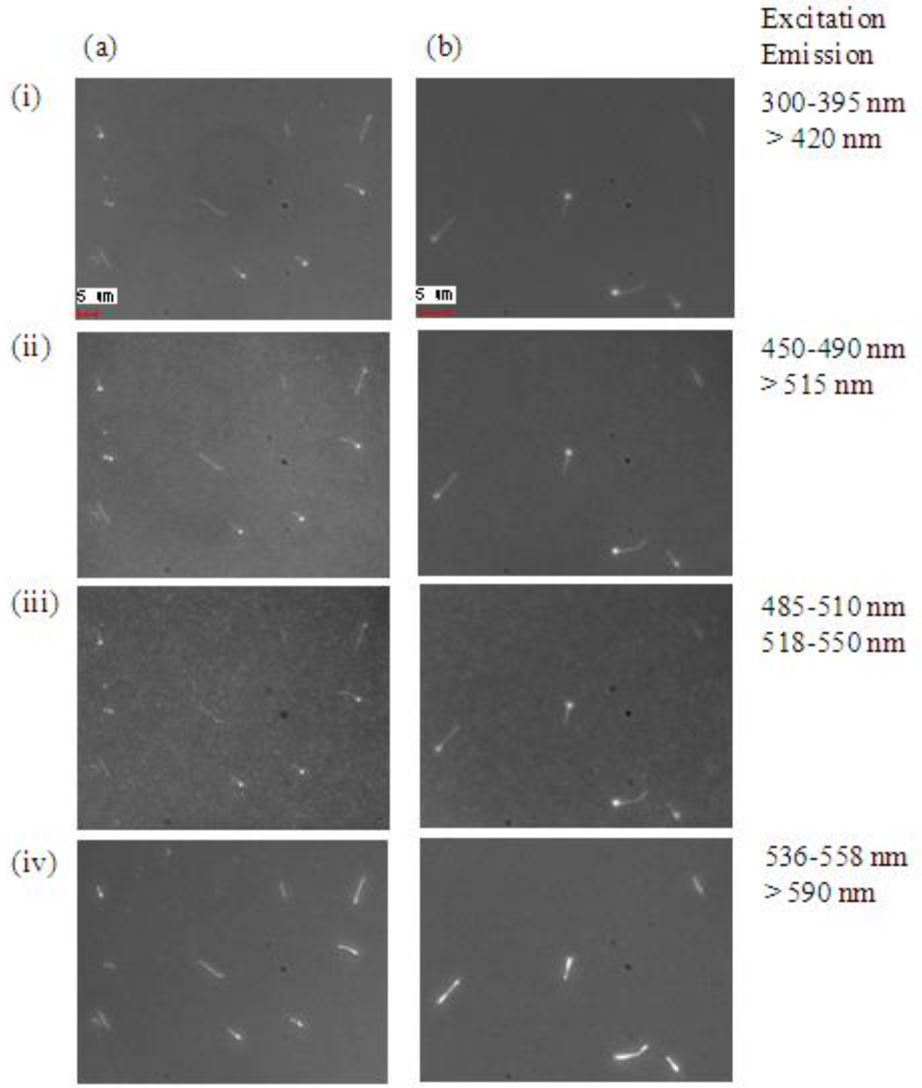

Figure 3.22: Fluorescence images of mixture of Lambda-phage single-stranded DNA and QDs stretched over glass with excitation and emission as indicated to the right. The sample concentrations in sample buffer were equal to 200 nM QDs and 0.75 µg/mL (46 pM) DNA. Integration time(s) was equal to (a)(i)3.976 (b)(i)8.5472 (a)(ii)7.4336 (b)(ii)14.3264 (a)(iii)29.3656 (b)(iii)32 (a)(iv)16.1576 (b)(iv)26.9096 s. Magnification was equal to 100x oil (a) 1.0 opt (b) 1.6 opt. QDs were coated in peptide 4 (see Table 3.1 in section 3.2.1). DNA-QD incubation time was about 26 hours.

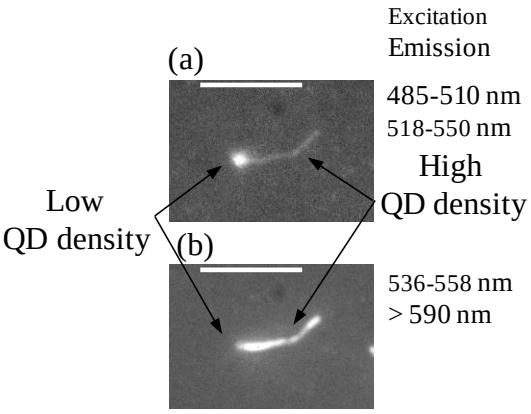

Figure 3.23: Comparison of a stretched DNA strand (expanded view of Figure 3.22(b)), showing differences in the fluorescence image as a function of emission wavelength.

Non-specific adsorption of double and single-stranded short oligonucleotides and double-stranded Calf-thymus DNA onto QD surfaces has been experimentally observed before.[185, 188, 192, 196] Non-specific DNA-QD association is suggested to be driven by (i) hydrogen bonding between protonated surface carboxyl groups (COOH) on the MAA-capping of QDs and the nucleotide bases, as observed with 19-mer oligonulceotides,[188] with QD-DNA association being more efficient with single-stranded compared to with double-stranded DNA,[188] and (ii) counter-ion exchange between CdS QDs and Calf-thymus DNA[196] and 16-mer double-stranded-oligonucleotides.[192] As the buffer solution in the samples used here does not contain divalent metal salts, the counter-ion-exchange mechanism is unlikely to have occurred here. However, similar to the MAA-coating, the peptide coating of the QDs contain carboxyl groups (section 3.2.1), so that it could be assumed that hydrogen bonding interaction between DNA and peptide coated QDs can occur. Thus, it is reasonable to suggest that the structures seen in Figure 3.22 are DNA to which QDs associate at high densities. Algar *et al.*[188] have experimentally shown that DNA lies across the QD surface and that although a weaker wrapping efficiency was observed at increased pH, QD-DNA wrapping was observed even at pH 9.4.[188] Sequence directed DNA structure/flexibility was also observed to improve QD-DNA association efficiency,[185] due to more closely matching the QD surface curvature. In particular, the GGCC sequence was found to improve the

QD-DNA binding efficiency by introducing kinks into DNA stands,[185] and is also contained within Lambda-phage DNA, suggesting that sequence directed structure/flexibility and hence improved binding at DNA sites containing the GGCC sequence play a role in binding between peptide coated QDs and Lambda-phage DNA. The absence of emitting strands in the fluorescent images of QDs incubated with double-stranded Lambda-phage DNA stretched over glass, unlike with single-stranded DNA, could be because QDs interact more weakly with double-stranded DNA compared to single-stranded DNA, as experimentally observed by Algar *et al.*,[188] and thus QD-DNA structures do not withstand the stretching forces when stretched by capillary action. Single-stranded, compared to double-stranded DNA, is also more flexible[235, 236] and might thus be expected to associate better to the curved QD surface.

3.3.2 Dry Atomic Force Microscopy Studies

There is clear evidence that QDs associate with Lambda-phage DNA in single-stranded and double-stranded form. This was surprising given the fact that peptides are non-polar and hydrophobic within the sequence closest to the QD shell (i.e. CLL GG (peptide 2) or CAV FLG (peptide 4)) and polar and hydrophilic (i.e. EDD E) at the aqueous interface; the carboxyl functional groups (COOH) of the polar, hydrophilic groups are anticipated to be negatively charged and thus unlikely to associate with the DNA phosphate backbone. Thus, AFM studies were done to investigate how the DNA interacts with the QD-peptide 4 conjugates.

3.3.2.1 AFM images of DNA Strands

At a DNA concentration of 0.4 µg/mL in solution, DNA strands formed a network of interconnecting strands when deposited onto mica (appendix B.8). A reduction of the DNA concentration to 0.2 µg/mL prevented the formation of a DNA network on mica, and instead DNA formed complex structures containing multiple loops (Figure 3.24(a) and (c)). The measured strand height ranges from 0.23 nm to 0.70 nm (Figure 3.24(b), while the strand width ranges from 30 nm to 40 nm (Figure 3.24(b)). A peak of 1.15

nm high is seen at a bent DNA strand section (Figure 3.24(a)(i) and (b)). It is well known divalent metal salt crystals, such as Mg^{2+} and Zn^{2+}, cause bending in the DNA strand.[198-203] Thus, it is reasonable to suggest that the 1.15 nm high peak is due to coagulated salt crystals attaching to the oppositely charged DNA backbone and causing DNA bending. The height was measured as the difference in height between the DNA top and the substrate, and width as the full width of the DNA peak that is higher than the substrate signal. The height range measured here is consistent with previous reports for measured double-stranded DNA by TappingMode (TM) AFM in air, with reported values in the range of 0.3 to 1.2 nm.[237, 238] It is well known that AFM often yields heights less than the actual height of double-stranded DNA (2.0 to 2.2 nm[239]), which is attributed to sample dehydration in air[240], salt deposition,[241, 242] and to a minimal extent in TM-AFM, where the sample-tip contact is kept to a minimum, sample deformation by the tip.[241, 243, 244]

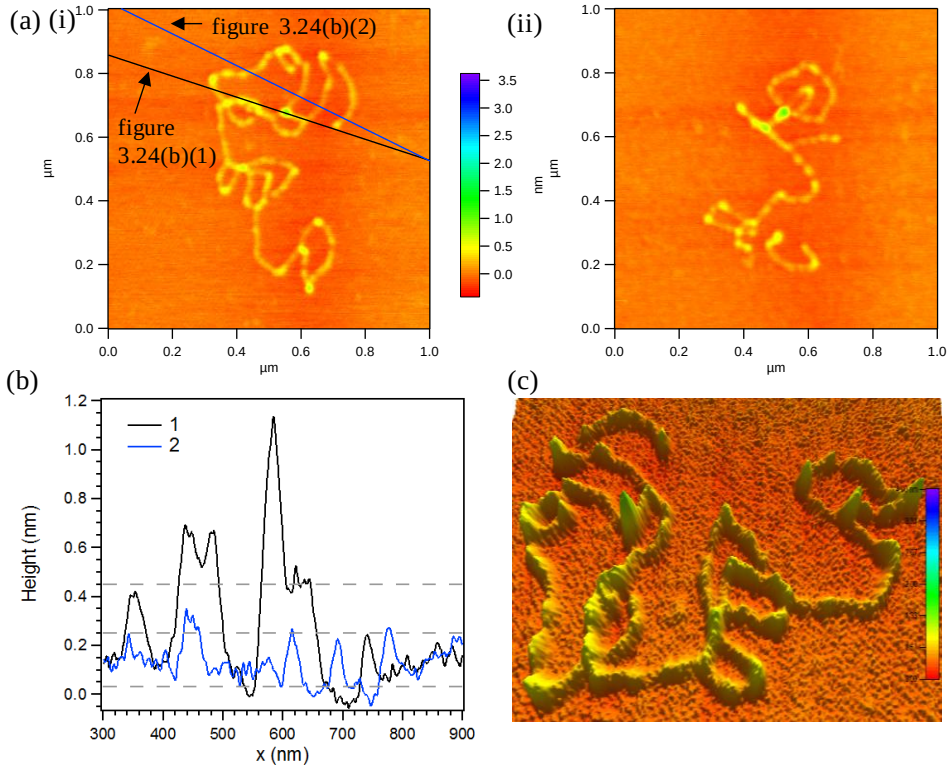

Figure 3.24: (a) AFM image of 0.2 µg/mL Calf-thymus DNA and (b) height measurements on DNA in Figure 3.24(a)(i), (c) 3D image of DNA in Figure 3.24(a)(i). The $MgCl_2$ concentrations during mica pre-treatment and in sample buffer are 25 mM. AFM tip ROC=10 nm.

Also, the DNA width measured here (30 to 40 nm) with a 10 nm ROC AFM tip is in agreement with previous values for double-stranded DNA measured by AFM (10-40 nm measured DNA width for ROC=20-50 nm[244]). The measured DNA width (30 to 40 nm) is broader than the actual DNA width (2 nm), as the radius of curvature of the AFM tip (ROC = 10 nm) is much broader than the DNA strand width, so that the width of the imaged feature is the convolution of the AFM tip width and the actual width of the imaged feature, and the AFM tip ROC limits the lateral resolution.[243, 244] It can be seen that regions of greater height in the imaged DNA structures tend to have broader lateral widths (Figure 3.24(b)), suggesting several DNA strands overlap in those regions. The DNA structures are repeatable upon successive AFM imaging (not shown), suggesting the DNA is well-adhered onto the mica substrate.

3.3.2.2 AFM Images of Mixtures of DNA Strands and QDs

Figure 3.25(a)(i), (b)(i) and (c)(i) show dry TM-AFM images of a QD-DNA mixture consisting of 0.2 µg/mL DNA and either 100 nM QDs (Figure 3.25(a) and (b)) or 10 nM QDs (Figure 3.25(c)) respectively (functionalised with peptide 4 (see Table 3.3 in section 3.3.1.2). Particles ranging in height from 1.4 nm to several nanometers and DNA strands can be clearly seen (Figure 3.25(a), (b) and (c)). In the absence of QD-peptide 4, particles of height of up to 1.15 nm have been observed on kinked sections of DNA strands (Figure 3.24(a)(i) and (b) in section 3.3.2.1), that might be salt cations binding to the negatively charged DNA backbone.

In general, the QD height, as measured with tapping mode (TM) AFM, is highly sensitive to the scanning parameters (tapping amplitude and force, driving frequency),[245] hydrophobicity of the substrate[245] and QD surface ligand.[245] It has been shown that the QD height as measured with TM-AFM can be more than 40% lower than the QD diameter due to variations in attractive interaction between AFM tip and sample when over the substrate compared to when over QDs: the cantilever will oscillate at a certain amplitude when driven at a certain frequency, with maximum amplitude occurring at the cantilever resonance frequency

in air. An attractive capillary force between sample surface and AFM tip dominates in the light tapping mode, and shifts the tip resonance frequency from that in air to a lower frequency, changing the oscillation amplitude at the sampling frequency.[245] The measured height is the topographical height and the effect of the amplitude damping. With increasing attractive force, the amplitude damping increases, which is interpreted by the feedback loop as an increase in sample height.[245] Thus, a reduced height in the QDs can appear if the amplitude damping is greater over the substrate than over the QD, which occurs if the attractive force over the mica is greater than over the QD.[245] The QD diameter, including the QD core and ZnS shell, is equal to about 3.6 nm (appendix B.6), which is 3.6 nm/2.0 nm= 1.8 times wider than a DNA strand, so that the QD width as measured by AFM is expected to a multiple of that measured of DNA. It is thus reasonable to suggest that the particles a few nanometers high and multiple times wider than a DNA strand are QDs, with particles exceeding about 3.6 nm height being QD coagulates, whereas smaller particles, up to about 1.2 nm in height, might be salt crystals left over from the mica salt treatment step or from the sample buffer. Spatial overlap between particles and the DNA strand does occur (Figure 3.25(a)(i), (b)(i) and (c)(i)), although many QDs are separate from DNA. DNA winding around QDs was considered to provide a shoulder around the QD with width similar to the DNA width, about 30 to 40 nm (section 3.3.2.1). Close-up 3D images from various perspectives of particles spatially coinciding with DNA strands in Figure 3.25 are shown in Figure 3.26. The 3D images show that some particles from 1.3 nm to several nanometers in height show no shoulder and thus no sign of DNA winding around particles (Figure 3.25(a)(ii) and Figure 3.26(a); Figure 3.26(b)(ii)(4) and Figure 3.26(b)(iv)).

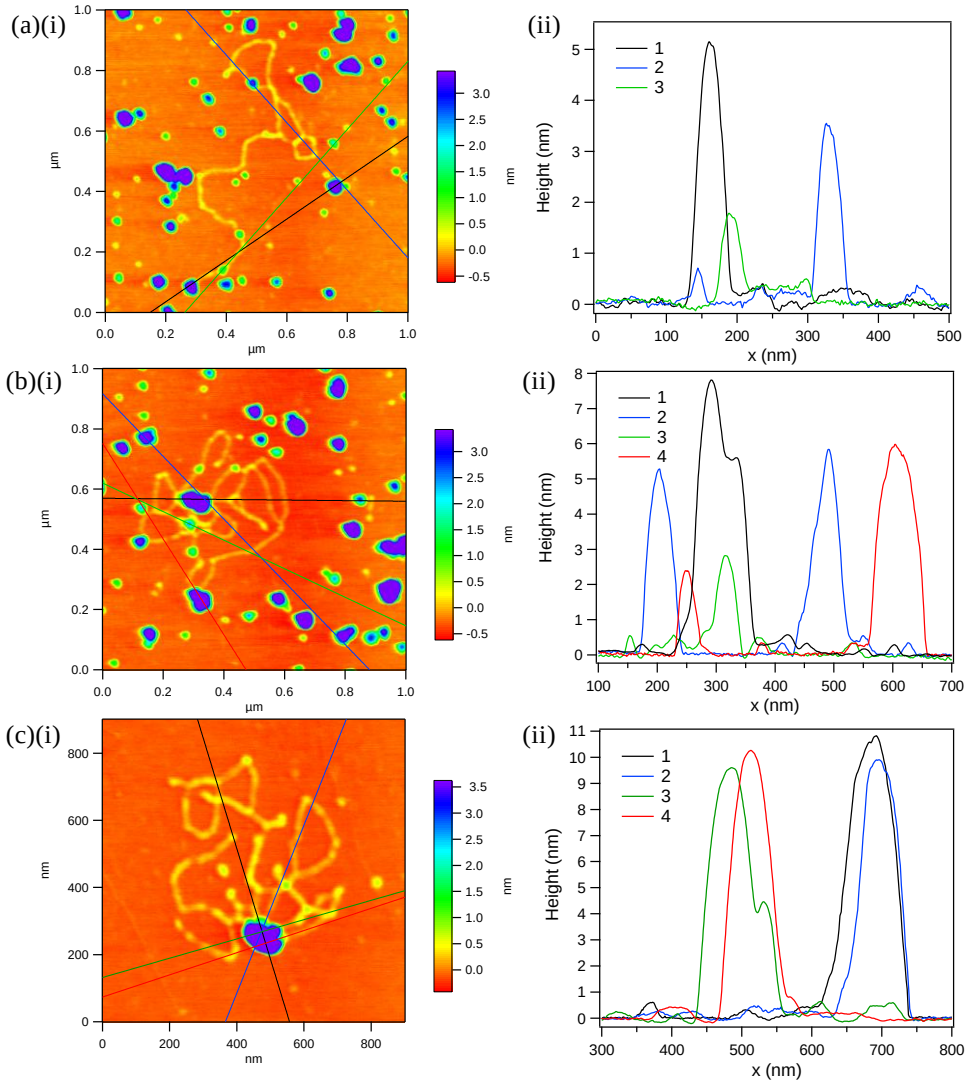

Figure 3.25: AFM images of Calf-thymus DNA (0.2 µg/mL) mixed in solution with QDs functionalised peptide 4 (a) 100 nM (b) 10 0nM (c) 10 nM ; (i):2D AFM images; (ii) height measurements along lines shown in (i); $MgCl_2$ concentration during mica pre-treatment and in sample buffer is 25 mM. AFM tip ROC=10 nm. The QD-DNA incubation time was equal to 24 hours.

The 8 nm high particle in Figure 3.25(b) shows a shoulder which is about 48 nm wide and about 5.5 nm high (Figure 3.25(b)(ii)(1) and Figure 3.26(b)(ii)) which, however, extends over a larger area than just the interface between particle and DNA strand (Figure 3.26(b)(ii)), and therefore is more likely part of the QD than a DNA strand. At the other side of the same particle at the base a shoulder about 30 nm wide, within the expected DNA strand width, and up to 1 nm high, occurs at the intersection between DNA strand and particle ((Figure 3.25(b)(ii)(1) and Figure 3.26(b)(i)); this shoulder is however, very steep, which suggests

that the particle partly sits ontop of the DNA strand, which does not allow the distinction between possible non-specific DNA and coincidental spatial overlap between QD and DNA strand.

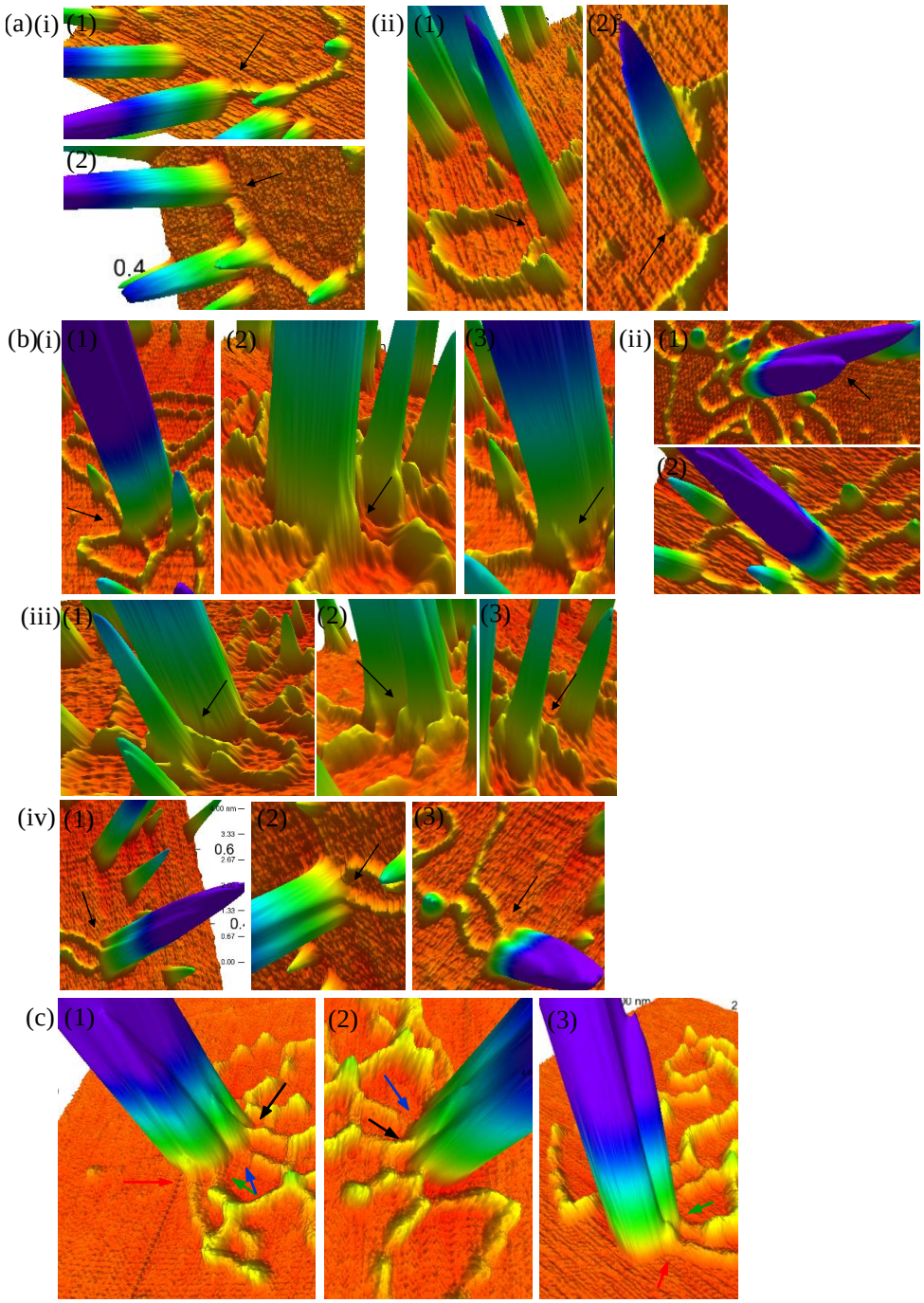

Figure 3.26: 3D images from various perspectives of Calf-thymus DNA mixed with QDs as imaged by AFM. 3D images are of the 2D AFM images shown in (a) Figure 3.25(a), and (b) Figure 3.25 (b), and (c) Figure 3.25(c).

A 2.8 nm high particle shows a shoulder about 23.2 nm wide and 0.68 nm high (Figure 3.25(b)(ii)(3). The size of the shoulder is within the size range

previously measured for DNA (section 3.3.2.1). 3D images reveal (Figure 3.26(b)(iii)) that this shoulder only exists at the base of the particle, suggesting the particle sits ontop of the DNA strands.

Figure 3.26(c) shows 3D images of a 10 nm high particle that spatially coincides with various DNA strands. The particle shows a shoulder at the particle-DNA intersection, which is about 38 nm wide and 4.4 nm high (Figure 3.25(c)(ii)(3), Figure 3.26(c)(1 and 3)), and slight asymmetries at three other DNA-strand–particle intersections (Figure 3.25(c)(ii)(1, 2, 4), Figure 3.26(c)(1 to 3)). However, these structures are only present at the base, near the particle-DNA intersection, and do not traverse over or along the side of the particle, so that these structures might just be part of the particle. Thus, in general, it is unclear from the AFM images whether the spatial overlap between particles and DNA is due to DNA winding around QDs or just coincidental.

In order to facilitate the analysis of whether DNA strands wrap around QDs, DNA strand condensation needs to be reduced and free, unbound QDs in solution must be removed from the QD-DNA mixture. Thus, as a next step, the aim is to reduce DNA condensation.

3.3.2.3 Optimisation Conditions for Non-Condensed DNA Strands

AFM studies have shown that DNA agglomeration is due to mechanisms: (i) divalent cations in the sample buffer neutralize the negative charge on the DNA phosphate-sugar backbone, reducing inter-strand repulsion between DNA strands, and thus encourage DNA agglomeration in solution[246] (appendix B.8), and (ii) in single-stranded DNA, intra-strand base-pairing leads to increased agglomeration in single-stranded DNA compared to in double-stranded DNA;[247] Although Calf-thymus DNA does contain some single-stranded DNA, the majority of DNA is double-stranded, and thus, reduced inter-strand repulsion due to divalent cations in the sample buffer is likely to be the more significant mechanism that drives DNA agglomeration/condensation here. Thus, in order to reduce DNA agglomeration, the Mg^{2+} cation concentration in sample buffer has to be

reduced. However, two factors limit the minimum $MgCl_2$ concentration in buffer: (1) the Mg^{2+} in the sample buffer must be high enough to induce DNA adhesion onto the negatively charged mica substrate (2) below a critical ratio of concentration of Mg^{2+} to Na^+ in sample buffer, adhesion of DNA to the mica surface is prevented,[248] as monovalent cations, unlike multivalent cations, cannot induce strong DNA binding onto mica, but still compete with multivalent cations in binding to the DNA backbone[248-250]. The Na^+-induced inhibition of DNA adhering onto mica must also be taken into account here, as the DNA fibres already do contain sodium, which forms a monovalent cation Na^+ in solution. Thus, the next step is to establish the minimum $MgCl_2$ concentration in the sample buffer that yields uncondensed DNA strands on mica, but which still allows strong DNA adhesion to the mica surface. Also, $MgCl_2$ pre-treatment of mica increases the attraction of DNA[249] and QDs to the mica substrate, so that variations in these will be investigated too.

Figure 3.27(b) shows AFM images of DNA strands at $MgCl_2$ concentrations reduced in the mica treatment step from 25 mM to 10 mM and in sample buffer from 25 mM to 2 mM. Reduced $MgCl_2$ concentrations yield more extended DNA strands without loops for most strands (Figure 3.27(b)), suggesting less efficient electrostatic neutralisation of the DNA backbone as fewer Mg^{2+} cations are present in sample buffer.

The DNA strand height is measured to be between 0.2 and 0.3 nm (Figure 3.27(a)), in agreement with double-stranded DNA previously measured by AFM[237, 238] (section 3.3.2.1). Successive AFM imaging of the same DNA strand yields the repeatable images (not shown), suggesting that the DNA is well-adhered to the mica surface due to a sufficient Mg^{2+} concentration in sample buffer and the mica pre-treatment. Present on the mica substrate and at the end of DNA strands are also particles less than 1 nm in height (Figure 3.27(a)(2) and Figure 3.27(b)(iii); Figure 3.27(a)(3 and 4) and Figure 3.27(b)(ii)) which might be salt crystals from the sample buffer or/and from the mica pre-treatment step. $MgCl_2$ concentrations lower than 10 mM in the mica pre-treatment or 2 mM in the sample buffer yielded very weak DNA adhesion to the mica

surface (appendix B.8), so that 10 mM and 2 mM $MgCl_2$ in the mica treatment and sample buffer, respectively, is considered the optimum conditions to yield uncondensed, well-adsorbed DNA on mica.

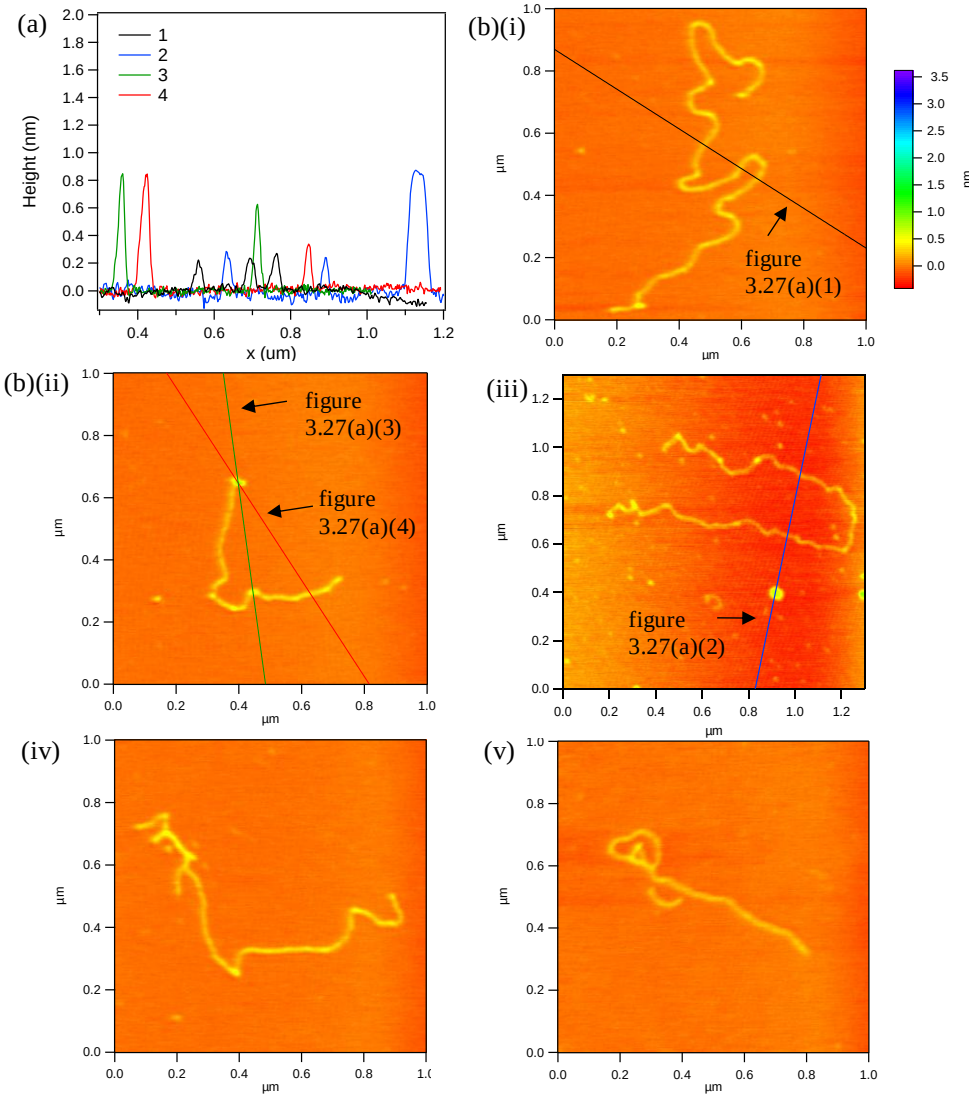

Figure 3.27: AFM image of Calf-thymus DNA (0.2 µg/mL) at optimum $MgCl_2$ concentration of 10 mM (mica pre-treatment) and 2 mM (sample buffer) (a)height measurement along coloured lines in figure (1) Figure 3.27(b)(i), (2) Figure 3.27(b)(iii), and (3 and 4) Figure 3.27(b)(ii); (b) AFM images of de-condensed DNA strands. AFM tip ROC=10nm.

3.3.2.4 Removing Excess QDs from QD-DNA Solution

The aim is to separate out free QDs from QDs that have associated to DNA in solution to facilitate AFM imaging of possible DNA wrapping around QDs. A protocol for DNA extraction from solution is applied to a QD-DNA solution that has been incubated for one day, which involves adding ethanol and sodium acetate to the incubated QD-DNA solution and leaving

overnight in a fridge to precipitate out DNA, followed by spinning at 13,000 rpm for 30 minutes to collect the DNA. Imaging the sample fluorescence under a UV lamp revealed that the precipitant of the treated QD-DNA solution is highly fluorescent, while the supernatant is non-fluorescent (not shown), suggesting that in addition to DNA, QDs also precipitate out, so that separation of free QDs and DNA has not occurred. The DNA extraction protocol was repeated but without ethanol, which condenses DNA, in order to produce pellets of QDs only.

Figure 3.28: Fluorescence images of (i) QDs mixed with CT-DNA (ii) CT-DNA, illuminated by a UV lamp. Sample are in sample buffer with sodium acetate (0.3 M), incubated in fridge for one day, and centrifuged at 13,000 rpm for (a) 0 mins (b) 30 mins and (c) 60 mins. Exposure time=200 ms.

However, after 30 minutes of centrifugation, the solution was still brightly fluorescent (Figure 3.28(a) and (b)), suggesting QDs to not separate out from DNA in solution by centrifugation. Increasing the centrifugation time to 60 minutes results in loss of QD fluorescence (Figure 3.28(c)), which might be due to QD disintegration under high centrifugal forces. Photo-bleaching is unlikely to have occurred, as exposure to the UV lamp was kept to a minimum.

3.3.2.5 AFM Imaging QD-DNA Mixtures

The incubation time of QD-DNA mixtures in solution was increased from one day to two weeks to allow more time for possible QD-DNA interaction to occur. Also, a narrower AFM tip with ROC=2 nm was used to image structures to allow for higher lateral resolution. Figure 3.29(a)(i) shows an AFM image of the sample where a particle spatially coincides with a DNA strand.

The particle is 4 nm high (Figure 3.29(a)(ii)(2)), suggesting this to be a QD coagulate. A shoulder less than 1 nm high, is seen at the intersection of the DNA strand at the base of the QD (Figure 3.29(a)(ii)(1)). However, 3D images reveal no shoulder across the particle

surface away from the DNA strand-QD intersection, suggesting that the particle is located on-top of the DNA strand, either by coincidence or due to DNA-QD interaction. Other AFM imaged DNA strands were discontinuous, suggesting weak adhesion of DNA onto mica. At the optimum $MgCl_2$ concentrations for DNA adhesion to mica, a weaker DNA adhesion to mica might be expected in the presence of QDs, as QDS require the mica to be pre-treated with $MgCl_2$ also in order to adhere to the like-charged mica substrate. Thus, the QD-DNA mixtures, incubated for 2 weeks, were deposited onto mica by doubling the mica pre-treatment $MgCl_2$ concentration from 2 mM to 4 mM.

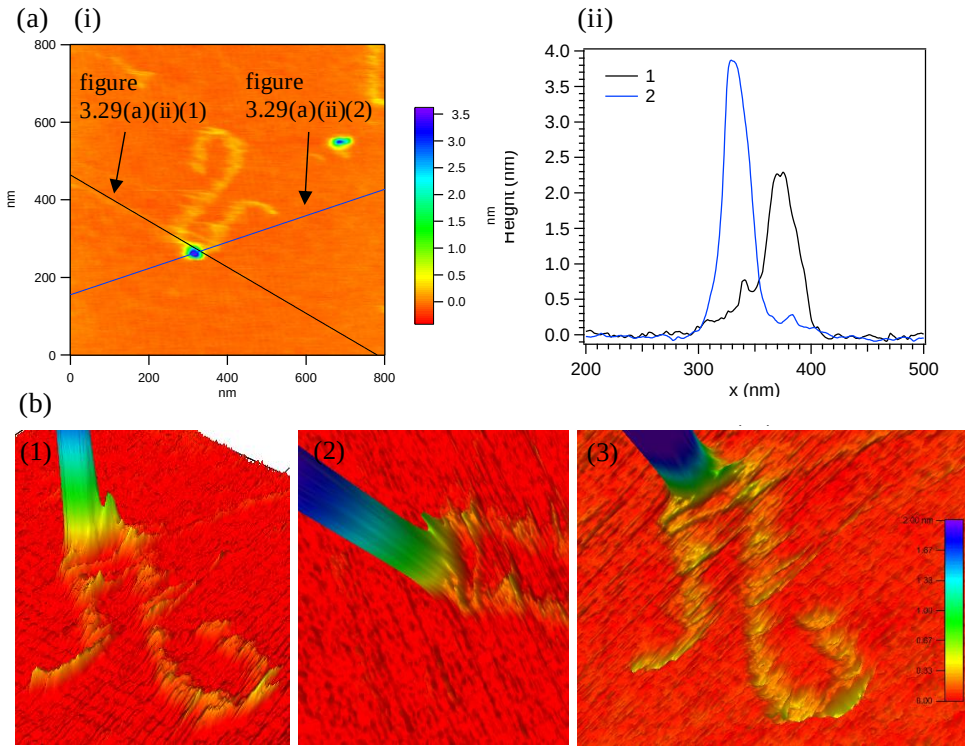

Figure 3.29: AFM image of Calf-thymus DNA (0.2 µg/mL) mixed in solution with QDs (10 nM) at $MgCl_2$ concentration of 10 mM (mica pre-treatment) and 2mM (sample buffer):(a)(i) 2D AFM image (a)(ii) height and profile measurement (b) 3D images from various perspectives the of 2D image in Figure 3.29(a)(i). AFM tip ROC=2 nm. The QD-DNA incubation time was two weeks.

Figure 3.30(a)(i) shows a further example of a possible QD-DNA assembly. The particle is about 4 nm high (Figure 3.30(a)(ii)(1)), as seen for the example in Figure 3.29, suggesting it might be a QD coagulate. At one side of the particle a shoulder about 9 nm wide is visible (Figure 3.30(a)(ii)(1)). However, the plateau is not located at a DNA-particle

intersection (Figure 3.30(b)), and a plateau width of about the DNA width, which is equal to about 35 nm (Figure 3.30(a)(ii)(3)), is expected for DNA winding around QDs. Thus, it is unlikely that the plateau on the particle is a sign of DNA winding around QDs.

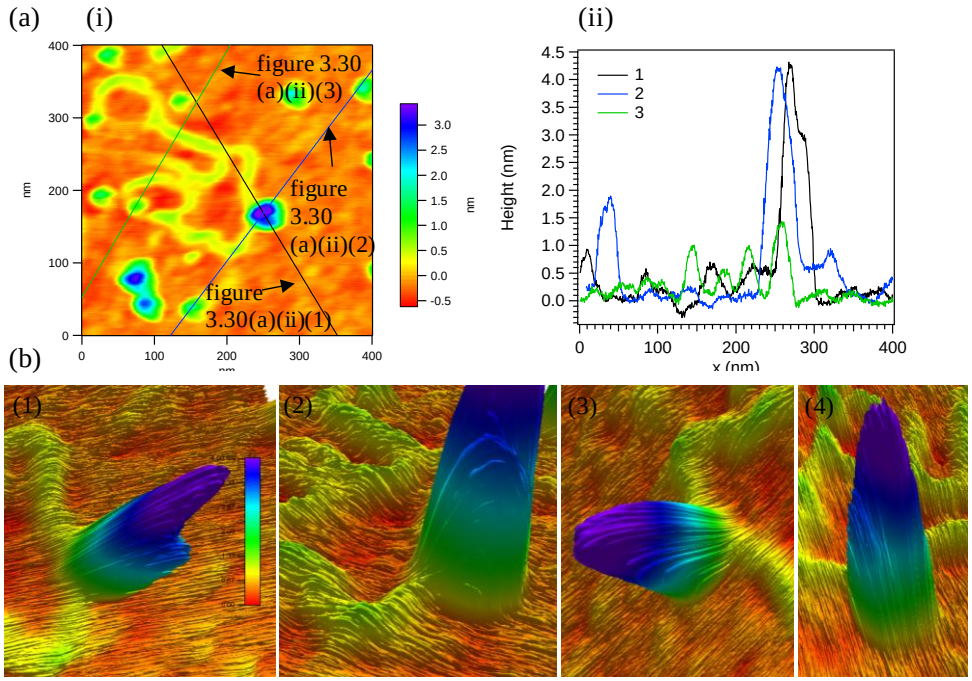

Figure 3.30: AFM image of Calf-thymus DNA mixed (0.2 µg/mL) in solution with QDs (10 nM) at $MgCl_2$ concentration of 10 mM (mica pre-treatment) and 4 mM (sample buffer: (a)(i) 2D AFM image (a)(ii) height and profile measurement (b) 3D images from various perspectives the of 2D image in Figure 3.30(a)(i). AFM tip ROC=2 nm. The QD-DNA incubation time was two weeks.

In summary, AFM imaging of mixtures of QDs and DNA have not provided clear evidence that DNA wrap around QDs, although spatial overlap between QDs and DNA strands was observed. Possible reasons for this might be that (a) no interaction between QDs and DNA takes place, or (b) the interaction is weak so that (i) only a small percentage of QDs interact with DNA, or (ii) DNA wound round QDs separate from the QDs during sample preparation for AFM imaging.

3.4 Conclusion

Using spectral analysis, fluorescence microscopy and atomic force microscopy we have investigated whether long genomic DNA strands (Lambda-phage and Calf-thymus DNA) wind around colloidal peptide-functionalised quantum dots in solution. We have found that with AFM imaged mixtures of QDs and double-stranded Calf-thymus DNA spatial overlap between QDs and DNA strands occurs, although no DNA winding about the side or top of QDs was experimentally observed, suggesting limited wrapping of double-stranded DNA around QDs, but possible QD association onto double-stranded DNA. Similarly, fluorescence images of drop-cast and stretched mixtures of double-stranded DNA and QDs revealed only limited association of QDs to double-stranded DNA. In contrast, fluorescence images of stretched mixtures of single-stranded DNA and QDs revealed association of assemblies of QDs to single-stranded DNA. Non-specific DNA-QD association is to be avoided when QDs are being used as DNA probes, so that in light of these results fluorescence dye labelled DNA probes are more suitable than QD labelled DNA probes for genetic analysis application.

Chapter 4

4 Fluorescence Enhancement of Fluorescently Labelled DNA Strands over Gold Nanovoids

In order to detect fluorescently labelled single sequences within single copies of DNA, highly sensitive detection systems are required. Most microscopy-based approaches are diffraction-limited, meaning that short DNA sequences labelled with a series of different fluorescent probes for about 100 base pairs, cannot be resolved. Here, gold nanovoids[21, 22] are evaluated as substrates for fluorescent enhancement of probes on DNA sequences. It is proposed that the fluorescence intensity of fluorophores, associated to DNA strands, stretched over gold nanovoids, varies with location over the nanovoid and with nanovoid dimension, as will be discussed later in this chapter. Although not part of the thesis, the rationale for examining the fluorescence intensity over plasmonic nanovoids was to establish whether microfluidic channels containing plasmonic nanovoids could be used for high resolution analysis for various DNA sequences. The incorporation of plasmonic nanovoids into microfluidic flow channels would be a novel approach to high resolution imaging of genomic DNA.

Presented are the fabrication method of gold nanovoid substrates, the stretching method and results of fluorescently labelled DNA strands over gold nanovoid substrates. The fluorescence intensity as a function of location over the nanovoid substrate is investigated and the fluorescence lifetime of fluorescently labelled DNA stretched over glass and gold nanovoid samples are compared.

4.1 The Effect of Gold Metallic Surfaces on Fluorescence- an Overview

In this thesis chapter, the potential for gold structured surfaces for DNA analysis is investigated. The use of metals for fluorescence enhancement of fluorophores associated to DNA molecules has been previously investigated.[251] Metals, such as gold or silver, are known to impact on the fluorescence of fluorophores in the following ways (i) quenching at distances less than 20 nm from the metal surface, in the visible spectral region[252] (ii) enhancement at distances between 10 to 400 nm from metal surfaces that exhibit nanometre scale surface roughness/periodicity or metal nanoparticles between 1 and 100 nm in size,[253-255] in the visible spectral region[256, 257] and (iii) fluorescence quenching or enhancement in the near-infrared spectral region by gold nanoparticles of different aspect ratios. [258] The fluorescence modulation by metal nanostructures is attributed to the interaction of the fluorophore with surface plasmon polaritons (SPP) modes supported by the metal nanostructure.[230, 257, 259-261] Before covering the principles of fluorescence enhancement by metal surfaces and optical cavities, the physical processes that yield fluorescence is discussed in more detail.

4.1.1 Absorption and Fluorescence

The absorption and emission process of a fluorescence emitter is illustrated by a Jablonski diagram (Figure 4.1). Considering molecules in thermal equilibrium at room temperature, Boltzmann statistics (appendix C.11) predicts most molecules occupy the lowest vibrational energy level v=0 in the electronic ground state S_0. Upon absorbing a photon of appropriate energy, a molecule in the S_0 (v=0) state is excited into an excited singlet electronic state (S_1 or S_2). The change in electron configuration during the absorption process takes place within about 10^{-15} s, which is much faster than the atomic nuclei, which are much heavier than electrons, can move, so that the nuclear coordinates most likely remain stationary during absorption i.e. electron transitions are vertical (Franck-Condon principle

(Figure 4.2(a)). The Franck-Condon Principle applies to all electron transitions i.e. also to fluorescence. Following the electron transition, the nuclei re-align themselves to the new equilibrium separation through vibrational relaxation. The probability of occupying a certain final vibrational state is equal to the square of the overlap integral between the initial and final vibrational wavefunctions of the respective electronic states (Figure 4.2(a)). The absorption spectrum reflects the vibrational states in the excited electronic state, with peak heights depending on the transition probability from S_0 (v=0) to S_n (v=n), where n>0 (Figure 4.2(b)). Following absorption, the excited molecule undergoes fast non-radiative relaxation to the lowest vibrational level in the first electronic excited state (S_1 (v=0))(Figure 4.1). The non-radiative decay occurs via vibrational relaxation and internal conversion, at a timescale of 10^{-14} to 10^{-11} s. The internal conversion rate between different electronic excited states is high as they are close in energy. However, the larger energy gap between the electronic ground state S_0 and the first excited electronic state S_1 slows the internal conversion rate down to 10^{-9} to 10^{-7} s for the $S_1 \rightarrow S_0$ transition, effectively competing with fluorescence.[262]

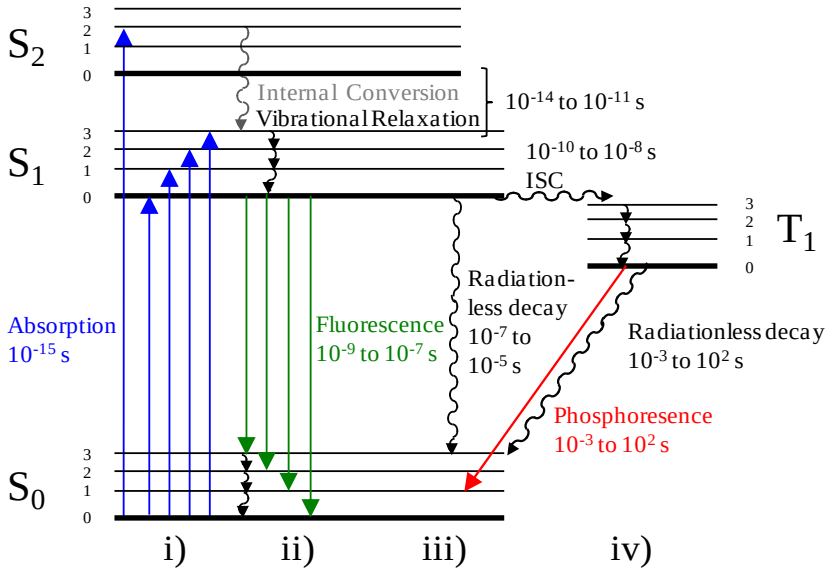

Figure 4.1: Jablonski diagram showing the electronic ground state (S_0), the first excited electronic singlet state (S_1) and the excited triplet state (T_1), with the vibrational levels of the electronic states labelled v=0,1,2,3. The processes are (i) excitation (blue) (ii) fluorescence (green) (iii) non-radiative decay (serpentine line) and (iv) phosphorescence (red). Non-radiative processes include internal conversion between different electronic excited states, and vibrational relaxation within the same electronic state.

From the S_1 (v=0) state, the molecule can undergo (i) fluorescence (ii) intersystem crossing followed by phosphorescence or (iii) radiationless decay. Fluorescence is the radiative decay between states of the same multiplicity, and usually occurs between the singlet states, such as from the first excited electronic state S_1 (v=0) to the electronic ground state S_0 (v=n) (Figure 4.1(ii)).

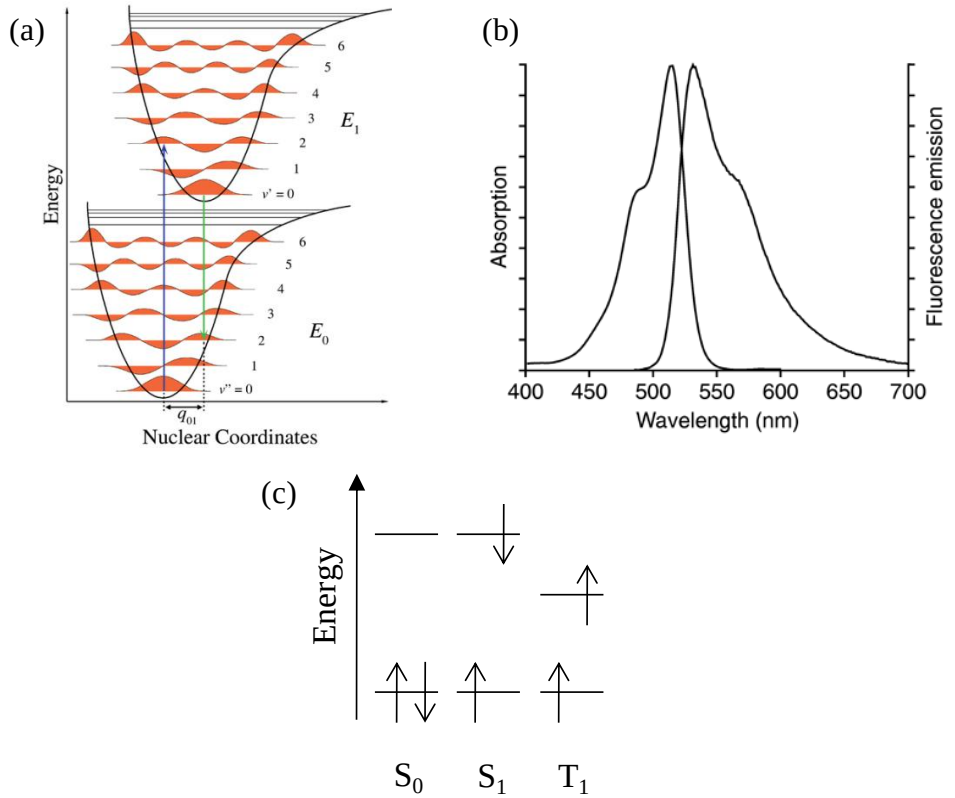

Figure 4.2: Absorption and emission of a fluorescent emitter (a) The potential energy curve of a molecule illustrating the Franck-Condon Principle- electronic ground state (E_0) and first electronic excited state (E_1).[264] A redistribution in electron configuration shifts the equilibrium separation of the nuclei of the molecule by q_{01}. The vibrational wavefunction amplitude in the electronic states are shown in orange. As nuclear (vibrational) motion is slower than electronic transitions, the inter-nuclei separation is assumed not to change during an electronic transition, resulting in vertical electronic transitions. The most probable final vibrational level then is the one with the highest vibrational wavefunction overlap between initial and final vibrational state. (b) absorption (left) and fluorescence (right) spectrum of TOTO-1[265] (c) electron spin configuration in the electronic state S_0, S_1 and T_1, with spin up or down (1/2 or -1/2) indicated by an upwards or downwards pointing arrow, respectively.)

A singlet state has paired electron spins, i.e. the total spin=0 and multiplicity M=2*spin+1=1 (Figure 4.2(c)). The fluorescence decay occurs within 10^{-9} s, which is slower than the non-radiative decay to S_1 (v=0) (10^{-14} to 10^{-11} s). As a result, fluorescence always occurs from the lowest vibrational level S_1 (v=0) (Kasha's rule), irrespective of the absorption

energy, and the fluorescence energy is less than the absorption energy (Stokes shift) (except for the S_0 (v=0)→S_1 (v=0) and S_1(v=0)→S_0(v=0) transition, where no non-radiative relaxation occurs) (Figure 4.2(b)). Like absorption, fluorescence follows the Franck-Condon principle, i.e. the transitions are vertical and occur with a probability equal to the square of the overlap integral between wave-functions in the initial and final state. The vibrational levels in the S_0 and S_1 electronic state are similarly spaced in energy, so that the transition probabilities from the v=0 to the v=n vibrational state are the same for the transitions S_0→S_1 (absorption) and S_1→S_0 (fluorescence) (Figure 4.2(a)) i.e. the fluorescence and absorption spectrum between S_0 and S_1 are mirror images of each other (Figure 4.2(a) and (b)).

A fluorescent molecule in S_1 can also undergo a spin reversal of the excited electron, resulting in a final state with two unpaired electrons of the same spin and hence total spin=1 (M=3), a triplet state T_1 (Figure 4.2(c)). The non-radiative transition between states of different multiplicity is called inter-system crossing (ISC) and although forbidden, is possible due to spin-orbit coupling.[263] ISC occurs on the order of 10^{-9} s, and is followed by vibrational relaxation to the lowest vibrational level of T_1. The radiative transition from T_1 to S_0, termed phosphorescence (Figure 4.1(iv)), requires spin-reversal (Figure 4.2(c)) and is thus quantum-mechanically forbidden, resulting in longer phosphorescence lifetimes (of the order of 10^{-3} to 10^{2} s) than fluorescence lifetimes. As an alternative to radiative relaxation, radiationless decay to the ground state can occur, due to internal mechanisms, such as phonon relaxation or external mechanisms, such as quenching or collisional de-activation. The rate of non-radiative decay is of the order of 10^{-7} to 10^{-5} s for the S_1 →S_0 transition, and 10^{-3} to 10^{2} s for the T_1 →S_0 transition (Figure 4.1(iii)). In the ground state the fluorescent molecule returns to the lowest vibrational level via vibrational relaxation. Delayed fluorescence, in which the molecule non-radiatively returns from T_1 to S_1, followed by fluorescence, can also occur (not shown).

4.1.2 Fluorescence Quantum Yield and Fluorescence Lifetime

The fluorescence efficiency is quantified by the fluorescence quantum yield. Consider a spontaneous emitter in the excited electronic state S_1, which can return to the electronic ground state S_0 either radiatively, at rate k_r, or non-radiative, at rate k_{nr}. Assuming the absence of any external quenchers, the fluorescence quantum yield is equal to

$$Q_0 = \frac{k_r}{\sum k} = \frac{k_r}{k_r + k_{nr}} \tag{4.1}$$

where $\sum k$ is the total depopulation rate from S_1. The radiative (or natural) lifetime (τ_r) quantifies the excited state lifetime in the absence of any non-radiative decay, i.e. $k_{nr}=0$ and $Q_0=1.0$, and is given by

$$\tau_r = \frac{1}{k_r} \tag{4.2}$$

The observed fluorescence lifetime (τ_0) is the average time the emitter spends in S_1 before it decays to S_0, and, in the absence of external quenchers, is given by

$$\tau_0 = \frac{1}{k_r + k_{nr}} \tag{4.3}$$

According to equation (4.1), the quantum yield can theoretically range from 1.0, if $k_{nr}=0$, to 0, but in practice 1.0 is never reached as k_{nr} is never 0. In summary, changes in both k_r and k_{nr} affect both the quantum yield and the observed fluorescence lifetime.

4.1.2.1 Fluorescence Quenching

Fluorescence quenching is the reduction in fluorescence quantum yield due to an increase in the non-radiative decay rate k_{nr}, usually due to newly introduced non-radiative decay channels. As an example, consider the effect of collisional quenching on a spontaneous emitter: a collisional quencher increases the non-radiative decay from k_{nr} to $k_{nr}+k_Q$, changing

the quantum field and observed lifetime from a non-quenched value of Q_0 and τ_0 to

$$Q_Q = \frac{k_r}{k_r + k_{nr} + k_Q} < Q_0 \text{ and } \tau_Q = \frac{1}{k_r + k_{nr} + k_Q} < \tau_0 \qquad (4.4)$$

It is clear that quenching reduces both the quantum yield and the observed lifetime. Metal surfaces are well-known fluorescence quenchers, with quenching dominant within 50 nm of the metal surface.[256, 257] Quenching by metal is mainly attributed to coupling to non-radiative surface plasmon polariton modes (SPP) on flat metal surfaces and to lossy surface waves.[256, 257] The energy transfer to lossy surface waves occurs via dipole-dipole interaction, with the energy non-radiatively transferred to an electron-hole pair inside the metal, which is then lost as heat.[266] The transfer rate to lossy surface waves increases with decreasing distance, *d*, from the metal surface with a d^{-4} dependence. The evanescent nature of SPP modes also results in stronger non-radiative coupling with decreasing fluorophore-metal separation.[267] For a flat metal-dielectric interface, coupling to non-radiative SPP dominates for distances *d=20-200 nm*, while coupling to lossy surface waves dominates for *d<20 nm*.[266]

4.1.2.2 Enhanced Quantum Yield

An enhanced fluorescence quantum yield is usually the result of an increased radiative decay rate k_r. Supposing that the radiative decay rate of a spontaneous emitter is increased from k_r to $k_r + k_R$, by some mechanism, then the quantum yield and observed lifetime is changed from Q_0 and τ_0 to

$$Q_R = \frac{k_r + k_R}{k_r + k_R + k_{nr}} > Q_0 \quad \text{and} \quad \tau_R = \frac{1}{k_r + k_R + k_{nr}} < \tau_0 \qquad (4.5)$$

Thus, an increase in the intrinsic radiative decay rate k_r increases the fluorescence quantum yield and decreases the observed lifetime. Contrast this with quenching, where an increase in the non-radiative decay rate k_{nr} reduces both the quantum yield and observed lifetime.

We will now consider how the radiative decay rate can be altered. The spontaneous emission rate k_r is given by Fermi`s Golden Rule (appendix C.1), and is equal to

$$k_r = \frac{2\pi}{\hbar^2}\left|M_{if}\right|^2 \rho(\varpi_{if}) \tag{4.6}$$

where $\hbar\varpi_{if}$ the transition energy, M_{if} is the transition matrix element and describes the interaction strength between the perturbing field and the emitter dipole, $\rho(\varpi_e)$ is the photonic mode density (PMD) at the transition energy (also called density of states), and is defined as the number of energy states per unit volume at in the energy interval E to $E+dE$. In the case of spontaneous emission, the perturbing field that causes spontaneous emission is the vacuum field, so that spontaneous emission can be considered as being radiative emission stimulated by fluctuations in the vacuum field. It can be shown that in a homogeneous medium of refractive index n, the spontaneous emission rate is equal to[268]

$$k_r = \frac{1}{\tau_r} = \frac{4d_{if}^2\varpi_{if}^3 n}{3\hbar c^3} \tag{4.7}$$

where d_{if} is the emitter`s electric dipole moment and $\hbar\varpi_{if}$ is the transition energy. Thus, the free space spontaneous emission rate k_r depends on the transition energy, the refractive index and the electric dipole moment, and is therefore an intrinsic property of the spontaneous emitter. In 1946 Purcell first predicted the possibility of controlling the spontaneous emission rate by changes in the photonic mode density the emitter can emit into. Later, experiments have confirmed this, and enhanced or suppressed spontaneous decay rates have been observed in structures such as inside photonic crystals[269, 270] and optical cavities,[271-273] near a silver film[274-276] and near surface-plasmon-polariton (SPP) supporting metal nanostructures.[277, 278] The gold nanovoids grown in this thesis can theoretically induce enhancement in fluorescence intensity (radiative decay rate) by coupling with radiative SPP modes supported by the nanovoids and when the nanovoids are setup as an optical cavity. Thus, the following

sections treat the cases of enhanced emission rates induced by optical cavities and SPP supporting metal surfaces in more detail.

4.1.2.2.1 Modulation of Radiative Decay Rate Induced by Optical Cavities

An optical cavity is an arrangement of mirrors that can support light of only certain discrete wavelengths.[279] For simplicity consider an optical cavity consisting of two parallel planar mirrors separated by distance *L* (Figure 4.3(a)).

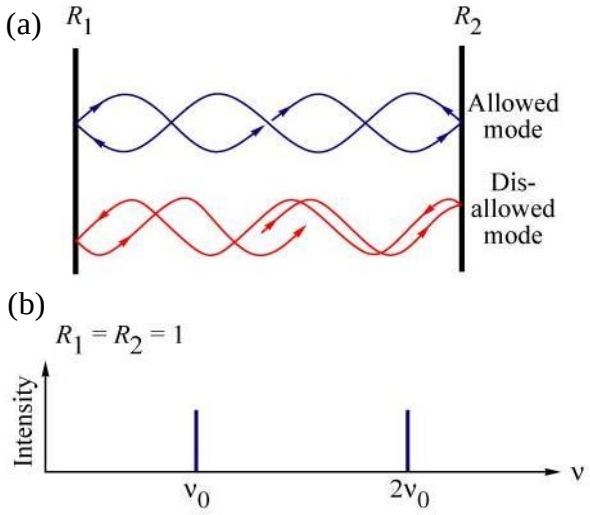

Figure 4.3: Optical cavity (a) consisting of two parallel mirrors R_1 and R_2 (b) resonant cavity modes.[280]

Only optical modes that satisfy the criterion

$$m\frac{\lambda}{2} = L \tag{4.8}$$

can form standing waves and thus exist within the optical cavity (Figure 4.3(a) and (b)), where λ is the wavelength and *m* is a positive integer, so that the total number of available optical modes within an optical cavity is lower than in free space. However, as resonant cavity modes form standing waves, the electric field strength varies with location within the cavity, with a strong field at the anti-nodes and a zero field at the nodes (Figure 4.3(a)).

Recall that the fluorescence decay rate of a spontaneous emitter varies with the density of optical states, $\rho(\varpi_{if})$, it can decay into (equation (4.6) in section 4.1.2.2). The modulation of the electric field strength by an

optical cavity means that the local density of optical states (LDOS) in an optical cavity varies with (i) energy and (ii) position within the cavity. Specifically, the LDOS inside an optical cavity is equal to[281]

$$\rho(r,d,\varpi) = \sum_{all\,modes} \left| d \cdot E_m(r) \right|^2 \delta(\varpi_m - \varpi) \qquad (4.9)$$

where ω_m is a cavity mode frequency, ω is the transition frequency of the spontaneous emitter, $\delta_{ij} = \begin{cases} 1 \\ 0 \end{cases}_{,if \quad i \neq j}^{,if \quad i=j}$, $E_m(r)$ is the electric field strength of a cavity mode at position *r* and *d* is the unit vector of the electric dipole moment for the transition of the emitter. The LDOS is thus dependent on (i) the electric field strength *E(r)* of the cavity mode, (ii) the orientation of the dipole moment of the spontaneous emitter relative to electric field of the cavity mode, and (iii) the energy resonance between excited emitter and cavity mode. Assuming the emitter dipole is parallel to the electric field, then equation (4.9) can be simplified to[281]

$$\rho(r,d,\varpi) = \sum_{all\,modes} \left| E_m(r) \right|^2 \delta(\varpi_m - \varpi) \qquad (4.10)$$

It can be seen that the LDOS varies with (i) the electric field strength *E(r)* of the cavity mode, which is highest at the anti-nodes, and (ii) the energy resonance between the fluorescence energy of the spontaneous emitter and the cavity mode. Thus, a spontaneous emitter placed at an anti-node within a resonant cavity sees a higher LDOS than in free space resulting in an enhanced radiative decay rate and enhanced fluorescence intensity. In contrast an emitter, either out of resonance with a cavity mode, or placed at a node within a resonant cavity, has no final states to decay into and will stay in the excited state for longer. Drexhage has experimentally shown that the LDOS is even changed in front of a single mirror, resulting in radiative lifetime modulations dependent on the emitter-mirror separation.[275]

Assuming the radiative decay rate inside a resonant cavity and in free space is equal to k_{cav} and k_{free}, respectively, then the enhancement in the radiative decay rate induced by a resonant cavity can be quantified by the Purcell factor, F_P, and has a maximum value equal to[282] (appendix C.5)

$$F_P = \frac{k_{cav}}{k_{free}} = \frac{3}{4\pi^2}\frac{\lambda_C^3}{n^3}\frac{Q}{V_{eff}} \tag{4.11}$$

where n is the refractive index of the medium filling the cavity, V_{eff} is the effective mode volume and λ_C is the cavity mode wavelength. Q is the cavity quality factor and quantifies the cavity loss. Maximum enhancement occurs for emitter dipoles aligned parallel to the cavity mode field (equation (4.9)). Cavities with a low loss (high Q) and small mode volumes produce high Purcell factors. It has been shown that spherical gold microcavities can achieve increased mode confinement by reducing the cavity dimension to the micron scale and, in addition to the usual longitudinal confinement, provide additional confinement in the lateral direction by replacing one of the mirrors with a spherical mirror[283] (appendix C.6).

4.1.2.2.2. Enhanced Decay Rate Induced by Radiative Surface-Plasmon-Polaritons

Surface Plasmon Polaritons (SPP) are charge oscillations at a metal-dielectric interface with an associated strong electric field that is pinned to the metal surface and decays exponentially with perpendicular distance from the interface (section 4.2). The density of states in SPP (ρ_{SPP}) is higher than that in free space (ρ_{free}), mainly because of the low SPP group velocity[259] (Figure 4.4(c) in section 4.2), so that an excited emitter placed near a metal surface within the exponential SPP electric field quickly couples non-radiatively to a SPP. Emitter-SPP coupling occurs via dipole-dipole interaction.[267] Assuming the non-radiative coupling rate from the excited emitter to a SPP mode, and the radiative decay rate of the excited emitter in free space, is equal to k_{SPP} and k_{free}, respectively, then the Purcell factor is equal to[259]

$$F_P = \frac{k_{SPP}}{k_{free}} \approx \frac{\rho_{SPP}}{\rho_{free}} \tag{4.12}$$

The SPP can quickly re-radiate the emission energy into the far-field under certain conditions (section 4.2.1), which has the net effect of increasing the radiative decay rate and the fluorescence intensity of the nearby emitter.

SPP-induced emission rate enhancement is limited by how much more efficiently the excited SPP mode can emit into the far-field than the fluorophore can fluorescence in free space (appendix C.3). SPP-induced enhanced emission rates have been observed experimentally.[230, 284] For instance, CdSe QDs have shown a 23-fold enhancement in fluorescence intensity and 2-fold increase in the fluorescence decay rate when deposited onto an evaporated gold film as compared to when on a flat quartz surface, due to quickly re-radiating SPP.[285] As with optical cavities, coupling from excited emitter into radiative SPP modes requires (i) energy resonance between excited emitter energy and SPP mode, and (ii) spatial overlap between excited emitter and the strong evanescent electric field of the SPP modes. The exponential decay of the evanescent field strength limits the maximum emitter-metal surface separation at which SPP excitation is efficient to below 200 nm.[266] Although the coupling efficiency from an excited state spontaneous emitter to a resonant SPP mode increases with smaller separation, for separations below 20 nm, non-radiative energy-transfer to lossy waves on the metal surface dominates, and quenches the fluorescence.[266] It should be noted that SPP on a flat metal surface cannot radiate into the far-field (section 4.2.1) and therefore quench fluorescence. SPP can be made radiative via prism coupling or nanometre-scale corrugations on the metal surface (section 4.2.1). Metal surfaces with nanometre-scale corrugations support radiative SPP modes (section 4.2.1) with SPPs excitable over the whole metal surface and with maximum evanescent field at the metal-dielectric interface, where quenching effects are strong. In contrast, spherical gold nanovoids have been shown to support special SPP modes that are localised within the voids, and with strong fields that can be engineered to be located within tens of nanometers above the nanovoid.[21, 22] This localisation of the SPP field above the voids offers the potential to provide fluorescence enhancement at discrete locations above the nanovoids. The SPP modes of such spherical microvoids are explained in more detail in section 4.2.2.

4.1.2.2.3. Enhanced Excitation Rate by Surface-Plasmon-Polaritons

We have seen in the previous section 4.1.2.2.2 that excited fluorophores can non-radiatively transfer their excitation energy to SPP modes on a metal dielectric interface, provided the emission energy is resonant with the SPP mode and the fluorophore is located within the SPP evanescent field. This mechanism is also reversible, which means that SPP can excite fluorophores via non-radiative energy transfer, provided the SPP is resonant with the fluorophore absorption energy, and the fluorophore is within the SPP near-field. The strong evanescent field of SPP near a metal-dielectric interface can increase the excitation rate of nearby fluorophores compared to in free space.[261] SPP-induced enhanced absorption rates have been treated theoretically (appendix C.4).[261] Enhanced fluorescence intensities of fluorophores nearby SPP-supporting metal structures have been experimentally demonstrated.[286] For instance, the fluorescence intensity of rhodamine excited by SPP on a metal grating, which in turn have been excited by the excitation source via grating coupling, was shown to be up to 10 times higher compared to rhodamine excited directly by the far-field excitation radiation.[286] Note that the enhanced absorption rate does not affect the fluorescence decay rate, leaving the fluorescence lifetime unchanged.

4.2 Surface Plasmon Polaritons- an Overview

Under certain conditions, electromagnetic waves incident onto a metal surface can couple to longitudinal charge oscillations on the metal surface (surface plasmon), resulting in a mixed state between electromagnetic wave and a surface plasmon, called a surface-plasmon-polariton (SPP) (Figure 4.4(a)). The electric field associated with a SPP is pinned to the surface of the metal, and decays exponentially with distance perpendicular from the metal-dielectric interface (Figure 4.4(b)).

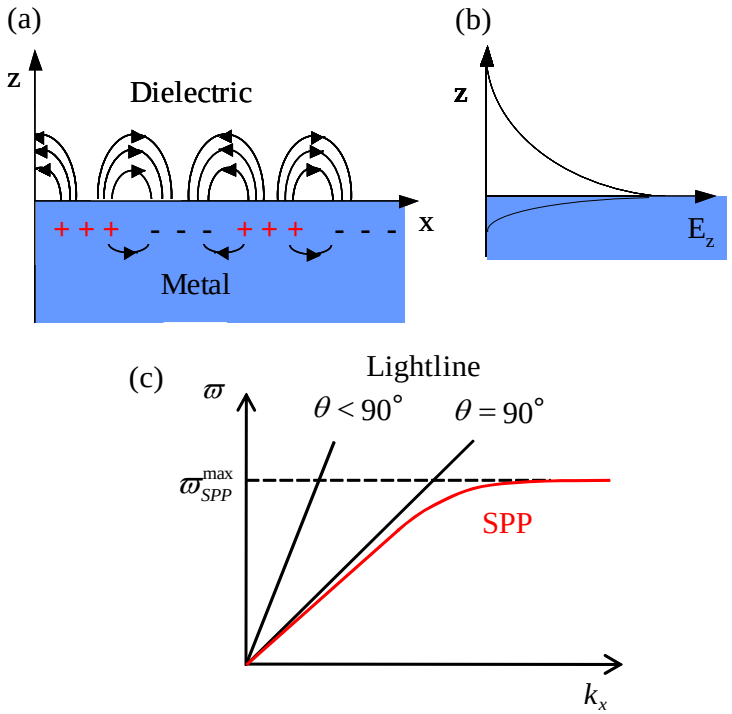

Figure 4.4: Surface plasmon polaritons (a) Electric field and surface charge (b) electric field strength perpendicular to the interface (c) dispersion curve of a surface plasmon polariton (red, k'_x) and light in a dielectric medium incident at θ<90° and θ=90° to the normal of the dielectric-metal interface (black line).

The dispersion relation of a SPP mode can be found by solving Maxwell`s equations for an optical mode at a metal-dielectric interface (assumed to be along the x-axis), and assuming the dielectric constant of the dielectric and

metal are equal to ε_d and $\hat{\varepsilon}_m$ respectively, is equal to (appendix C.7.3.1 and C.7)

$$\hat{k}_x = \frac{\varpi}{c}\sqrt{\frac{\hat{\varepsilon}_m \varepsilon_d}{\hat{\varepsilon}_m + \varepsilon_d}} \tag{4.13}$$

where $\hat{k}_x$ is the complex SPP wavevector along the interface. The real and imaginary parts can be evaluated using $\hat{k}_x = k_x' + ik_x''$ and $\hat{\varepsilon}_m = \varepsilon_m' + \varepsilon_m''$, and are equal to (see appendix C.7.3.1)

$$k_x' = \frac{\varpi}{c}\sqrt{\frac{\varepsilon_m' \varepsilon_d}{\varepsilon_m' + \varepsilon_d}} \text{ and } k_x'' = \frac{\varpi}{c}\left(\frac{\varepsilon_m' \varepsilon_d}{\varepsilon_m' + \varepsilon_d}\right)^{\frac{3}{2}} \frac{\varepsilon_m''}{2(\varepsilon_m')^2} \tag{4.14}$$

The dispersion relation of a SPP and that of an electro-magnetic wave freely propagating in a dielectric medium are shown in Figure 4.4(c).

For small values of k_x, the SPP dispersion tends towards that of the lightline, while for large k_x, the SPP frequency ω tends towards the surface plasmon frequency ω_P, and has a maximum value equal to (appendix C.7.8)

$$\varpi_{SPP}^{\max} = \frac{\varpi_p}{\sqrt{1+\varepsilon_d}} \tag{4.15}$$

As $\hat{k}_x$ is complex it represents attenuation of the SPP wave with propagation along the interface, due to absorption in the metal. The propagation length of a SPP, L_{SPP}, is the distance a SPP travels along the interface before its electric field intensity has dropped by 1/e of its original value, and is equal to [360]

$$L_{SPP} = \frac{1}{2k_x''} = \lambda_0 \frac{(\varepsilon_m')^2}{2\pi\varepsilon_m''}\left(\frac{\varepsilon_m' + \varepsilon_d}{\varepsilon_m' \varepsilon_d}\right)^{\frac{3}{2}} \tag{4.16}$$

where λ_0 is the wavelength in vacuum. Metals with small values of ε_m'', and large negative values of ε_m', due to long scattering times of electrons with positive ions (appendix C.7.1), have low loss and hence long L_{SPP}. The frequency dependence of both ε_m'' and ε_m' (equation C.46 in appendix C.7.2) introduces a frequency dependence into $L_{SPP}(\varpi)$, with long L_{SPP} at

low frequencies, which becomes shorter as ω approaches the plasmon resonance frequency $\varpi_{SPP}^{\max}$.

The momentum of a SPP perpendicular to the interface (the z-direction), k_z, is also complex (equation C.49 and C.50 in appendix C.7.3.1), representing an attenuated wave/electric field amplitude that decays exponentially with distance from the interface (z-direction). The skin depth quantifies the extent of the SPP electric field in the z-direction, and inside the dielectric and metal, respectively, is equal to [360]

$$\delta_d = \frac{\lambda}{2\pi}\sqrt{\left(\frac{\varepsilon_m' + \varepsilon_d}{\varepsilon_d^2}\right)} \text{ and } \delta_m = \frac{\lambda}{2\pi}\sqrt{\left(\frac{\varepsilon_m' + \varepsilon_d}{\varepsilon_m'^2}\right)} \qquad (4.17)$$

At a gold-air interface and at 600 nm the skin depths equals $\delta_d = 300\ nm$ n air and $\delta_m = 30\ nm$ in gold, i.e. the evanescent field decays slower in the dielectric than in the metal (Figure 4.4(b)).

4.2.1 Surface Plasmon Polariton Coupling with Far-Field Radiation

For far-field radiation to couple to SPP, energy and momentum must be conserved. Consider incident far-field radiation, inside a dielectric medium of refractive index $\sqrt{\varepsilon_d}$, of frequency ω_0 and wavevector k_0, incident onto a flat metal-dielectric interface at an angle θ to the normal (Figure 4.5(a)). If the SPP wavevector in the plane of the metal-dielectric interface and the SPP frequency is equal to k_{SPP} and ω_{SPP}, respectively, then SPP-far-field coupling occurs when

Energy conservation $\qquad \varpi_0 = \varpi_{SPP} \qquad (4.18)$

Momentum conservation $\qquad \frac{\varpi_0}{c}\sqrt{\varepsilon_d}\sin\theta = k_{SPP} \qquad (4.19)$

where c is the speed of light in vacuum. Figure 4.5(c) illustrates the dispersion relation of a SPP at a flat metal-dielectric interface and far-field radiation inside the same dielectric. In the case of a flat dielectric-metal interface geometry, the in-plane wavevector of the incident far-field radiation is always smaller than the SPP wavevector, so SPP do not couple

to an optical field. The SPP do not radiate, and conversely, SPP cannot be excited by incident light. The larger SPP momentum is due to the SPP binding to the surface [287].

The momentum mismatch can be circumvented by two approaches to allow SPP-optical field coupling (a) prism coupling (b) scattering from a diffraction grating. Prism coupling achieves coupling by (i) increasing the momentum of the far-field radiation by use of a high refractive index prism, and by turning, via total internal reflection, the incident far-field radiation into an evanescent field, which can carry the increased momentum over a distance, exciting a SPP at a nearby metal-dielectric interface. Two prism configurations, the Otto and Kretschman-Reather configuration, exist (appendix C.7.9). However, both techniques require very precise geometry.

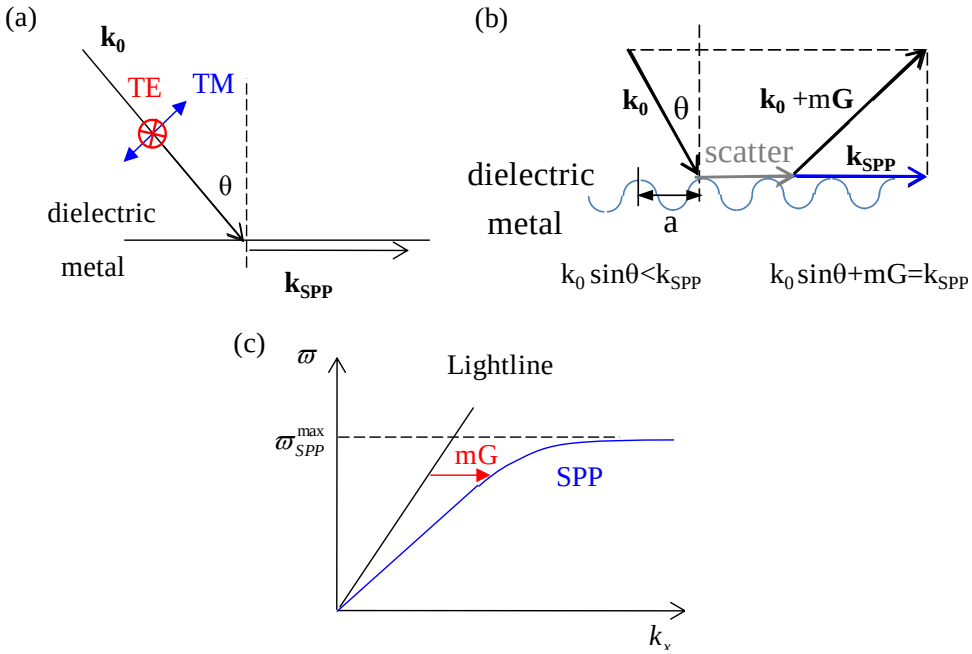

Figure 4.5: SPP coupling with far-field radiation (a) vector diagram showing the wavevectors of a plane wave incident onto a metal dielectric interface and a SPP and the electric field of transverse magnetic (TM) and transverse electric (TE) polarisation (b) scattering of incident light (wavevector k_0 and x-component $k_0 sin\theta$) by the metal corrugation gives the scattered photon enough in-plane momentum ($k_0 sin\theta + mG$) to couple to a surface plasmon polariton mode (SPP) of wavevector k_{SPP} (c) In-plane momentum-matching condition of the coupling process illustrated in a dispersion diagram.

In contrast, grating coupling uses a periodically corrugated metal surface, period $\vec{a}$, as illustrated in Figure 4.5(b). The incident radiation can scatter off the periodicity, acquiring extra momentum in the plane of the

corrugation, of magnitude equal to *mG*, where *G* is the grating wavevector, equal to $G = \frac{2\pi}{a}$, and *m* is an integer. SPP can travel in the forward or backward direction along the corrugation, so that coupling between far-field radiation and SPP occurs when

$$\frac{\varpi_0}{c}\sqrt{\varepsilon_d}\sin\theta \pm mG = k_{SPP} \tag{4.20}$$

From equation 4.20 it can be seen that SPP excitation by far-field radiation is tuneable with incident angle, incident wave energy, as well as the corrugation periodicity of the metal surface. Forward coupling is illustrated in Figure 4.5(b) and Figure 4.5(c).

As SPP are transverse-magnetic modes, only p-polarised light can couple to SPPs (Figure 4.5(a)) (appendix C.7.3.1). SPP excitation is detected by a dip in the reflection spectrum of the incident p-polarised radiation at the resonance frequency. Likewise, SPP can couple to far-field radiation and become radiative by scattering off the metal-periodicity. SPP emission is p-polarised and highly directional (equation 4.20).

4.2.2 SPP Modes of a 2D Hexagonal Nanovoid Substrate

The substrates used for this thesis consist of a two-dimensional hexagonal lattice of close-packed, spherical, truncated nanovoids (Figure 4.6).

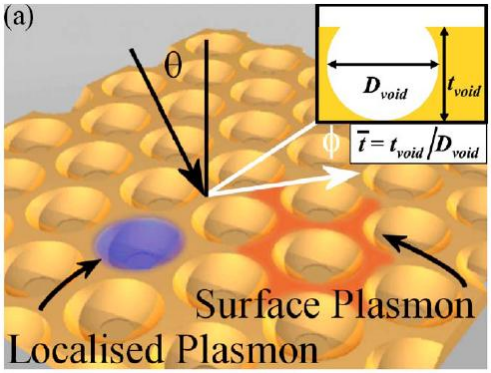

Figure 4.6: Illustration of the substrate, incident light incident onto the substrate at an angle to the normal θ and substrate orientated at an azimuthal angle φ. The two surface plasmon modes supported by the substrate are localised (blue) or delocalised (orange). Inset: nanovoid parameters are void diameter (D_{void}), void thickness (t_{void}) and normalised void thickness ($\bar{t}$).[21]

The substrates are made of chemically inert gold. The voids are parameterised by the void diameter D_{void}, void thickness t_{void} and normalised void thickness $\bar{t} = \frac{t_{void}}{D_{void}}$ (inset in Figure 4.6).

The substrates can support two types of surface plasmon polariton modes (i) delocalised plasmons that propagate on the sample surface (Bragg plasmons) and (ii) plasmons localised and confined spatially inside the nanovoids (Mie plasmons) (Figure 4.6). Bragg plasmons are excited by incident light that resonantly scatters off as a result of the sample periodicity, while Mie plasmons result from Bragg plasmons reflecting off sharp asperities such as the void upper rim, resulting in self-interference and localisation of the SPP within the void volume.[287]

The dispersion relation of Bragg and Mie plasmons in the nanovoid substrate have been investigated experimentally and explained theoretically by Kelf *et al.*,[21, 287], Teperik *et al.*[288] and Cole *et al.*[22] and are explained in detail in sections 4.2.2.1 and 4.3.2.2.

4.2.2.1 Bragg Plasmon Modes

Coupling between far-field radiation and Bragg plasmons occurs via scattering off the sample periodicity. The weak-scattering approximation ignores the actual surface structure and only considers the sample periodicity, and can be invoked for thin samples.[287] A void centre constitutes a scattering site, so that the scattering sites are extended from the 1D case in section 4.2.1 to a flat 2D, close-packed hexagonal arrangement. The 2D array of scattering sites can be assigned with primary lattice vectors $\vec{a}$ and $\vec{b}$, which are of equal magnitude $|\vec{a}| = |\vec{b}| = a$, where a is the centre-to-centre distance between neighbouring voids, and are oriented 60° relative to each other (Figure 4.7(i)). The scattering periodicity of the 2D hexagonal lattice is equal to the separation between the planes of scatter, which is now derived. Consider the reciprocal k-space, which has primary reciprocal lattice vectors $\vec{A}$ and $\vec{B}$ that are separated by a 120° angle (Figure 4.7(ii)).

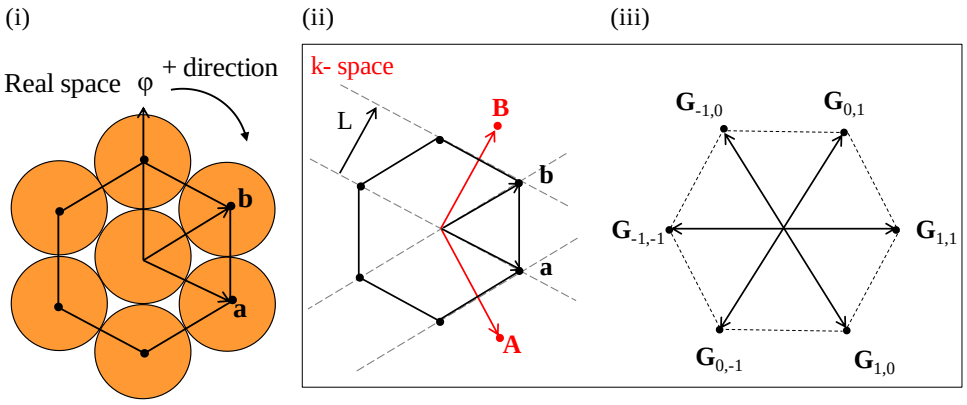

Figure 4.7: Delocalised Bragg Plasmons (i)2D array of close-packed voids, and its unit cell (black),characterised by direct lattice vectors a and b and sample orientation (azimuthal angle)φ, which can be represented in (ii) k-space: the Fourier transform of the hexagonal lattice creates peaks at the periodicities (black points), from which the scattering planes can be drawn (dashed lines),and the inter-plane distance L derived, as illustrated for the (n,m)= (0,1) and (1,0) scattering direction. There is a 30° shift between the lattice vectors in real space (a,b) and in k-space (A,B), and hence in the respective unit cells. (iii) full set of primary reciprocal lattice vectors (black arrows) defining the reciprocal unit cell (dashed line).

In general, the scattering planes are oriented in the direction of $m\vec{A}+m\vec{B}$, where m and n are integers (Figure 4.7(ii)). Neighbouring scattering planes are separated by a distance equal to (Figure 4.7(ii))

$$L=(\cos 30°)\cdot a=\frac{\sqrt{3}}{2}a \tag{4.21}$$

Equation 4.21 can be generalised to scattering in the direction of $m\vec{A}+m\vec{B}$, yielding a scattering periodicity equal to

$$\vec{L}_{nm}=\cos 30°\cdot a(m\hat{A}+n\hat{B})=\frac{\sqrt{3}}{2}a(m\hat{A}+n\hat{B}) \tag{4.22}$$

where $\hat{A}$ and $\hat{B}$ are the unit vectors along the $\vec{A}$ and $\vec{B}$ direction, respectively, and *n* and *m* are the number of scattering planes in the $\hat{A}$ and $\hat{B}$ direction, respectively. The reciprocal lattice vector is then equal to

$$\vec{G}_{nm}=m\vec{A}+n\vec{B}=\frac{2\pi}{\vec{L}_{nm}} \tag{4.23}$$

From equation 4.21, the magnitude of the primary reciprocal lattice vectors is equal to $\left|\vec{A}\right|=\left|\vec{B}\right|=\frac{2\pi}{L}=\frac{4\pi}{a\sqrt{3}}$, so that $\vec{A}=\frac{4\pi}{a\sqrt{3}}\hat{A}$ and $\vec{B}=\frac{4\pi}{a\sqrt{3}}\hat{B}$. For simplicity, we only consider first order scattering

(scattering off neighbouring voids only). A single void is surrounded by 6 neighbouring voids. This 6-fold symmetry of the 2D hexagonal lattice allows scattering off neighbouring voids to occur along any of the 6 directions, yielding 6 scattering solutions. Figure 4.7(iii) shows the first set of reciprocal lattice vectors $\vec{G}$ for a 2D hexagonal lattice.

Resonant coupling between far-field radiation and Bragg modes occurs when momentum and energy are conserved. Consider light of wavevector $\vec{k}_0$, incident at an angle θ to the normal, with in-plane light wavevector equal to $k_0 \sin\theta$. From Figure 4.8(i)) it can be seen that provided energy is also conserved, the incident light excites a Bragg SPP that will propagate in the direction

$$\vec{k}_{SPP} = \vec{k}_0 \sin\theta + \vec{G}_{nm} \qquad (4.24)$$

From equation 4.24 it can be seen that the 6-fold symmetry of the 2D hexagonal lattice allows incident light to be scattered into one of 6 different reciprocal lattice directions, $\vec{G}_{nm}$, exciting one of 6 possible Bragg modes (Figure 4.8(i)). Using equation (4.24), the wavevector and energy of the excited Bragg SPP are related via[21]

$$E(\theta,\varphi) = \hbar c \sqrt{\varepsilon_m^{-1}(E) + \varepsilon_d^{-1}}\, f(\varphi) \left| \vec{k}_0 \sin\theta + \vec{G}_{nm} \right| \qquad (4.25)$$

where *f(φ)* is a function that accounts for the dependence in sample orientation of the ingoing beam on the 6-fold symmetric surface, φ is the azimuthal angle of the 2D grating (Figure 4.6), ε_d is the dielectric constant of medium above the metallic surface and $\varepsilon_m(E)$ is the energy dependent complex dielectric function of gold. The solutions to equation (4.25) give the allowed plasmon modes that can be excited by the incident light. Equation (4.25) predicts that the SPP mode energy can be tuned with sample pitch a (via the grating vector $\vec{G}_{nm}$ (equation (4.24))), the incidence angle (θ) and sample orientation (azimuthal angle φ) (Figure 4.8(i) and (ii)). Equations (4.24) and (4.25) predict energy degeneracy for SPP that have the same magnitude in wavevector k_{SPP}, which has been

experimentally verified (Figure 4.8(i) and (iii)). In general, the weak-scattering model agrees well with experimental results (Figure 4.8(iii)).

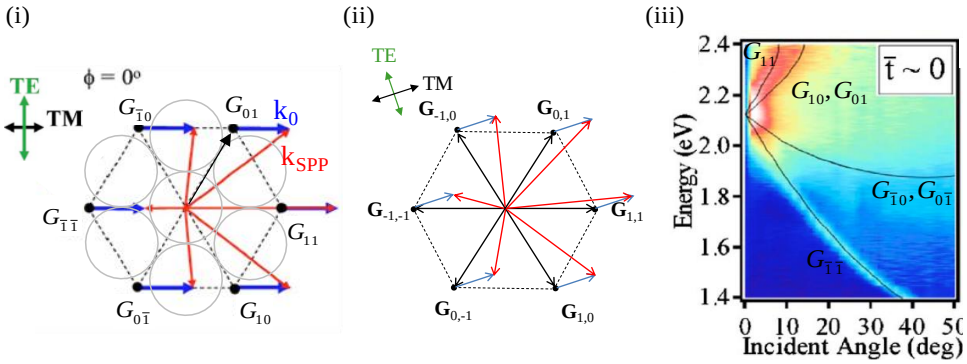

Figure 4.8: Coupling of Delocalised Bragg Plasmons with Light (i and ii) wavevector diagram at φ= (i)0°and (ii) 15°, showing the in-plane wavevector component of the incident light (blue),the first order grating vector, G_{nm}, (black) and the excited Bragg SPP (red) (adapted from (i)[21] and (ii)[288]) (iii) experimental (coloured) and theoretical (black lines) Bragg plasmon dispersion relation for thin substrate (normalised thickess ~0), red/blue signifies strong/weak absorption of incident light due to strong/weak coupling of incident radiation into Bragg plasmons modes(adapted from[21]).

The geometry of the 2D lattice allows not only allows TM polarised light, as on a 1D surface, but also TE polarised light, to excite Bragg SPP: incident light must have an electric field component parallel to the SPP propagation direction in order to couple to a SPP mode (section 4.2.1). Bragg SPP coupling with TM and TE polarised light is best illustrated with an example. Figure 4.8(ii) shows all 6 first order grating vectors, *G*, of the 2D hexagonal lattice (black line) and the in-plane wavevector, k_0, of light incident at $\varphi=15°$ (blue line). Wavevctor conservation (equation (4.24)) yields 6 possible SPP propagation directions, each being the vector sum of k_0 and *G* (Figure 4.8(ii), red arrows). In this case, TM polarised incident light has a large electric field component along the propagation direction of the *(n,m)=(1,1)* and *(n,m)=(-1,-1)* Bragg modes, while TE polarised light has a large electric field component along the propagation direction of *(n,m)=(-1,0)* and *(n,m)=(1,0)* Bragg modes (Figure 4.8(ii)), allowing efficient excitation of the particular SPP mode by the respective polarisations to occur.[288] The electric field overlap with the propagation direction of the *(n ,m)=(0,1)* and *(n,m)=(0,-1)* Bragg mode is similar for both TE and TM incident light, yielding similar coupling efficiencies for both polarisation states (Figure

4.8(ii)).[288] Thus, TE and TM polarised incident light has different electric field alignment relative to the SPP propagation directions, so that the SPP excitation efficiency depends on the polarisation state of the incident light and the SPP propagation direction.[21]

4.2.2.2 Mie Plasmon Modes

Within a 2D hexagonal lattice of gold nanovoids, Mie plasmons are surface plasmon polariton modes localised within the nanovoid volume (Figure 4.6 in section 4.2.2). As Mie modes within neighbouring nanovoids couple only weakly, inter-void coupling can be neglected and only a single nanovoid considered when modelling Mie SPP. Mie modes predicted within a single isolated nanovoid agree relatively well with experimental results[22] The Mie modes are simulated by modelling the electric field within a single nanovoid. First the Mie modes of a fully encapsulated nanovoid are considered, before the effect of void truncation is explained.

4.2.2.2.1. Fully Encapsulated Voids

A fully encapsulated void forms a dielectric spherical cavity within an infinite expanse of gold, and has normalised thickness equal to $\bar{t} = 1$. The electromagnetic modes of a single dielectric sphere fully encapsulated within a metal can be obtained by solving Maxwell`s equations in spherical coordinates, with appropriate boundary conditions, which gives a set of equations (equation C.83 in appendix C.8).[21, 287] The solutions to these equations give the electromagnetic modes. The same set of equations and hence solutions/electromagnetic modes are obtained by Mie theory, which describes the scattering of plane waves off a dielectric sphere encapsulated within a metal.[287] The electromagnetic modes (Mie modes) have energies that depend on the sphere radius R and the dielectric function of dielectric sphere and the surrounding metal. The quantum numbers *l=1, 2…= P, D…*(angular momentum) and *m=0,1…*(azimuthal) can be assigned to each Mie mode, and for each Mie mode the electric field distribution within the dielectric sphere resembles that of the spherical harmonic function $Y_{(l\text{-}1,m)}$. As an example, the modelled electric field profile for the

lowest Mie modes *l=1 (P)* are shown in Figure 4.9(i), showing that the *l=1 (P)* Mie mode has a p-like dipole charge oscillation within the surrounding metal, but a s-like (*l=0*) single-peak intensity distribution within the void. From symmetry arguments, the *l = 0 (S)* mode cannot exist in a dielectric cavity.[22]

(i) (ii)

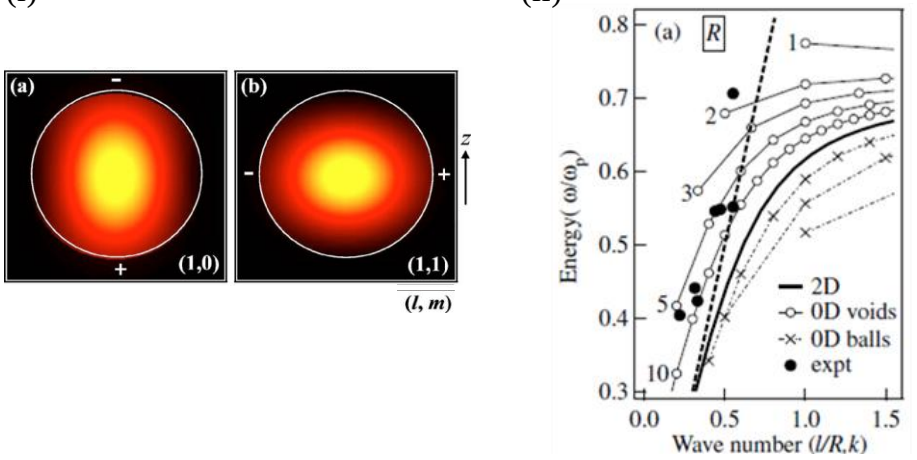

Figure 4.9: (i) Modelled electric field distribution of Mie plasmon modes (l, m) in a dielectric void fully encapsulated within a metal[21] (ii) Mie plasmon dispersion relation according to Mie theory, R is the void radius, l/R has dimensions of wavenumber k, the plotted dispersions are 2D SPP (thick line), photon in air (dashed line), Mie plasmons in dielectric voids in expanse of gold according to Mie theory (white circle) and gold spheres (crosses). Each curve for spheres and voids corresponds to a different radius R. Voids: lines 1,2,3,5,10 are voids of increasing radius.[289]

With increasing angular momentum *l*, the Mie modes become increasingly confined to the metal surface (appendix C.8). The energy of the Mie modes (*l, m*) increases with *l*, but is energy degenerate with respect to m due to spherical symmetry of the fully encapsulated dielectric cavity.[289] The dispersion relation of Mie modes in a fully encapsulated dielectric cavity can be derived, by noting that the wavevector *k* is equal to *l/R* (appendix C.8), where *R* is the sphere radius, and by using the solutions to Maxwell`s equations for the energy of the Mie modes. The Mie plasmon dispersion is plotted for dielectric cavities of different sizes (Figure 4.9(ii)), showing that relative to Bragg SPP modes on a flat 2D surface, the dispersion relation of Mie plasmons in a fully encapsulated void is blue-shifted. The blue-shift increases as the void radius decreases, that is, the more the void deviates from a flat metal surface. The origin of the blue-shift has been rationalised by the increased confinement/concentration of the electric field

lines within the dielectric sphere (appendix C.8)[289] compared to a flat metal surface. An important consequence of the blue-shift is that, unlike Bragg SPP, part of the Mie plasmon dispersion in dielectric spheres is located within the radiative region of the dispersion graph (i.e. left to the light line) (Figure 4.9(ii)), allowing strong and direct coupling between Mie plasmons and an incident optical waves to occur.[289] In contrast to dielectric spheres, metal particles have a dispersion relation that is red-shifted relative to that of Bragg SPP on a flat surface, and the red-shift increases with reduced particle size (Figure 4.9(ii)). As we have just seen, in contrast to metal particles, dielectric voids show a high coupling efficiency with incident plane waves, as well as high structural stability within the metal surrounding, making voids suitable for use as plasmonic substrates. However, in order to couple light into the voids, the voids must open up to a dielectric medium.

4.2.2.2.2 Truncated Voids-the Boundary Element-Method

Although Mie theory accurately describes Mie modes in fully encapsulated voids with $\bar{t} \approx 1$, Maxwell`s equations cannot yet be solved analytically in the case of $\bar{t} < 1$,[22] and thus require the use of alternative models for Mie plasmons within truncated voids. Among the models developed for truncated voids is the 1D standing wave model[21] (appendix C.10), as well as the more accurate Boundary Element Method (BEM).[290, 291, 296] The Boundary Element Method expresses the electromagnetic field in terms of charges and currents on the metal surface as a result of an incident plane wave,[290] and assumes a frequency-dependent dielectric constant for the metal,[291] (according to the Drude model). The voids are parameterised with the normalised thickness defined as $\bar{t} = d/2R$; here d is the metal film thickness and R is the void radius (Figure 4.6 in section 4.2.2). Modelling requires the following parameters to be set/input: the void thickness, void diameter, and the upper rim rounding, *s*, as well as the incident wave energy, polarisation state and angle of incidence θ (Figure 4.6 in section 4.2.2). Using the BEM, Mie plasmons in truncated voids can be simulated in two ways (a) Mie mode energy as a function of void

truncation (Figure 4.10(ii)) in terms of the absorption cross section, and (b) the 2D spatial distribution of the electric field intensity $|E|^2$ of particular Mie modes in the z-x or z-y plane (Figure 4.10(iii)), where z is the vertical dimension and x and y are the two orthogonal horizontal dimensions (Figure 4.10(i)), and E is the Mie plasmon electric field amplitude normalised to the electric field amplitude of the incident plane wave. As in the Mie scattering model, the BEM model assigns each Mie mode the quantum numbers l (angular momentum) and m (azimuthal), where $l=1, 2\ldots=P, D\ldots$and $m=0, 1,\ldots$ Each Mie mode can then be labelled ${}^{m}L={}^{0,1\ldots}P,D,F\ldots$(Figure 4.10(ii). While m is specified as an input parameter, the quantum number l is assigned to each mode from Mie theory solutions for fully encapsulated voids of equivalent radius (Figure 4.10(ii)).

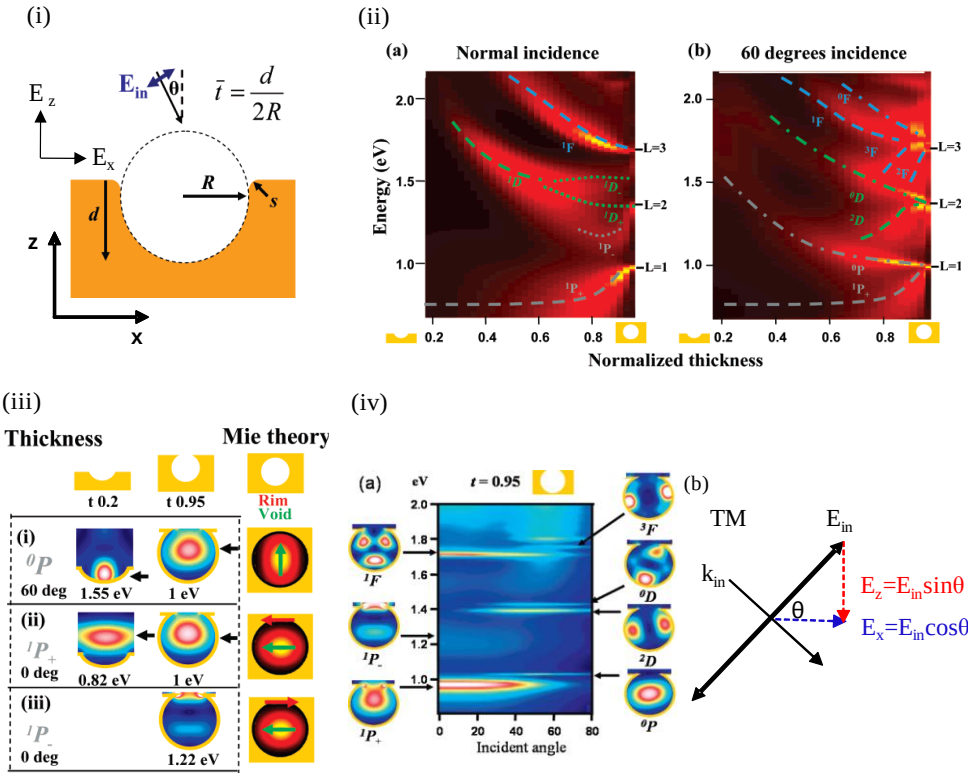

Figure 4.10: Mie plasmon modes modelled in truncated voids by the Boundary Element Method (i) parameterisation of the void and incident plane wave (ii) modelled absorption for R=500nm voids at (a) normal incidence (b) 60° incidence, dashed lines are guides to the eye[22] (iii) modelled 2D electric field distribution of Mie modes ${}^{m}L$=(i) ${}^{0}P$ and (ii and iii) ${}^{1}P$. To the right are indicated the electric field alignment of the void Mie modes (green) and rim modes (red).[22] (iv)(a) modelled dispersion relation of ${}^{m}L$ Mie modes for a void of radius R=500 nm and normalised thickness=0.95[22] (iv)(b)Electric field components of TM polarised incident light, k_{in} is the incident wave wavevector, E_{in} is the electric field of the incident wave, θ is the incident angle to the normal, E_x and E_z is the field component in the horizontal x and vertical z direction, respectively.

Figure 4.10(ii) shows the modelled energy dependence upon void truncation exemplified for *R=500 nm* voids, showing clearly the evolution in Mie mode energy with truncation, and, as $\bar{t}$ approaches 1, spectral narrowing towards the Mie solutions for fully encapsulated but otherwise equivalent voids. The energy- evolution of each Mie mode with truncation depends upon the field distribution of the particular mode.[22]

Figure 4.10(ii)(b) also shows that the energy degeneracy that exists in a fully encapsulated void for different m-modes is lifted upon void truncation. Furthermore, in truncated voids, charge build-up at the rim occurs, which form rim dipole modes with *m=1* symmetry of the electric-field vector. These rim modes strongly couple to *m=1* Mie void modes, splitting the *m=1* Mie mode into high and low energy modes, such as $^1P_+$ and $^1P_-$, respectively, in the case of the ^1P mode (Figure 4.10(ii)(a)).[22] The efficiency at which the split Mie modes couple to an optical field depends on the relative alignment of the electric field vector of the Mie mode and rim mode: parallel alignment, as occurs for the lower-energy $^1P_+$ mode, results in an enhanced field and thus strong optical coupling, while antiparallel alignment, as occurs for the higher-energy ^1P- mode, results in weak optical coupling (Figure 4.10(ii)(a) and (iii)). Thus, truncation allows *m=1* modes to couple to rim modes, which produce a lower energy state that couples strongly to an optical field.[22]

Localised Mie modes are non-dispersive, that is, their energies are invariant with the incident angle (Figure 4.10(iv)(a)). However, each Mie mode most strongly couples to an optical field at certain incident angle (Figure 4.10(iv)(a)). For instance, the ^1P mode and ^1F mode strongly couple to normally incident light, while the ^0P mode strongly couples to non-normally incident light (Figure 4.10(iv)(a)). This angle dependence is explained by the relative alignment of the electric field vector of the Mie mode and the incident light. For instance, the electric field vector of the ^1P mode is aligned horizontally (Figure 4.10(iii)), which is parallel to the electric field alignment of normally incident TM polarised light, resulting in strong coupling between the two at normal incidence. In contrast, at

higher incident angles the horizontal electric field component of the incident light decreases, reducing the coupling efficiency (Figure 4.10(iv)(a) and (iv)(b)). Likewise, the ^{0}P mode has a vertical electric field vector (Figure 4.10(iii)), allowing strong coupling at high incidence angles where the incident light has a strong vertical field component, E_z (Figure 4.10(iv)(a)).[22]

4.3 Design of Spherical Gold Nanovoids for Fluorescence Enhancement

In section 4.1.2.2 it is shown how radiative surface-plasmon-polariton modes on a non-flat metal surface can enhance the fluorescence or absorption rate of a nearby emitter, increasing the fluorescence intensity. Mie plasmon modes localised within gold nanovoids can directly couple to far-field radiation (section 4.2.2.2.1). Fluorophores located within the strong Mie field and energetically in resonance with the Mie mode are thus expected to experience fluorescence enhancement either by the enhanced absorption rate or enhanced emission rate mechanism. Following this, it is envisaged that a fluorescently labelled DNA strand stretched over the nanovoid region will experience fluorescence enhancement under the correct resonance conditions between attached fluorophore and Mie plasmon mode. As the Mie plasmon energy and electric field distribution within or just above the nanovoid region can be controlled by the exact nanovoid dimensions[292] (section 4.2.2.2.2), in this chapter gold nanovoids are designed that yield Mie modes that would allow fluorescence enhancement to occur for TOTO-1 fluorophores associated to DNA and then stretched over a gold nanovoid substrate (section 4.5.3). TOTO-1 is being used as the fluorophore of choice as it has a high binding affinity to DNA and it shows a high contrast of florescence emission efficiency between DNA-bound TOTO-1 and free TOTO-1 (section 4.4.2).

Nanovoids are grown using an electroplating template method, in which the size of the template spheres determines the final void diameter (section 4.4.1). For void growth, polystyrene spheres with diameter of 500 nm, 780 nm, 989 nm and more than 2 μm are commercially available. However, experiments have shown that 500 nm spheres do not self-assemble into a single monolayer or ordered array easily by the methods available (section 4.5.1.1.2), and are therefore not suitable for use in void growth. Similarly, spheres larger than 2 μm might be too large to allow

Lambda-phage DNA strands, which have a fully extended length of about 16.5 µm, to be stretched over nanovoids without sinking into the void volume (Figure 4.11). Thus, the Mie plasmon modes of 780 nm and 989 nm diameter voids are modelled in detail in this chapter.

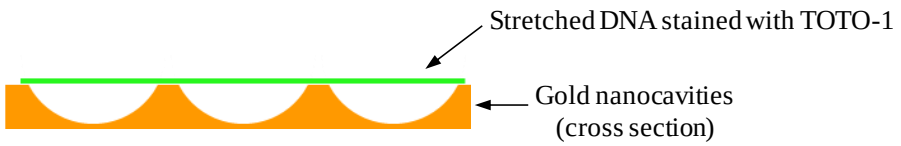

Figure 4.11: Envisaged fluorescence enhancement setup: a TOTO-1 stained DNA strand (green) is stretched over and located above a Mie plasmon substrate consisting of a 2D-array of spherical gold nanovoids (orange).

The nanovoid material is chosen to be gold, as, unlike other metals, it does not oxidize in the presence of water and/or oxygen, ensuring long-lasting substrate stability. This is because oxidation produces a thick oxidation layer, which increases the spatial separation between emitter and metal surface, reducing the efficiency with which fluorophores can interact with the surface plasmon polariton modes.

4.3.1 Requirements for Mie Plasmon-induced Fluorescence Enhancement of TOTO-1

SPP induced fluorescence enhancement occurs either via an increase in the absorption rate or the emission rate of the fluorophore in question (section 4.2.2.2.2 and 4.2.2.2.3). In the following argument we assume that SPP are radiative, either due to prism coupling, a metal surface corrugation or because the Mie plasmon mode lies in the radiative part of the dispersion graph. An enhanced absorption rate can be induced when incident light excites resonant SPP modes on a metal surface, which in turn quickly excite a nearby fluorophore when the absorption energy and momentum of the fluorophore is in resonance with that of the SPP. An enhanced emission rate, in contrast, can be induced when incident light excites a fluorophore from the electronic ground state to an electronic excited state, and the excited state fluorophore loses its energy to resonant SPP modes on a nearby metal surface, which occurs when the emission energy of the fluorophore is in resonance with that of the SPP. The excited SPP in turn

quickly re-radiate the excitation energy if the SPP is radiative (section 4.2.1).

The absorption and emission peak of TOTO-1 is located at 2.41 eV (514 nm) and 2.34 eV (531 nm), respectively. SPP are only supported up to certain a maximum energy (section 4.2), which, assuming a surface plasmon energy of gold of $\omega_p = 2.6\ eV$,[293] is theoretically equal to $\varpi_{SPP}^{\max} = 1.56\ eV$ with water as the dielectric medium ($n=1.33$) (equation 4.15 in section 4.2). The maximum energy at which a Mie plasmon mode can exist within a truncated nanovoid is likely to be higher than 1.56 eV, as (1) the Mie plasmon modes in gold nanovoids are shifted above the SPP dispersion curve for a planar surface[289] (Figure 4.9(ii) in section 4.2.2.2.1) and (2) the Mie plasmon mode energy increases with increasing void truncation[22] (Figure 4.10(ii) in section 4.2.2.2.2). Thus, Mie plasmon modes excited at the fluorescence energy, rather than at the higher excitation energy, are modelled here in order to decide on the optimum void dimensions to be used in this thesis for fluorescence enhancement of TOTO-1-DNA. For the experiments, the fluorescence detection range of fluorescently-imaged TOTO-1-DNA stretched over nanovoid substrates is set by the emission filter used in the fluorescence microscope, the transmission range of which lies between 2.26 eV and 2.39 eV, or 550 nm to 520 nm (Figure 4.27 in section 4.4.2.1). For simplicity, Mie plasmons at 2.26 eV will be modelled.

Generally, the SPP-induced enhancement in the spontaneous emission rate of a fluorophore is determined by two factors (a) the in-coupling efficiency, which is the efficiency at which excited state TOTO-1 loses its energy non-radiatively to SPP modes in the plasmon substrate, and (b) the out-coupling efficiency, the efficiency at which SPP re-radiate the excitation energy[259, 260] (appendix C.3). A high in-coupling efficiency occurs when the excited state fluorophore (i) is located within the electric field of a Mie plasmon mode (spatial overlap), and (ii) is energetically in resonance with a Mie plasmon mode. Also, a high Mie plasmon density of states compared to the photonic density of states in free space increases the

in-coupling rate (equation 4.12 in section 4.2.2.2.2). The density of states is inversely proportional to the gradient of the dispersion curve. As the gradient of the dispersion curve of Mie plasmon modes within a given void size is smaller than that of far-field radiation in free space (Figure 4.9(ii) in section 4.2.2.2.1),[294] an excited-state fluorophore within the electric near-field of a Mie plasmon mode is expected to quickly transfer the excitation energy to the Mie plasmon mode rather than fluoresce. For TOTO-1-DNA stretched over a gold nanovoid substrate, spatial overlap means that the electric field of the Mie mode should extend to where the TOTO-1-DNA is located, which is just above the void top, and that the Mie mode should have energy equal to the fluorescence energy of TOTO-1 in the microscope detection range, which is between 2.26 and 2.39 eV. For efficient out-coupling, the Mie plasmon mode must emit efficiently and experience little non-radiative loss.[295] The radiation efficiency of a Mie plasmon mode is related to the efficiency at which a far-field incident wave couples to that same Mie mode.[261] The Boundary Element Method (BEM) is used to model Mie modes excited by an incident plane wave (section 4.2.2.2.2), and provide models for the radiative Mie modes. The energy and emission angle of radiative Mie modes is determined by energy and wavevector conservation, respectively. Non-radiative loss of SPP, on the other hand, scales with the SPP energy (equation 4.16 in section 4.2), and the SPP energy must be in resonance with the TOTO-1 fluorescence energy. Thus, SPP loss depends on the fluorophore used, and is therefore independent of the void geometry.

4.3.2 Mie Plasmon Modes in 780 nm and 989 nm Diameter Gold Voids

The Boundary Element Method (section 4.2.2.2.2) is used to model the Mie plasmon mode energies as a function of void thickness (d), and the 2D spatial distribution of the electric field of Mie plasmon modes at 2.26 eV. The truncated voids are parameterised as having a diameter of either $D_{void}=780\ nm$ or $D_{void}=989\ nm$, with a metal film thickness d, normalised

void thickness equal to $\bar{t} = \frac{d}{D}$, and rounding upper rim equal to *s=10 nm*, although the electric field profile and absorption cross-section is independent of s for *s<100 nm*.[22] The DNA is stretched over the nanovoid substrate in water, so that the refractive index of the void volume is set to that of water, which equals *n=1.33* (at 20°C). The dielectric constant of gold is energy dependent in accordance with the Drude model.[296] The incident plane wave is set to a p-polarised state. For a first approximation for the modes present in D_{void}*=989 nm* and D_{void}*=780 nm* voids, the incidence angle is set to θ*=0°*, for which *m=1* modes exist but *m=0* modes are not excited due to the electric field alignment of those modes (section 4.2.2.2.2).[22]

4.3.2.1 Variation of Mie Plasmon Mode Energy with Void Truncation

Figure 4.12 shows the Mie plasmon modes in 780 nm and 989 nm diameter voids immersed in water, at normal incidence, as modelled by the BEM. Indicated to the right of each graph is the angular momentum index of the Mie modes in fully enclosed voids of the same radius (appendix C.9). The evolution in energy with void truncation is clearly seen in both void diameters. The rise in energy with increasing void truncation can only be explained by an intuitive model, according to which the Mie modes in truncated voids resemble those in a fully enclosed void at normalised thickness near 1, but approach the 2D SPP dispersion with increasing truncation.[22] Compared to in the 780 nm void, in the 989 nm diameter void the Mie modes have lower energy. This reduction in energy with increasing void diameter can be explained by the standing wave model (appendix C.10) in terms of a larger void diameter increasing the rim-to-rim distance of the void, which increases the wavelength of resonant modes within the void.

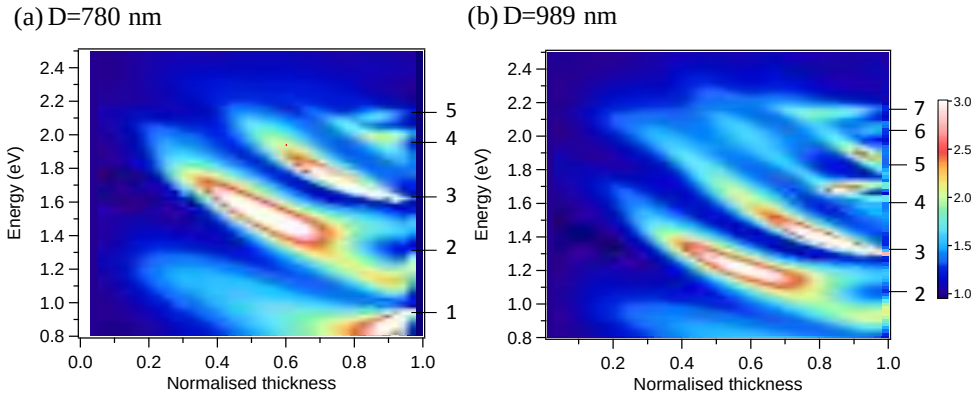

Figure 4.12: Normalised absorption (Mie modes), modelled by BEM, at normal incidence, for water-immersed voids of diameter (a) D_{void}=780 nm and (b) D_{void}=989 nm. To the right of each image are indicated the angular momentum indices, l, of Mie modes as predicted by Mie theory for equivalently fully enclosed voids.

Due to this energy shift in resonant modes with void diameter, the larger D_{void}=*989 nm* diameter void supports higher angular momentum Mie modes compared to the smaller D_{void}=*780 nm* diameter void (Figure 4.12). In both void sizes, energy splitting of the *l=2* and *l=4* modes is observed upon void truncation, which is attributed to mixing with *m=1* rim modes[292] (section 4.2.2.2.2). The coupling strength of the split mode with far-field radiation differs between the lower and higher energy split mode (Figure 4.12): consider, for instance, the *l=2* mode: for the lower energy mode, the coupling is strong due to parallel alignment of the electric field of the Mie mode relative to that of the rim mode, while in the higher energy mode antiparallel alignment leads to weaker coupling[22] (section 4.2.2.2.2).

From Figure 4.12 it is evident that coupling between the Mie modes and far-field radiation is strongest below about 2.2 eV. At 2.26 eV and above, only weaker coupling occurs. Furthermore, the coupling efficiency between far-field radiation and Mie plasmon modes is very strong for normalised thickness exceeding 0.6 for both void sizes. An exception is the *l=2* Mie mode, in which case the strongest coupling occurs for a normalised void thickness of between 0.3 and 0.8. However, for excited state TOTO-1 to efficiently excite Mie modes, the Mie modes, must, in addition to being in resonance with the TOTO-1 emission energy, be located outside or just above the nanovoid to allow spatial overlap with the

TOTO-1-DNA that is stretched over the nanovoid volume. From Figure 4.12 the energies of Mie plasmon modes at specific film thickness can be read off, allowing then the electric field profile of the Mie mode energies at various void thicknesses to be simulated.

4.3.2.2 Variation of Mie Plasmon Electric Field Profile with Void Truncation

In Figure 4.13 are the modelled 2D spatial distribution of the Mie Plasmon field intensity, $|E(r)|^2$, within 780 nm and 989 nm diameter truncated nanovoids immersed in water. *E(r)* is the Mie plasmon electric field amplitude normalised to that of the incident plane wave, so that $|E(r)|^2$ represents the enhanced Mie SPP field with respect to the incident wave.

First the electric field profile of Mie modes in a 780 nm diameter void is analysed. At very high normalised thicknesses ($\bar{t} \geq 0.9$), the Mie modes are confined within the nanovoid volume (Figure 4.13(a)(iii), (a)(v) and (a)(vi)) and/or at the rounding upper rim (Figure 4.13(a)(i), (a)(iii), and (a)(iv)). As the void is increasingly truncated, the Mie modes extend further into the space above the void, which is clearly seen for the *l=2* mode (Figure 4.13(a)(i)). Also, at a given void truncation, those Mie modes with lower angular momentum (and hence lower energy) extend more into the space above the void volume and have a stronger electric field outside the void volume than higher energy modes. This increase in Mie mode confinement with Mie mode energy can be clearly seen when comparing the *l=2* and *l=3* modes at normalised thicknesses of 0.3 to 0.5 (Figure 4.13(a)(i) to (a)(iii)). As a result, modes with angular momentum larger than 3 are mostly confined within the nanovoid volume (Figure 4.13(a)(iv) to (a)(vi)).

(a) 2R = 780 nm

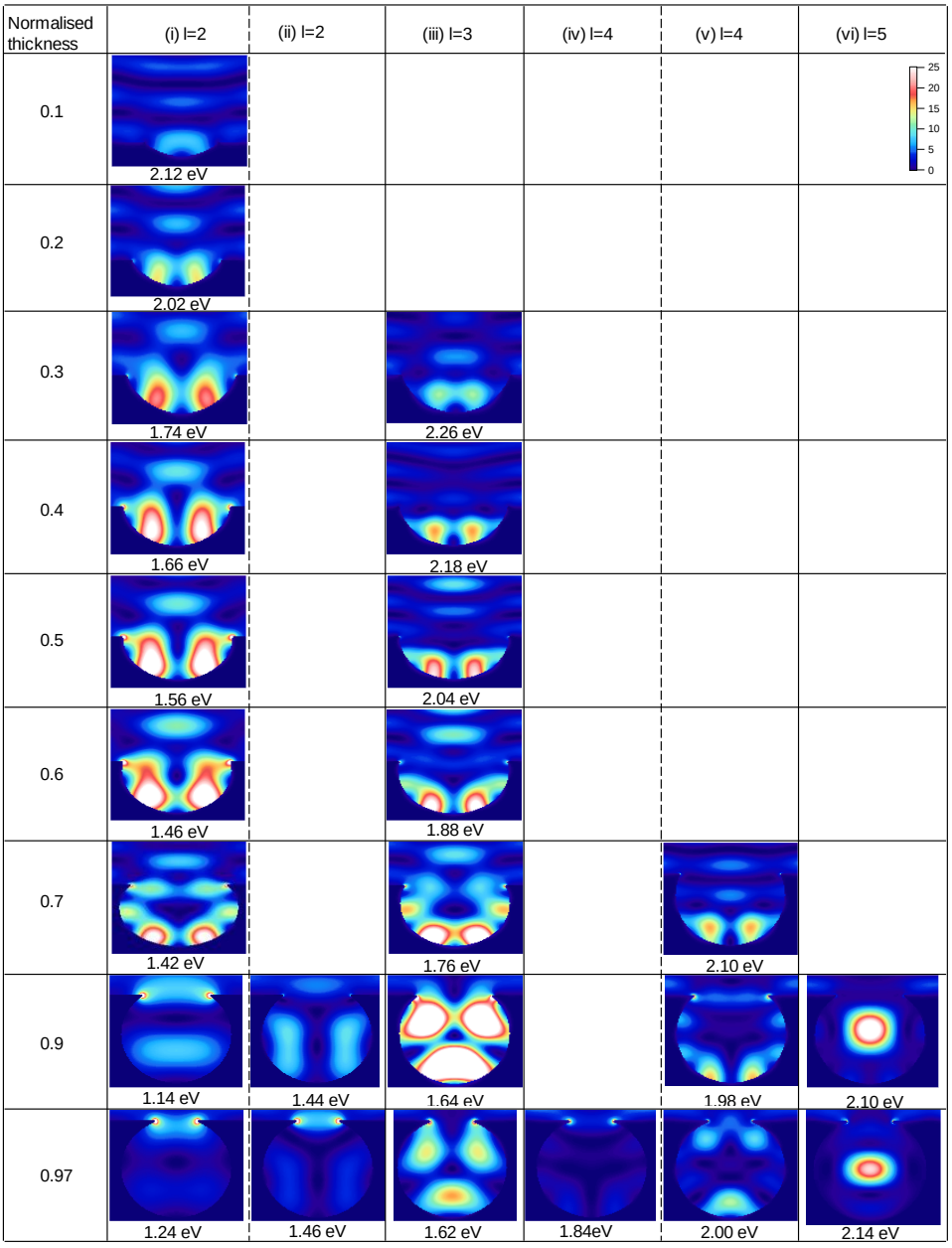
Normalised thickness
(i) l=2
(ii) l=2
(iii) l=3
(iv) l=4
(v) l=4
(vi) l=5
25
20
15
10
5
0
0.1
2.12 eV
0.2
2.02 eV
0.3
1.74 eV
2.26 eV
0.4
1.66 eV
2.18 eV
0.5
1.56 eV
2.04 eV
0.6
1.46 eV
1.88 eV
0.7
1.42 eV
1.76 eV
2.10 eV
0.9
1.14 eV
1.44 eV
1.64 eV
1.98 eV
2.10 eV
0.97
1.24 eV
1.46 eV
1.62 eV
1.84eV
2.00 eV
2.14 eV

(b) 2R = 989 nm

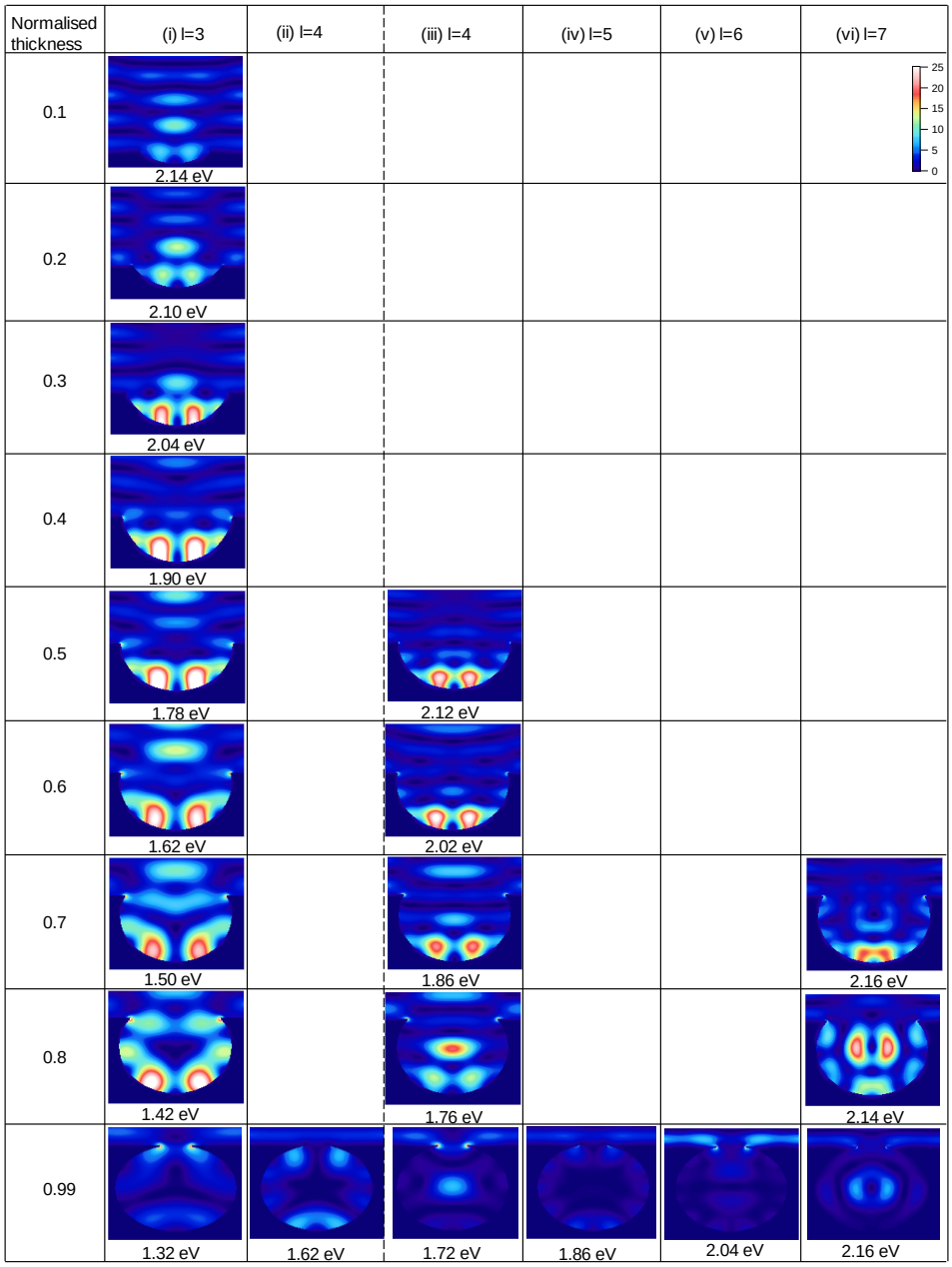

Figure 4.13: Modelled 2D profile of the square of the magnitude of the electric field of Mie modes, normalised to the incident field at normal incidence, for various void thicknesses of water-filled voids of diameter (a) D_{void}=780 nm and (b) D_{void}=989 nm, Modelling was by BEM.

For the 989 nm diameter voids, the same general observation can be made as for 780 nm diameter voids, in other words (a) void truncation leads to a reduced confinement of the Mie mode within the nanovoid volume (Figure 4.13(b)(i)), an increase in the Mie mode energy (Figure 4.13(b)(i)) and a weakening in the Mie field intensity (Figure 4.13(b)(i)). Also, modes with lower angular momentum extend further into the space above the void

volume at any given truncation (Figure 4.13(b)(i) and (b)(iii)), and modes with *l>3* have very little field outside the void volume (Figure 4.13(b)(ii) to (b)(vi)). The main difference between 989 nm and 780 nm diameter voids is that the Mie modes in the smaller diameter void are higher in energy than the same modes in the larger diameter void. For instance, at normalised thickness $\bar{t} = 0.3$, the *(m, l)=(1, 3)* mode has energy equal to 2.26 eV (D_{void}*=780 nm*) and 2.04 eV (D_{void}*=989 nm*). However, for that particular mode at that particular void thickness, it is in the D_{void}*=989 nm* void that the Mie field intensity above the nanovoid volume is stronger (Figure 4.13(a)(iii) and (b)(i)).

In order to enhance fluorescence of TOTO-1-DNA located above the nanovoid volume, the void must support a Mie plasmon mode at 2.26 eV that also extends to outside the void volume. Thus, the next step is to plot the electric field profile of Mie modes in 989 nm and 780 nm diameter voids at 2.26eV.

4.3.2.3 Mie Mode Electric Field Profile at 2.26 eV

Figure 4.14 shows the 2D intensity profile of Mie modes, as modelled by BEM, at 2.26 eV for 989 nm and 780 nm diameter voids. In both void diameters it can be seen that at 2.26 eV, as the void is increasingly truncated, the modes become less confined within the void volume, tending to yield stronger fields above the nanovoid volume, but also the maximum Mie field intensity and thus the maximum coupling strength between Mie mode and far-field radiation reduces with truncation. For efficient Mie plasmon out-coupling, efficient coupling to far-field radiation and thus strong Mie field intensities are required. Generally, and at a given void truncation, at 2.26 eV the larger diameter 989 nm void consistently shows stronger maximum Mie field intensities than the smaller 780 nm void (Figure 4.14). For instance, at truncations of $\bar{t} = 0.3$ and $\bar{t} = 0.2$, the maximum field intensity is equal to 14.2 and 13.1 (D_{void}*=989 nm*) and 11.8 and 8.9 (D_{void}*=780 nm*) (Figure 4.14(b)(ii), (b)(iii) and (a)(i), (a)(ii)). Thus, 989 nm voids are better suited for efficient Mie plasmon out-coupling at 2.26 eV than 780 nm voids.

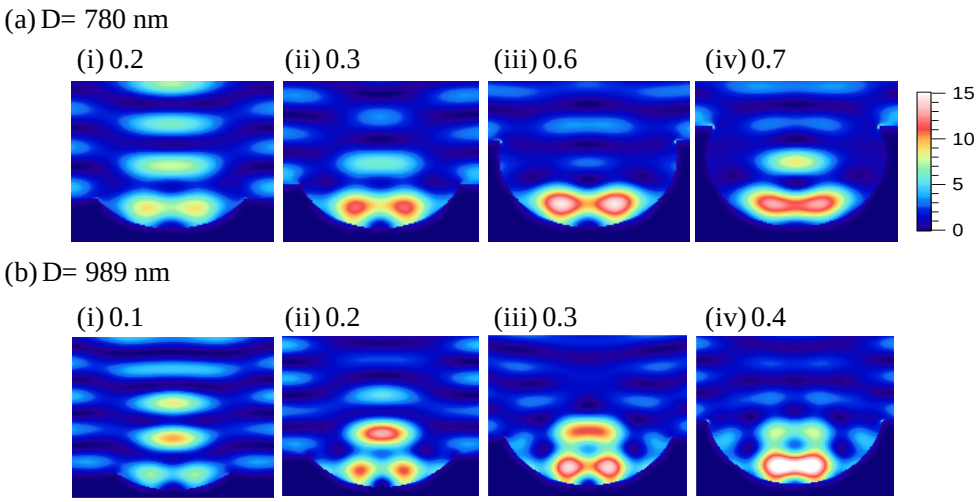

Figure 4.14: Modelled 2D profile of the square magnitude of the Mie plasmon electric field, normalised to the incident field, at 2.26 eV, for voids of diameter D_{void}= (a)780 nm and (b) 989 nm, at normalised void thicknesses of: (a)(i)0.2 (a)(ii) 0.3(a)(iii) 0.6 (a)(iv) 0.7 and (b)(i)0.1 (b)(ii) 0.2(b)(iii)0.3(b)(iv) 0.4; normal incidence, m=1, in water. Modelling was by BEM.

For efficient Mie plasmon in-coupling at 2.26 eV, spatial overlap between excited fluorophore and Mie mode requires the 2.26 eV Mie mode to extend to just above the nanovoid volume, where the stretched out TOTO-1-DNA is located. Both the 780 nm and 989 nm voids show stronger Mie field intensities above the nanovoid volume with increasing void truncation (Figure 4.14). However, the Mie field intensities above the nanovoid volume are stronger in the 989 nm void compared to in the 780 nm void. For instance, the maximum field intensity above the void top plane (i.e. *z>0*) for truncations of 0.3 and 0.2 is equal to 11 and 13 (D_{void}*=989 nm*) at *z=33 nm* and *z=125 nm*, and 6 and 8 (D_{void}*=780 nm*) at *z=105 nm* and *z=145 nm*, respectively (Figure 4.14(a)(i), (a)(ii) and (b)(ii), (b)(iii)). It is also apparent that at any given void truncation the modes in the larger 989 nm diameter void are located nearer to the top void plane than modes in the 780 nm void. In 989 nm voids of truncations 0.4, 0.3, 0.2 and 0.1 the maximum field intensity in the top void plane (*z=0*) is equal to 4, 10, 5 and 7, respectively (Figure 4.14(b)). In 780 nm voids, and truncations of 0.7, 0.6, 0.3 and 0.2, the maximum field intensity at *z=0* is equal to 3, 1.4, 2 and 6, respectively (Figure 4.14(a)). Thus, at 2.26 eV, in general a stronger Mie field intensity exists nearer to and at the top void plane in truncated

989 nm compared to in truncated 780 nm voids. Thus, truncated 989 nm voids are expected to yield more efficient Mie plasmon in-coupling from excited state TOTO-1-DNA located above the top void plane than truncated 780 nm voids.

In truncated 989 nm voids, the maximum Mie field intensity above the nanovoid volume for truncations between 0.4 and 0.1 are equal to 4 to 10, at *z=0 nm* to *z=185 nm* (Figure 4.14(b)), with Mie field intensities in the top void plane ranging from 4 at 0.4, up to 10 at 0.3 and 7 at 0.1. In summary, a 2D hexagonal array of 989 nm diameter voids with truncations between 0.1 and 0.4 present a better Mie plasmon substrates for fluorescence enhancement of TOTO-1-DNA stretched above the nanovoids substrate than truncated 780 nm voids.

4.4 Materials and Methods

4.4.1 Spherical Gold Nanovoid Fabrication

The growth of spherical nanovoids involves several steps, which are explained in this chapter. Spherical nanovoids are grown using a template method, in which polymer spheres are used as a template around which gold is grown electrochemically, and their removal yields spherical voids (Figure 4.15). Voids of diameters ranging from several hundred of nanometres to several tens of micrometers can be grown with the template method.[23] The radius of curvature of the voids is dictated by the sphere diameter.

The nanovoids are made up of gold. First, a flat glass substrate was cleaned by sonication under acetone, isopropanol and then deionised water, for 20 minutes each, followed by drying under dry nitrogen gas flow. Then a 20 nm thick layer of chrome was deposited onto the cleaned substrate, which was followed by deposition of a 100 nm thick gold layer. The chrome layer helps gold adhesion to the substrate. Chrome and gold deposition was done using a vacuum deposition technique, which involves placing the substrate and metal under vacuum inside an evaporator (BOC Edwards, E306A) and heating the metal, which results in metal atoms evaporating onto the substrate surface.

The hydrophobic gold substrate was then cleaned by immersion in isopronanol (IPA) for 24 hours, and then made hydrophilic to allow spheres, which are slightly hydrophilic and dispersed in aqueous solution, to settle in an ordered close-packed manner on top of the gold film. This improves the directional order of the sphere lattice. The film was made hydrophilic by surface-functionalizing the gold film with cysteamine thiols. Surface-functionalisation involves immersion of the film in ethanolic solution of 10 mMolar cysteamine hydrochloride for a minimum of 24 hours. The samples were then rinsed under a gentle stream of deionised water and dried under dry argon flow, before they were templated by depositing a monolayer of polymer spheres onto the gold-

coated substrate surface. Templating is described in more detail in section 4.4.1.1. Once the spheres are set on the substrate, gold can be grown electrochemically around the spheres (section 4.4.1.2). Finally, the spheres are removed by immersion of the substrate into DMF for more than 24 hours.

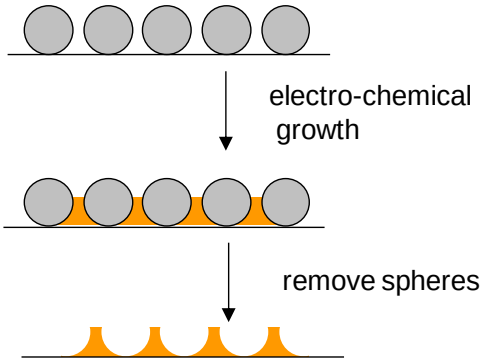

Figure 4.15: Template method for growth of spherical gold nanovoids.

4.4.1.1 Sphere Deposition

The aim is to deposit a monolayer of nanospheres in a close-packed, regular order onto a gold-coated glass substrate for subsequent growth of gold nanovoids. Two methods have been tried to give a close-packed monolayer of spheres, which are (1) the Meniscus method[297] and (2) the Template method.[23] The spheres used were (a) 780 nm diameter, supplied by Duke scientific, carboxylated with parking area (sphere area per carboxyl group) of 51 $Å^2$ per group, 4% solids in water, and (b) 989 nm diameter polystyrene spheres, uncoated (Brookhaven Instruments) and (c) 500 nm diameter carboxyl polystyrene spheres, supplied by Polysciences, 2.65% solid in deionised water, with a coefficient of variance equal to 3%. However, for 500 nm spheres, there is no information on the surface charge density. For the meniscus method, 780 nm spheres were diluted from 4% to 1% into a 50% ethanol-50% deionised water solution. For the template method, 500 nm diameter spheres were diluted to 1% solid in deionised water.

Deposited spheres were imaged with a Scanning Electron Microscope (SEM) (Leo, 1455vp) Deposited sphere samples were prepared for imaging by coating in 6 nm gold layer by a sputterer for better image

contrast, or if used for later electrochemical growth, they were not sputtered.

4.4.1.1.1 Meniscus Method

After cleaning, as described in section 4.4.1, the gold-coated, cysteamine-covered samples are prepared by covering one end of the sample with parafilm for later use as an electrical contact in the electrochemical depositioning step. For this, the sample is placed on top of a pre-cleaned glass slide and heated on a hot plate at about 39°C. The parafilm is placed on top of one end of the gold coated film, and left for a few minutes, and then kept at room temperature for another few minutes to ensure close contact between parafilm and gold surface.

The meniscus method is the deposition method used by Weekes *et al.*,[297] who have deposited polystyrene spheres of diameter 120 to 950 nm, terminated by carboxyl groups and average sphere surface area per carboxyl group (parking area) of 8-120$Å^2$ per group, onto silicon, polymers and metal films. A hydrophobic Teflon bath, consisting of a rectangular Teflon slab with a rectangular volume cut out, is cleaned by rinsing first with isopronanol and then in deionised water. Teflon sliders and sample holders are cleaned by sonication in isopropanol and then deionised water for about 10 minutes each. A detergent coated (1 % w/v of sodium dodecyl sulphate (SDS)) hydrophilic glass slide is also rinsed with deionised water before being used. The setup is shown in Figure 4.16(a). The bottom of the bath is covered with black adhesive tape to improve the visibility of spheres during the deposition stage. The bath is slightly overfilled with 18 MΩ deionised water so that a convex water meniscus forms by surface tension. The samples are then stuck on top of a cylindrical Teflon sample holder using carbon tape, and slowly immersed to below the meniscus level. The hydrophilic glass slide is slowly immersed at one end of the bath and held at about a 45° angle. Any bubbles and impurities inside the water bath are removed using a syringe. The meniscus surface is then cleaned by sweeping Teflon sliders on top of the meniscus several times. The spheres

are inserted by slow pipetting of the sphere solution, in aliquots of 20 to 100 µL, onto the hydrophilic glass slide just above the water level.

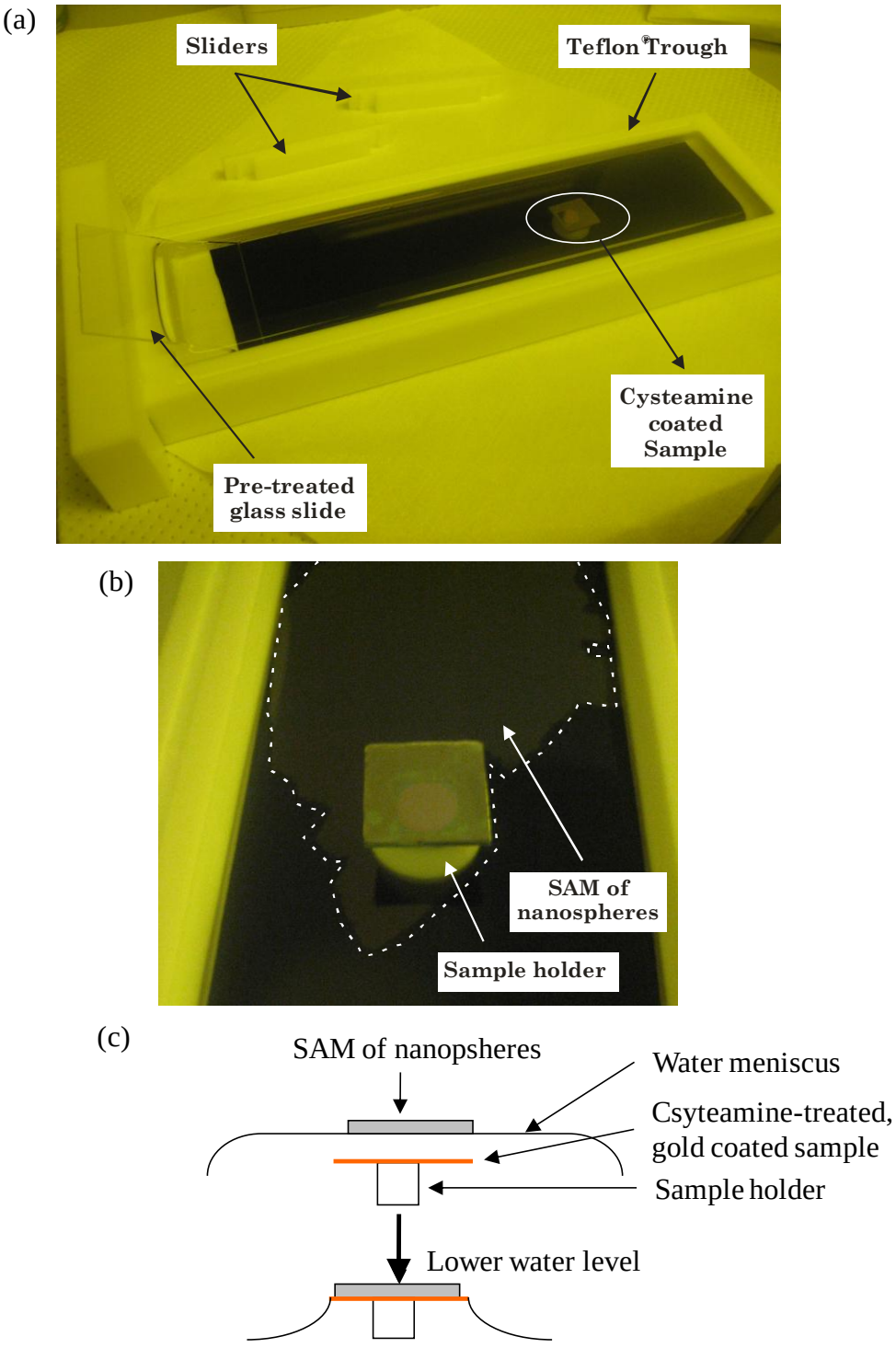

Figure 4.16: Setup of Meniscus method for sphere deposition (a) photograph of Teflon bath with water-immersed sample, pre-treated glass slide and Teflon sliders (b) photograph of self-assembled monolayer (SAM) of nanospheres on top of a water meniscus and water-immersed sample, dotted line shows boundary of SAM (c) drying step (a and b are courtesy of Chien Fat Chau).[298]

The spheres then self-assemble into a monolayer of hexagonally arranged spheres on the meniscus surface. This is repeated until a large enough self-assembled sphere monolayer forms to cover the sample area. The spheres are then compressed into a close-packed lattice by reducing the distance between two Teflon sliders, in contact with the water meniscus, which enclose the sphere lattice. Too strong a compression, however, introduces lattice defects. A visible diffraction pattern allows identification of ordered domains (Figure 4.16(b)). The substrate, which is held under the water surface, is then positioned underneath a defect free area of the lattice using a syringe needle. Water is then slowly removed from the bath, specifically from the area between bath end and a slider to cause minimum disturbance to the lattice, using a syringe. The water is removed until the water meniscus forms on top of the substrate surface (Figure 4.16(c)). The setup is covered to minimize disturbance, and the sample is left to dry. Once the sample is dry, the parafilm is removed from the sample surface by gentle heating at 39°C.

The order of the sphere lattice is very sensitive to the surface charge of the spheres (parking area). Self-assembly into hexagonally arranged sphere lattice is most efficient for a surface charge of about 50$Å^2$/surface group.[297] Two forces influence the order (i) attractive capillary force yields long range order, and (ii) repulsive electrostatic force between spheres provides the spheres with mobility. Both forces arise from a mismatch in the dielectric constant of the water and air at the water-air interface, resulting in an asymmetric charge distribution on spheres at the air-water interface and a resulting dipolar electric field. The dipolar field (a), via electric stress, deforms the water meniscus, producing the attractive capillary force, and (b) produces electrostatic repulsion. Large range order is achieved when a balance between these two forces exist, which can be influenced by the sphere parking area, with optimal order at a parking area of about 50$Å^2$/surface group. A higher parking area has reduced surface charge density and thus reduced repulsion/reduced mobility, resulting in immediate assembly into microscopic domains. The reduced mobility prevents reassembly into a large macroscopic domain. On the other hand, a

parking area of much less than 50 $Å^2$/surface group increases the charge density. The electrostatic repulsion then greatly exceeds the attractive capillary force, resulting in no assembly.

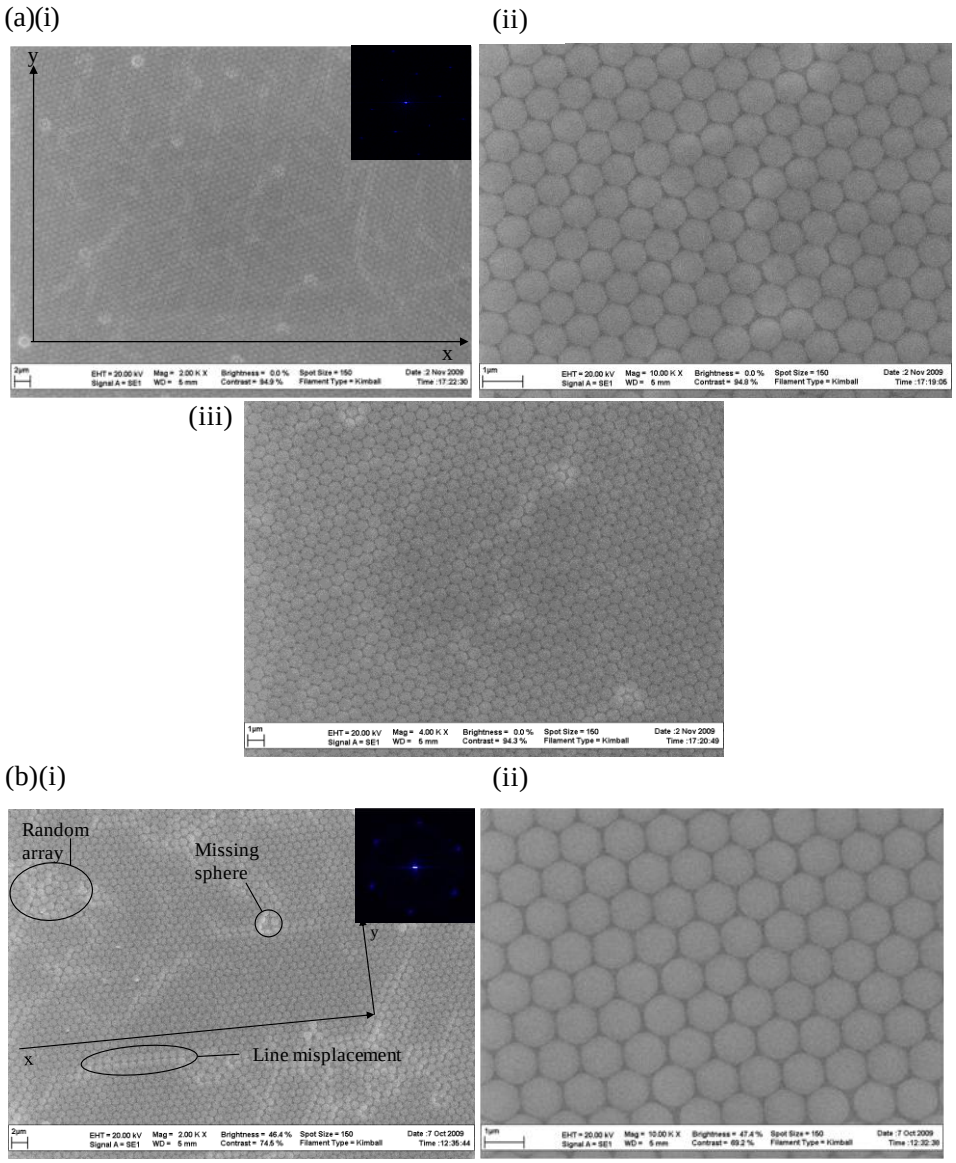

Figure 4.17: SEM images of self-assembled monolayer of polystyrene nano-spheres on a gold substrate, sphere diameter is equal to (a) 780 nm (b) 989 nm; Magnification of (i) 2 k (ii) 10 k (iii) 4 k; Inset: Fourier Transform (FT); lengths: (a)(i) x = 57.1 ±1.1µm, y=35.4 ±0.7 µm and (b)(i) x=52.0 ±1.0 µm, y=14.2±0.3 µm; deposition was by the bath method.

Figure 4.17(a) and (b) show deposited spheres, via the meniscus method, of 780 nm and 989 nm diameter, respectively. The spheres self-assemble in a monolayer with close-packed, hexagonal lattice order. However, defects, such as line dislocations, missing spheres (vacancies) and a random arrangement of spheres are present (Figure 4.17(b)(i)). The lattice of 780 nm spheres generally shows a larger range order/larger defect

free domains than that of the 989 nm spheres. For instance, the defect free area of the 2D lattice made up of 780 nm and 989 nm diameter spheres shown in Figure 4.17(a)(i) and (b)(i), respectively, equals $x*y=2021.3\ \mu m^2$ and $x*y=738.4\ \mu m^2$, respectively. The larger defect free area of the 780 nm diameter sphere lattice can be attributed to the differing surface charge: 780 nm spheres have a surface charge of 50$Å^2$/surface group, very close to the ideal value to achieve maximum order, while 980 nm diameter spheres are not surface-functionalised.

4.4.1.1.2. Template Method

This method uses a template, made of parafilm (Figure 4.18(a)), and was reported by Abdelsalam *et al.*[23] The inner angle is cut to 120°, to match the hexagonal lattice geometry. The template is adhered to the gold substrate by gentle heating at 39°C, and then covered by a glass cloverslip, leaving some space at the top for later insertion of the sphere solution (Figure 4.18(a)).

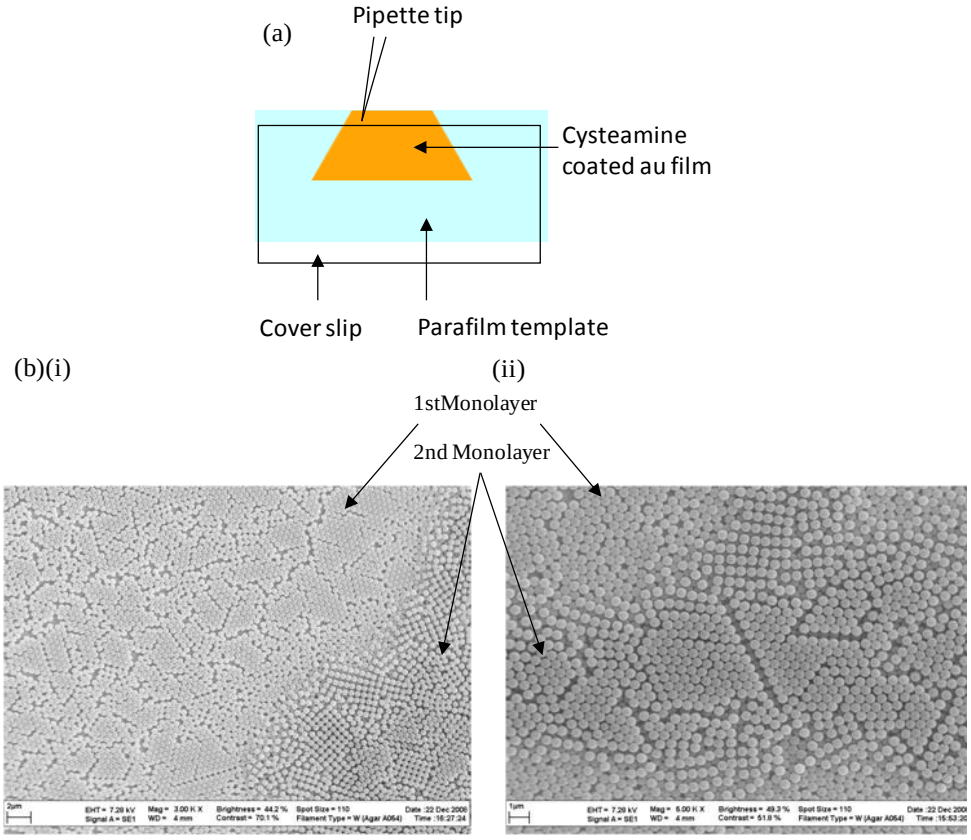

Figure 4.18: Template method for sphere depositioning (a) setup (b) SEM images of deposited spheres, 500 nm diameter, at magnification (i) 3k (ii) 5k.

From the top, the trapezoid is very slowly filled with sphere solution by pipetting. Gentle knocking can help the filling of the edges. Once filled, the sample is stored in an upright position inside a box, with a dampened deionised water soaked tissue inside to reduce the evaporation rate, and left to dry by water evaporation. Once dry, the parafilm template is removed by gentle heating. Figure 4.18(a) and (b) show deposited spheres, via the template method, of 500 nm diameter. The spheres self-assemble into multiple monolayers, with significantly smaller defect free areas than the Meniscus method (Figure 4.18, see Figure 4.17 in section 4.4.1.1.1).

4.4.1.2 Electrochemical Growth of Spherical Gold Mirrors

The growth of thin films by electrochemistry has several advantages. First, it allows precise control of the grown film thickness by controlling the total charge passed to the deposited film. Secondly, the film deposits at a high density around the template, so that the removal of the template will not result in film shrinkage and the resulting film has the exact dimensions of the template. In this case, the sphere diameter directly controls the diameter of the resulting spherical mirror.

An electrochemical cell is a device that converts chemical energy into electrical energy, or vice versa, through an electrochemical reaction. In this thesis, a three-electrode electrochemical cell is used (Figure 4.19(a)), consisting of (1) a working electrode, which is the conducting sample onto which the film is deposited (2) a counter electrode that completes the circuit, and (3) a reference electrode that detects the charge flow through the cell. The working electrode in this thesis is the templated, cysteamine-functionalised, gold-coated sample, the counter electrode is a large area (>1 cm^2) platinum wire mesh gauze (*area~1.1*1.1 cm^2*, fabricated by the glassblowing services in the School of Chemistry, University of Southampton), and the reference electrode is a saturated calomel reference electrode. To build an electrochemical cell, a glass beaker is cleaned by rinsing thoroughly in deionised water and thoroughly drying with clean-room tissue and drying in an oven. The counter electrode is cleaned by rinsing in a stream of deionised water followed by holding in a

butane/propane fire torch for a few seconds until dry. The reference electrode, usually stored in saturated potassium chloride (KCl) solution, is cleaned by rinsing under a stream of deionised water and drying with a clean room tissue. The drying step is very important as the gold plating solution becomes unstable if in contact with water. The electrodes are arranged inside the cell so that the counter and working electrode are opposite each other (Figure 4.19(b)) and the reference electrode is held near the working electrode, but does not obstruct the sample area. The beaker is filled with gold plating solution so that it covers the deposition area of spheres on the working electrode completely, but does not cover the gold coated area used for electrical contact with the potentiostat (Figure 4.19(a)).

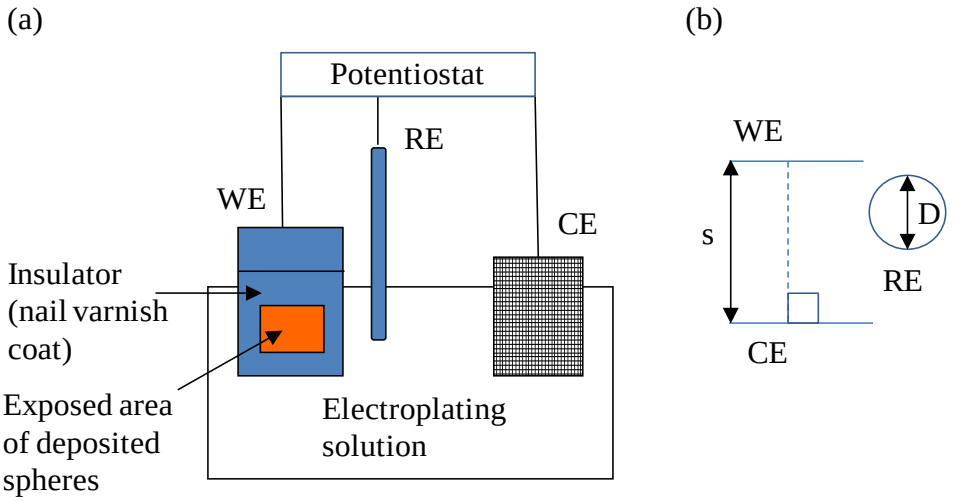

Figure 4.19: Three-electrode electrochemical cell setup (a) components (b) top view of optimum relative position of electrodes; CE=counter electrode (platinum wire mesh, area is about 1cm x 1cm), WE=working electrode (sample,total area is about 0.8 cm x 2 cm, exposed area is max 5mm · 5 mm), RE=reference electrode (saturated calomel reference electrode, diameter (D) is equal to about 0.6 cm, the separation (s) between WE and CE is about 1 cm.

The reference electrode has an electrochemical potential that allows calibration of the electrochemical cell.[299] An Auto lab PGSTAT30 potentiostat controls the three-electrode cell by monitoring the cell parameters such as current, voltage, charge and deposition time. During electrodeposition, a voltage is applied across the working and counter electrode, such that gold ions (Au^{3+}), present in the plating solution, reduce at the working electrode surface, forming a gold film on the working

electrode. The gold plating solution, supplied by Metalor, is EC60, a low bright cyanide free plating solution containing 10g/l gold and no water. The gold is added to the solution in the form of potassium gold sulphite $K_3Au(SO_3)_2$, which forms the $Au(SO_3)_2^{3-}$ ion when in solution. During film growth, the reduction reaction then is $[Au(S_2O_3)_2]^{3-} + e- \rightarrow Au + 2S_2O^{2-}_3$. [300]

Two parameters need to be controlled during film deposition (1) film thickness and (2) deposition speed. Firstly, for a given electrolyte solution, the film thickness t is proportional $t \propto \frac{Q}{A}$, where Q is the total charge passed to the working electrode and equals, $Q = \int Idt$ where I is the current and t is time and A is the deposition area. The film thickness is accurately controlled by accurate measurement of the deposition area A, and measuring the total charge that has passed through the cell for a given area A. The deposition area A is prepared by coating the sample with an insulator (transparent nail varnish) except for a rectangular area, A, which contains the sphere templates around which gold is to be grown. The deposition area A is measured and the total charge (Q) needed to grow a certain film thickness is calculated using equation 4.26 (appendix C.12)

$$Q(C) = 96500 \frac{\rho}{0.8 * 10^7 W} xyt \left[1 - \frac{1}{2\sqrt{3}} \frac{t}{R^2} (3R - t) \right] \qquad (4.26)$$

where W is the atomic weight, 197.0 grams/mole in the case of gold, ρ (g/cm^3) is the density of the metal, 19.32 g/cm^2 in the case of gold, t (nm) is the film thickness, R (nm) is the sphere radius, and $x*y$ (cm^2) is the rectangular deposition area. During electrochemical growth, the current is monitored. Figure 4.20(b) shows a typical current/time graph during deposition, which shows that the deposition process consists of various stages: initially the electrode charges, seen as an initial drop in the current. This is followed by deposition of a thin film on the electrode surface, which is seen as an increase in current. As the available surface area starts to decrease, due to the shape of the template spheres, the current decreases. The film thickness increases, until the desired total charge/film thickness is reached, when the software will automatically stop deposition.

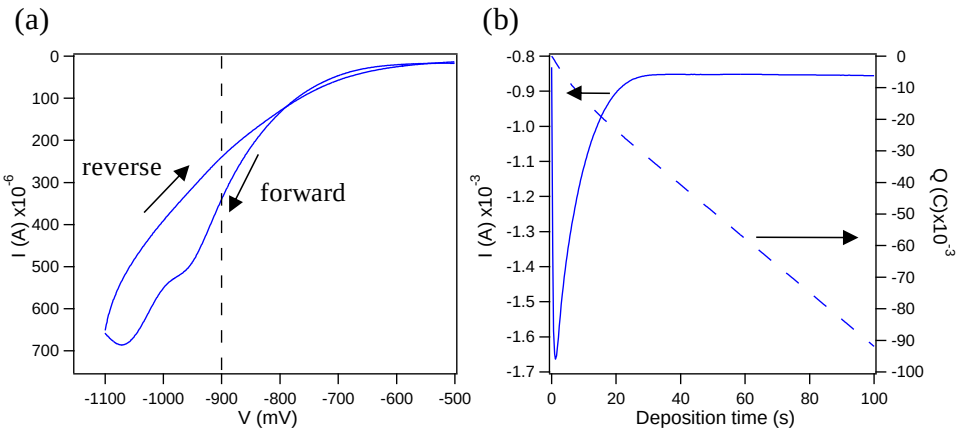

Figure 4.20: Typical graph showing (a) a cyclic voltammogram (current versus potential) and (b) the electrochemical deposition of gold (current and charge versus time), for a substrate templated with 780 nm diameter spheres.

Secondly, the deposition speed determines the film roughness: a slower speed results in a smoother film. Also, a fast growth speed can produce a hole at the bottom of the void. The deposition speed is controlled by the voltage difference between the working and counter electrode. To obtain the optimum deposition speed for each substrate, a cyclic voltammogram is run before deposition. A cyclic voltammogram plots the current-voltage characteristic of a particular electrochemical cell. Figure 4.20(a) shows a typical voltammogram containing a gold-coated substrate templated with 780 nm diameter spheres, showing how the current changes as the voltage is swept from -0.5 V to a negative potential of -1.1 V and back to -0.5 V. At small potentials, no reaction occurs and little current flows. Above a certain potential, the activation point, the reaction starts i.e. gold is being deposited, which is seen as an increase in the current (Figure 4.20(b)). Further increase in the potential increases the reaction/deposition rate, seen as a further increase in the current (Figure 4.20(b)). The reaction rate has reached a maximum when the current and the material/ion-flow to the deposition site balance. Ions cannot reach the working electrode any more quickly, such that a further increase in the potential reduces the reaction rate. The deposition of gold was done at a voltage at around -0.9 V versus a saturated calomel reference electrode.

After depositioning, the nail varnish coat is removed by quickly placing the sample inside a void containing DMF where it is kept immersed for 24 hours.

4.4.1.2.1. Electrochemical Growth Issues

The surface of the grown voids depends on growth speed. At too high a voltage, and hence growth speed, results in the appearance of hole in the voids (Figure 4.21), which have to be avoided. For voltages of less than -0.9 V in magnitude no holes appear, so that -0.9 V was adopted as the voltage the voids were grown at.

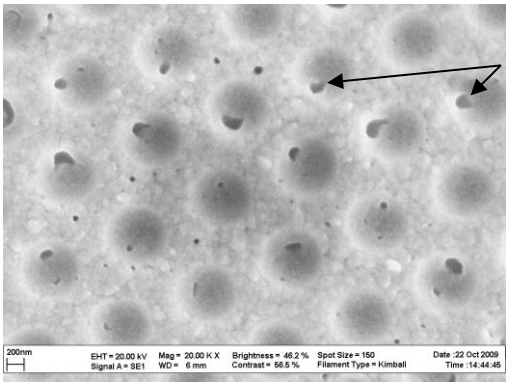

Figure 4.21: SEM image of gold voids grown at -0.925 V.

It was found that a matt gold plating solution produces voids with high surface roughness. The surface roughness can be reduced by adding brightener into the gold plating solution, yielding (a) matt solution, which contains no brightener up to a lustrous solution, which contains a maximum of 5 mL of brightener per 1 L of plating solution. E3 brightener was obtained from Metalor. Figure 4.22 shows voids grown with different amount of brighteners. A matt solution yields roughness of about 93 nm, as determined from averaging the measured size of the grains (Figure 4.22(a)), while lustrous solution produces a very smooth surface, with either no roughness at all, or a roughness of less than 20 nm (the SEM resolution limit) (Figure 4.22(b)). The E3 brightener will not have an effect on the plating thickness. The E3 brightener acts by being absorbed onto the plating surface and encouraging formation of new grains - hence the brighter deposit.

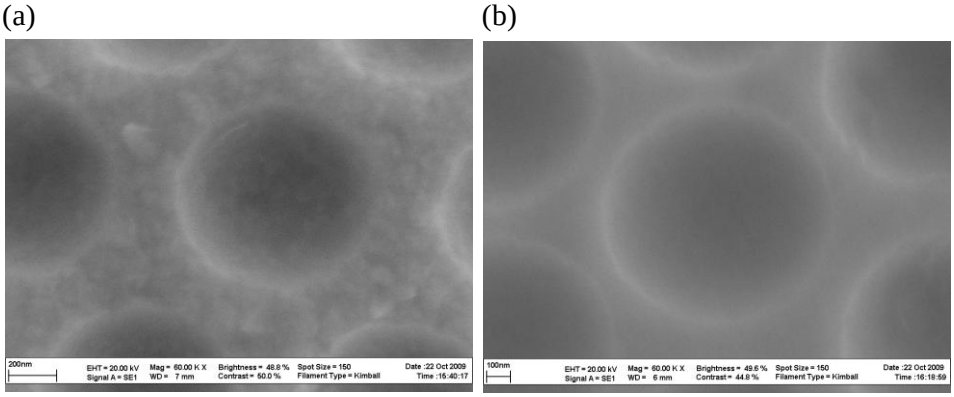

Figure 4.22: Effect of adding brightener: (a) matt plating solution, which contains no brightener (b) lustrous plating solution, which contains 5 mL of brightener per 1 L of plating solution.

It was also found that on some samples the film thickness is higher at the edge of the deposition area than at the centre (Figure 4.23). The growth rate at the periphery of the sample is higher than at the centre. The reason for this is that planar diffusion occurs at the centre, whereas edge diffusion occurs at the edge. The edge effect can be minimised by the cell design: (i) keeping the deposition area to less than 5 mm^2 (ii) ensuring the counter electrode is flat and parallel to the working electrode (Figure 4.19(b) in section 4.4.1.2) (iii) although the reference electrode should be theoretically at the centre of the working area, this would disturb the field lines, so as a compromise, the reference electrode is positioned close to the working area, without being in between the working and counter electrode. The actual thickness grown does not agree with that predicted by equation 4.26 in section 4.4.1.2. The discrepancy in the predicted versus the actual height can vary quite considerably from sample to sample. For instance, for 989 nm diameter spheres, conditions where a predicted height of 75 nm/ 185 nm were used yielded an actual height grown of 360 nm/ 470 nm. This is an extra factor of 4.8/ 2.5. Conversely, the predicted conditions for a height of 457 nm yielded an actual height of 200 nm, when 780 nm diameter sphere templates were used. This effect seemed independent of the brightener content. One possible reason for this discrepancy in predicted and actual height is the presence of lattice defects in the substrate, which is not taken into account by equation 4.26. Lattice defects would increase the space between spheres, and thus reduce the actual

height grown. Also, due to the small sphere size, small inaccuracies in the measured deposition area *x*y*, and hence calculated charge, can result in large deviations in grown and predicted height. For instance, assuming a measuring error of 0.5 mm in the x and y direction each, and an actual area of 3.5*3.5 mm, the measured area ranges from 9 to 16 mm^2, a value 31% higher/27% lower than the actual area. Thus, the fabrication of the substrates had to be done using only estimated parameters.

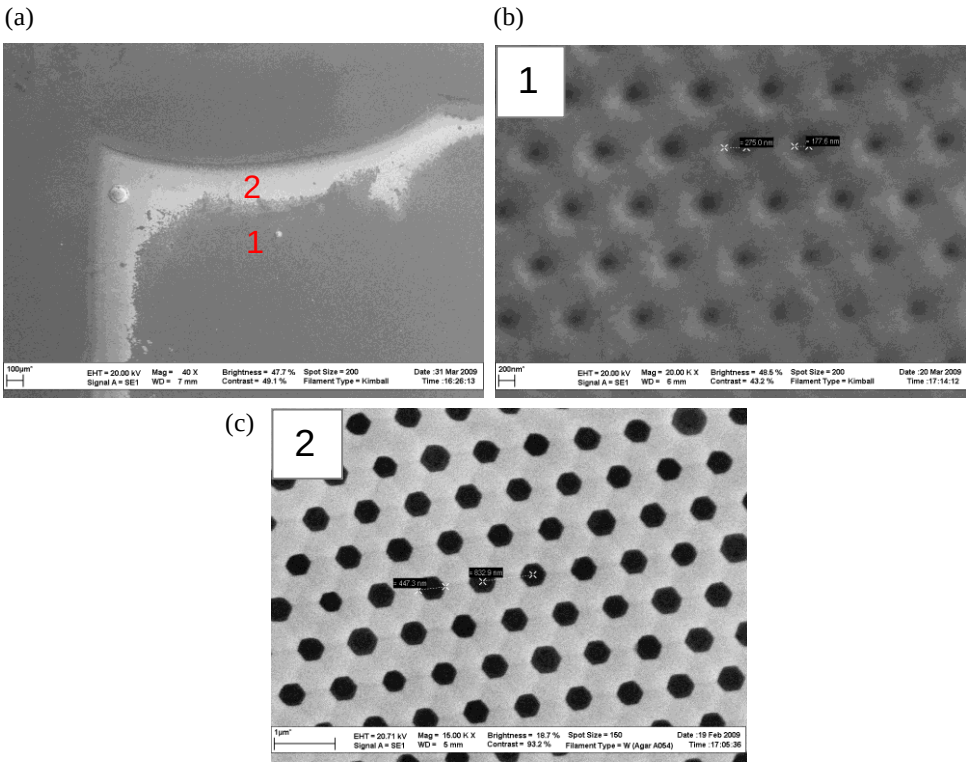

Figure 4.23: SEM images illutsrating the variation in grown film thickness with location on the nanovoid sample: (a) SEM image of the a nanovoid sample showing the the rim (area 2) and centre region (area 1) of the nanovoid area; Close-up SEM image of (b) the centre of the nanovoid sample (area 1 in Figure 4.23(a)), and (c) the edge of the nanovoid sample (area 2 in Figure 4.23(a)), the diameter of the speheres is equal to 780 nm.

4.4.2 TOTO-1 Absorption, Fluorescence and Association to DNA

The DNA staining dye TOTO-1 is a dimer of thiazole orange (TO). TO is a cyanine dye, which consists of two nitrogen containing chromophoric, hetero-aromatic rings (rings containing 6-C with more than one type of atom) linked by a polymethine bridge. Specifically, in TO the methine chain (-CH=) links the benzothiazole ring to the quinoline ring (Figure 4.24(i)). The length of the methine bridge is indicated by the number

following the dye name,[301] e.g. TOTO-1 contains 1 carbon (Figure 4.24(ii)). The dimeric derivative of TO, TOTO, is formed by joining 2 monomers at the quinoline rings via a bis-cationic linker[301] (Figure 4.24). The absorption and emission spectrum can be red-shifted with increasing methine chain length, but is practically unchanged by dimerisation.[302]

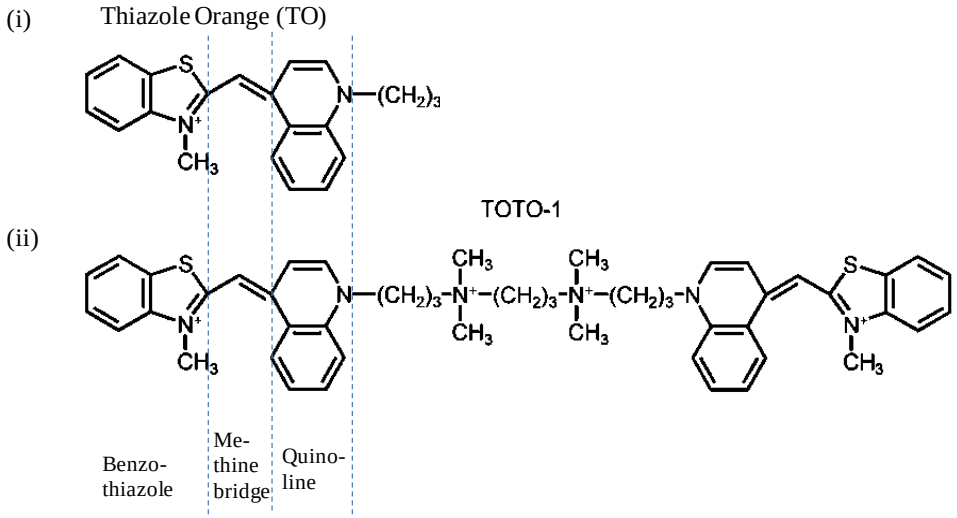

Figure 4.24: Chemical structure of (i) TO and (ii) TOTO-1, adapted from[303, 304].

Nuclear Magnetic Resonance (NMR) studies have shown that TOTO binds to single and double stranded DNA via bis-intercalation. Intercalation is a non-covalent binding mechanism, in which flat aromatic intercalating groups insert themselves between adjacent base pairs[305] (Figure 4.25(c)). TOTO-1 contains 2 intercalating groups, each of which consists of (i) a benzothiazole, which intercalates between 2 pyrimidine bases (C,T), and (ii) a quinoline, which intercalates between 2 purine bases (A,G)[305] (Figure 4.25(a) and (b)). TOTO-1, a dimeric derivative of TO, contains 2 intercalating moieties, twice as many as the monomeric derivative of TO, TO-PRO-1, resulting in a 100 fold higher binding affinity to double-stranded DNA of TOTO-1 compared to TO-PRO-1.[306] The binding affinity of TOTO-1 is also up to 1,000 higher than that of the DNA staining dye ethidium bromide.

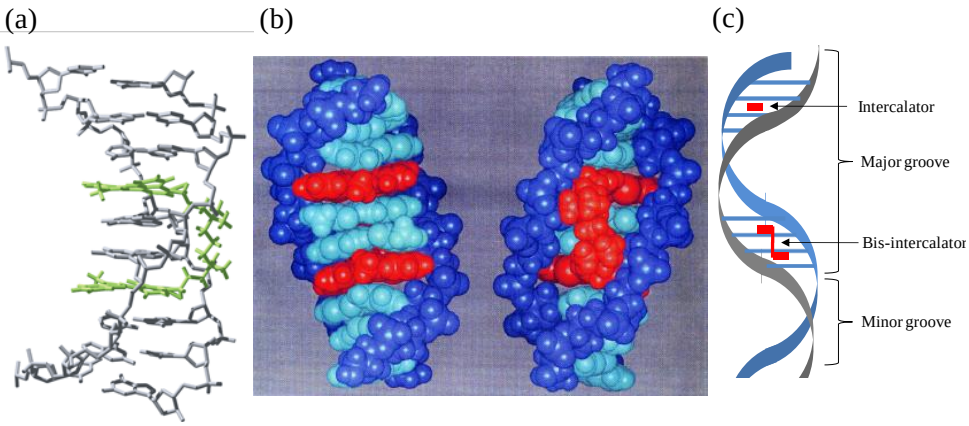

Figure 4.25: Bis-intercalation of TOTO-1 molecule into to double-stranded DNA (a) NMR image: TOTO-1 (green) and DNA (grey)[307] (b) structure, as calculated from NMR studies, of TOTO (red) bis-intercalated into DNA,[308] showing the nucleobases (light blue), and the sugar-phosphate backbone (blue), view into the minor groove (left) and major grove (right) (c) schematic of binding of bis-intercalating and intercalating molecules to DNA (adapted from[307]).

TOTO-1 preferentially binds to the 5`-CTAG-3` sequence, which shows a 100 fold higher binding affinity compared to other base sequences,[308-310] and is explained by the ability of the TOTO molecule to adapt to the structural twist of this base sequence.[305, 311] Bis-intercalation into the CTAG sequence occurs at the C-T and A-G steps.[308] The maximal staining density equals 1 TOTO-1 molecule every 4 nucleotide base pairs.[312] Excited state TOTO-1 that is free in solution decays non-radiatively to the ground state via rotation of the benzothiazole ring about the methine bond relative to the quinoline ring (Figure 4.26(i)). Hence, TOTO-1 in solution is practically non-emissive. However, when intercalated into DNA, the chromophores are inserted between bases, and are thus held much more rigidly, preventing rotation about the methine bridge (Figure 4.26(ii)), and excited TOTO-1 intercalated into DNA relaxes via fluorescence.[313] The restricted rotational motion, and hence reduced non-radiative loss, of DNA-bound compared to free TOTO results in an increase in fluorescence quantum yield of DNA bound compared to free TOTO-1 by 1,100 times.[312]

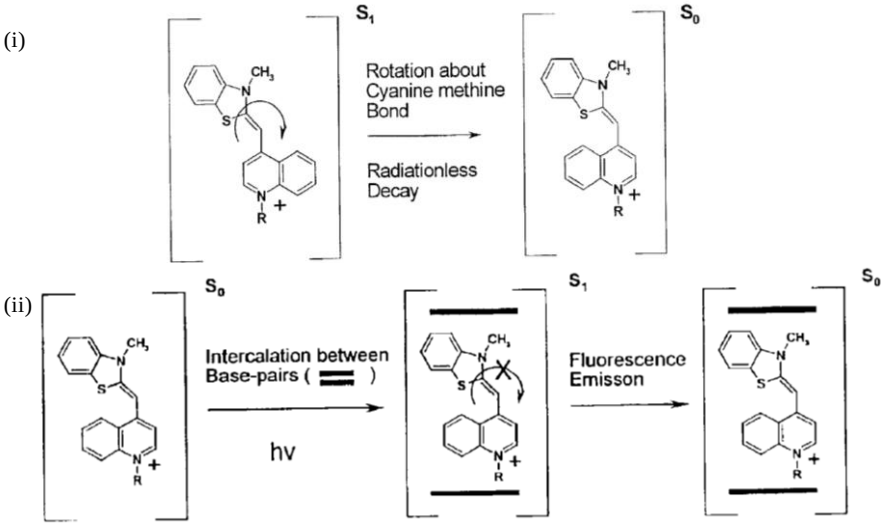

Figure 4.26: Schematic decay path of a cyanine dye from the excited singlet state (S_1) to the ground state (S_0) in (i) solution, where rotation about the methine bridge results in radiationless decay (ii) when intercalated into DNA, when rotational restriction about the methine bridge results in fluorescence decay.[314]

The high binding affinity and the high increase in quantum yield upon DNA binding means that TOTO-1 is very useful for the detection of low DNA concentrations.

The average fluorescence lifetime of DNA bound TOTO-1 is equal to 2.2 ns,[315] 1.96 ns (Calf-thymus DNA)[316] or 1.70 nm (Lambda-phage DNA).[317] Binding to double-stranded DNA reduces the non-radiative decay rate and therefore increases the observed lifetime and fluorescence quantum yield of TOTO-1 and other cyanine dyes.[316] For instance, the average excited state lifetime of TOTO-1 bound to Calf-thymus DNA was measured to be equal to 1.96 ns, with an accompanied enhancement in quantum yield by 1,400 times relative to unbound TOTO-1.[316] The fluorescence quantum yield of TOTO-1 bound to Calf-thymus DNA was measured to be equal to 0.34.[316]. The non-radiative lifetime of free and DNA-bound TOTO-1 can be estimated, by assuming the same radiative lifetime, τ_r, for free and DNA-bound TOTO-1,[316] which would predict a non-radiative lifetime of free TOTO-1 and DNA-bound TOTO-1 equal to $\tau_{nr}^{free} = 1.4ps$ and $\tau_{nr}^{DNA} = 2.9ns$, respectively (appendix C.19).

The fluorescence lifetime of TOTO-1 has been shown to vary with nucleotide base sequence, due to different binding modes with double-

stranded DNA, resulting in various amounts of torsional constriction and hence reduced non-radiative decay.[316] For instance, the average excited state lifetime of TOTO-1 in $(dAdT)_{10}$ oligomers, $(dGdC)_6$ duplex oligomers and Calf-thymus DNA was measured to be equal to 1.02 ns, 2.03 ns and 1.96 ns, respectively.[316]

Figure 4.27 shows and absorption and emission spectrum of TOTO-1 intercalated into DNA. The absorption and emission peak of TOTO-1-DNA is centred at 514 nm (2.41 eV), and 531 nm (2.34 eV), respectively.

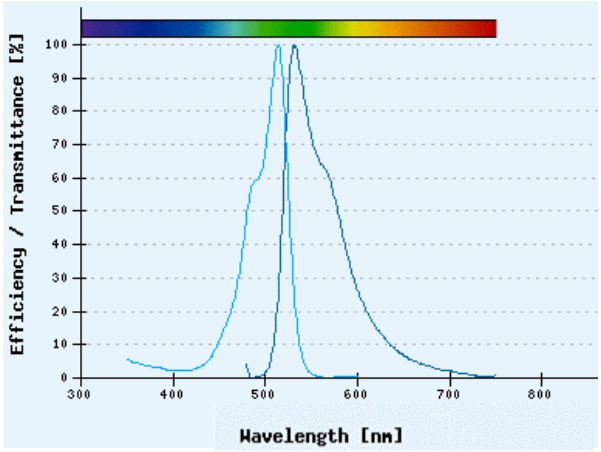

Figure 4.27: Absorption and emission spectrum of TOTO-1-DNA.[318]

4.4.2.1 Fluorescence Microscopy

The samples were imaged with Fluorescence Microscopy (Zeiss), which uses a broadband Mercury/Xenon lamp as an excitation source. Imaging was with a 100x oil objective (Zeiss, 100x oil, NA=1.4, plan-apochromat) in the reflectance mode, and with the filter set 46HE, containing the excitation filter, beam splitter and emission filter BP 500/25 DMR 25, FT 515 HE and BP 535/30 DMR 25 (with the transmission cut off of the emission filter at 535 ± 15 nm), respectively (Figure 4.28). The transmittance cut-off of the emission filter is very sharp (Figure 4.28), with a greater than 50% transmission between 520 nm (2.39 eV) and 550 nm (2.26 eV). Thus, most of the detected fluorescence is expected to lie in the energy range between 520 nm (2.39 eV) and 550 nm (2.26 eV), and these are the energies considered in the theoretical modelling of SPP.

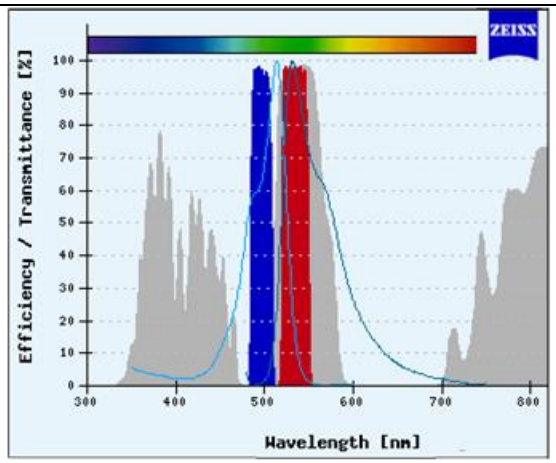

Figure 4.28: Fluorescence detection: excitation filter BP 500/25 DMR 25 (blue), beamsplitter FT 515 HE (grey), emission filter BP 535/30 DMR 25 (red), TOTO-1 absorption spectrum (light blue line) and emission spectrum (dark blue line).[318]

4.4.3 Combing of DNA stained with TOTO-1 by Capillary Force Flow over glass substrates

The DNA stretching method used is an adaptation of Ting-Fung Chan *et al.* [319] and is based on capillary action of fluid between two glass slides. Lambda-phage-DNA molecules (Promega, D1501, double stranded, 48,502 base pairs (bp), assuming 0.34 nm per base pair gives length of roughly 16.5 µm long, MW=660 daltons) is stained with TOTO-1 (TOTO-1 iodide in DMSO, Invitrogen), as follows. DNA fibres are dissolved into TE buffer, in future referred to as just TE buffer, at pH 7.5, containing 10 mM Tris and 1 mM EDTA (EDTA inhibits enzymes from breaking down DNA). For staining, 10 µL of 1 mM TOTO-1 stock solution was diluted with 90 µL TE buffer, and mixed by vortexing, to give 100 µL of 100 µM TOTO-1. Then, 100 µL of 40 µg/mL of DNA was dissolved in 800 µL TE buffer to give 4.4 µg/mL DNA. DNA was dissolved by gentle pipetting. The DNA, in closed loops, is then linearised, under dark conditions wrapped in aluminium foil, by heating at 65.3°C for 5 minutes, followed by immediate storage in an ice-bath for 5 minutes. The 100 µL of 100 µM TOTO-1 solution was then pipetted into the 900 µL linearised 4.4 µg/mL DNA solution and the DNA-TOTO-1 solution mixed by gentle pipetting followed by incubation at room temperature, under dark conditions (wrapped in aluminium foil) for another hour. For imaging, the resulting

DNA-TOTO-1 solution (4 µg/mL DNA and 10 µM TOTO-1) was diluted in 20% volume 2-Mercaptoethanol and 80% volume TE buffer resulting in a working solution of 3.2 µg/mL (100 pM) DNA and 8 µM TOTO-1, with a ratio of base pairs to TOTO-1 molecules (bp: TOTO-1) equal to 1:1.6. 2-Mercaptoethanol is a reducing agent that scavenges oxygen in the solution, minimising photobleaching of TOTO-1. Other sample solutions containing bp:TOTO-1 equal to $1:1.6x10^{-1}$ and $1: 1.6x10^{-2}$ were also prepared by adjusting the TOTO-1 concentration accordingly.

Glass coverslips, used for DNA stretching by capillary force, were prepared by coating in three layers of charged polyelectrolyes as follows. The coverslips, of dimension 25 x 50 mm^2, were cleaned by sonication in 2% volume MICRO-90 soap solution (ColePalmer) for 20 minutes. They were further cleaned by boiling in RCA solution (6:4:1 high purity 18 MΩ deionised water: 30% volume ammonium hydroxide (NH_4OH):30% volume hydrogen peroxide (H_2O_2). The coverslips were then coated. For this, poly(acrylic acid) (PAcr) (Sigma Aldrich, MW 1,800) and poly(allylamine) (PAA) (Polysciences Inc, MW 1,000) were each dissolved in high purity, 18 MΩ deionised water at 2 mg/ml. The pH was adjusted to 8.0 by adding either HCl (for PAA) or NaOH (for PAcr), and the resulting polyelectrolyte solutions were passed through a 0.22 µm filter. The RCA-cleaned coverslips were then coated in positive (PAA) and negative (PAcr) polyelectrolyte solutions according to +/wash/-/wash/+/wash. A coating step involved immersion of the coverslip in a polyelectrolyte solution for 30 minutes on a shaker at 1,500 rpm, and the wash step involved 3 rinses either side with high purity, 18 MΩ, deionised water. The coated coverslips were stored in high purity, 18 MΩ, deionised water at room temperature in a glass container wrapped by aluminium foil.

The polyelectrolyte coated coverslip was cut to a dimension of 10 x 20 mm^2, to fit on top of the eventual gold nanovoid substrate (Figure 4.19 in section 4.4.1.2). Dust was removed from the glass slide substrate by dry nitrogen flow, followed by removal of moisture by heating under a butane-propane flame torch for several seconds. For gold-void substrates, moisture was removed by purging and storing the substrate under dry nitrogen flow

overnight, i.e. at least 16 hours. The polyelectrolyte covered coverslip was then placed on top of the substrate and 1.6 µL of DNA-TOTO-1 sample solution was slowly pipetted to the edge of the coverslip-substrate interface, and the solution was drawn underneath the coverslip by strong capillary action, anchoring the negatively charged DNA strands onto the positively charged Poly-allylamine coating, stretching and aligning the DNA strands on the modified coverslip in the process (Figure 4.29). The coverslip was then sealed with clear nail varnish.

DNA stretching over all substrates, i.e. glass, gold and nanovoids, was conducted at a DNA concentration of 25 pM, with bp:TOTO-1 equal to 1:0.16 and using a drop-cast volume of 1.6 µL and a 10 x 20 mm^2 coverslip. All samples were imaged with a Fluorescence Microscope (Zeiss).

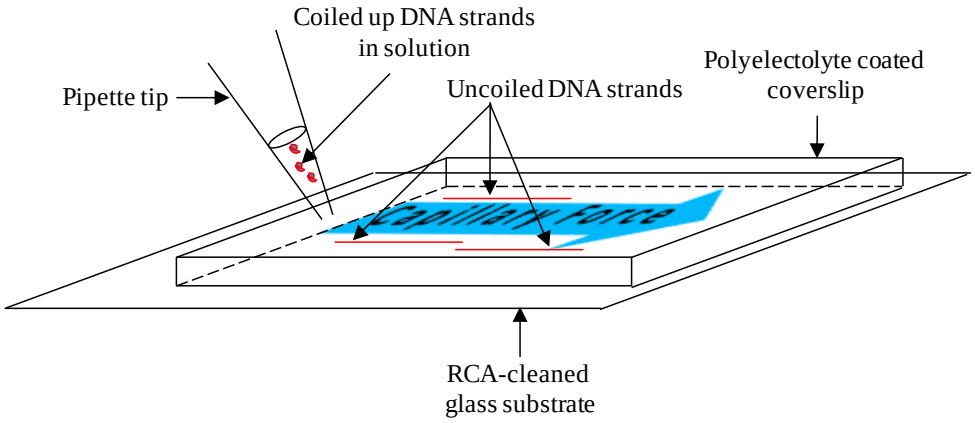

Figure 4.29: Schematic of DNA combing over a glass substrate.

Figure 4.30 shows fluorescence images of DNA (100 pM) stretched over a glass slide at various TOTO-1 concentrations. Strong DNA coagulation occurs at high TOTO-1 concentrations, with nucleotide base pair to TOTO-1 molecule ratio bp:TOTO-1 equal to 1:1.6 (not shown). Lower TOTO-1 concentrations of 1:0.16 and 1:0.016 yield DNA strands that are separated from each other (Figure 4.30(a) and (b). DNA coagulation at high TOTO-1 concentration can be attributed to the positive electric charge of TOTO-1. Similar to TOTO-1, the staining molecule YOYO is positively charged, and can induce DNA aggregation for bp: YOYO below 1 to 0.2.[312, 320] DNA is negatively charged as a result of the phosphate sugar backbone, the

positively charged TOTO-1 associates and intercalates in the DNA, but also can result in reduced aqueous solubility of the TOTO-1 if present in excess. However, at bp:TOTO-1of 1:0.016 the much lower TOTO-1 concentration yields weaker intensity fluorescence signals from the stretched DNA strands (under the microscopy conditions used) as compared to the DNA sample at bp:TOTO-1 of 1:0.16, decreasing the signal to noise ratio (Figure 4.30(a) and (b)). Thus, in subsequent DNA combing methods, bp: TOTO-1 of 1:0.16 is prepared. The polyelectrolyte multilayer coated coverslip is said to have low background levels, due to electrostatic repulsion of the charged polymer multilayer, making it suitable for single molecule imaging.[319]

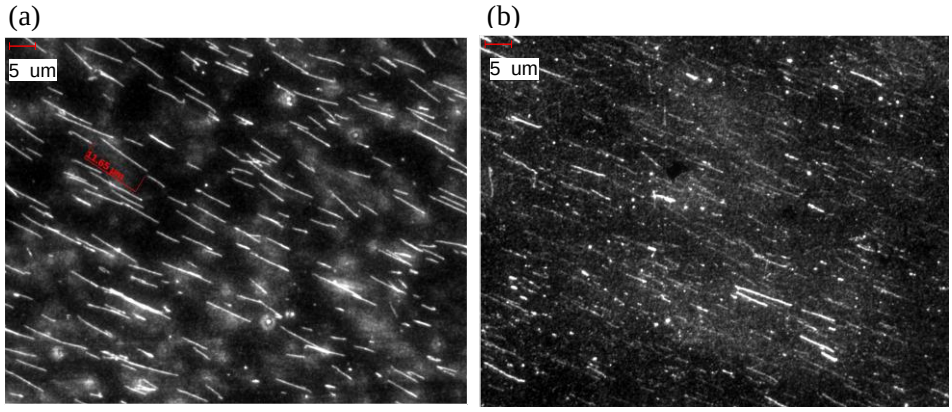

Figure 4.30: DNA stretching-dependence on TOTO-1 concentration: fluorescence images of TOTO-1-DNA stretched over a glass substrate at bp:TOTO:1 equal to (a) 1:0.16 , (c) 1:0.016. The coverslip dimension is equal to 25x25 mm^2, with a drop-cast volume of 5 µL, and DNA concentration of 100 pM, 100x oil immersion. Excitation was at 485 to 510 nm, emission detection was at 518 to 550 nm (see Figure 4.28 in section 4.4.2.1).

The DNA distribution and stretching efficiency was found not to be uniform across the coverslip, but to dependent on the distance from the drop-cast site (Figure 4.31). The DNA density is highest nearest the drop-cast site, and deceases with distance from the drop-cast site (Figure 4.31(a-d)). The proportion of unstretched DNA also increases with distance from the drop-cast site. It is observed that the speed at which the sample solution is drawn under the coverslip is highest just after drop-casting, and decreases the further the sample solution has travelled away from the drop-cast site. Thus, the reduced DNA stretching efficiency with increasing distance away from the drop-cast site might be due to a slower capillary flow and thus lower stretching force.

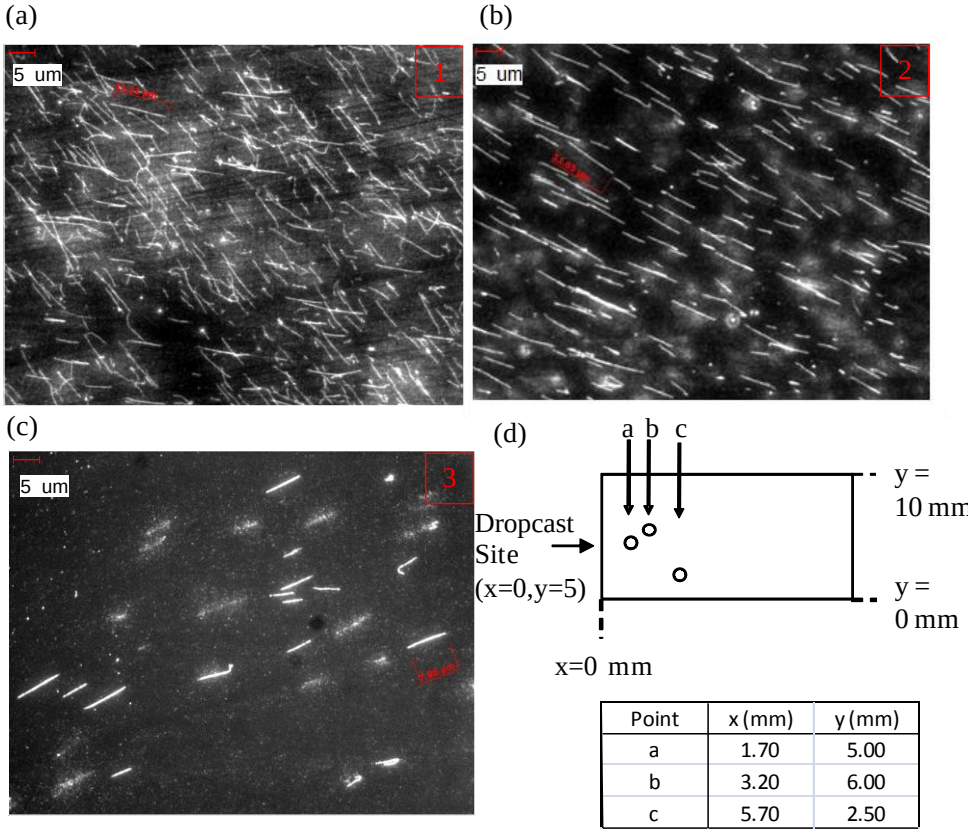

Point	x (mm)	y (mm)
a	1.70	5.00
b	3.20	6.00
c	5.70	2.50

Figure 4.31: DNA stretching-dependence on distance from drop-cast site: (a), (b) and (c): Fluorescence images of TOTO-1 stained DNA, stretched over a glass substrate, at various distances from the drop-cast site; (d) distances from the dropcast site of the images in Figure 4.31(a), (b) and (c). The DNA concentration is equal to 100 pM, bp: TOTO-1=1:0.16, the coverslip dimension is equal to 20x10 mm^2, the drop-cast volume is equal to 1.6µL, 100x oil immersion.

4.4.3.1 DNA Combing over a Rough Gold Substrate

The gold surface was grown by electrochemical growth without polystyrene spheres using a matt gold plating solution and the same electroplating conditions as the nanovoid sample discussed in Figure 4.32(b) in section 4.4.3.2, resulting in surface roughness of few tens of nanometres up to 100 nm, as determined from SEM images (not shown).

4.4.3.2 DNA combing over Gold Nanovoids

Gold nanovoids were grown with lustrous and matt gold plating solutions, resulting in a smooth substrate surface and surface roughness of a few tens of nanometres, respectively (Figure 4.22 in section 4.4.1.2.1). The setup for combing DNA strands over gold nanovoids was optimised by stretching TOTO-1 DNA over a number of gold nanovoid substrates, and

the optimum combing setup is illustrated in Figure 4.32(a): the poly(electrolyte)-covered coverslip is placed over the gold nanovoid substrate, leaving a narrow strip of the nanovoid region free onto which the TOTO-1 DNA solution can be drop-cast. Drop-casting directly onto the nanovoid substrate ensures that the DNA strands are stretched over the nanovoid region. This is because DNA stretched over the surrounding gold region will only cover the surrounding gold region, due to the slightly higher height of the nanovoid region compared with the surrounding gold surface, a result of the electroplating process.

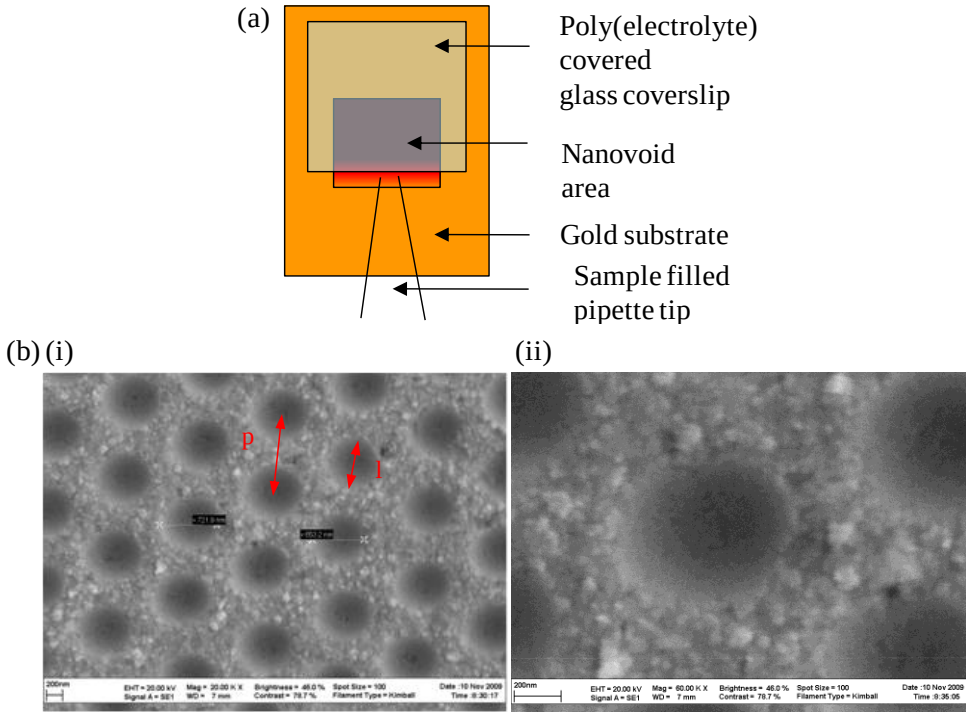

Figure 4.32: DNA stretching over gold nanovoids (a) optimised stretching setup (b) SEM image of the gold nanovoid sample discussed in the text, at a SEM magnification equal to (i) 20k (ii) 60k , p is the nanovoid periodicity, and l is the length of the void diameter at the void top.

The void dimension of the gold nanovoid substrate was studied with Scanning Electron Microscopy (SEM). Figure 4.32(b) shows SEM images of a gold nanovoid substrate over which DNA combing was successful and its effect on DNA fluorescence were investigated in more detail (section 4.5.3). This particular sample was grown with 989 nm diameter spheres and a matt gold electroplating solution, yielding a rough gold surface with surface roughness of up to 95 nm (Figure 4.32(b)(ii)). From the SEM images the average void periodicity (p, the distance between the centres of

adjacent voids) and the average length of the opening of the void top (*l*) can be measured (Figure 4.32(b)(i)). From *l*, the average void thickness, *t*, can be estimated (Appendix C.13). For the sample shown in Figure 4.32(b), the void dimensions were measured to be equal to a periodicity of *p=1090 nm*, length of the void diameter at the void top *l=722 nm* and depth of void *t=157 nm* (Figure 4.32(b)(i) and Appendix C.13).

4.4.4 Fluorescence Lifetime Measurements

For fluorescence lifetime measurements, a 2D fluorescence intensity map of the samples was built by scanning the excitation source across a sample area. Each excitation spot represents a single pixel of 3 x 3 µm in size. The pixel size of 3 x 3 µm was the smallest pixel size possible to use without photobleaching of the sample. The total area of the 2D intensity map was 30 x 30 µm. The fluorescence lifetime of individual pixels of a map was evaluated. In the experimental setup the excitation source was a white light continuum laser (Fianium, V4), with pulse width of ~5 ps and a repetition rate of 40 MHz. The excitation laser passed through a LC tunable filter (VariSpec, Cri), which selected the excitation wavelength to 490 nm, at which point the TOTO-1 absorption efficiency is about 60% (Figure 4.28 in section 4.4.2.1), which then passed a sp 500 excitation filter. The excitation light was passed through an Olympus BX51 microscope through home- made modifications, and focussed to a spot size of about 0.5 µm onto the sample by a 0.88 NA objective (100x magnification) (according to Rayleigh minimum spot size $= 0.61\lambda/NA = 0.61\ 490\ nm/0.88 = 340\ nm$ in a perfect diffraction limited regime, with plane parallel beam overfilling the objective back aperture). The fluorescence emission, collected in the backscattered geometry, passed through a lp530 emission filter and was coupled by an optical fibre to an avalanche diode, PDM 50 (MPD). Time-correlated single photon counting (TCSPC) methods (appendix C.17), were used for measurement of the fluorescence decay, employing an avalanche diode and TimeHarp 200 (PicoQuant) acquisition board, to provide synchronisation of the laser with the detection, by photon counting, between pulses. The curve for the fluorescence decay was collected at

different times after the pulse was recorded as in a histogram with a 37 ps resolution (using the TimeHarp 200 single photon counting board). The fluorescence intensity decay curves were analysed using IGOR software, smoothed by two smoothing operations and fitted to a single or double exponential curve according to $I(t) = y_0 + \sum_i^m a_i \exp\left(-\frac{t}{\tau_i}\right)$, where m=1 or 2 for single and double exponential decay, respectively. Each experimental curve was fitted using the least squares fitting method, in which data points that describe the experimental curve are calculated, and the calculated points are optimised by reducing the deviation of the calculated points from the experimental data points. Chi-squared (χ^2) provides the deviation of the fitted curve from the experimental curve, and is defined as, $\chi^2 = \sum_{j=1}^{n}\left[\frac{\Delta y_j}{\sigma_j}\right]^2$ where $\Delta y = y(t) - Y(t)$, and $y(t)$ and $Y(t)$ are the experimental and fitted data points, respectively, σ is the standard deviation of $y(t)$ and n is the total number of data points. The least square technique is iterative, meaning that successive iterations converge to an optimum fit with minimum deviation (minimum χ^2). If the best fit is a multi-exponential curve, then the average fluorescence lifetime was assumed to equal the amplitude weighted lifetime, which is equal to

$$\tau_{av} = \frac{\sum_i a_i \tau_i}{\sum_i a_i} \qquad (4.27)$$

where for the ith component a_i and τ_i is the amplitude and fluorescence lifetime, respectively. For best fit, various factors were taken into account (1) an extra lifetime component was added only if it resulted in a significant reduction in χ^2. A reduction in χ^2 by more than 4% was regarded as significant (2) if a reduction in χ^2 occurred after the addition of an extra lifetime component, but the new lifetime is similar to an already present lifetime, then the extra component is not added (3) for a triple exponential fit, initial guesses for the amplitude and lifetime of each component had to be entered.

4.5 Evaluation of the Fluorescence of TOTO-1 within Combed DNA Strands over Glass, Rough Gold and Gold Nanovoid Substrates

This section describes the fluorescence intensity distribution along DNA strands that were fluorescently labelled with TOTO-1 and then stretched over a substrate that is either a flat glass surface, a rough gold surface or an array of rough gold nanovoids.

4.5.1 Combing of TOTO-1 Labelled DNA Strands over a Glass Substrate

Figure 4.33(a) shows a typical fluorescence image of TOTO-1-DNA combed over a flat glass substrate by capillary force flow, and Figure 4.33(b), (c) and (d) show the fluorescence intensity profile along individual stretched DNA strands. The stretched DNA strand length varies from between 5.5 µm (Figure 4.33(c)) to about 8 µm (Figure 4.33(b) and (d)). Thus, most DNA strands are stretched to less than their fully extended contour length of 16.5 µm. The three strands in Figure 4.33(a) are now evaluated in detail and are shown in Figure 4.33(b), (c) and (d). The profile of the fluorescence intensity along individual DNA strands is seen as one of the following forms (i) a uniform intensity along the whole DNA length (Figure 4.33(b)), (ii) a uniform intensity along most of the DNA strand, but with an increased intensity at one end of the DNA strand (Figure 4.33(d)), (iii) and particles of intensity several times higher than that of stretched DNA (Figure 4.33(a)(i)).

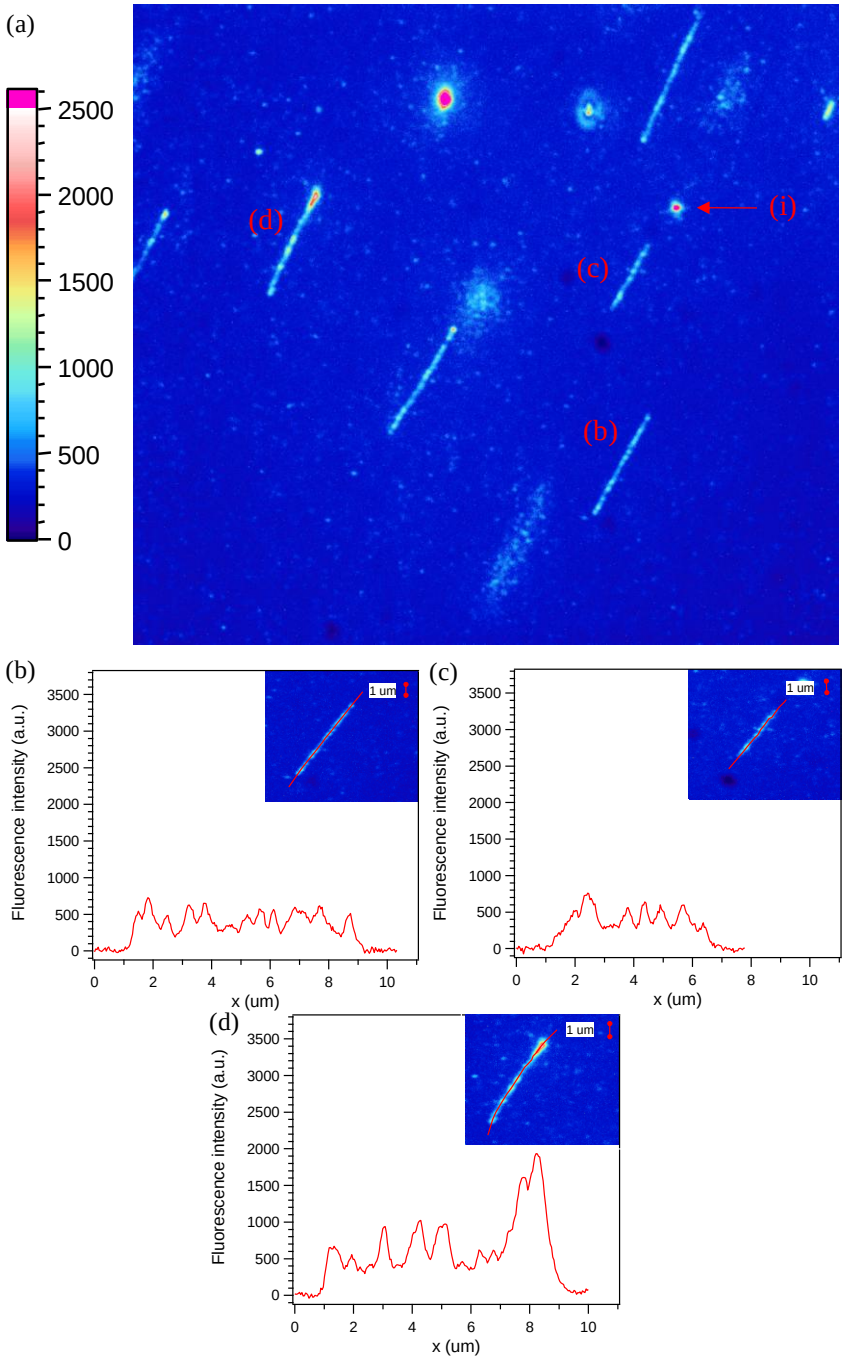

Figure 4.33: Fluorescence of TOTO-1-DNA stretched over a glass substrate (a) 2D Fluorescence image of TOTO-1-DNA stretched over glass; (b),(c), (d) fluorescence intensity profile along individual DNA strands, Inset: path of maximum fluorescence intensity (red line)(drawn by hand). The fluorescence images were obtained with 100x oil immersion, 1.6 optovar, the integration time equals 20.48 s. The fluorescence image and intensity profiles were normalised to 30 s integration time and the fluorescence background level due to the glass substrate was subtracted. The DNA concentration is equal to 25 pM, bp: TOTO-1 is equal to 1:0.1, the coverslip dimension is equal to 20 x 10 mm^2, and the drop-cast volume is equal to 1.6 µL.

The intensity along the most uniformly fluorescent DNA strand (Figure 4.33(b)) is seen to be approximately three times that in other regions. The

fluorescence intensity of the DNA strand shown in Figure 4.33(d) varies by 3.4 times, however. The high fluorescence intensity observed at the end of the strand is assumed to be a result of a looped section. The shorter DNA strand Figure 4.33(c) is similar to the slightly longer strand in Figure 4.33(b) with respect to the variation and the fluorescence intensity along the strand. Thus it is suggested that the strand in Figure 4.33(c) is a fragment of Lambda-phage DNA. The strand in Figure 4.33(d) stands out in having broader fluorescence intensity along the strand length compared to the two other strands shown in Figure 4.33(b) and (c): the typical strand width of an intensity peak along the strand centre is equal to about 0.73 µm (Figure 4.33(d)) compared to only 0.45 µm (Figure 4.33(c)) or 0.49 µm (Figure 4.33(b)) in the two other strands. This further suggests that the strand shown in Figure 4.33(d) is looped/folded.

Previous experiments[322] have shown the presence of fluorescence intensity peaks along otherwise uniform intensity profiles of DNA strands stretched in fluid flow, with peak intensities along DNA strand ends and along the DNA strand being attributed to local DNA strand folding in fluid flow.[322] It is also well-know that TOTO-1 preferentially binds to specific nucleotide base sequences, such as 5`-CTAG-3` (section 4.4.2).[308-310] The experimental intensity variation along the stretched strand length is not the same along each strand but appears random (Figure 4.33(b-d)), which suggests that the intensity variation is due to a non-uniform DNA configuration, rather than due to preferential binding of TOTO-1 to specific nucleotide base sequences, which would not be observed at the spatial resolution of these images anyway. The effect of preferential binding of TOTO-1 can thus be neglected. A variation in DNA configuration might be the result of a combination of non-uniform DNA stretching and local DNA strand folding.[322] The increased intensity at the strand ends can then also be attributed to coiled-up DNA strand ends due to incomplete stretching at the end, while the high intensity particles (Figure 4.33(a)(i)) may be coiled-up, unstretched DNA.

4.5.2 Evaluation of the Effect of a Rough Gold Substrate on the Fluorescence of TOTO-1 within Stretched DNA Strands

This section describes the fluorescence imaging results of a rough gold surface sample grown with a matt gold electroplating solution under the same electroplating conditions as that of the nanovoid sample discussed in section 4.5.3 (also see section 4.4.3.1). From SEM images (not shown), the size of the surface roughness of the sample was measured to range between a few tens of nanometres up to about 100 nm. Figure 4.34(a) shows a typical fluorescence image of TOTO-1-DNA strands stretched over the rough gold substrate, with the fluorescence intensity profile of individual strands shown in Figure 4.34(b) and (c).

Flat metal surfaces have been shown to quench fluorescence of nearby spontaneous emitters.[323] Fluorescence quenching by a flat metal surface is attributed to non-radiative energy transfer from the excited emitter to (i) non-radiative surface plasmon polaritons, which occurs for separation in the range of 20 nm up to several hundred nanometres[257] (ii) lossy surface waves on the metal surface for emitter-metal separations of less than 20 nm. [256, 257] On the other hand, nanoscale surface roughness on gold surfaces has been shown to enhance the fluorescence intensity of dyes attached directly onto the rough surface.[323, 324] This is attributed to SPP-dye coupling.[323, 324] These observations agree with the metal-enhanced fluorescence model,[324] according to which SPP on a flat metal surface cannot couple to far-field radiation, and therefore quench fluorescence, while SPP on a rough metal surface can couple out to far-field radiation, and therefore can enhance the fluorescence intensity of a nearby spontaneous emitter.

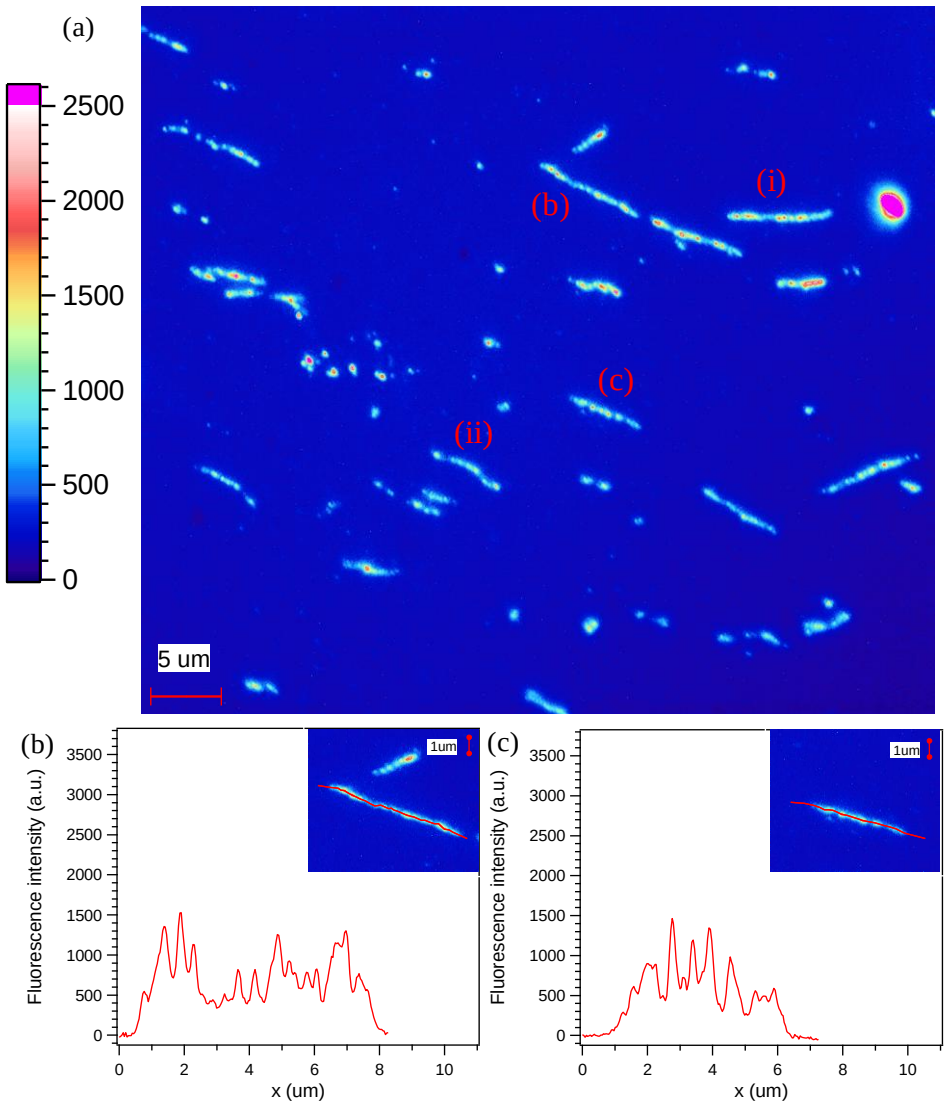

Figure 4.34: Fluorescence of DNA-TOTO-1 stretched over a rough gold surface (a) 2D fluorescence image f TOTO-1-DNA stretched over a rough gold substrate; (b), (c) fluorescence intensity profile of individual DNA strands, Inset: path of maximum fluorescence intensity (red line)(drawn by hand). The fluorescence images were obtained with 100x oil immersion, 1.6 optovar, the integration time equals 31.1768 s. The fluorescence image and intensity profiles were normalised to 30 s integration time and the fluorescence background level due to the rough gold substrate was subtracted. The DNA concentration is equal to 25pM, bp: TOTO-1 is equal to 1:0.16, the coverslip dimension is equal to 20 x 10 mm^2, and the drop-cast volume is equal to 1.6µL.

The main effect of the rough gold surface on stretched TOTO-1-DNA, is an increase in the fluorescence intensity along the stretched out DNA strand (Figure 4.33(b-d) and Figure 4.34(b) and (c)). If the data shown in Figure 4.34(b) and (c) is compared with that observed for DNA-TOTO-1 samples stretched over glass, the fluorescence is both higher and more variable in intensity along the strand. This increase in fluorescence

might be attributed to surface-plasmon-polariton induced fluorescence enhancement of TOTO-1 over the rough gold substrate, as previously observed for fluorophores near a rough gold surface.[323, 324]

4.5.3 Evaluation of the Effect of Gold Nanovoids on the Fluorescence of TOTO-1 within Stretched DNA Strands

This section describes the fluorescence imaging results of the particular nanovoid sample grown with a matt gold electroplating solution using spheres of diameter D_{void}*=989 nm*. The SEM image of this nanovoid sample used is shown in Figure 4.32(b) in section 4.4.3.1. From SEM images, the surface roughness of the sample was measured to be up to about 95 nm in size (Figure 4.32(b)(ii) in section 4.4.3.1), and thus the nanovoid sample has surface roughness similar to that of the rough gold surface discussed in section 4.5.2. In this nanovoid sample, the average void height was grown to *d=157 nm* (normalised height of 0.16) with periodicity *p=1090 nm* (Figure 4.32(b)(i) in section 4.4.3.1). From SEM images, the void height was derived from measurements of the length of the void top (*l*) (appendix C.13), which equals *l=722nm* (Figure 4.32(b)(i) in section 4.4.3.1).

Figure 4.35(a) and (c) show typical fluorescence images of TOTO-1-DNA stretched over the nanovoid substrate (D_{void}*=989 nm*, *d=157 nm*). The fluorescence from the stretched TOTO-1-DNA strands and the focussed light from the nanovoids are clearly visible. However, the position of the voids underneath the TOTO-1-DNA strands is obscured by the fluorescence signal from the TOTO-1-DNA strand above it. In order to locate the exact position of the voids underneath the TOTO-1-DNA strands, a bright field image is taken, which shows the location of all voids (also see appendix C.15). A relative shift of a few pixels between the bright field and fluorescence image is zeroed by overlaying both images into a single overlap image and zeroing the relative shift between the bright field and fluorescence image, at which point the voids of the bright field images should exactly overlap those in the fluorescence image. For any pixel

coordinate on the fluorescence image the equivalent bright field signal can then be obtained in a straightforward manner.

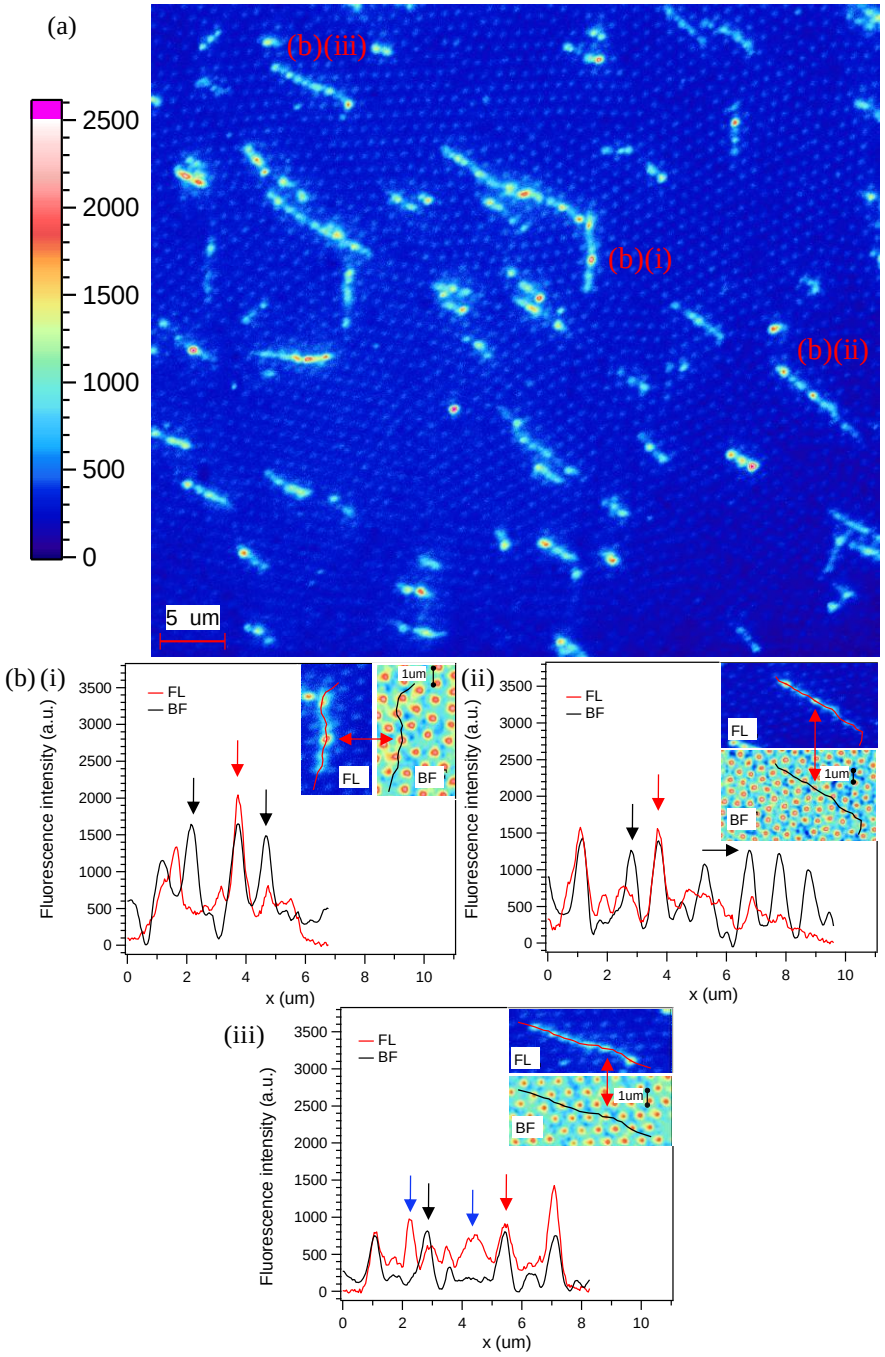

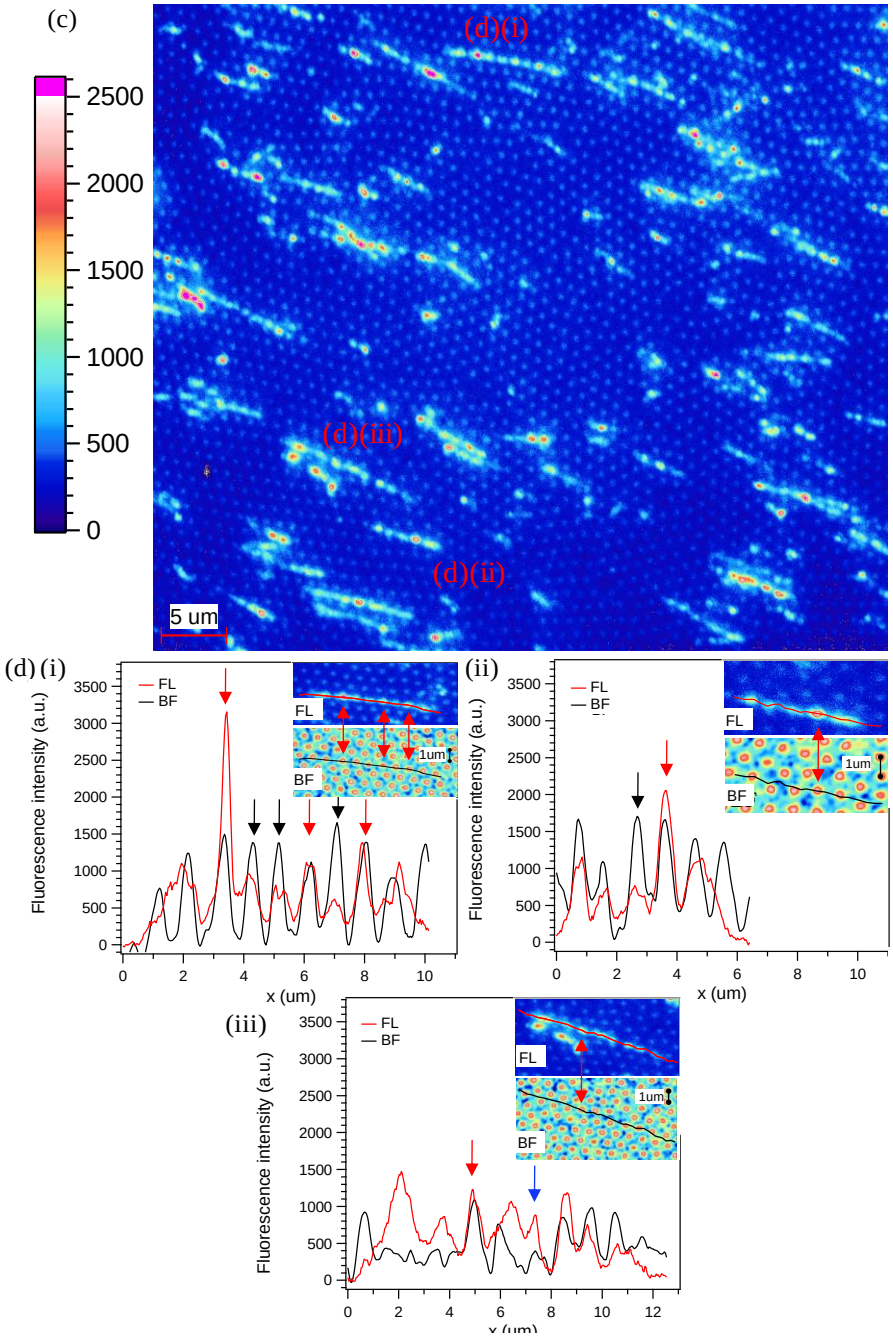

Figure 4.35: Fluorescence (FL) of DNA-TOTO-1 stretched over a gold nanovoid substrate; (a), (c) 2D FL image at two different sample locations; (b),(d) intensity profiles in FL (red line) and bright field (BF)(black line) along individual DNA strands (drawn by hand), inset: path of maximum FL intensity in the FL image (FL, red line) and BF image (BF, black line). Indicated are locations along the DNA profile where FL and BF peaks coincide (red arrows), where FL is almost unaffected by a nanovoid (black arrows), and where FL peaks occur above the rough top gold surface (blue arrows). The FL images were obtained with a 100x oil immersion, 1.6 optovar lens, the integration time equals 28.652 s (Figure 4.35(a)) and 26.5064 s (Figure 4.35(c)). The FL image and intensity profiles were normalised to 30 s integration time and the FL background level due to the top rough gold surface was subtracted. The DNA concentration is equal to 25pM, bp: TOTO-1 is equal to 1:0.16, the coverslip dimension is 20 x 10 mm^2, and the drop-cast volume is equal to 1.6µL.

Figure 4.35(b) and (d) show the fluorescence and bright-field intensity profiles of individual stretched-out TOTO-1-DNA strands from Figure 4.35(a) and (c), respectively. The intensity profiles were obtained by drawing by hand on the fluorescence image a line along the maximum fluorescence signal along the stretched DNA strand, and using that same line for the bright field image (inset in Figure 4.35(b) and (d)). The intensity profile contains fluorescence peaks that are located above nanovoids (red arrows in Figure 4.35(b) and (d), and appendix C.14).

In general, the following observations can be made for TOTO-1-DNA stretched over gold nanovoids: (i) some fluorescence peaks are located above nanovoids, with peak heights ranging from 900 to 3,200 counts (red arrows in Figure 4.35(b) and (d)), (ii) no considerable change in fluorescence intensity occurs above nanovoids (black arrows in Figure 4.35(b) and (d)), (iii) above the rough gold surface fluorescence peaks are present, with intensities between about 800 to 1,000 counts (blue arrows in Figure 4.35(b) and (d)).

The fluorescence intensity peaks above the nanovoids could have various origins (i) fluorescence enhancement induced by resonant Mie modes supported by the nanovoid (ii) enhanced fluorescence due to the void focussing the excitation light, increasing the excitation light intensity and therefore the TOTO-1 absorption rate.[325] The focus is located at a distance of half the void radius above the bottom of the void; (iii) unstretched or folded over regions in the DNA strand are located within the nanovoid volume. Set by the excitation filter of the fluorescence microscope (Figure 4.28 in section 4.4.2.1.), the energy of the excitation light ranges from about 513 nm to 482 nm (2.43 eV to 2.58 eV), which is near the plasmon frequency of gold (2.6 eV).[293] As a result, reflection of the excitation light by gold nanovoids and thus enhanced fluorescence intensity due to a focussed excitation beam is expected to be minimal. Also, the minimum fluorescence intensity over the rough gold region of the nanovoid substrate is comparable to that over glass or rough gold, suggesting that either fluorescence quenching over the rough gold surface

is not considerable, or fluorescence quenching does occur but its effect on fluorescence intensity is offset by enhanced reflection of the fluorescence light by the gold compared to glass. If fluorescence quenching does occur over gold top plane, then the florescence peaks above nanovoids might also be due to reversal of fluorescence quenching over the nanovoid region as the separation between the TOTO-1-DNA and the gold surface increases to more than 20 nm. However, de-quenching would only explain intensity peaks of heights up to the maximum value as that observed over glass.

4.5.4 Comparison of the Fluorescence Intensity Distribution of TOTO-1 within Stretched DNA Strands over Glass, Rough Gold and Gold Nanovoids

Figure 4.36 shows the 3D fluorescence images of individual TOTO-1-DNA strands stretched over glass (Figure 4.36(a)), rough gold (Figure 4.36(b)) and rough gold nanovoids (Figure 4.36(c) and (d)). Over both glass and rough gold, the fluorescence intensity is not uniform along the DNA strand length. However, for TOTO-1-DNA stretched over rough gold higher fluorescence intensities are seen (Figure 4.36(b)) as compared to similar DNA strands stretched over glass (Figure 4.36(a)). For the TOTO-1-DNA strands stretched over gold nanovoids, the fluorescence has a pattern consistent with the periodicity of the underlying nanovoid structure (Figure 4.36(c) and (d)).

The fluorescence intensity seen for some regions of the DNA stretched over the gold nanovoids is significantly greater than for gold or glass (Figure 4.36(a-d)). In order to evaluate the fluorescence peak intensities of TOTO-1-DNA stretched over gold nanovoids, background due to the nanovoid structure is subtracted, and the location of the fluorescence peaks relative to the nanovoids considered. First, the fluorescence image was rotated to align the individual strand of interest horizontally (Figure 4.37(a)).

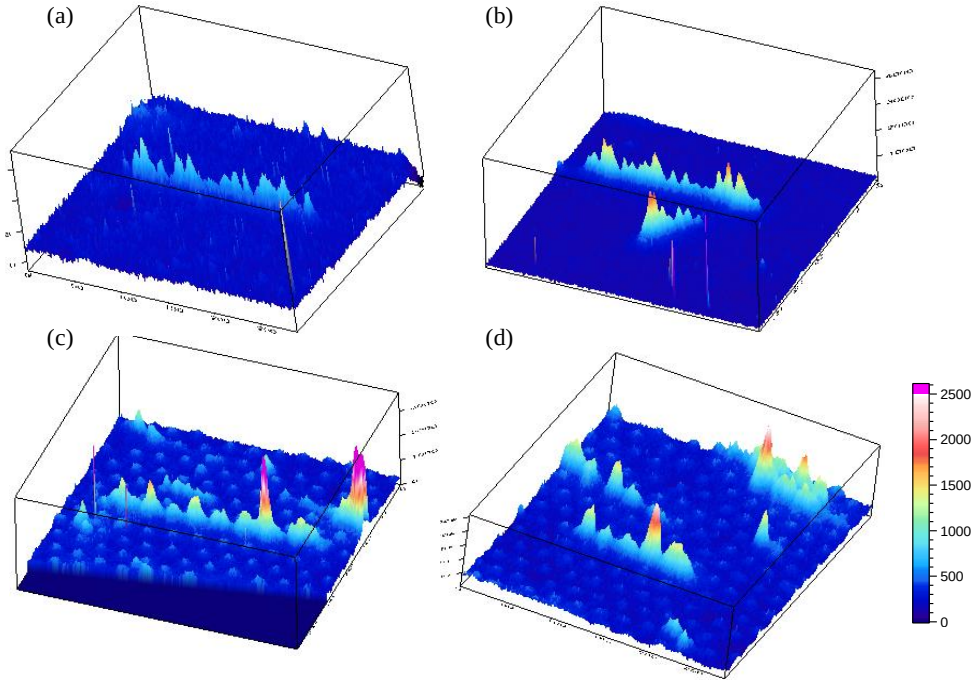

Figure 4.36: 3D Fluorescence images of DNA-TOTO-1 stretched over (a) glass (b) a rough gold surface (c) and (d) gold nanovoids. The fluorescence image and intensity profiles were normalised to 30 s integration time and fluorescence background due to the substrate surface was subtracted. The DNA strands can be seen in figure (a) Figure 4.33(b) in section 4.5.1, (b) Figure 4.34(b) in section 4.5.2, and (c) Figure 4.35(d)(i), and (d) Figure 4.35(d)(ii) in section 4.5.3.

The maximum fluorescence intensity line along the DNA strand was found from the rotated fluorescence image (red line in Figure 4.37(a)). Each point of the maximum intensity line was then extended by 20 pixels either side to form a line perpendicular to the DNA section (green line in Figure 4.37(a) and (d)). The fluorescence intensity of each point of that perpendicular line was then summed to give the total intensity of the perpendicular line. For DNA stretched over glass, rough gold and over the nanovoid substrate outside the nanovoid region (dark blue region in Figure 4.37(b)) the average fluorescence background intensity from sample regions free of DNA was determined ("average value"). The minimum fluorescence intensity where DNA is present (the "threshold value") was determined for each sample.

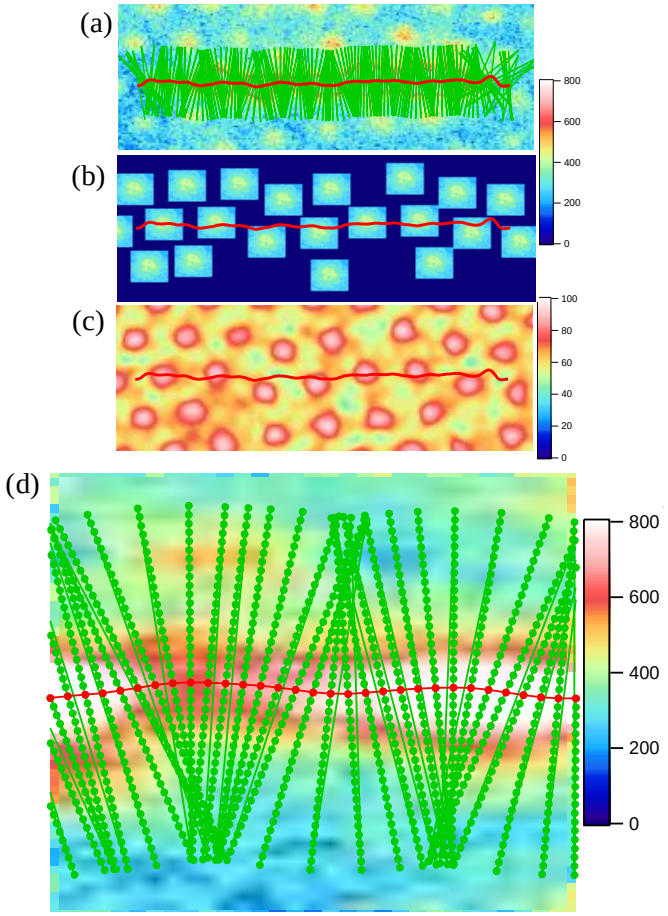

Figure 4.37: Method for obtaining the total background-subtracted fluorescence signal integrated over the TOTO-1 DNA cross-sectional fluorescence width. All images are rotated so the DNA strand is aligned horizontally, and all images show the line of maximum fluorescence intensity (red line); (a), (d) fluorescence image showing the line perpendicular to the maximum fluorescence intensity line (green), Figure 4.37(d) is a close-up along a section of the DNA strand in Figure 4.37(a); (b)background fluorescence image due to nanovoids in the vicinity of the DNA strand, each square represents the average fluorescence signal due to a number of nanovoids nearby the DNA strand; (c) bright field image, showing the location of all nanovoids.

For each substrate the fluorescence background intensity at each pixel along the perpendicular line was taken to be (a) the fluorescence intensity of that pixel, if the pixel intensity is below the "threshold value", or (b) a constant, equal to the "average value", if the pixel intensity exceeds the "threshold value". For regions of DNA strand located over a nanovoid (coloured squares in Figure 4.37(b)), the fluorescence background was taken to be the fluorescence intensity of an equivalent DNA-free region of nanovoid, as averaged over ten DNA-free nanovoids. The location of each nanovoid underneath a DNA strand (coloured squares in Figure 4.37(b)) was determined from the relevant bright field image (Figure 4.37(c)).

Figure 4.38 shows the total background-subtracted fluorescence signal integrated over the TOTO-1 DNA cross-sectional fluorescence width, along the TOTO-1-DNA strand length, for strands stretched over glass, rough gold and the gold nanovoid substrate. DNA strands stretched to a similar length are compared. Figure 4.38(a) shows the fluorescence profile of DNA stretched to about 8 to 10 μm. Over glass, the cross-sectional fluorescence intensity varies from 2,250 to 6,660 counts or 3,040 to 10,710 counts (Figure 4.38(a)(i)). Over rough gold, the intensity ranges from 3,250 to 11,420 or from 4,685 to 14,870 (Figure 4.38(a)(ii)). Over the gold nanovoids, the fluorescence intensity varies from 3,760 to 30,100 counts (Figure 4.38(a)(iii)) or from 3,460 to 17,640 counts (Figure 4.38(a)(iv)). Over the nanovoid substrate, the highest intensity peaks along the stretched TOTO-1-DNA strand are located above a nanovoid (red arrows in Figure 4.38(a)(iii) and (a)(iv)), and range between 11,470 and 30,100 counts, which is up to 4.6 times and 2.6 times the maximum fluorescence intensity seen over glass and rough gold, respectively.

Figure 4.38(b) shows the fluorescence profile of DNA stretched to about 6 μm. Over glass, the cross-sectional fluorescence intensity varies from 2,800 to 7,070 counts (Figure 4.38(b)(i)). Over rough gold, the intensity ranges from 2,370 to 11,340 counts or from 3,090 to 14,360 counts (Figure 4.38(b)(ii)). Over the gold nanovoids, the background-subtracted intensity varies from 6,800 to 25,230 counts (Figure 4.38(b)(iii)), or from 4,280 to 22,800 counts (Figure 4.38(b)(iv)). Again, for TOTO-1-DNA stretched over the nanovoid substrate, the highest intensity peaks along the stretched DNA strand are located above a nanovoid (red arrows in Figure 4.38(b)(iii) and (a)(iv)), varying between 22,800 and 25,230 counts, which is up to 3.6 times and 2.2 times the maximum fluorescence intensity over glass and rough gold, respectively.

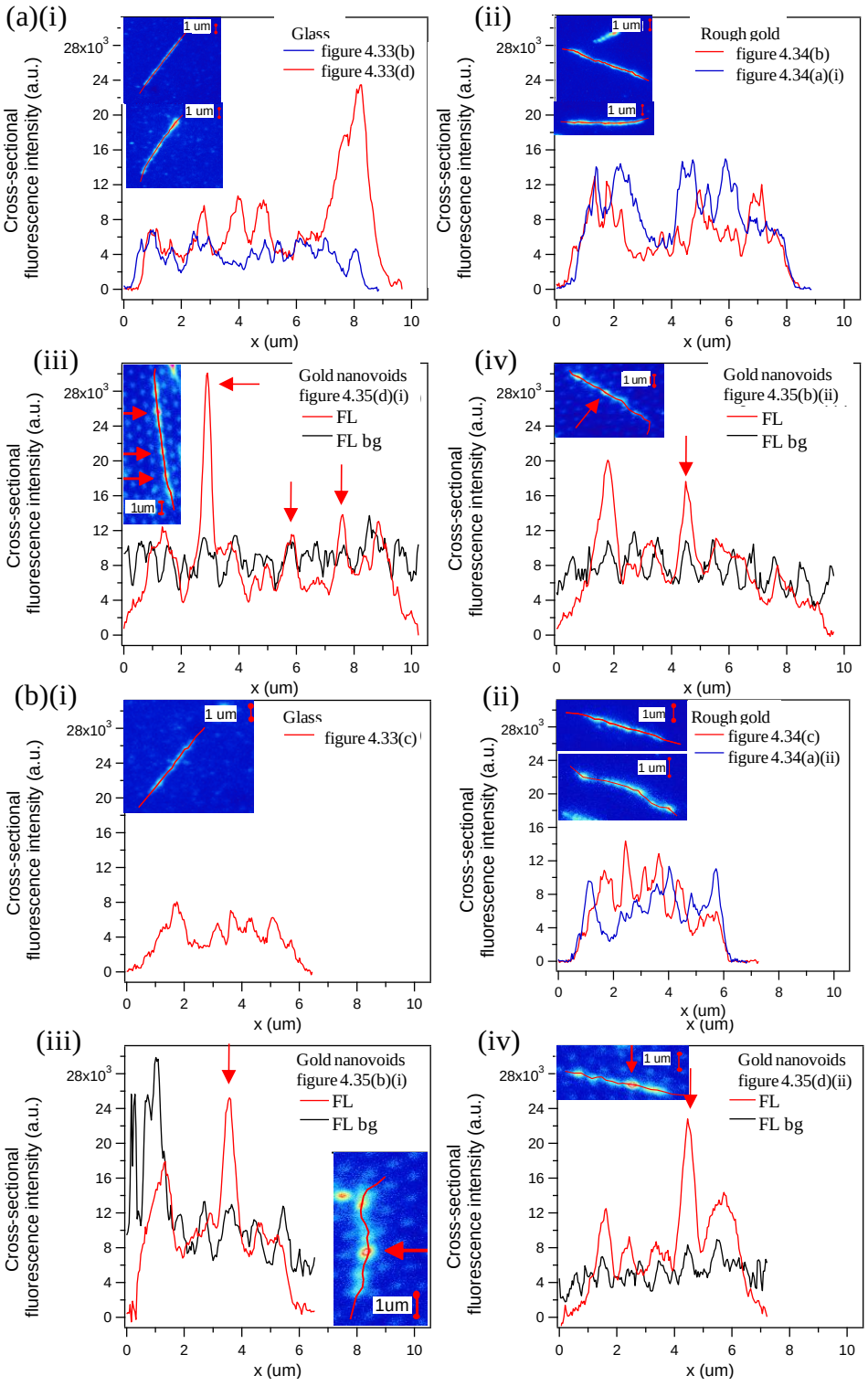

Figure 4.38: Total fluorescence (FL) signal integrated over the fluorescence cross-sectional width of TOTO-1 DNA, for stretched lengths equal to (a) 8 to 10 µm or (b) 6 µm, over (i) glass (ii) rough gold and (iii), (iv) gold nanovoids. Red/blue and black lines are the profiles of the total fluorescence (background subtracted) (FL) and of the total fluorescence background due to the nanovoid substrate (FL bg), respectively. Each DNA strand can be seen in the figure indicated in the legend.

Comparing the minimum cross-sectional fluorescence intensities over glass with those over rough gold and the gold nanovoid substrate, the lowest intensities occur over glass, suggesting fluorescence quenching by the rough gold surface is either not taking place or its effects are negated by other processes, such as fluorescence enhancement by radiative SPP over rough gold or higher reflectivity of the fluorescence signal off gold compared to glass.

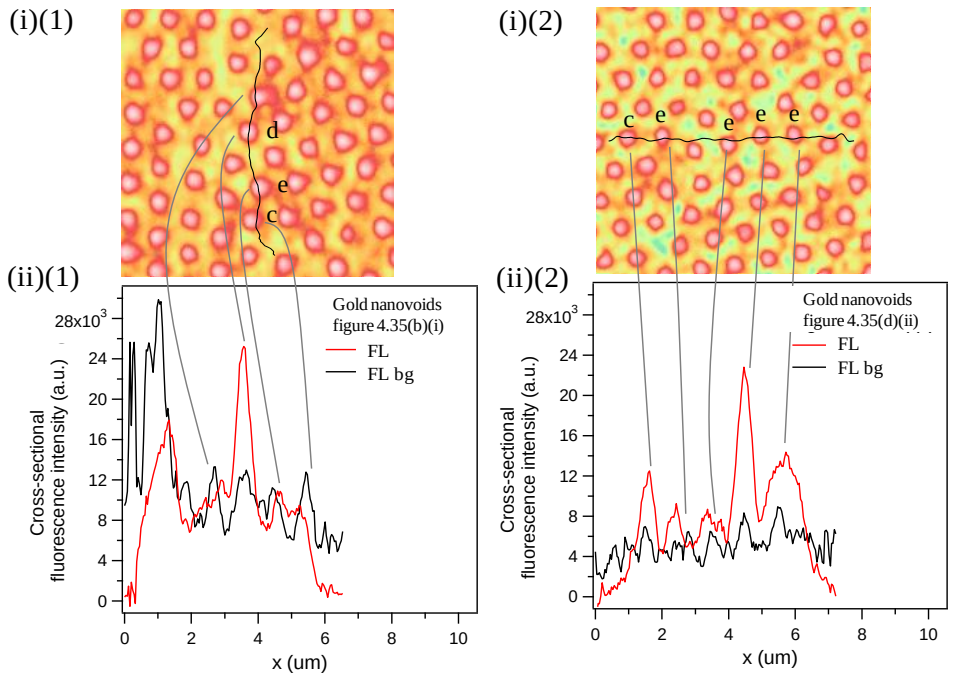

Figure 4.39: (i) Bright field images of the nanovoid sample showing the profile of the maximum fluorescence intensity signal along the stretched TOTO-1-DNA; (ii) The total fluorescence (background subtracted) (FL) and the total fluorescence background due to the nanovoid substrate (FL bg) integrated over the fluorescence cross-sectional width of TOTO-1 DNA; Each DNA strand can be seen in the figure indicated in the legend. Letters in Figure 4.39(i) illustrate possible DNA configurations as shown in Figure 4.40.

The following configurations of stretched TOTO-1-DNA over nanovoids can be envisaged to occur, as illustrated in Figure 4.40: (a) DNA fully stretched over the nanovoid (b) DNA partially stretched over the nanovoid (c) DNA ends ending inside a nanovoid (d) DNA over the nanovoid centre, and (e) DNA strand offset from the nanovoid centre. If the fluorescence peaks over the nanovoids are due to Mie-SPP induced fluorescence enhancement, then the fluorescence enhancement would depend on the relative position of the TOTO-1-DNA strand and the nanovoid. In order to understand the results obtained for the DNA strands with TOTO-1

stretched over the gold nanovoids we need to consider the Mie and Bragg SPP modes as well as the limitations of the imaging approaches.

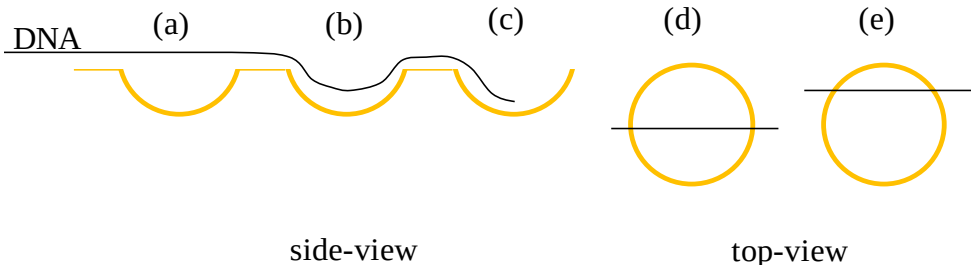

Figure 4.40: Proposed configurations of TOTO-1-DNA stretched over nanovoids (a) DNA fully stretched over the nanovoid (b) DNA partially stretched over the nanovoid (c) DNA strand ends inside a nanovoid (d) DNA located over the nanovoid centre, and (e) DNA strand offset from the nanovoid centre.

4.5.5 Evaluation of the fluorescence Images of DNA-TOTO-1 Molecules Stretched over Gold Nanovoids in Light of the Surface Plasmon Polariton Modes Supported by the Gold Nanovoid Substrate

Experimental data is compared with theoretical data obtained for the plasmon modes for a water-immersed void of diameter $D_{void}=989\ nm$, film thickness $d=157\ nm$, at 2.26 and 2.39 eV (which is the range in which fluorescence is detected) (Figure 4.28 in section 4.4.2.1).

4.5.5.1 Mie Plasmon Modes

The strongest Mie mode at normal incidence is the ^{1}F mode ($m=1$, $l=3$) (Figure 4.12(b) in section 4.3.2.1 and Figure 4.13(b) in section 4.3.2.2). It is proposed that excited state TOTO-1-DNA located within the highest electric field of the ^{1}F mode and energetically in resonance with the ^{1}F mode can non-radiatively excite the ^{1}F Mie mode via a resonant near-field interaction (section 4.1.2.2.2). The Purcell factor, which quantifies how much quicker an excited fluorophore non-radiatively excites a resonant SPP mode compared to coupling to resonant far-field radiation, depends on the density of states of the SPP mode compared to that of far-field radiation in free space[259] (equation 4.12 in section 4.1.2.2.2). Thus, the efficiency at which TOTO-1-DNA excites the ^{1}F Mie mode (the in-coupling efficiency) is expected to increase with increasing near field

intensity of the ^{1}F mode at the TOTO-1-DNA fluorescence energy. The excited ^{1}F mode can then quickly couple to far-field radiation of the same energy. The efficiency at which the ^{1}F Mie mode couples to far-field radiation (the out-coupling efficiency) increases with the optical density of states of far-field radiation,[259] which increases with energy (appendix C.2). Using the BEM model, the 2D intensity profile and strength of Mie modes excited by far-field radiation of a given energy, polarisation state and incidence angle can be modelled. The resulting Mie mode intensity indicates the efficieny at whicha particular far-field radiation state excites the SPP mode. The out-coupling efficiency of a SPP mode to far-field radiation is proportional to the efficiency at which far-field radiation excites the SPP mode [260], so that the intensity of a Mie mode excited by a given far-field radiation state indicates the out-coupling efficiency to that same far-field radiation state. The net effect of fast coupling from excited state TOTO-1-DNA located within the electric field of an energetically resonant ^{1}F Mie mode and subsequent ^{1}F Mie mode emission into the far-field is an increase in the radiative decay rate and thus fluorescence intensity.

Figure 4.41(a) and Figure 4.42(a) shows the 2D and radial intensity profile, respectively, of the ^{1}F mode, as excited by 2.26 eV, p-polarised light at normal incidence. It can be seen that the strongest electric field intensity, which equals 12.5, is located at the void centre ($x=0$ *nm*) at height $z=158$ *nm* above the top void plane (Figure 4.41(a) and Figure 4.42(a)). With reducing vertical height z above the top void plane, the intensity at the void centre ($x=0$ *nm*) falls, with two intensity maxima developing at $z<65$ *nm* (Figure 4.42(a)). At $z=0$ *nm*, the two maxima have intensity equal to 5.3, and are located at a radial distance equal to $|x| = (112 \pm 8)$ *nm*, while the central intensity (at $x=0$ *nm*) is reduced to 4 (Figure 4.41(a) and Figure 4.42(a)). As a reminder, the electric field intensity is referred to as the magnitude of the square of electric field amplitude, normalised to that of an incident plane wave.

The variation in ^{1}F Mie profile with *x* and *z* suggests that the efficiency at which excited state TOTO-1-DNA couples to the ^{1}F Mie mode (in-coupling) and hence Mie plasmon-induced fluorescence enhancement depends on the vertical and radial location of the TOTO-1-DNA above the nanovoid. Efficient in-coupling is expected at normalised SPP intensities greater than 1. The highest in-coupling efficiency is expected to occur at the void centre ($|x| = 0\ nm$) for *z>65 nm*, and at larger radial distances, of up to $|x| = 112\ nm$, for *z* between 0 and 65 nm (Figure 4.42(a)). However, the double peak in the electric field intensity profile seen in the bottom of the void at *z=0 nm* to *z=65 nm* is optically irresolvable due to diffraction effects (section 4.5.5.3). The in-coupling efficiency will be greatest at *z=158 nm*, *x=0 nm*, and will reduce with decreasing height *z*, according to the Mie field intensity evolution with *z*.

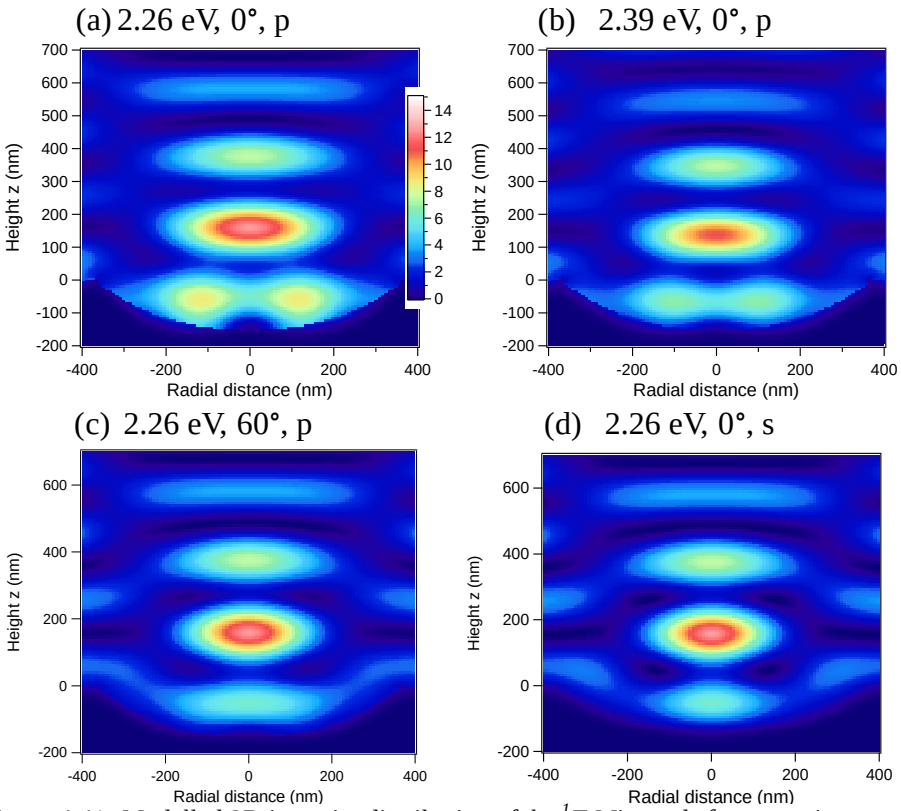

Figure 4.41: Modelled 2D intensity distribution of the ^{1}F Mie mode for water-immersed gold nanovoid of diameter D_{void}=989 nm and height d=157 nm, incident light parameters are (a) 2.26 eV, 0° incidence, p-polarised, (b) 2.39 eV, 0° incidence, p-polarised (c) 2.26 eV, 60° incidence , p-polarised (d) 2.26 eV, 0° incidence, s-polarised. Modelled by BEM.

Figure 4.41(b), (c), (d) and Figure 4.42(a), (b), (c) show the effect upon the ^{1}F Mie mode intensity profile of changing the energy, incident angle, and polarisation state of the incident light, resepctively. The 2D intensity profile of ^{1}F Mie mode that couples to s-polarised light (2.26 eV, normal emission angle) is shown in Figure 4.41(d) and Figure 4.42(c)). The ^{1}F mode couples equally strong to s and p-polarised light at x=0 nm (Figure 4.42(c) and (d))., and more strongly to p-polarised light than to s-polarised light for $|x| > 0$ *nm* (Figure 4.42(c)). Thus, it is expected that Mie radiation contains more p-polarised than s-polarised light. However, both s-and p-polarised light is detected experimentally.

The variation of the 2D field distribution of the ^{1}F mode with the angle of the incident light is discussed in more detail below. With oil-immersion (refractive index *n=1.515*) and an imaging objective (plan-apochromat x100, numerical aperture *N.A.=1.4*), the fluorescence microscope has a maximum acceptance angle equal to $\theta = \sin^{-1}\left(\frac{NA}{n}\right) = \sin^{-1}\left(\frac{1.4}{1.515}\right) = 67.5°$. Thus, emission from Mie plasmons directed into an angle of up to 67.5º can be detected. The 2D intensity profile of ^{1}F Mie mode that couples to 2.26 eV, p-polarised light at an emission angle of 60° is shown in Figure 4.41(c). At *x=0 nm*, the ^{1}F Mie mode couples equally strong to far-field radiation of emission angles between 0° and 60° (Figure 4.42(b) and (d)), and at *x>0 nm*, the ^{1}F Mie mode couples strongest to far-field radiation with zero emission angle, and increasingly weakly to radiation with increasing emission angles (Figure 4.42(b)). Thus, TOTO-1-DNA located at *x=0 nm* will be equally likely to result in Mie plasmon radiation that is emitted into angles of 0° to 60° to the normal, and TOTO-1-DNA located *at x>0 nm* will result in ^{1}F Mie plasmon-induced enhanced fluorescence that is more likely to be emitted into an emission angle at 0° than into larger emission angles. The difference in coupling efficiency to different emission angles would depend on *z* and *x* (Figure 4.42(b)). However, in the microscopy image, all emission angles up to 67.5° are detected, and therefore the different

coupling efficiencies to different emission angles up to 67.5° should not affect the actual image intensity.

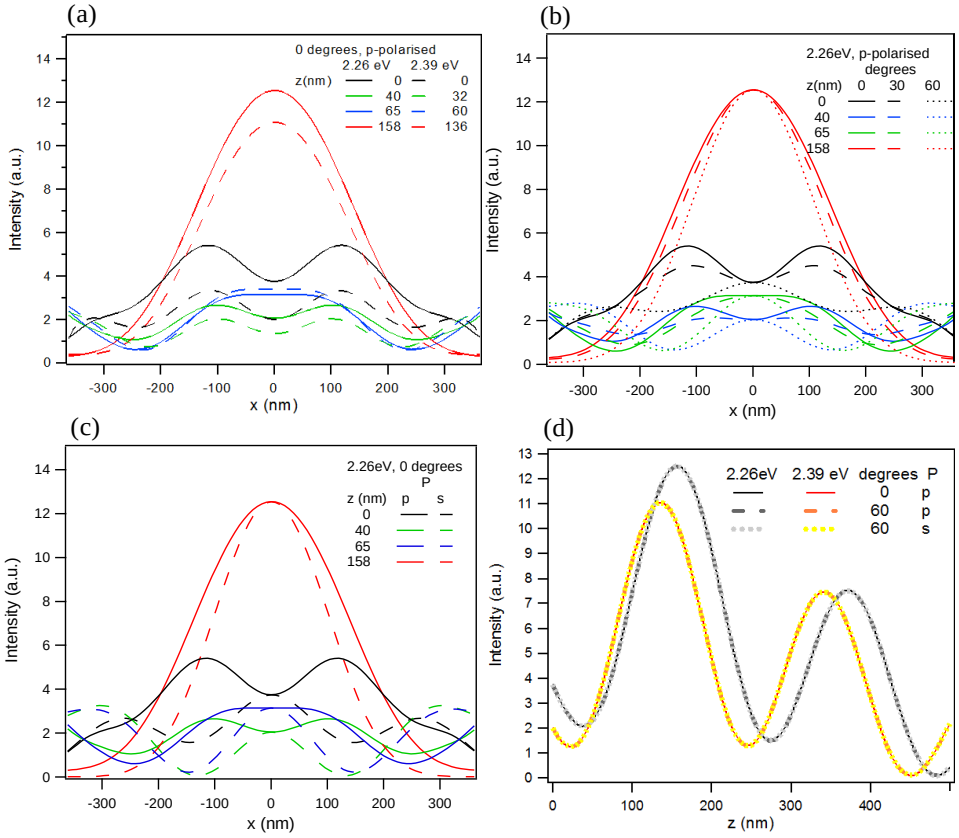

Figure 4.42: Modelled intensity profile of the ^{1}F Mie mode in a water-immersed nanovoid of diameter D=989 nm and height d=157 nm: (a-c) radial intensity profile at different heights z above the top void plane, dependence on incident light (a) energy(b) incidence angle (c) polarisation state; (d) intensity profile at radial distance x=0 nm, dependence on the distance above the top void plane (z), energy, polarisation state and incidence angle; x is the radial distance from the void centre, z is the vertical distance above the top void plane. Modelled by BEM.

At 2.39 eV, the electric field intensity distribution of the ^{1}F Mie modes does not change significantly to that seen at 2.26 eV (Figure 4.41(a) and (b) and Figure 4.42(a)). The main changes that do occur with increasing energy are a reduction in the peak intensity and a shift of the Mie field intensity distribution to lower *z* values by a few nanometers (Figure 4.42(a) and (d) and Figure 4.41(b)). In particular (i) the maximum intensity at *x=0 nm* is reduced from 12.5 (2.26 eV) to 11.1 (2.39 eV) and is located at a reduced height of *z=136 nm* (Figure 4.42(a) and (d)), (ii) a single peak intensity at *x=0 nm* is maintained for heights exceeding *z>60 nm* (2.39 eV) instead of *z>65 nm* (2.26 eV) (Figure 4.42(a)), (iii) the

double intensity peak at *z=0 nm* is located at the same radial distance (Figure 4.42(a)), but reduced in intensity from 5.3 (2.26 eV) to 3.3 (2.39 eV) (Figure 4.42(a)). As a result, the fluorescence enhancement efficiency for TOTO-1-DNA located above a nanovoid will have a slightly different dependence on vertical position above the nanovoid top plane depending on the energy (Figure 4.42(d)).

4.5.5.2 Bragg Plasmon Modes

In modelling Bragg plasmon modes of the nanovoid substrate, only plasmon scatter off the nearest voids are considered, as Bragg plasmon bands due to scattering from voids further away are much weaker.[287] Also, the high order periodicity of the substrate allows incident light to diffract off the substrate. These non-plasmonic diffraction modes, however, are much weaker than the Bragg plasmon modes, and are thus neglected in the model here.[287]

Figure 4.43 shows the modelled Bragg plasmon modes on a 2D lattice of gold nanovoids of periodicity *p=1090 nm*, immersed in water, at sample orientation angle $\varphi=0°$ and $\varphi=90°$. The Bragg plasmon modes that are in resonance with the detected TOTO-1 emission energy (between 2.26 and 2.39 eV) are *(m,n)=(1,1), (0,1) (1,0)* and *(m,n)=(0,-1)* (Figure 4.43), and are thus expected to get excited via near-field dipole-dipole interaction by nearby excited state TOTO-1-DNA. Excited SPP either relax non-radiatively via heat, which quenches fluorescence intensity (section 4.1.2.1), or quickly re-emit the excitation energy, which is associated with fluorescence enhancement (section 4.1.2.2.2). SPP radiation of the excited Bragg modes between 2.26 and 2.39 eV occurs into specific angles below the 67.5° cut-off limit set by the fluorescence–microscope objective, and can therefore be detected in fluorescence images.

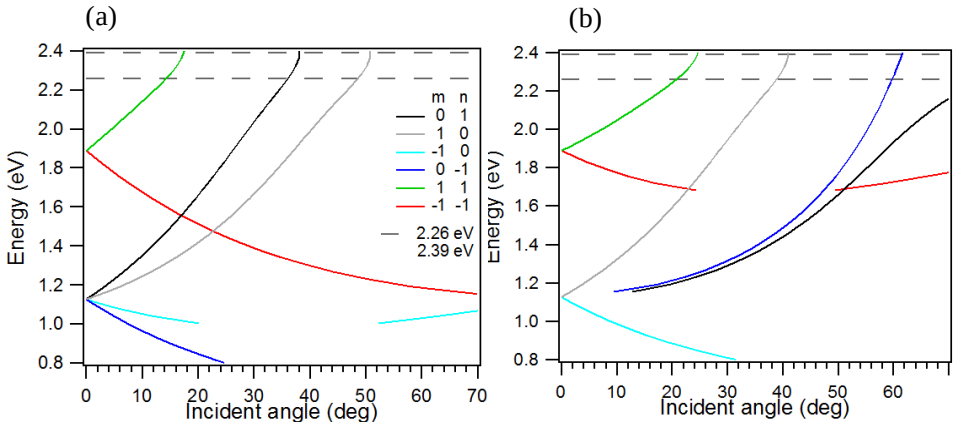

Figure 4.43: Modelled Bragg modes in a 2D hexagonal gold nanovoid lattice of periodicity p=1090 nm, immersed in water, at sample orientation phi equal to (a) 0° (b) 90°.

4.5.5.3 Fluorescence Imaging Limitations

We will now consider the limitations of the imaging method for the samples studies here. The fluorescence is focussed with a microscope objective lens (plan-apochromat x100) and detected with a CCD camera, such that diffraction effects by the lens and pixelation of the CCD camera need to be taken into account. Light passing through an objective lens will undergo interference at the image plane, causing an interference pattern, consisting of a central intensity peak and concentric, lower intensity circles, an Airy diffraction pattern, to form for each light emitting point of the sample. The DNA staining concentration was bp:TOTO-1=1:0.16 (or 6.25:1). Assuming a fully stretched DNA strand contains 10 bp per 3.4 nm of extended DNA strand, then 6.25 bps (1 TOTO-1 molecule) occupy *6.25*3.4/10~2.1 nm*. The modelled radial Mie field intensity profile contains 1 data point every 8 nm, which is less frequent than the theoretical TOTO-1 staining (which has 1 about TOTO-1 every 2.1 nm), so that each point on a Mie intensity curve can be approximated to represent the SPP-coupled fluorescence intensity of a TOTO-1 molecule along a DNA strand extended over a nanovoid. Assuming fluorescence is incoherent, in which case intensities can be summed up, the diffraction-corrected intensity at point *x* on the Mie curve is modelled by summing the contributions from the Airy pattern intensity of each point in the Mie intensity curve at point

x. Figure 4.44(a) shows the theoretical effect of diffraction on a hypothetical Mie-SPP enhanced fluorescence intensity profile.

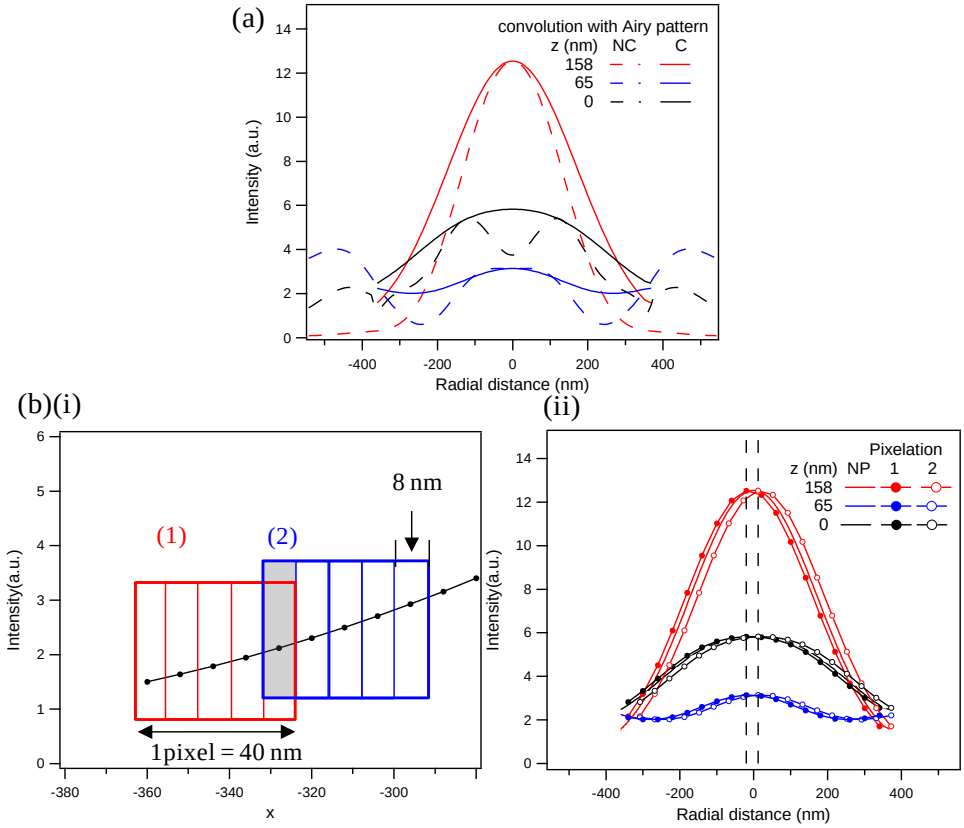

Figure 4.44: Theoretical effect of (a) diffraction and (b) CCD pixelation, on hypothetical Mie-SPP induced fluorescence enhancement curve, for TOTO-1-DNA located at various heights z above the nanovoid top plane. (a) Diffraction by a circular lens gives rise to an Airy pattern at each point along the Mie intensity curve, which each contributes to the intensity at each point. Non-convoluted (NC) and convoluted (C) Mie intensity curves are displayed. The Airy pattern is estimated with a Gaussian curve, and the convoluted curve is normalised to the highest intensity peak on the non-convoluted curve. (b)(i) two possible locations of a pixel (red and blue squares) relative to a specific data point (grey area) (ii) theoretical effect of pixelation on the Mie electric field profiles for the convoluted Airy pattern (NP), and convoluted Airy pattern, for pixel locations for which the first pixel contains (1) all the first 5 data points or (2) only the last of the first 5 data points of the Mie curve. The Mie profiles were those at 2.26eV, for p-polarised emission at 0°.

It can be seen that diffraction effects broaden the intensity profile and makes the double peak at *z=65 nm* irresolvable, as well as reducing the intensity contrast (Figure 4.44(a)). The double peak in the Mie intensity profile, present for heights $0<z<65$ *nm*, is not resolved as it is separated by at most 225 nm (at *z=0 nm*), which is less than the theoretically least resolvable separation, the Rayleigh distance, which is equal to $1.22*\lambda/(2*NA)=1.22*(520 \text{ to } 550 \text{ nm})/(2*1.4)=227 \text{ to } 240$ *nm*, where λ is

the wavelength, and *NA* is the numerical aperture. Thus, diffraction effects introduced by the optical detection system are expected to yield only a single fluorescence intensity peak centred at the void centre. The full-width-half-maximum (FWHM) of the convolved intensity profiles at *z=158/65/0 nm* is equal to *FWHM=370/256/464 nm*. The peak height was assumed to equal the peak height minus the minimum intensity on the convolved curve. Figure 4.44(b)(ii) shows the effect of CCD pixelation on the convoluted intensity profile. Each pixel extends over ~ 40 nm, while each point on the modelled curve occupies 8 nm, so that each pixel intensity was approximated as the average intensity over *40/8=5* data points (Figure 4.44(b)(i)). The exact position of the fluorescence peak relative to the pixel area determines the shift in fluorescence peak induced by pixelation (Figure 4.44(b)(i)). The maximum shift in fluorescence peak due to pixelation is 20 nm (Figure 4.44(b)(ii)(1)). This agrees with findings from Stelzer,[327] according to which pixelation introduces ambiguities as to the exact position of intensity maxima and minima, as well as reducing contrast and hence resolution. However, the pixel size on our camera is small enough as not to significantly affect resolution (Figure 4.44(b)(ii)).

In summary, for TOTO-1 labelled DNA stretched over a gold nanovoid substrate, the fluorescence intensity modulation is expected to depend on the location above the nanovoid substrate. It is expected that DNA strands located over the top gold plane show similar fluorescence intensities as observed for TOTO-1-DNA stretched over a rough gold substrate (section 4.5.2). Non-radiative coupling to Bragg SPP and subsequent energy loss by heat (fluorescence quenching) or re-emission of the excitation energy is also expected to occur over the top gold plane (Figure 4.43 in section 4.5.5.2), for emitter-metal separations up to 200 nm.[266] Such SPP induced fluorescence enhancement would be visible as the SPP emission angle is within the angular detection cone of 67.5° of the objective used in the fluorescence microscopy setup (Figure 4.43 in section 4.5.5.2). Over the gold nanovoid region it is expected that the ^{1}F Mie plasmon mode can be non-radiatively excited by TOTO-1-DNA located

within the strong Mie electric field, which occurs for vertical distances above the top void plane of *z=0 nm* up to about *z=270 nm* (Figure 4.42(d) in section 4.5.5.1). The in-coupling efficiency to the ^{1}F Mie mode is anticipated to be greatest at the void centre at heights between *z=136 nm* and *z=159 nm* above the top void plane, where the Mie electric field intensity is the highest (Figure 4.42(a) in section 4.5.5.1). The in-coupling efficiency is expected to be lower at lower points within the nanovoid, due to a weaker Mie plasmon field intensity. Diffraction effects introduced by the optical imaging system are expected to yield minor differences as shown in Figure 4.44, and the greatest fluorescence intensity is predicted to be over the void centre for all heights of TOTO-1-DNA over the nanovoid, while pixelation will only introduce peak shifts by up to 20 nm.

4.5.6 Radial Fluorescence Intensity Profiles of TOTO-1 Incorporated into DNA Strands Stretched over Gold Nanovoids

We have seen in section 4.5.5.1 that the non-radiative coupling efficiency from excited state TOTO-1-DNA to the ^{1}F Mie mode in the gold nanovoid and hence fluorescence enhancement is expected to depend on the radial distance from the void centre and the vertical distance above the top void plane at which the TOTO-1-DNA is located. To consider the possibility of ^{1}F Mie plasmon-induced fluorescence enhancement of TOTO-1-DNA stretched over gold nanovoids, the experimental fluorescence intensity along the centre of the stretched TOTO-1-DNA strand as a function of radial distance from the void centre is now evaluated. For this, the maximum fluorescence intensity line profile of DNA strand stretched over nanovoids is automatically determined with a macro from the rotated fluorescence image (section 4.5.4), and drawn onto the bright field image that is rotated by the same amount (Figure 4.45(b) top and middle images). The offset in the x and y direction between fluorescence and bright field image is zeroed by overlapping the fluorescence and bright field image and shifting the bright field image by an amount in the x and y direction so that the voids in both images exactly overlap. The void centre is determined

from the bright field images (Figure 4.45(b) bottom), allowing the variation in fluorescence intensity of the stretched TOTO-1-DNA as a function of radial distance from the void centre to be determined, and the fluorescence background due to the nanovoid to be subtracted. Voids with bright field intensities that are not radially symmetric (Figure 4.45(b)(ii)(2) and (b)(ii)(3)) are not analysed further, as the void asymmetry might change the Mie plasmon field distribution from that of radially symmetric voids modelled here. The fluorescence and bright field images of all analysed strands are shown in appendix C.16. Figure 4.45(a) shows the experimental radial fluorescence intensity profiles constructed for those sections of DNA strand where a fluorescence peak is located above a gold nanovoid in Figure 4.35(a) and (c) in section 4.5.3. It can be seen that the experimental fluorescence intensity increases the closer the distance to the void centre is, and in most cases, is symmetric about the void centre, with the fluorescence peak located over the void centre (Figure 4.45(a)(2-3) and (a)(5-8)). However, one curve shows a shift in peak location by about 100 nm (Figure 4.45(a)(4), while another curve shows a slightly steeper gradient for positive compared to negative radial distances (Figure 4.45(a)(1)). Uncertainties in the location of the fluorescence peak might be introduced in various steps in the analysis: (i) the relative x-y shift between the fluorescence and bright field image can be undone to a maximum accuracy of *1 pixel=40.3125 nm* (ii) the void centre can be located to within 1 pixel. Furthermore, pixelation of an image itself has been shown to introduce ambiguities in the position of intensity maximas,[327] with a pixelation-induced shift in the peak fluorescence with a pixel size of 40.3125 nm being about 20 nm (Figure 4.44(b)(ii) in section 4.5.5.3). Unsymmetrical intensity profiles, on the other hand, might be due to non-uniform DNA strand stretching.

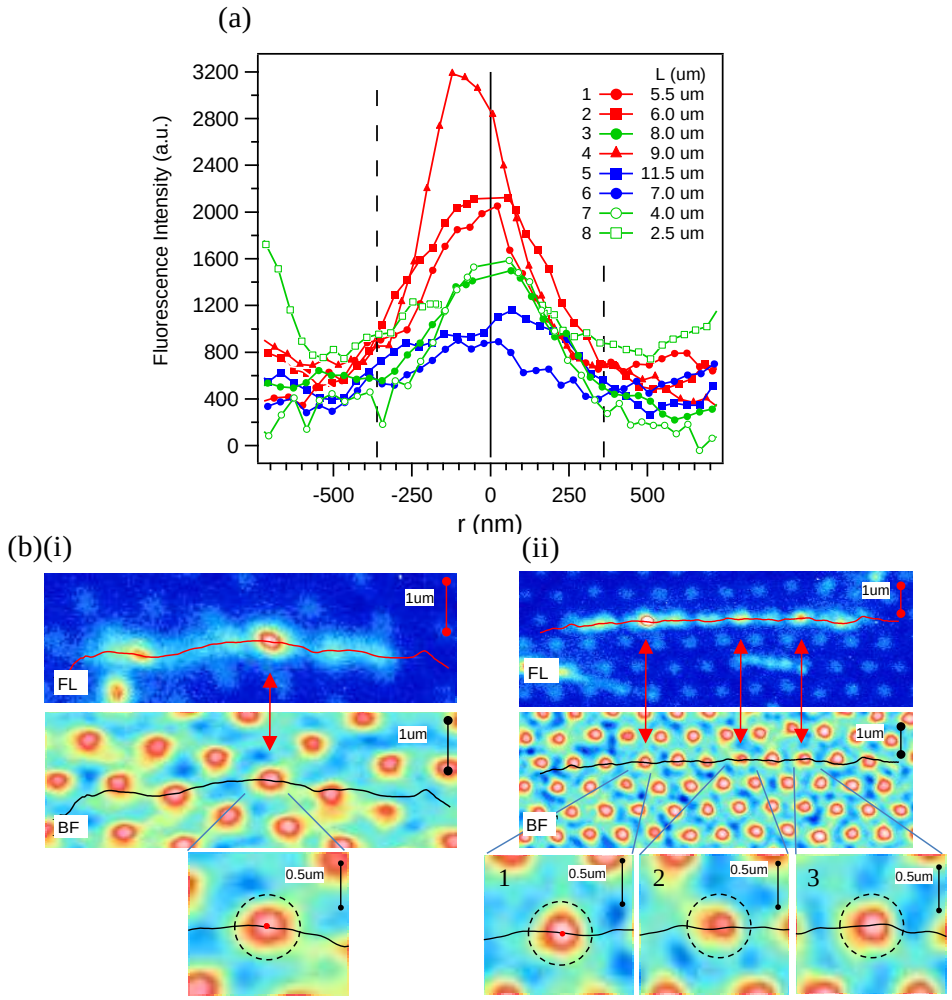

Figure 4.45: (a) Radial Fluorescence intensity profiles of the section of stretched TOTO-1-DNA that is located over a gold nanovoid as indicated with red arrows in (1)Figure 4.35(b)(i), (2) Figure 4.35(d)(ii), (3) Figure 4.35(b)(ii), (4) Figure 4.35(d)(i), (5) Figure 4.35(d)(iii), (6) Figure 4.35(b)(iii), and in appendix C.14, (7) b, (8) c; solid and dashed line indicate the void centre and void rim at r=0 nm and r=722/2=361 nm, respectively; (b)fluorescence (top)(FL) and bright field images (middle)(BF) of the individual stretched DNA strands, line in red (top) and black (middle) indicate line of maximum fluorescence intensity signal along stretched TOTO-1-DNA strand (drawn using a macro), close-up of the bright field-image (bottom) indicate the estimated location of the void rim (dashed circle) and the void centre (red dot) relative to the DNA strand (black line), DNA strands are from (b)(i) Figure 4.35(b)(i), and (b)(ii) Figure 4.35(d)(i) in section 4.5.3. The corresponding images of other DNA strands used in Figure 4.45(a) are shown in appendix C.16.

The increase in fluorescence intensity over the nanovoid region is not the same for all strands located over a nanovoid (Figure 4.45(a)). For instance, consider strands 3 and 4 in Figure 4.45(a), both stretched to a similar length. For strand 3 and 4, the fluorescence intensity within about 60 nm from the void centre is equal to 3,060 and 1,500 counts, respectively, compared to about 770 and 530 counts, respectively, over the

void rim, which is an enhancement by a factor of *3,060/770=4.0* and *1,500/530=2.8*, respectively, compared to over the void rim. The fluorescence increase for sections of TOTO-1-DNA located over the void centre compared to the void rim is summarised in Figure 4.46(b) for all strands in Figure 4.45(a).

The variation in fluorescence enhancement over a nanovoid compared to over glass for different DNA strands is further illustrated. The fluorescence peak intensity over a nanovoid for DNA stretched to about 6 µm ranges between 2,020 to more than 2,100 counts (Figure 4.45(a)(1) and (a)(2)), which represents an increase relative to DNA over glass stretched to a similar length by a factor of ~3.2 (Figure 4.33(c) in section 4.5.1). For DNA stretched to about 9 µm in length, the fluorescence peak intensity over the nanovoid varies from more than 1,410 counts to more than 3,100 counts (Figure 4.45(a)(3) and (a)(4)), which is up to ~ 5.0 times the maximum measured intensity measured for TOTO-1-DNA stretched to a similar length over glass (Figure 4.33(b) in section 4.5.1). The maximum intensity for strands stretched to other lengths varies from 890 to more than 1580 counts (Figure 4.45(a)(6) and (a)(7), respectively). Note that the enhancement in the fluorescence peak for DNA over a nanovoid compared to over glass is slightly different when using the cross-sectional fluorescence width of the TOTO-1-DNA images (section 4.5.4). For instance, when considering the the line of maximum fluorescence intensity along the TOTO-1-DNA strand and the cross-sectional fluorescence intensity width of the TOTO-1-DNA strand, respectively, an enhancement factor of up to 3.2 and 3.6, respectively, is found for DNA stretched to 6 µm in length, and an enhancement factor of up to ~ 5.0 and 4.6, respectively, is found for DNA streteched to 9 µm in length. However, both methods used for evaluation of the fluorescence intensity along the strand give similar enhancement factors.

(a)

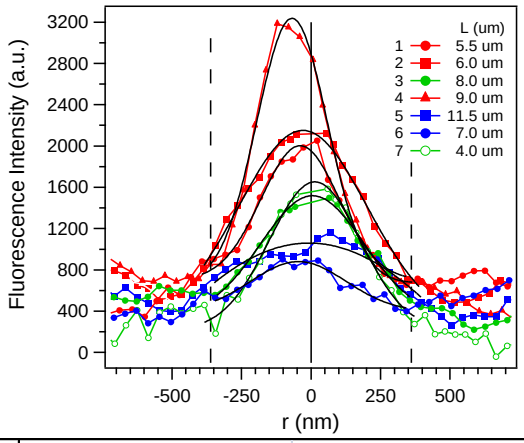

(b)

DNA	Fluorescence intensity		Fluorescence intensity	
	rim	peak	enhancement	FWHM (nm)
1	770	2020	2.6	333
2	810	2110	2.6	549
3	530	1500	2.8	433
4	770	3180	4.1	300
5	600	1100	1.8	1932
6	470	880	1.9	400
7	370	1560	4.2	383

Figure 4.46: Fluorescence peak width along DNA strand length of TOTO-1-DNA strands stretched over the nanovoid centre from Figure 4.45(a) (a) experimental fluorescence intensity profiles (coloured) and Gaussian fits (black) (b) table showing experimental fluorescence intensity enhancement over the nanovoid centre relative to the nanovoid rim, and FWHM of each DNA strand section located over a nanovoid.

Theoretically, above the nanovoid region, SPP- mediated fluorescence enhancement scales with the coupling efficiency to Mie SPP, which scales with the SPP Mie electric field intensity, so that a correlation in the width and intensities between the Mie SPP intensity and the TOTO-1-DNA fluorescence might be expected if the fluorescence is enhanced by fast coupling to radiative Mie SPP. The FWHM of the experimental fluorescence intensity profiles of DNA stretched over the nanovoid centre has been obtained from Gaussian fits to the radial intensity curves of DNA stretched over the void centre (Figure 4.46(a)), and mostly ranges from 300 nm to 550 nm (Figure 4.46(b)). This compares to a predicted FWHM range of 256/370/464 nm of Mie SPP intensity profiles at *z=65/158/0 nm* (for p-polarised light at 2.26eV, 0° incidence, which takes into account the diffraction effects by the detection optics) (Figure 4.44(a) in section

4.5.5.3). The different peak widths at FWHM and fluorescence enhancements for each DNA strand might indicate a variation in DNA-TOTO-1 location above the nanovoid top plane (see Figure 4.46). Variations in height of TOTO-1-DNA above a nanovoid might be introduced by local variations in stretching efficiency along a DNA strand and between different DNA strands. Also, variations in the SPP Mie field distribution might occur between different nanovoids due to slight variations in void size.

In order to investigate further the origin of enhanced fluorescence intensities above nanovoid, fluorescence lifetime measurements were conducted.

4.5.7 Fluorescence Lifetime Measurements

A 2D fluorescence intensity map (30x30 μm) of DNA-TOTO-1 stretched over a glass substrate (Figure 4.47(a)(i)) or the gold nanovoid substrate (Figure 4.47(a)(ii)) is constructed, and the fluorescence intensity decay profiles of individual pixels measured with TCSPC by building a histogram of the delay times between the excitation pulse and single fluorescence photons. The smallest pixel size (highest excitation intensity) that did not result in photobleaching was used, which was 3 μm x 3 μm in size. The pixel fluorescence intensity over the gold nanovoid is consistently higher than over the glass substrate, ranging from 18 to 41 counts and 2 to 12 counts, respectively (Figure 4.47(a)). The increased detected fluorescence intensity over the gold nanovoid substrate compared to the glass substrate might be attributed to (i) higher reflectivity of gold compared to glass, resulting in less loss of TOTO-1-DNA fluorescence (ii) fluorescence enhancement at each pixel (iii) higher DNA density (number of DNA molecules per pixel) over the nanovoid substrate, due to variations in DNA distribution from sample to sample and with location on the sample (Figure 4.31 in section 4.4.3). Figure 4.47(b) shows a typical fluorescence intensity decay curve of DNA-TOTO-1 stretched over a glass substrate (Figure 4.47(b)(i)) and over the gold nanovoid substrate (Figure

4.47(b)(ii)). The experimental intensity decay curve was fit with a multi-exponential curve according to

$$I(t) = y_0 + \sum_{i=1}^{n} a_i \exp\left(-\frac{t}{\tau_i}\right) \tag{4.28}$$

with an average lifetime equal to[316]

$$\langle \tau \rangle = \frac{\sum_{i=1}^{n} a_i \tau_i}{\sum_{i=1}^{n} a_i} \tag{4.29}$$

The relative emission amplitude a_i quantifies the proportion of the sample emitting at lifetime τ_i.[316] The values for a_i and τ_i that best fit the curves are listed in appendix C.18. Over glass a single exponential fit best fits the curve, while over the gold nanovoid substrate a double exponential fit best fits the curve. Depending on the location on the glass substrate (within the 30 x 30 μm^2 map area), the average lifetime over glass ranges from 3.21 ± 0.12 ns to 3.58 ± 0.13 ns (appendix C.18). The fluorescence lifetime of TOTO-1 bound to DNA is reported to be less than that and equal to between 1.7 ns and 2.2 ns.[315-317] It is known that the TOTO-1 fluorescence lifetime increases upon binding to DNA due to increased TOTO-1 torsional confinement about the central methine bridge (section 4.4.2). Torsional confinement reduces the non-radiative decay rate k_{nr}, which increases both the observed decay lifetime t_0 and the fluorescence quantum yield Q_0,[316] according to

$$\tau_0 = \frac{1}{k_r + k_{nr}} \text{ and } Q_0 = \frac{k_r}{k_r + k_{nr}} = \frac{\tau_0}{\tau_r} \tag{4.30}$$

Torsional constriction in carbocyanine dyes has also been shown to occur upon adsorption onto SiO_2 and quartz surfaces, resulting in an increase in lifetime by up to 40 times.[328] Thus, it is reasonable to suggest that the longer lifetime observed for DNA-TOTO-1 stretched over glass surface, of between 3.21 and 3.58 ns, compared to the quoted value of up to 2.2 ns[315-317] for unstretched DNA, could be due to increased TOTO-1 confinement due to the DNA stretching. The range in observed fluorescence lifetime over glass from 3.21 to 3.58 ns could be due to local variations in DNA stretching efficiency.

The fluorescence lifetime measurement for TOTO-1 in DNA strands stretched over the nanovoid substrate contains two lifetime components, which are $1.55\ ns < t_1 < 2.85\ ns$ and $4.93\ ns < t_2 < 7.60\ ns$, with relative amplitudes of $71\% < a_1 < 97\%$ and $3\% < a_2 < 29\%$ (appendix C.18). The majority (71%-97%) of the observed fluorescence comes from the fast lifetime component (<2.85 ns). The second, longer lifetime component over the nanovoid substrate ($4.93\ ns < t_2 < 7.60\ ns$) is longer than the single lifetime component observed over glass ($3.21\ ns < t < 3.58\ ns$). Because (i) DNA stretching might increase the confinement of TOTO-1 and thus increase the observed lifetime, (ii) the stretching efficiency generally reduces with distance from the drop-cast site, and (iii) the variation in stretching efficiency with distance from the drop-cast site is non-identical between different samples (and substrates), then the longer lifetime over the nanovoid substrate compared to over glass might be explained by a locally higher stretching efficiency than over the probed glass area. Figure 4.47(c) shows the lifetime dependence as a function of pixel intensity over the nanovoid substrate. Variations in fluorescence intensity from pixel to pixel due to variations in local DNA concentration cannot be excluded, with a lower DNA concentration expected to yield a lower pixel intensity. Furthermore, the variation in stretching efficiencies of individual DNA strands would be expected to lead to a variation in the long lifetime component and thus fluorescence intensity, with more efficiently stretched DNA strand inducing more torsional confinement in the TOTO-1 and thus increasing the observed lifetime and fluorescence intensity.

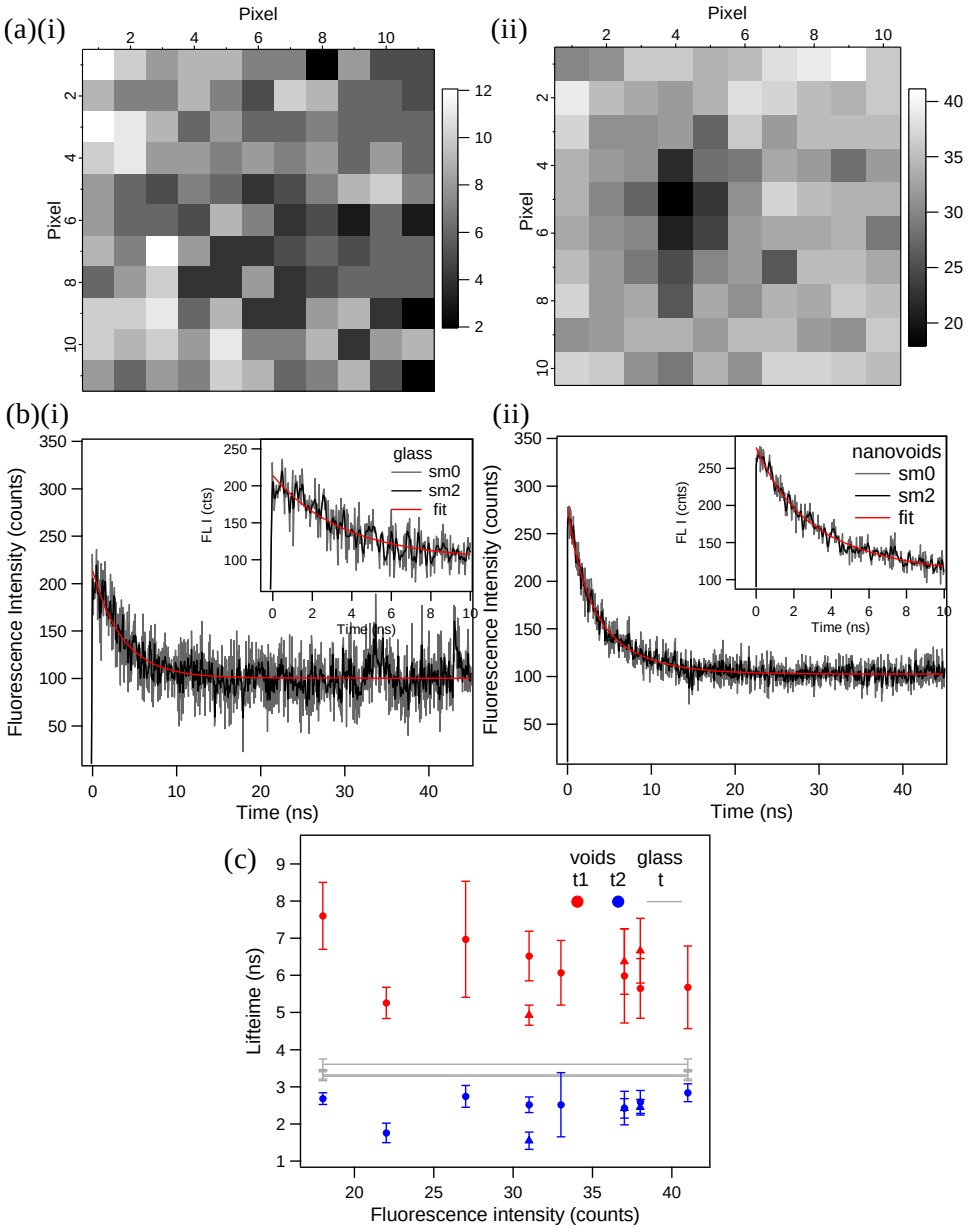

Figure 4.47: Fluorescence lifetime measurements (a) 2D fluorescence intensity map for TOTO-1-DNA stretched over (a)(i) a glass substrate or (a)(ii) a gold nanovoid substrate (b) typical fluorescence intensity decay curve for DNA-TOTO-1 stretched over (b)(i) a glass substrate (b)(ii) gold nanovoid substrate, showing the experimental curve, not smoothed (grey) and smoothed by 2 (black), and the exponential fit to the smoothed curve (red); (c) a plot of the fluorescence lifetime components τ_1 (red) and τ_2 (blue) as measured over the gold nanovoid substrate. Grey line is a guide to the eye of the single exponential lifetime measured over glass. The gold nanovoid substrate is that shown in Figure 4.32(b).

While the shorter lifetime is approximately invariant with intensity, there is a trend towards reduced lifetimes with increased intensity for the longer lifetime component. For example, at fluorescence intensity 18 counts, the long lifetime component equals t_1=*7.60 ns* compared to t_1=*5.68 ns* at 41

counts (Figure 4.47(c) and appendix C.18); The increase from 18 to 41 counts constitutes an intensity increase by 56%, which is accompanied by a reduction in t_1 by 25%, and an increase of t_2 by 9%. According to equation 4.33, a reduction in observed lifetime t_0 coupled with an increase in fluorescence quantum yield is due to an increased radiative decay rate k_r. This contrasts with quenching, which increases the non-radiative decay rate k_{nr}, and thus reduces both the lifetime and the quantum yield (equation 4.4 in section 4.1.2.1). It has been shown that fluorophores nearby SPP supporting metal structures experience enhanced fluorescence intensities and reduced lifetimes due to fast de-excitation to radiating SPP.[324] Thus, the decrease in the longer lifetime component with increased fluorescence intensity seen here could be attributed to SPP coupled emission. Enhanced fluorescence intensities, relative to over glass, have been observed for stretched TOTO-1-DNA located above nanovoids (section 4.5.3 and 4.5.4). Thus, the increased fluorescence intensity and reduced radiative lifetime could correspond to DNA-TOTO-1 located above a nanovoid and within the SPP electric field.

4.6 Conclusion

This chapter presented experimental results on the modulation of the fluorescence intensity and fluorescence lifetime of dyes attached to stretched DNA located over gold nanovoids and compared the experimental results with theoretical predictions of the plasmon resonance modes supported by gold nanovoids of the same dimensions. It was found that the fluorescence intensity increased by up to 5 times when located over the nanovoid centre compared to when over glass. For DNA strands stretched over gold nanovoids, compared to over glass, an extra fluorescent lifetime component was measured and a correlation between increased fluorescence intensities and decreased fluorescence decay lifetimes for the longer decay lifetime component was observed, suggesting that surface Mie plasmon induced fluorescence enhancement occurs over the gold nanovoid region. The intensity increase observed over gold nanovoids compares modestly with other plasmonic gold nanostructures.[18, 329] For instance, a 6 fold fluorescence intensity enhancement observed for AlexaFluo555-labelled anti-Rabbit IgG deposited onto evaporated gold films,[18] while a 8-9 fold enhancement was observed for Alexa488 molecules near a 80 nm gold particle.[329] The fluorescence intensity enhancement might be increased by using dyes that fluoresce at lower energies than TOTO-1, where the Mie SPP resonances are stronger. The advantage of using gold nanovoids as plasmonic substrates is their relative ease of fabrication and the tunability across the visible spectrum of the localised Mie plasmon modes with nanovoid dimensions.

Chapter 5

5 Conclusion and Future Work

5.1 Thesis Summary and Conclusion

There exists a need for a low cost, high throughput, non-invasive and sensitive DNA diagnostic method for cancer patients. It is well known that low copy numbers of aberrant DNA strands are shed into the blood stream of cancer patients, and detection and identification of these could be used as a non-invasive tool for diagnosis. Experiments have shown that (a) the fluorescence of a QD-single stranded oligonucleotide conjugate is quenched upon hybridisation to a complementary oligonucleotide sequence attached with a gold nanoparticle, and that the quenching is reversible upon addition of 10x excess of complementary, unlabelled oligonucleotides.[330] This could be used for a novel detection method of mutations in aberrant DNA strands, which requires stable QD-single-stranded DNA conjugates. The aim of this thesis was to investigate the feasibility of fluorescent colloidal quantum dots (QDs) as potential fluorescent tags to DNA probes and the use of plasmonic nanostructures as a substrate for an increased sensitivity for fluorescence detection of single DNA molecules.

It was found that core/shell QDs are unsuitable for quantitative bio-analysis methods. QD illumination experiments and photo-illumination product analysis under various atmospheric conditions suggest the formation of (i) a water-stabilised trap state in the presence of water molecules and (ii) oxygen radical anions under oxygen. The formation of

oxygen radical anions makes the use of QDs even more unsuitable for bio-analysis, as oxygen radical anions have been shown to induce damage in DNA.[331, 332] Fluorescence microscopy results suggest that single-stranded DNA interacts non-specifically with QDs, whereas evidence for interaction between double-stranded DNA and QDs is limited. This further makes QDs unsuitable for DNA probes, which require specific interaction with DNA only, and thus, fluorophores, instead of QDs, were used as fluorescent labels on DNA strands. Unlike SERS substrates, which require contact with the molecule to be detected, and other plasmonic substrates, a gold nanovoid substrate predicts fluorescence enhancement at greater distances, up to several hundreds of nanometres, from the substrate surface. We have experimentally observed fluorescence enhancement by up to 5 times for fluorophores attached to DNA strands stretched over the gold nanovoid region compared to over glass.

5.2 Suggestions for Future Work

This thesis has investigated the feasibility of quantum dots and gold nanodishes for high resolution and high sensitivity DNA detection. This chapter presents some of the possible future work than can be done.

In future, gold nanovoids could be used in a variety of configurations, including incorporated inside a fluidic microchannel. Molecules inside a fluidic microchannel will be transported along a predictable path, due to the predictable fluid flow profile inside a microchannel, eliminating the dependence on the plug shape, and allowing precise positioning of elongated DNA molecules over gold nanovoids for maximum fluorescence enhancement. The fluidic flow inside a microchannel is pressure driven and laminar (Reynolds number <<1), and the fluid flow profile across the channel width is parabolic, with maximum flow velocity at the centre of the channel and zero velocity at the channel walls[333-336] (Figure 5.1). Thus, an elongated DNA strand will be transported along the centre of the fluidic microchannel.

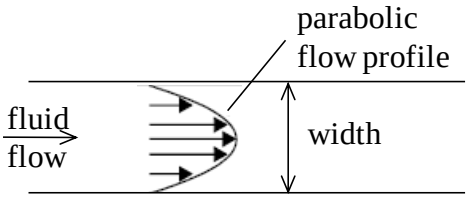

Figure 5.1: Flow profile of laminar fluid flow in a microchannel (adapted from[334]).

In future experiments, a microfluidic flow channel would be printed into the gold nanodish top plane by, for instance, nanolithography,[337] to allow a single elongated double stranded DNA molecule to flow over gold nanodishes along a precise path. Gold nanodishes, compared to randomly patterned plasmonic substrates, would allow fluorescence enhancement at a longer distance from the substrate surface, suitable for fluorescence enhancement of fluorescent emitters in fluid flow, due to surface plasmon polaritons localised within and above the gold nanodishes. Thus, fluorophores tagged to specific sequences in the DNA strand would experience localised surface plasmon polariton- induced fluorescence

enhancement over the gold nanodish region. A DNA strand, tagged with a single fluorophore, flowing over an array of dishes inside a microchannel and fluorescence detection over the whole nanochannel region would yield a sequence of fluorescence peaks, separated in time by time *T* (figure 5.2b).

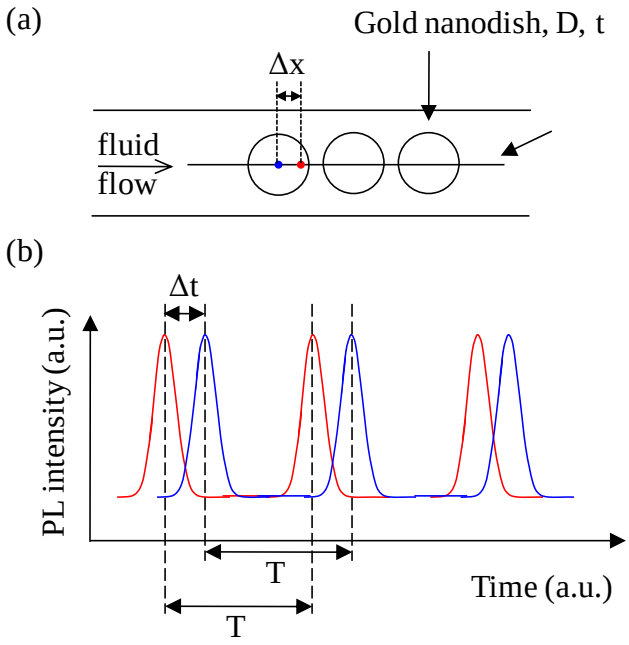

Figure 5.2: Proposed DNA analysis using gold nanodishes (a) a stretched DNA strand is fluorescently tagged at specific DNA sequences, separated by distance Δx, with fluorophores of different fluorescence colours, fluorophore 1(red) and fluorophore 2 (blue). The DNA is transported along the centre of the microchannel, which has gold nanodishes, of diameter D and thickness t, incorporated into it (b) the fluorescence intensity signal from fluorophore 1 (red) and fluorophore 2 (blue) as detected over dishes. The fluorescence peaks of the same fluorophore are separated by time T, and the fluorescence peaks of different fluorophores separated by distance Δx are separated by time Δt.

The fluorescence signals detected in the time domain can be analysed by applying a Fourier Transform, which would yield a specific frequency that depends on the fluidic flow speed, v_{flow}, and the dish diameter, *D*. It is envisaged that by employing fluorophores of different fluorescence wavelengths, mutations in the DNA strand, such as deletions, insertions or single nucleotide polymorphisms, can be detected. For instance, consider two fluorophores, which emit at different wavelengths, separated by a distance *Δx* along a DNA strand (Figure 5.2(a)). As the DNA molecule flows over the nanodishes, both fluorophores will emit with a yield which is dependent upon the position over the nanodishes and thus the intensity will vary with time. The spatial separation between the two fluorophores

will result in a time lag, $\Delta t=\Delta x/v_{flow}$, between the fluorescence intensity peaks of the two fluorophores (Figure 5.2(b)), which, when a Fourier Transform is applied to it, will yield a frequency Δf. A change in DNA length, such as an insertion or a deletion, will result in a change in Δx and thus a change in the time delay Δt, which can easily be detected as a change in the frequency Δf using Fourier Transform. The incorporation of dishes of different diameters into sections along the length of the microchannel would allow more rigorous analysis.

Single nucleotide polymorphism would be detected by using a short single stranded DNA probe that is complementary to the non-mutated sequence or mutated sequence, attached with a different fluorescence wavelength for each case, so that depending on the presence or absence of a single nucleotide polymorphism, a different fluorescence colour will be detected (Figure 5.3).

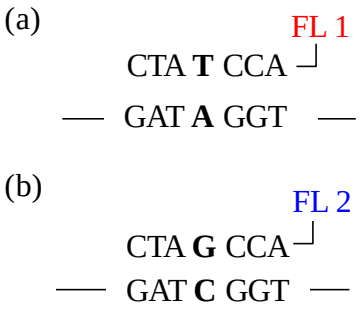

Figure 5.3: Principle for detection of single nucleotide polymorphisms: (a) non-mutated DNA sequence GAT A GGT and (b) mutated DNA sequence GAT C GGT: hybridization between the non-mutated or mutated DNA sequence and fluorescently tagged short complementary DNA sequence occurs, with the fluorescence wavelength of the fluorophore differing for the non-mutated and mutated DNA sequence (bold).

The concept of fluorescence enhancement can be further developed by capping truncated spherical gold microdishes with a planar, semi-transparent mirror to create a hemi-spherical microcavity. Such microcavities have been shown to support confined optical modes at different wavelengths[338, 339] with an intensity enhancement relative to resonant incident light of more than 25 times,[339] which could also be exploited for fluorescence enhancement of fluophores tagged to specific DNA sequences.

A Appendix A

A.1 Electron Energy States in a Semiconductor

Quantum Dots are semiconductor nanocrytsals a few nanometres in diameter in which an electron is confined in all three spatial dimensions, leading to quantum effects. We first consider the case of a bulk semiconductor in 3 dimensions. In the case of a free electron gas the periodic ionic potential from the core ions is neglected and is assumed to be a constant. The time-independent Schrödinger equation for a free electron is equal to

$$-\frac{\hbar^2}{2m_e}\nabla^2\psi(\vec{r})+V\psi(\vec{r})=E\psi(\vec{r}) \qquad \text{(A.1)}$$

where $\vec{r}=(x,y,z)$ is the position vector, m_e is the electron mass and $\nabla^2=(\frac{\partial^2}{\partial x^2}+\frac{\partial^2}{\partial y^2}+\frac{\partial^2}{\partial z^2})$. The wavefunction represents a plane travelling wave, and is equal to

$$\psi(\vec{r},t)=A\exp(i\vec{k}\cdot\vec{r}) \qquad \text{(A.2)}$$

Normalisation yields

$$\int_{-\infty}^{+\infty}\psi^*\psi dV=A^2V=1 \qquad \text{(A.3)}$$

so that

$$\psi(\vec{r})=\frac{1}{\sqrt{V}}\exp(i\vec{k}\cdot\vec{r})=\frac{1}{L^{3/2}}\exp(i\vec{k}\cdot\vec{r}) \qquad \text{(A.4)}$$

The energy of the plane-wave solution is given by the kinetic energy, which is equal to

$$E(KE)=\frac{\hbar^2k^2}{2m_e} \qquad \text{(A.5)}$$

Inside a one dimensional box of length *L*, the wavefunction is a mixture of forward and backwards travelling wave, and is equal to

$$\psi(\vec{r}) = A\exp(i\vec{k}\cdot\vec{r}) + B\exp(-i\vec{k}\cdot\vec{r}) \qquad \text{(A.6)}$$

Applying the boundary condition

$$\psi(x = y = z = 0) = 0 \qquad \text{(A.7a)}$$

yields *A*=-*B*, and the boundary condition

$$\psi(x = y = z = L) = 0 \qquad \text{(A.7b)}$$

yields

$$k_x = n_x \frac{\pi}{L}, k_y = n_y \frac{\pi}{L}, k_z = n_z \frac{\pi}{L} \qquad \text{(A.8)}$$

where *n* is a positive integer, so that states are separated in k-space by π/L. For macroscopic values of *L*, the separation in k-space is small, so that the energy levels merge into a continuous energy band. In 3D, the wavefunction can also be written as

$$\psi(\vec{r}) = \frac{1}{L^{3/2}}\sin(k_x x)\sin(k_y y)\sin(k_z z) \qquad \text{(A.9)}$$

In a periodic lattice of period *a*, the periodic ionic potential due to the core ions can be assumed to be sinusoidal, and takes the form

$$V(x) = 2V\cos\left(\frac{2\pi x}{a}\right) = 2V\cos(gx) \qquad \text{(A.10)}$$

where the grating vector is defined as $g=2\pi/a$.

Taking into account the periodic lattice, of period *a*, electrons diffract off the periodic lattice potential from the positive core ions, leading to energy bands separated by an energy gap. In semiconductors the Fermi level lies within the bandgap, so that the valence band is completely filled with electrons, while the conduction band is empty of electrons.

A.2 Principle of XPS

XPS (X-ray Photo-electron Spectroscopy) is an experimental technique that relies on the photo-electric effect to identify the atomic and molecular composition of a sample surface. The XPS setup is shown in Figure A.1(a). Under high vacuum conditions, an X-ray beam a few cm wide is incident onto a sample, and penetrates the sample for a few micrometers (Figure A.1(a)).The X-ray energy is absorbed by a bound core electron from an atom on the sample surface, and is emitted from the atom. Emitted photo-electrons are collected over a narrow solid angle, roughly 1 mm across the sample surface (Figure A.1(a)). The kinetic energy is analysed to identify the surface atom the photo-electron originates, using the photo-electric effect. According to the photoelectric effect, the kinetic energy of the emitted photoelectron (*KE*) is equal to

$$KE = hf - (BE + \varphi) \qquad \text{(A.11)}$$

where *hf* is the X-ray energy (h is Planck's constant and *f* is the frequency of the X-ray), ($BE+ \varphi$) is the minimum energy required to free the bound electron from the atom, where BE is the binding energy of the bound electron relative to the Fermi level and φ is the sample workfunction, which is the energy needed to move the electron from the Fermi level to the vacuum level (Figure A.1(c)). By measuring the kinetic energy of each photo-electron, the binding energy can be deduced. The binding energy depends upon the electrostatic electron-nucleus attraction, which increases the binding energy, and the electrostatic electron-electron repulsion, which reduces the binding energy, and therefore will depend on which orbital in the atom the photo-electron initially occupies and the identity of the atom. Specifically, the binding energy of the bound electron depends upon (i) the quantum numbers *n* (principal), *l* (angular) and *s* (spin), allowing the identification of the subshell (*(n, l)=1s, 2s, 2p,* etc.)) the photo-electron has originally occupied (Figure A.1(b)), and (ii) the atomic number, *Z*, of the element the photo-electron originates, allowing XPS to differentiate between elements of different *Z* values. This is because for a given energy level, the binding energy increases with increasing atomic number. The

XPS peak intensity depends upon the number of electrons detected and the ionisation cross-section. Thus, the relative areas of the XPS peaks give the relative concentrations of elements present on the surface of the sample.

Only electrons within a few nanometers (10 nm) of the sample surface can escape the sample intact (Figure A.1(a)). Electrons from deeper lying elements in the sample are inelastically scattered while still inside the sample and loose some of their energy to electron oscillations (plasmons), crystal vibrations (phonons), and excitons. The range of such randomly lost energies contributes to a continuous background signal. Electrons from even deeper lying elements loose all their kinetic energy before they reach the sample surface, and thus cannot escape the sample. As a result, only elements near the sample surface (up to about 10 nm deep) can be probed.

XPS can also detect chemical shifts. The energy levels and thus binding energies of core electrons shift when in a molecule, and the shift depends on the atom's chemical surrounding. For instance, the binding energy of the 1s orbitals is higher in carbon dioxide (CO_2) than in methane (CH_4) (298 eV and 290.7 eV, respectively[340]). This is due to a different electrostatic interaction: oxygen (O) is more electronegative than hydrogen (H), so oxygen will tend to take away more of the charge from the carbon (C) atom by polarizing the outer valance electrons. This leaves a weaker electron-electron interaction at the C-atom, increasing the binding energy of localised electrons. Thus, the chemical shift is related to the effective charge for an atom in a molecule. Core levels have a higher binding energy if they are in a higher oxidation state (loss of electrons, leaving atom in a more positive state) compared to the same atom in a lower oxidation state.

Secondary processes, such as Auger emission, can follow photoelectron emission and are visible in the XPS spectrum. An emitted photoelectron leaves behind a vacant electron state in the core (Figure A.1(c)), which is being filled by the radiative or non-radiative relaxation of an electron in a higher energy state. Radiative relaxation emits an X-ray, while with the non-radiative decay, an Auger-electron is being emitted due to energy conservation (Figure A.1(d)). Unlike the photoelectron, the

Auger electron kinetic energy is independent of the incident X-ray energy, and is visible as a broad XPS peak.

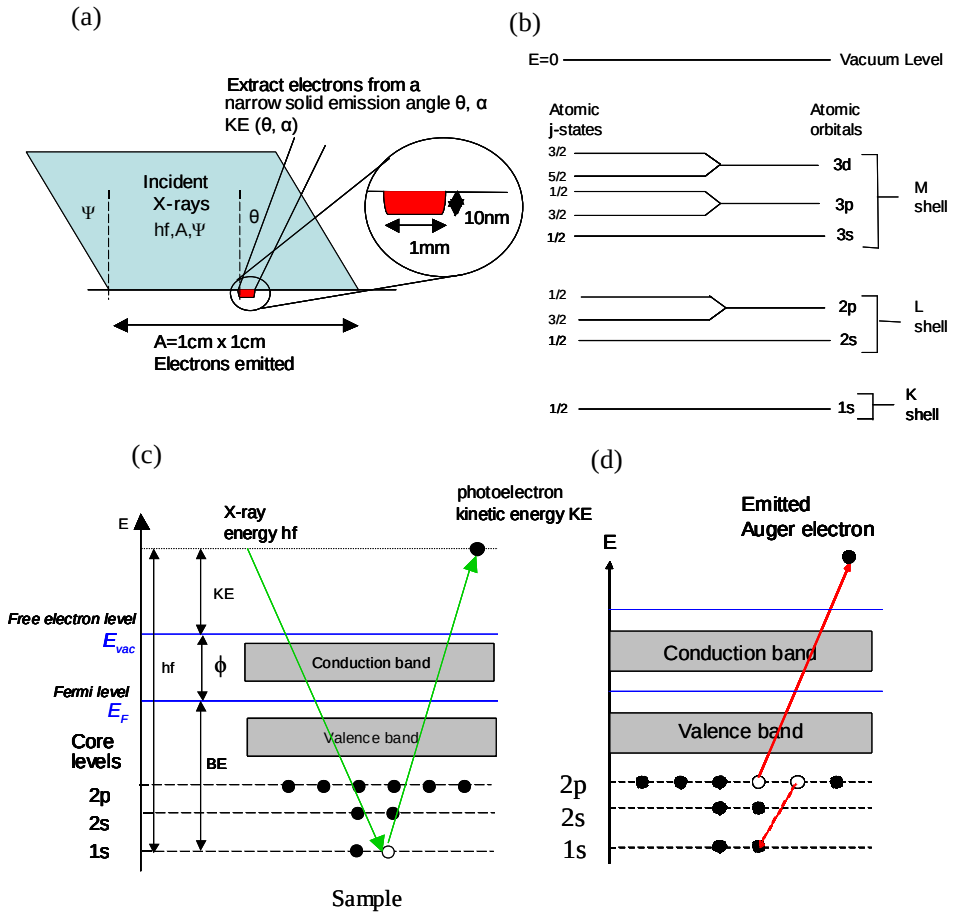

Figure A.1: XPS: (a) setup: Monochromatic X-rays of energy. hf, where h is the Planck`s constant and f is the X-ray frequency, and polarisation A, are incident onto the sample at an angle Ψ to the normal of the sample surface. An analyser collects photoelectrons of kinetic energy KE emitted from the sample surface. KE depends on the experimental parameters e.g. emission angle of θ and α[341] (b) splitting of degenerate energy states by spin-orbit coupling (c) the photoelectric effect: E_{vac} is the vacuum energy level, at which the electron is free from the atom and has zero kinetic energy, E_F is the Fermi energy level, the highest occupied electron state, KE is the photoelectron's kinetic energy and ϕ is the sample work function, BE is the binding energy of the bound electron (d) illustration of the Auger effect occurring as a result of photoelectron emission from the 1s energy level. Adapted from [342]

B Appendix B

B.1 Fluorimeter Setup

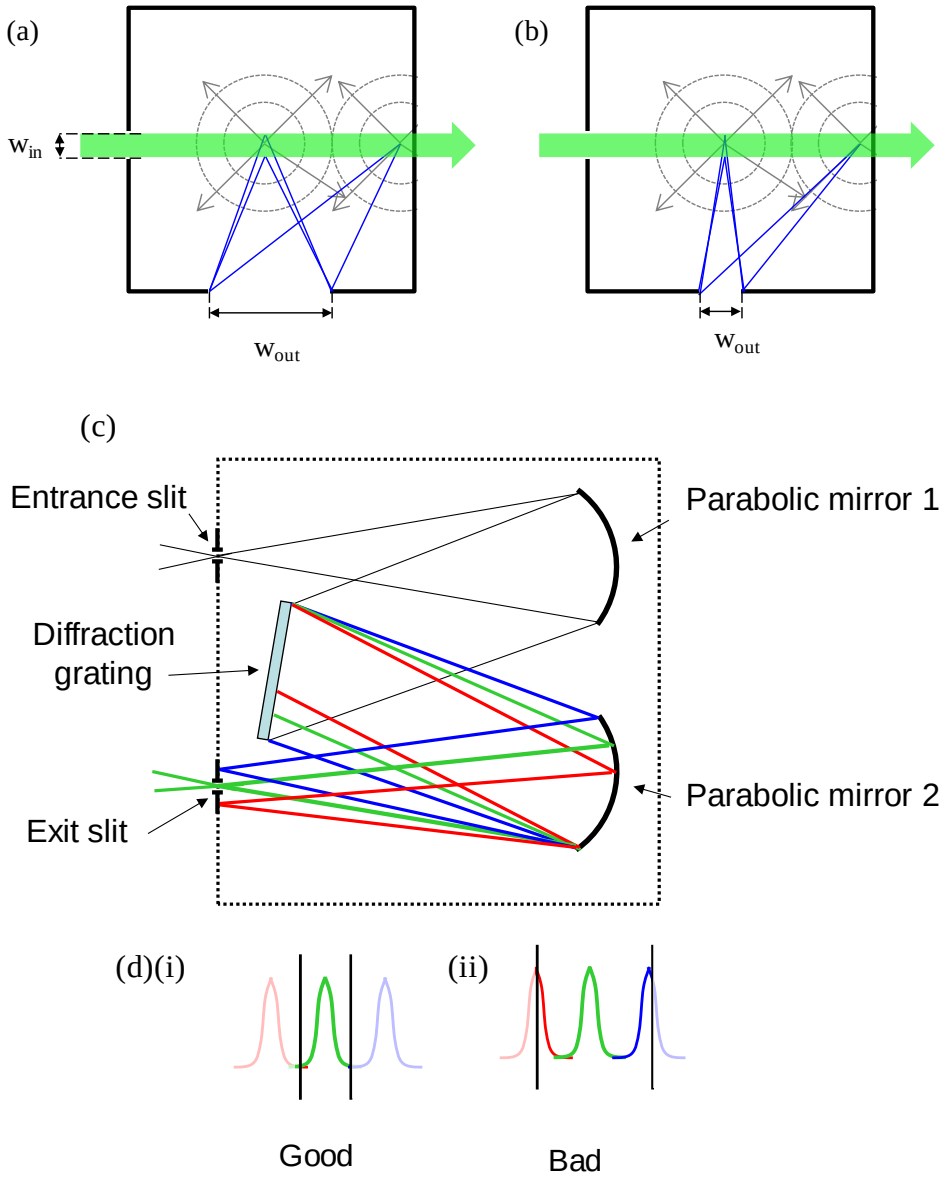

Figure B.1: Schematic of the fluorimeter setup at two different exit slit widths (a) wide exit slit (b) narrow exit slit. The width of the entrance slit and exit slit are denoted w_{in} and w_{out}, respectively. Monochromatic excitation light (green arrow), sphere of fluorescence light emanating from a fluorescent point source within the excitation beam path (grey), range of detected fluorescence light from a fluorescent point source (blue) (c) setup of a monochromator: a broad-band light source is separated into spectral component by diffraction (d) spectrally separated components at the exit slit of the monochromator (i) narrow exit slit and (ii) broad exit slit.[343]

B.2 Fluorescence Filter Sets

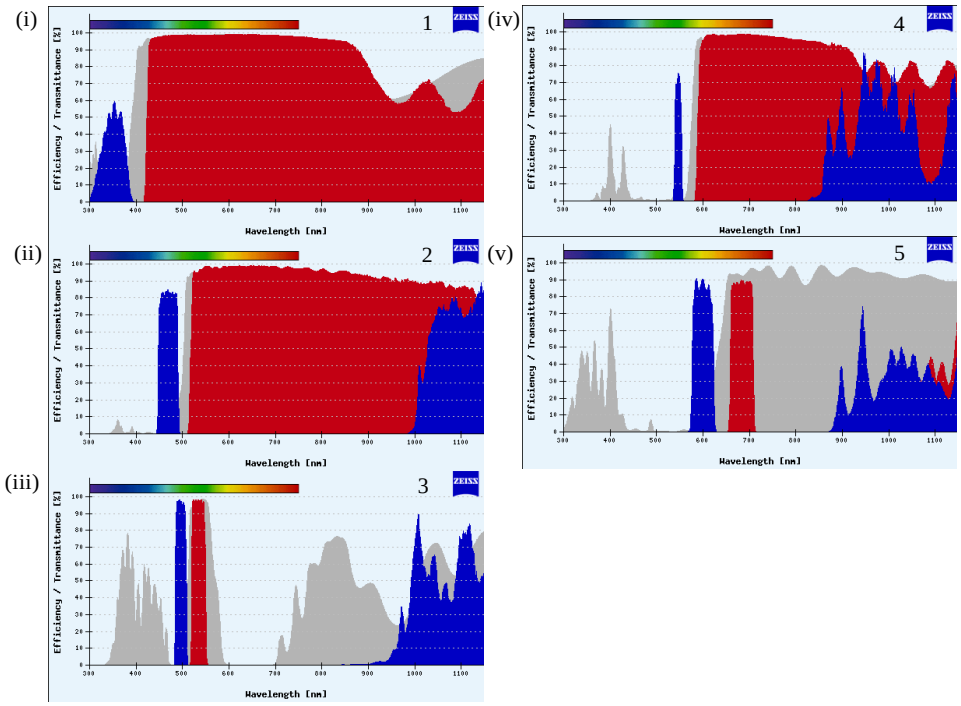

Figure B.2: Fluorescence filter sets: transmission spectrum of the excitation filter (blue), beam splitter (grey) and the emission filters (red) of various filter sets. Filter sets are from Zeiss.[344]

filter set	excitation	beam splitter	emission
1	G 395	FT 395	LP 420
2	BP 450-490	FT 510	LP 515
3	BP 500/25 DMR 25	FT 515 HE	BP 535/30 DMR 25
4	BP 546/12	FT 580	LP 590
5	BP 575-625	FT 645	BP 660-710

Table B.1: Excitation, beam splitter and emission range for various filter sets.[344]

B.3 pKa

The pH and pK_a are related by the Henderson-Hasselbach equation:[345]

$$pH=pK_a+log[(A^-)/(HA)] \quad \text{(B.1a)}$$

$$pH=pK_a+log[(B)/(HB^+)] \quad \text{(B.1b)}$$

where HA/HB^+ is the protonated form, and A^-/B the deprotonated form of the acid *A*/base *B*. Acids have $pK_a<7$, while bases have $pK_a>7$. At $pH=pK_a$, the number of protonated and deprotonated molecules is equal. For instance, acetic acid has $pK_a=4.8$. At low $pH<<pK_a$, e.g. at $pH=2.8$, 99% the acetic acid molecules will be protonated i.e. CH_3COOH), while at high $pH>>pK_a$ e.g. at $pH=6.8$, 99% of the molecules will be deprotonated CH_3COO^-.[345]

B.4 Peptides

A peptide is a short amino-acid chain. The general structure of an amino acid is shown in Figure B.3(a), which consists of R-C-H, where R denotes a side chain, and two functional groups at either end: the carboxyl group (COOH) (C-terminus) and the amino group (NH_2) (N-terminus). Amino acids can be either hydrophilic or hydrophobic, due to containing either a polar (acidic) or non-polar side chain, R, respectively. Polar amino acids contain a side chain R capable of hydrogen bonding, making them hydrophilic, while non-polar amino acids contain neutral side chains, making them hydrophobic. The amino acid cysteine contains a thiol (SH) in the side chain (Figure B.3(b)). Under neutral pH conditions, the SH group in the cysteine amino acid is deprotonated, and a strong bond between the sulphur of the cysteine and the Zn of the CdSe/ZnS QD can form. An amino acid binds to another amino acid by forming a (covalent) peptide bond (OC-NH) between the two amino acids. The peptide bond forms between the NH_2 group of one amino acid and the COOH group of another (Figure B.3(c)). Peptide bond (OC-NH) formation requires the prior removal of the OH from the COOH and the H from the NH_2, as the maximum number of bonds of C and H is 4 and 1, respectively. The removed OH and H combine to form water as a side product of peptide bond formation (condensation) (Figure B.3(c)).

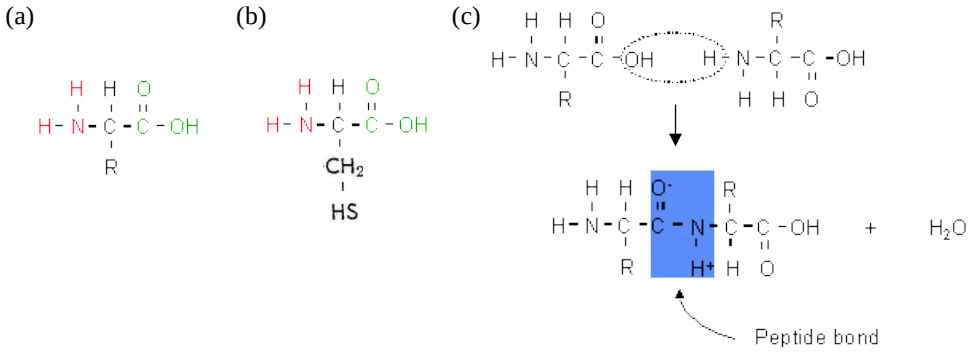

Figure B.3: Peptide structure and peptide bond formation (a) general molecular composition of an amino acid, which consists of an amino group (NH_2)(red), a carboxyl group (COOH) (green), and HCR, where R denotes the amino acid side chain[346] (b) molecular composition of the amino acid Cysteine (c) the formation of a Peptide bond (blue) between two amino acids, yielding waterH_2O as a side product.[346]

B.5 Structure of Designed Peptides

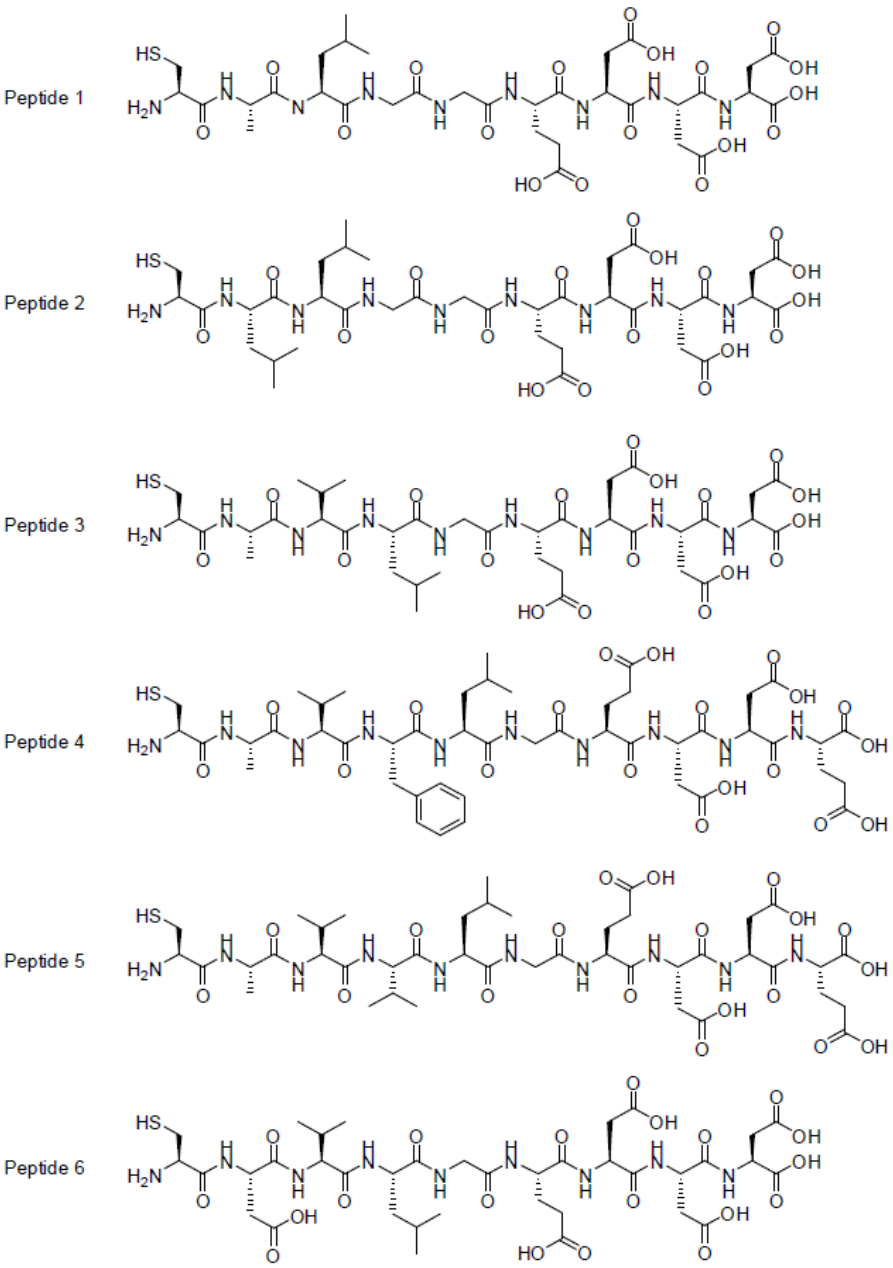

Figure B.4: Structure of designed peptides.[227]

B.6 Core Size and Solvent Effects on CdSe/ZnS Core/Shell QD Emission

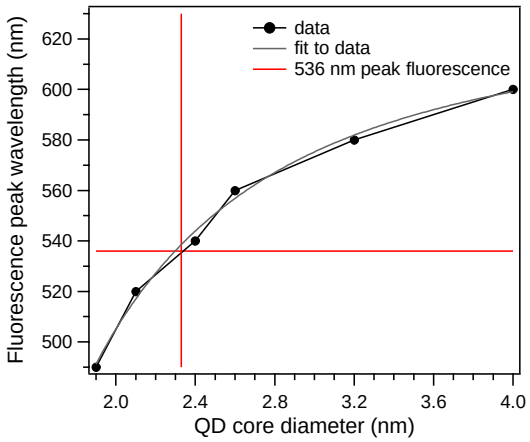

Figure B.5: Graph of wavelength of the fluorescence peak versus diameter of the QD core for long-chain-amine molecule-coated CdSe/ZnS core/shell QDs (values are quoted by Evident Technology)[347].The red lines are values of the fluorescence peak and extrapolated QD diameter for 536 nm fluorescence peak CdSe/ZnS QDs (coated in long chain amine molecules) (Evident Technologies).

The CdSe QD core was extrapolated to be equal to 2.33 nm in diameter, using values of fluorescence peak wavelength and core diameter quoted from Evident Technologies[347] (Figure B.5) The ZnS shell was 2 monolayers thick (Evident Technologies),[348] where one ZnS monolayer is equal to 0.312 nm.[349] Thus, the total diameter of a single QD is equal to [*2.33 nm+2·(2*0.312 nm)] ~ 3.6 nm.*

In the solvent effect, the dipoles of a polar solvent align with the dipole of the excited dye, reducing the excited state energy, and thus red-shifting the fluorescence peak (increasing the Stoke`s shift).[350, 351] As reported by Chunyang *et al.*,[232] a blue-shift in the QD fluorescence peak has been observed after conjugation of CdSe/ZnS QDs with trichosanthin (TCS). TCS was suggested to reduce the Stokes (red-)shift as it is less polar than the aqueous surrounding.[232]

B.7 Tapping Mode Atomic-Force-Microscopy (TM-AFM)

In tapping mode, the AFM tip is attached to a cantilever that oscillates at several kHz and at a constant amplitude (the set point amplitude). The constant oscillation amplitude is maintained by a feedback loop (Figure B.6(a)). Height data is collected as illustrated in Figure B.6(b). As the tip passes over a feature of positive height, the cantilever has less room to oscillate and the amplitude falls. As a result, the feedback loop raises the amplitude back to its set point value by moving the tip upwards by an according distance using a z-piezo-actuator. The variation in z can then be scanned over the whole sample. Similarly, a feature of negative height will increase the oscillation amplitude, and the feedback loop will reduce the height of the cantilever until the oscillation amplitude has reduced back to the set point value.

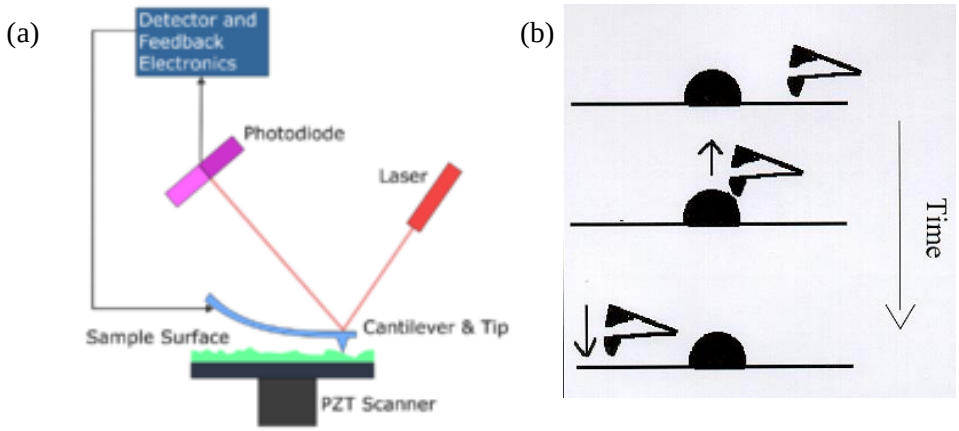

Figure B.6: TM-AFM (a) setup[352] (b)tip detecting variations in surface height.[353]

B.8 DNA Adhesion onto a Mica Surface, Optimisation for AFM Studies

For dry AFM studies, samples are immobilised onto an atomically flat substrate, such as freshly cleaved mica. However, both DNA, due to the phosphate in the sugar-phosphate backbone (Figure B.7(a)), and mica are negatively charged, repelling each other. However, the repelling force can be overcome, and weak electrostatic immobilisation of DNA onto mica can be achieved by the use of divalent cations in the sample buffer solution, with or without prior treatment of the mica surface with divalent cations. The mechanism of divalent-cation-induced DNA attachment to the like-charged mica surface is thought to be the sharing of the cations bound to DNA and mica between the like charged DNA and mica surface, a so-called charge-bridge between the two, giving rise to a short range net attractive electrostatic force between DNA and mica (Figure B.7(b)).[249] Thus, divalent cations must (i) bind to both the DNA backbone and the mica surface, and (ii) be water-soluble for imaging of DNA under physiological conditions. The attractive force can be further enhanced by mica pretreatment with divalent cations.[249] Magnesium (Mg^{2+}) and Nickel (Ni^{2+}) fulfill these two requirements and have been shown to bind to the phosphate backbone. Mg^{2+} is the preferred choice, as its binding to phosphate sites in the DNA backbone is non-specific, and its coordination to DNA bases is weak.[249] The adsorption of DNA onto mica depends on various factors. Firstly, the attraction force between like-charged DNA and mica is mediated by counterion correlation and depends on their surface charge densities (and the valency Z of the multivalent counterion).[248] Both DNA and mica are highly charged, resulting in strong DNA to mica adsorption. Secondly, only multivalent counterions, with valency $Z>1$, can induce an attractive force between DNA and mica. Unlike multivalent counterions, monovalent counterions do not contribute to DNA adsorption to mica. However, both counterions, mono-and multivalent, can bind to DNA. The resulting binding competition between multi-and monovalent counterions to DNA results in a DNA-mica attractional force that depends

on the ratio of the concentration of multi-to monovalent counterions in the buffer (i.e. charge densities). Above a certain monovalent counterion concentration, DNA cannot adsorb onto the mica. A high concentration of monovalent salt then requires a higher multivalent counterion concentration to achieve the same adsorption. Thirdly, it is observed that above a critical concentration of multivalent counterions, C*, the DNA does not adsorb onto the mica surface anymore.[248] This is attributed to overcharging of the mica and/or DNA, resulting in repulsive behavior and hence non-adsorption of DNA to mica. C* depends on the particular multivalent salt, and equals about 800 mM for Mg^{2+}. C* is *independent* on the monovalent counterion concentration present in the buffer up to a monovalent counterion concentration of 300 mM,[248] after which C* is proportional to the ratio of divalent to monovalent counterions, due to the binding competition between mono-and multivalent counterions to DNA mentioned earlier.[248]

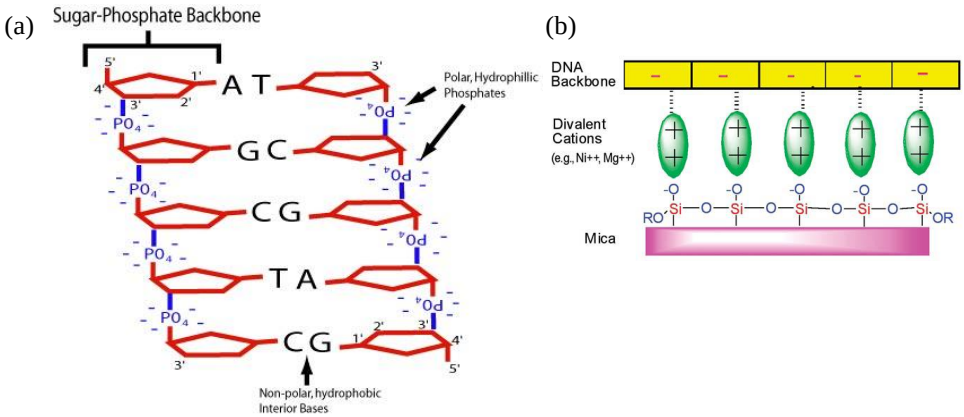

Figure B.7: Schematic representation of (a) charged DNA backbone consisting of negatively charged phosphate (blue) and sugar (red),[354] and (b) DNA immobilisation onto mica via the use of divalent cations.[355]

DNA agglomeration can occur due to reduced inter-strand repulsion induced by divalent cations. Divalent cations in the sample buffer neutralize the negative charge of the phosphate-sugar backbone of DNA strands, and thus reduce inter-strand electrostatic repulsion between negatively charged DNA phosphate-sugar backbones of different DNA strands, and thus encourages DNA agglomeration in solution;[246] once transferred onto the mica surface, the Mg^{2+} cations at the DNA-DNA interface will localize at the DNA-mica interface, due to the higher surface

charge of the mica compared to DNA, spreading the DNA aggregates onto the mica surface;[246, 248] as an example, dry AFM images of pUC10 plasmid DNA in buffer containing various concentrations of trivalent spermide (Sp^{3+}) have shown that with increasing Sp^{3+} concentration, the DNA molecules form increasingly condensed structures, starting with single loops in individual strands at low concentrations, which with increasing SP^{3+} concentration yields multiple loops per strand and eventually flower-like DNA structures.[246, 248]

Figure B.8 shows the dry AFM image of 0.4 µg/mL DNA using a $MgCl_2$ concentration of 25 mM in both the mica pretreatment and the sample buffer, and with incubation times of 2 and 3 minutes in the mice pretreatment step and sample depositioning step, respectively. The DNA strands are interconnected, forming a network-like structure. Successive AFM images on the same sample area yield repeatable AFM images, suggesting the DNA strands are immobilised well onto the mica surface.

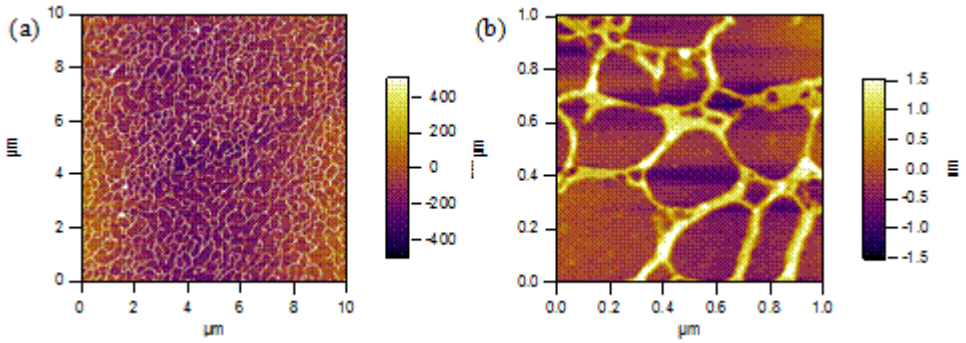

Figure B.8: AFM image of Calf-thymus DNA (0.4 µg/mL) at (a) large scale and (b) close-up. $MgCl_2$ concentrations during mica pretreatment and in sample buffer were 25 mM. AFM tip ROC=10 nm.

Figure B.9 shows dry AFM images of 0.2 µg/mL DNA strands under various $MgCl_2$ concentrations in the sample buffer and the mica-pretreatment. A 4-fold reduction, compared to the optimum $MgCl_2$ concentrations, in the sample buffer $MgCl_2$ concentration from 2 mM to 0.5 mM causes the DNA molecules to change from an extended configuration to being globules (Figure B.9(a)). Similar DNA configuration changes upon changes in relative ratios of multi to monovalent counterions in the sample buffer have been observed before,[248] and are attributed to weak DNA binding to the mica surface as

the relative monovalent counterion concentration increases, causing the DNA to be in a transitional state between adsorption and non-adsorption.[248]

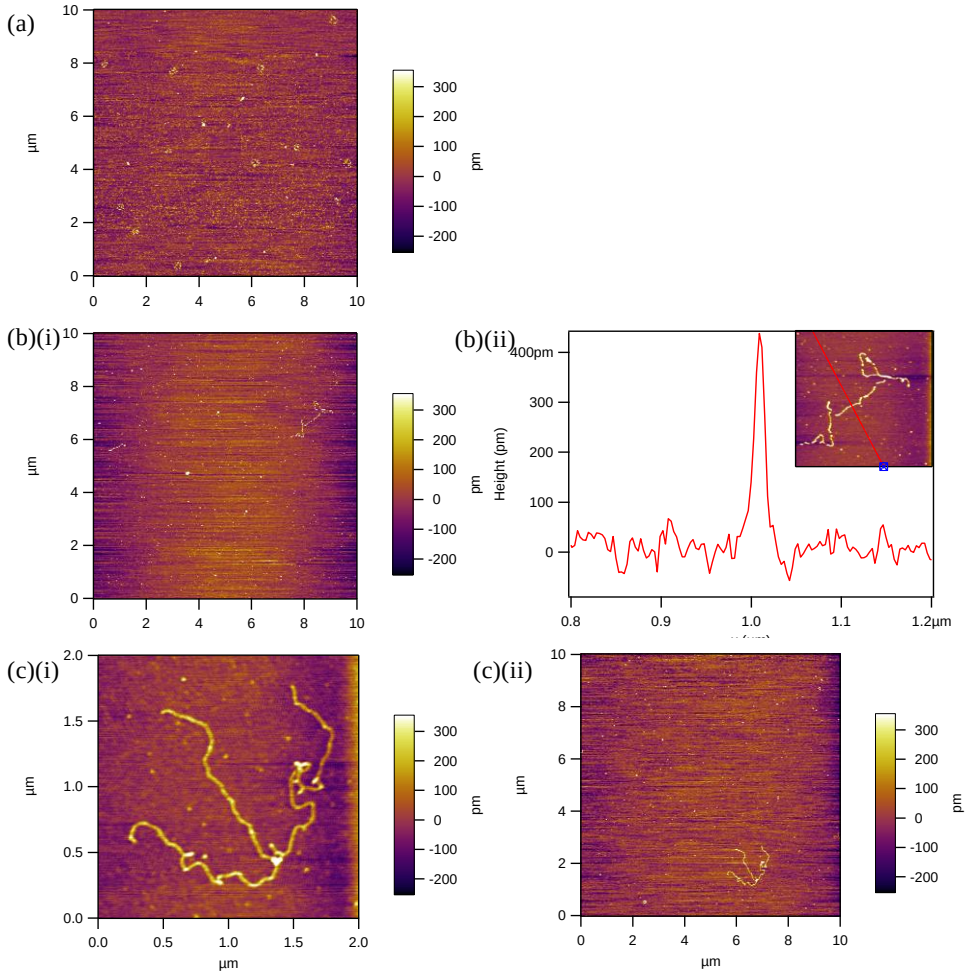

Figure B.9: Effect on AFM images of Calf-thymus DNA (0.2 µg/mL) of (a) reduced $MgCl_2$ concentration in sample buffer to 0.5 mM (b) reduced $MgCl_2$ concentration during mica pretreatment to 5 mM (c) reduced incubation time during mica pretreatment to 1 min. Except where otherwise stated, $MgCl_2$ concentrations were 10 mM (pretreatment) and 2 mM (sample buffer) and incubation time during mica pretreatment was 2 mins, AFM ROC=10 nm.

A 2-fold further reduction, compared to the optimum $MgCl_2$ concentrations, from 10 mM to 5 mM of $MgCl_2$ in the mica-pretreatment step causes discontinuities in the adsorbed DNA stands to appear (Figure B.9(b)(i)). Discontinuities suggest weakly adsorbed DNA onto the mica surface due to an insufficiently strong attractive force between DNA strand and the mica, due to a too low Mg^{2+} counterion concentration. Breakages in AFM-imaged DNA strands have also been observed under a too strong

applied force.[242] While an increased loading force in TM-AFM has been shown to reduce the imaged DNA height,[237] the height measured here is equal to 0.4 nm (Figure B.9(b)(ii)), within the range of previously measured dsDNA heights (see chapter 3.3.2.1). Thus, the discontinuities in the imaged DNA strands are most likely due to very low $MgCl_2$ concentration in the mica pretreatment step causing weak DNA adhesion onto the substrate. A reduced DNA surface coverage also suggests weak DNA adhesion (Figure B.9(b)(i)). Thus, a reduced $MgCl_2$ pretreatment concentration of 5 mM weakens DNA adhesion to the mica substrate, lowering the DNA surface coverage and causing discontinuities in the imaged DNA strand to appear.

Reduction of the mica pre-treatment incubation time with $MgCl_2$ form 2 mins to 1 min leads to a reduced DNA surface coverage (Figure B.9(c)(i)), but no major change in the DNA configuration or adhesion efficiency of DNA onto mica (Figure B.9(c)(ii)).

B.9 π-Stacking in DNA

π-stacking in a DNA molecule refers to the stacked arrangement of nucleotides in a DNA molecule due to overlapping π-bonds between adjacent nucleotides.

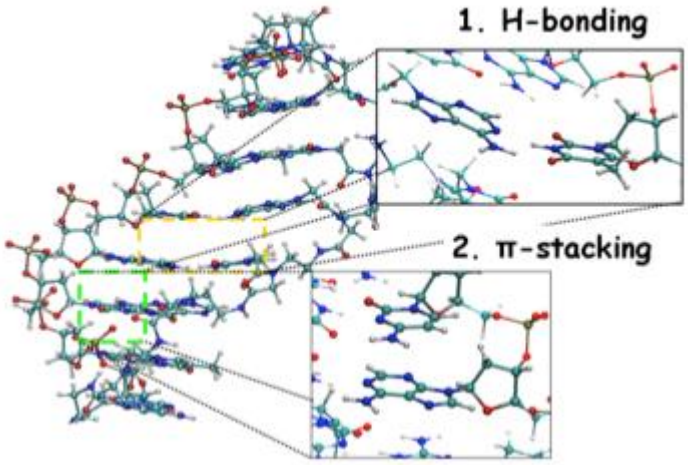

Figure B.10: Structure of a DNA molecule: complimentary base pairing occurs via (non-covalent) hydrogen bonding. While GC form 3 H-bonds, TA from only 2 H-bonds.[356]

π-stacking increases the stability of DNA molecules. Each nucleotide consists of a sugar, a phosphate, which forms the DNA backbone, and a base. The bases contain aromatic rings which in a DNA molecule are arranged such that the faces of the aromatic rings are aligned almost perpendicular to the DNA strand length, and thus faces of neighbouring aromatic rings are aligned parallel to each other (Figure B.10(2)). The π-bonds of consecutive bases overlap with each other, stabilizing the DNA molecule.

B.10 A and B-DNA

Figure B.11 shows the structure of A-DNA and B-DNA.

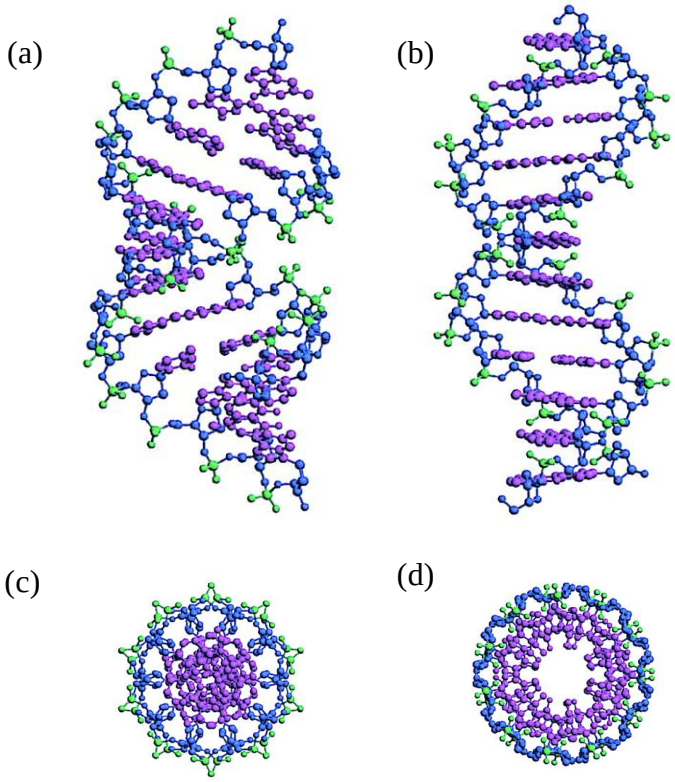

Figure B.11: Structure of (a, c) A-DNA and (b, d) B-DNA as viewed from the (a, b) side or (c, d) top.[357]

C Appendix C

The following section provides the theory that forms the background to the studies described in chapter 4. Some of the theory is well-established and other parts are theories developed by previous researchers in Southampton working in the field.

C.1 Fermi`s Golden Rule

Fermi`s golden rule gives the transition rate from an initial state $|i\rangle$ to a final state $\langle f|$, the final state being part of a continuum of states, due to a perturbing potential, H`, applied to the system and is given by[358]

$$\Gamma_r = \frac{1}{\tau_r} = \frac{2\pi}{\hbar}\left|\langle f|H`|i\rangle\right|^2 \rho(\varpi_e) \qquad \text{(C.1)}$$

where $\left|\langle f|H`|i\rangle\right| = \left|M_{if}\right|$ is the transition matrix element and quantifies the coupling strength between the initial and final state, and τ_r is the radiative lifetime, and $\rho(\varpi_e)$ is the density of final states, defined as the number of energy states per unit volume in the energy interval *E* to *E*+*dE*, and $\hbar\varpi_e$ is the energy separation between initial and final state. Spontaneous emission occurs due to interaction of an emitter dipole with the vacuum electromagnetic field, and can be considered as stimulated emission due to the fluctuations in the vacuum field.

C.2 Derivation of the Photonic Density of States

Consider a 1D cavity of length *L*. Only electromagnetic waves with zero electric field at the cavity edge can exist within the cavity, that is

$$L=m\lambda/2 \tag{C.2}$$

where *m* is a positive integer. Noting that $k=2\pi/\lambda$, equation C.2 leads to

$$E=E_0 sin(kx)=E_0 sin(2\pi x/\lambda)=E_0 sin(m\pi x/L) \tag{C.3}$$

so that states are separated in k-space by π/L. Extending from a 1D to a 3D, the volume in k-space per state equals $(\pi/L)^3$. The number of states between *k* and *k+dk* equals to the volume of the thin shell of thickness *dk* divided by the volume per state, i.e.

$$D(k)dk = 2\cdot\frac{4\pi k^2 dk}{\left(\frac{\pi}{L}\right)^3}\frac{1}{8} = \frac{1}{\pi^2}k^2 dk L^3 \tag{C.4}$$

The division by 8 is added because only positive *k*-values are considered, and the factor of 2 takes account of two polarisation states (**s**enkrecht and **p**arallel-polarisation). The dispersion relation of an electromagnetic wave travelling in a dielectric medium of refractive index *n* equals

$$E = \hbar\varpi = \hbar c_n k \tag{C.5}$$

so that

$$\frac{d\varpi}{d\kappa} = c_n = \frac{c}{n} \text{ and } k = \frac{\varpi}{c_n} \tag{C.6}$$

where c_n and *c* is the speed of light inside a dielectric of refractive index *n* and inside vacuum, respectively. Substituting for *k* into equation C.4 yields

$$D(k)dk = \frac{1}{\pi^2}\left(\frac{\varpi}{c_n}\right)^2 L^3\frac{d\varpi}{c_n} = \frac{V}{\pi(c_n)^3}\varpi^2 d\varpi \tag{C.7}$$

where *V* is the box volume. The number of states, *N*, between ω and $\omega+d\,\omega$ is the same as those between *k* and *k+dk*, thus

$$N=D(\omega)d\,\omega=D(k)dk \tag{C.8}$$

Substituting equation C.7 into C.8 gives

$$D(\varpi)d\varpi = \frac{V}{\pi(c_n)^3}\varpi^2 d\varpi \tag{C.9}$$

$$D(\varpi) = \frac{Vn^3}{\pi (c_n)^3} \varpi^2 \qquad \text{(C.10)}$$

C.3 Enhanced Fluorescence Emission Rate Induced by Surface Plasmon Polaritons

The principle of SPP-induced enhanced fluorescence decay rate is illustrated in Figure C.1. An excited-state fluorescent emitter within the SPP near field can quickly non-radiatively couple to a SPP mode on the metal surface, which, due to the metal corrugation, quickly re-emits into the far-field.

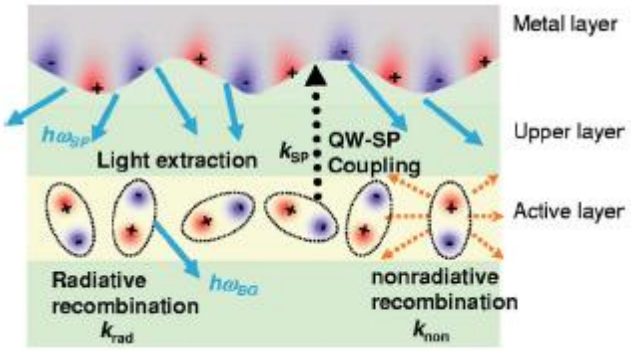

Figure C.1: Principle of emission rate enhancement via near-field coupling of excited emitter (in this case, InGaN quantum well with emission frequency of ω_{BG}) and subsequent SPP emission into the far-field via grating coupling.[230]

Enhanced emission rates induced by SPPs can be theoretically treated in terms of an increased local density of states due to SPP.[259, 260] In this case, consider an excited emitter in free space and nearby a metal surface. In free space the non-radiative and radiative decay rate equals k_{nr} and k_r, respectively, while nearby a metal surface, the excited emitter can also decay into a surface plasmon polariton (SPP) mode at a rate of k_{SPP}. According to Fermi`s Golden Rule (appendix C.1), the decay rate is equal to the final density of states, resulting in a modified decay rate nearby a metal surface. The Purcell factor, F_P, is equal to [259]

$$F_P = \frac{k_{SPP}}{k_r} \approx \frac{\rho_{SPP}}{\rho_0} \qquad \text{(C.11)}$$

where ρ_{SPP} is the SPP density of states (SPP evanescent field strength) and ρ_0 is the vacuum field (radiation field) density. The density of states is inversely proportional to the group velocity v_g or the dispersion curve gradient [259]:

$$\rho \propto \frac{1}{v_g} = \frac{1}{\frac{\partial \varpi}{\partial k_x}} \tag{C.12}$$

The dispersion curve gradient is always lower for SPP than for far-field radiation, so that SPP have a higher density of states than far-field radiation. With increasing wavevector, the SPP dispersion curve gradient decreases and thus the SPP density of states increases. Thus, with increasing wavevectors, the efficiency of decay into SPP modes and hence the Purcell factor increases. Using equation C.11, the efficiency of coupling into a SPP mode (in-coupling efficiency) is equal to [259]

$$\eta_{in} = \frac{k_{SPP}}{k_{SPP} + k_{nr}} = \frac{F_P k_r}{F_P k_r + k_{nr}} \tag{C.13}$$

The excited SPP then subsequently either (a) emits into the far-field, at a rate of $\kappa_{pr} \propto \rho_0$, a result of losing momentum when scattering off the metal grating periodicity, or (b) decays non-radiatively, at a rate of κ_{nr}, due to energy loss to heat. The SPP thus couples into the far-field at efficiency equal to

$$\eta_{pr} = \frac{\kappa_{pr}}{\kappa_{pr} + \kappa_{nr}} \tag{C.14}$$

As Surface-Plasmon-Polariton radiation requires efficient SPP excitation by the excited emitter (η_{in}) and subsequent efficient SPP-coupling to the far-field (η_{pr}), using equation C.13, the overall efficiency of SPP radiation is equal to

$$\eta_{SPP} = \eta_{pr}\eta_{in} = \eta_{pr}\frac{k_{SPP}}{k_{SPP} + k_{nr}}$$

$$= \eta_{pr}\frac{F_P k_r}{F_P k_r + k_{nr}} \tag{C.15}$$

Assuming that the efficiency of the excited emitter radiating directly into the far-field is equal to $\eta_r = \frac{k_r}{k_r + k_{nr}}$, then the enhancement in emission efficiency due to SPP coupling is equal to

$$F_{SPP} = \frac{\eta_{SPP}}{\eta_r} = \eta_{pr} \frac{F_P k_r}{F_P k_r + k_{nr}} \left(\frac{1}{\eta_r} \right)$$

$$= \eta_{pr} \frac{F_P}{\left[F_P + \frac{k_{nr}}{k_r} \right]} \left(\frac{1}{\eta_r} \right)$$

But from the equation $\eta_r = \frac{k_r}{k_r + k_{nr}}$, it can be shown that $\frac{k_{nr}}{k_r} = \frac{1}{\eta_r} - 1$, so that

$$F_{SPP} = \eta_{pr} \frac{F_P}{\left[F_P + \frac{k_{nr}}{k_r} \right]} \left(\frac{1}{\eta_r} \right)$$

$$= \eta_{pr} \frac{F_P}{\left[F_P + \frac{1}{\eta_r} - 1 \right]} \left(\frac{1}{\eta_r} \right)$$

$$= \eta_{pr} \frac{F_P}{\left[\frac{F_P \eta_r + 1 - \eta_r}{\eta_r} \right]} \left(\frac{1}{\eta_r} \right)$$

$$F_{SPP} = \frac{\eta_{pr}}{\eta_r + (1 - \eta_r) F_p^{-1}} < \frac{\eta_{pr}}{\eta_r} \qquad \text{(C.16)}$$

Thus, the SPP induced enhancement F_{SPP} is limited by the SPP radiation efficiency η_{pr} relative to the fluorophore emission efficiency in free space η_r. Generally, high enhancements are only possible with emitters of medium to low radiative decay efficiencies, of less than 10%.[259]

Throughout fluorophore-SPP coupling, energy is conserved, yielding SPP emission energy $\hbar\varpi_{SPP}$ equal to the fluorophore emission energy $\hbar\varpi_F$ i.e. $\varpi_F = \varpi_{SPP}$. SPP-far-field resonance also requires in-plane momentum conservation, resulting in directional SPP emission.

C.4 Enhanced Absorption Rate Induced by Surface Plasmon Polaritons

Consider a ground-state fluorophore nearby a metal surface. A SPP mode on the metal surface can excite the fluorophore more quickly than far-field radiation due to the evanescent field of the SPP being stronger than the electric field of far-field radiation. Coupling between SPP and fluorophore occurs provided the SPP energy is in resonance with the fluorophore absorption energy, and the fluorophore is located within the SPP near field. The SPP-induced emission enhancement in the grating-coupling geometry has been treated theoretically before, and explained below.[261] Consider a fluorophore in free space and nearby a metal surface. In free space, the absorption rate of free-space radiation equals R_0, while nearby a metal surface; the fluorophore can be excited by a SPP at a rate of R_{SPP}, resulting in a modified absorption rate near the metal-surface. The Purcell factor, F_P, is equal to

$$F_P = \frac{R_{SPP}}{R_0} \tag{C.17}$$

In free space, the absorption rate is related to the incident radiation power density at the metal-dielectric interface $|D|^2$ as

$$R_0 = \alpha_F |D|^2 \tag{C.18}$$

where α_F is the fluorophore absorption coefficient. On the other hand, assuming an energy density of a SPP equal to $|a|^2$, where a is the amplitude of the SPP, and SPP decay rate (due to coupling to a fluorophore) of Γ_{abs}, then the fluorophore absorption rate by SPP is equal to

$$R_{SPP} = \Gamma_{abs} |a|^2 \tag{C.19}$$

Due to the exponentially decaying nature of the SPP field with perpendicular distance from the metal surface z (section 4.2), Γ_{abs} falls with increasing z according to $e^{(-2k_{z,d}z)}$, where $k_{z,d}$ is the SPP wavevector in the z-direction inside the dielectric. The SPP skin-depth, δ_{SPP}, quantifies

the extent of the SPP field into the dielectric with *z* (section 4.2). A short skin depth corresponds to strongly concentrated SPP field, which increases the SPP decay rate, i.e. $\Gamma_{abs} \propto 1/\delta_{SPP}$.[259] The SPP energy density $|a|^2$ scales with the incident radiation power density $|D|^2$ and the efficiency of far-field coupling into SPP modes, η_{in}. We now consider η_{in}. The coupling rate of far-field radiation into SPP mode κ_{in} scales with the coupling rate of SPP into far-field radiation γ_r, but SPP can also decay/be lost at a rate of $2\varpi''$, where the complex SPP frequency is equal to $\varpi = \varpi' + i\varpi''$. Thus

$$\eta_{in} = \frac{\gamma_r}{\gamma_r + 2\varpi''} \tag{C.20}$$

and

$$|a|^2 \propto \frac{\gamma_r}{\gamma_r + 2\varpi''}|D|^2 \tag{C.21}$$

The SPP-induced absorption-rate enhancement is thus equal to

$$F_P = \frac{R_{SPP}}{R_0} \propto \frac{1}{\delta_{SPP}} \frac{\gamma_r \varpi'}{(\gamma_r + 2\varpi'')^2} e^{(-2k_{z,d}z)} = \frac{1}{\delta_{SPP}} \frac{Q_r}{(Q_r + Q_{nr})^2} e^{(-2k_{z,d}z)} \tag{C.22}$$

where the Q-factors are defined as $Q_r = \frac{\gamma_r}{\varpi'}$ and $Q_{nr} = \frac{2\varpi''}{\varpi'}$, and are a measure of the efficiency of SPP in-coupling (far-field radiation into SPP mode) and the SPP loss, respectively. First of all, F_P decreases rapidly with increasing *d*, due to the exponential decay of the SPP evanescent field with *d*. There is also a frequency-dependence: at low frequencies ($\varpi << \varpi_{SPP}$), the skin depth is large (section 4.2), yielding weak concentration of SPP field, and hence low efficiency of coupling into SPP modes (low Q_r). With increasing frequency, the skin depth decreases, increasing the SPP field concentration and hence in-coupling efficiency, yielding a peak in F_P just below the SPP plasmon frequency $\varpi_{SPP} = \frac{\varpi_P}{\sqrt{1+\varepsilon_m}}$. In summary, high SPP-induced absorption enhancements requires (a) efficient coupling from excitation far-field into the SPP mode, i.e. a *high* radiative SPP decay rates,

and (ii) a high SPP evanescent field strength, requiring a *low* total SPP decay rate (such as SPP radiation, SPP absorption or loss).

C.5 Fluorescence Enhancement inside Optical Cavities

Optical cavities can change the vacuum field and thus the spontaneous decay lifteime.[359] Relative to free space, an optical cavity reduces the total number of available states and increases the density of optical states at the cavity resonance frequencies. For instance, the optical density of states of a single-mode cavity is Lorentzian and equals[358]

$$\rho_C(\varpi) = \frac{2}{\pi} \frac{\Delta\varpi_C}{[4(\omega - \omega_C)^2 + \Delta\varpi_C^2]} \qquad \text{(C.23)}$$

where ω_C is the cavity mode resonance frequency and $\Delta\varpi_C$ is the full width at half maximum (*FWHM*) at the mode resonance. The density of states depends on the detuning of the frequency ω from the cavity resonance ω_C (equation C.23). At the cavity resonance frequency, the density of states is higher than in free space (Figure C.2), so that an emitter with emission energy equal to a cavity mode experiences an increased emission rate compared to in free space. On the other hand, an emitter out of resonance with a cavity mode has no final states to emit into and will stay in the excited state for longer compared to in free space. According to Heisenberg`s uncertainty principle, $\Delta E \cdot \Delta t \geq \hbar/2$, where ΔE and Δt is the uncertainty in energy and time, respectively, of a given quantum system. For an emitter, $\Delta E = \hbar\Delta\varpi$ and $\Delta t = \tau$, where $\Delta\varpi$ is the uncertainty in emission frequency and τ is the spontaneous decay lifetime. Thus, with respect to free space, an emitter in/out of resonance with a cavity mode experiences a reduced/increased fluorescence lifetime, respectively, and a broader/narrower emission bandwidth, respectively (Figure C.2).

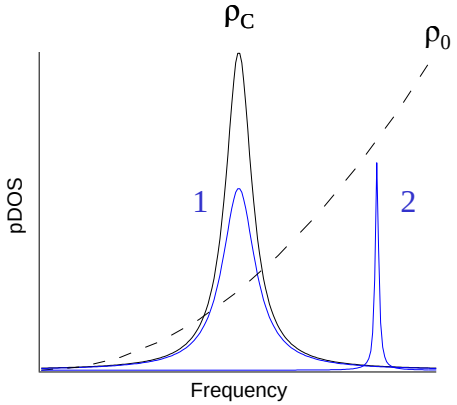

Figure C.2: photonic density of states (pDOS) versus frequency, of free space (dashed black line, ρ_0) and a cavity mode (continuous black line, ρ_C). The emission spectrum of an emitter inside a cavity (blue line) in resonance (1) or out of resonance (2) with a cavity mode. Adapted from [358]

Assuming spectral and spatial overlap between emitter and optical cavity, the spontaneous decay rate in a cavity relative to free space is enhanced by the Purcell factor F_p, and equals[358]

$$F_P = \frac{3}{4\pi^2}\frac{\lambda_C^3}{n^3}\frac{Q}{V_{eff}} \tag{C.24}$$

where n is the refractive index of the medium filling the cavity, V_{eff} is the effective mode volume, λ_C is the cavity mode wavelength, and Q is the cavity quality factor. Q describes the cavity loss and is equal to $Q=2\pi*energy\ stored/energy\ lost\ per\ round\ trip = \frac{\varpi_C}{\Delta\varpi_C} = \frac{nL}{\lambda_C}F$, where $\Delta\omega_C$ is the cavity mode bandwidth, L is the cavity length (mirror separation) and F is the cavity Finesse. Thus, high Purcell factors can be achieved with high Q-factor cavities and small cavity mode volumes (i.e. high mode confinement).

C.6 Optical Modes of a Spherical Metal Microcavity

Pennington *et al*.[338] have experimentally and theoretically mapped the cavity modes of spherical gold microcavities. This section summarises their findings.

A spherical microcavity consists of a planar mirror separated by distance *L* from a spherical micromirror of radius of curvature *R* (Figure C.3(a)). The planar mirror gives rise to longitudinal modes (of index *n=1, 2*,..), while the spherical mirror confines the modes laterally, giving rise to additional transverse modes with axial (*p=0, 1*,..) and azimuthal (*q=0, 1*,..) mode indices (Figure C.3(b)). The transverse modes are axially symmetric with a circularly symmetric Gauss-Laguerre mode profile, in which the radial index *p* corresponds to the number of zeros of the field in the radial direction, and the azimuthal index *q* is equal to the phase winding number of the mode, forming circular modes of increasing diameter (Figure C.3(b), inset). For each longitudinal mode (*n*), 2 families of transverse GL modes appear (*p=0, p=1*), each with increasing azimuthal mode index *q=0, 1, 2*.... (Figure C.3(b)). Although the transverse mode structure cannot be fully described theoretically at present, they are similar to the modes of a paraxial cavity with parabolic optical elements. In such a cavity the transverse mode profile $G_{pq}(r,\varphi,z)$ is be expressed in terms of generalised Gauss-Laguerre polynomials, $L_p^q(x)$, of order *p* and parameter *q*. In the plane of minimum beam waist, ω_0, $G_{pq}(r,\varphi,z)$ equals

$$G_{pq}(r,\varphi,z)=\frac{(\sqrt{2}r)^{|q|}}{\sqrt{2\pi}\varpi_0}L_p^{|q|}(\sqrt{2}\frac{r^2}{\varpi_0^2})\exp(\frac{-r^2}{\varpi_0^2}+iq\varphi) \qquad \text{(C.25)}$$

The total mode profile includes the longitudinal component, and equals

$$\mathrm{E_{npq}}=A_{npq}=G_{pq}(r,\phi,z)\exp(i\pi nz) \qquad \text{(C.26)}$$

where, *z* is the coordinate along the cavity axis (scaled to cavity length *L*), *r*, φ are the polar coordinates in the transverse plane, with *r* being the radial distance in units of $\sqrt{L\lambda}/\pi$, and λ is the wavelength.[338]

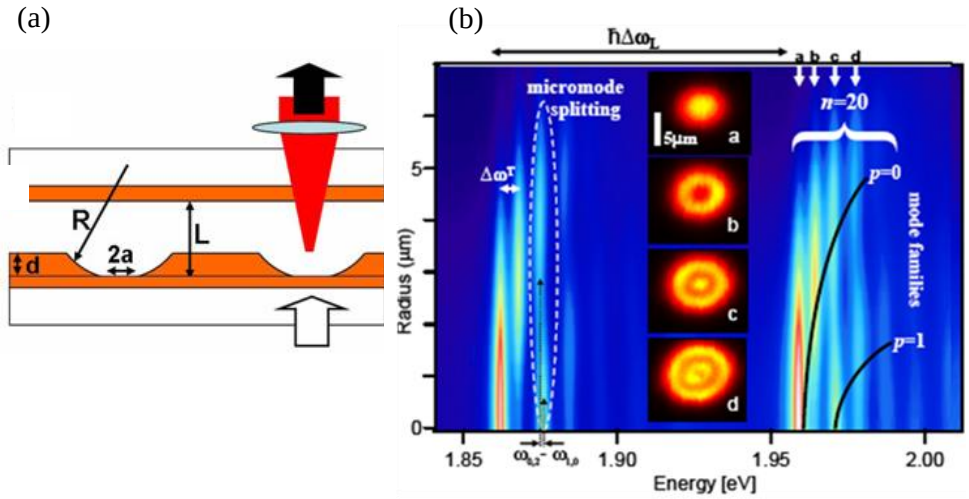

Figure C.3: Spherical Microcavity-(a) microcavity geometry and experimental setup (b) Experimental radial intensity profile of cavity modes spanning two longitudinal mode families, inset: spatial intensity distribution at energies indicated by white arrows, Cavity parameters: R=10μm, L=6.5μm.[338]

In the paraxial approximation (which assumes all rays are parallel to the optic axis so that $sin\theta \sim \theta$) the cavity mode frequencies are equal to[338]

$$\varpi_{npq} = \frac{\pi c}{L}[n + (2p + q + 1)\sin^{-1}\sqrt{\frac{L}{R}}] \qquad \text{(C.27)}$$

and the expected transverse mode spacing equals

$$\Delta\varpi_T = (\frac{\pi c}{L})\sin^{-1}\sqrt{\frac{L}{R}} \qquad \text{(C.28)}$$

Thus, according to theory, GL modes with the same value of $|2p+q|$ are frequency degenerate (i.e. the same frequency) (equation C.27), that is $\delta\varepsilon_q = \varpi_{p+1,q-2} - \varpi_{p,q} = 0$, and transverse modes are equispaced (i.e. independent of p and q) (equation C.28). However, transmission measurements show that in wavelength-scale spherical microcavities the frequency degeneracy associated with GL modes is lifted i.e. $\delta\varepsilon_q \neq 0$, yielding split modes (Figure C.3(b)). Degeneracy lifting is due to the micron (wavelength) scale of cavity, in which the paraxial approximation breaks down, and the non-parabolic spherical mirror. The splitting $\delta\varepsilon$ increases with q as the mode experience more of non-parabolic mirror edges.

C.7 Derivation of the SPP Dispersion Relation.

This section derives the dispersion relation of surface-plasmon-polaritons on a metal-dielectric interface.[287, 360]

C.7.1 Optical Properties of Metal

A metal can be approximated as being an isotropic material of dielectric constant/electric permittivity ε, magnetic permeability μ, and electrical conductivity σ. Maxwell`s equations in S.I. units then are

$$\nabla \times H - \varepsilon \frac{\partial E}{\partial t} = \sigma E \tag{C.29}$$

$$\nabla \times E + \frac{\partial B}{\partial t} = 0 \tag{C.30}$$

$$\nabla \bullet H = 0 \tag{C.31}$$

$$\nabla \bullet E = \frac{\rho}{\varepsilon} \tag{C.32}$$

where $\boldsymbol{E}$ is the electric field vector, $\boldsymbol{B}$ is the magnetic induction vector, $\boldsymbol{H}$ is the magnetic vector, where $\boldsymbol{B}=H\boldsymbol{\mu}$, ρ is the electrical charge density. The variation in electrical charge density in time can be obtained by taking the divergence ($\nabla\bullet$) of equation C.29 and substituting for $\nabla \bullet E$ from equation C.32, which gives

$$\nabla \bullet \frac{\partial E}{\partial t} = -\frac{\rho\sigma}{\varepsilon^2} \tag{C.33}$$

Differentiating equation C.32 with respect to time t, and eliminating $\frac{\partial E}{\partial t}$ using equations C.33, yields

$$\frac{\partial \rho}{\partial t} = -\frac{\rho\sigma}{\varepsilon} \tag{C.34}$$

Integrating C.34 with respect to time yields the solutions

$$\rho = \rho_0 e^{-\frac{t}{\tau}} \quad \text{where } \tau = \frac{\varepsilon}{\sigma} \tag{C.35}$$

The conductivity of metals is high (about $45\text{x}10^6$ $\text{Sm}^{-1}$for gold), so metals has a very short relaxation time τ, of the order of $30*10^{-15}$ s. The variation in time of the optical field is longer than τ, thus, the electric charge density

ρ can be assumed to equal zero. To obtain an expression for the wave equation inside a metal in terms of $\boldsymbol{E}$, $\boldsymbol{H}$ is eliminated by applying the curl operator $\nabla\times$ to (C.30) (and considering that $\nabla\times(\nabla\times a)=\nabla(\nabla\cdot a)-\nabla^2 a$) and differentiating (C.29) with respect to time, leading to the wave equation inside a metal of

$$\nabla^2 E = \mu\varepsilon\frac{\partial^2 E}{\partial t^2}+\mu\sigma\frac{\partial E}{\partial t} \tag{C.36}$$

For a monochromatic wave of angular frequency ω, the electric field equals

$$E = E_0\exp[i(k\cdot x-\omega t)] \tag{C.37}$$

so that by substituting (C.37) back into (C.36), the wave equation (C.36) becomes

$$\nabla^2 E+\hat{k}^2 E=0 \tag{C.38}$$

where $\hat{k}^2=\mu\varpi^2\left(\varepsilon+\frac{i\sigma}{\varpi}\right)$. This is the same as the wave-equation inside a non-conducting medium, which has solution of equation C.38 with real k only, if the complex dielectric constant (permittivity) $\hat{\varepsilon}$ and complex refractive index $\hat{n}$ is defined as

$$\hat{\varepsilon}=\varepsilon'+i\varepsilon''=\varepsilon+\frac{i\sigma}{\omega} \text{ and } \hat{n}=n'+in''=n+i\kappa \tag{C.39}$$

where κ is the attenuation/extinction coefficient. An expression for $\varepsilon'(n,k)$ and $\varepsilon''(n,k)$ from equation C.39 and $\hat{\varepsilon}=\hat{n}^2$ can be derived, giving $n^2-\kappa^2+2in\kappa=\varepsilon'+i\varepsilon''$. Equating the real and imaginary parts yields:

$$\varepsilon'=n^2-\kappa^2 \tag{C.40a}$$

$$\varepsilon''=2n\kappa \tag{C.40b}$$

From equations (C.40) it can be seen that $n(\varepsilon',\varepsilon'')$ and $\kappa(\varepsilon',\varepsilon'')$ is equal to (appendix C.7.4)

$$2n^2=\sqrt{\varepsilon'^2+\varepsilon''^2}-\varepsilon' \tag{C.41}$$

$$2\kappa^2=\sqrt{\varepsilon'^2+\varepsilon''^2}+\varepsilon' \tag{C.42}$$

Considering the complex wavevector $\hat{k} = \frac{\varpi \hat{n}}{c} = \frac{\varpi}{c}(n + i\kappa)$, the solution to the wave-equation in a conducting media of complex refractive index $\hat{n}$ (equation C.37) $E = E_0 \exp[i(\hat{k}x - \omega t)]$ becomes

$$E = E_0 \exp(-\frac{\varpi}{c}\kappa x) \exp[i\varpi(\frac{nx}{c} - t)] \tag{C.43}$$

The first part of the equation is real and corresponds to the absorption/attenuation of the wave, while the second part is imaginary and represents the oscillating electric field. The skin depth (δ) can be defined as the distance by which the wave has travelled through the material when the field strength has attenuated to 1/e of its initial value:

$$\delta(\lambda) = \frac{\lambda}{2\pi\kappa} \tag{C.44}$$

At near infrared frequencies, the skin depth of gold is about 20 nm, small compared to the wavelength of light. Gold is considered a perfect reflector at this frequency regime.

C.7.2 The Drude Model

In the previous section it was assumed that ε was invariant with frequency. In reality, ε does depend on frequency of the incident light ω, which can be derived with the Drude model, by looking at the electron response to the incident field.

According to the Drude model, metal consists of a background of immobile positive atoms through which electrons can move freely. Free electrons in the metal are assumed to behave as an electron gas. An incident oscillatory electric field E can apply a force to the free electrons, and the simple harmonic motion of electrons can be written as:

$$m\ddot{x} + (m/\tau)\dot{x} = -eE \tag{C.45}$$

where m and e is the effective electron mass in the metal and charge, respectively, τ is the relaxation time and describes the energy loss/damping due to scattering (collision) events with positive ions, the dot notates differentiation with respect to time and x is the electron displacement. Because the electrons are considered free, the natural restoring force for

bound charges $m\varpi_0^2$ is not included. To find dielectric constant as a function of incident frequency equation C.35 is solved, which yields the conductivity and the complex relative dielectric function $\hat{\varepsilon}/\varepsilon_0 = \hat{\varepsilon}_r = \varepsilon_r' + i\varepsilon_r''$ from which is obtained (appendix C.7.5)

$$\varepsilon_r' = 1 - \frac{\varpi_p^2 \tau^2}{1+\varpi^2\tau^2} \quad \text{and} \quad \varepsilon_r'' = \frac{\varpi_p^2 \tau^2}{\varpi(1+\varpi^2\tau^2)} \qquad \text{(C.46)}$$

where $\varpi_p^2 = \frac{Ne^2}{m\varepsilon_0}$ is the plasma frequency, due to collective oscillation of free electrons against a background of positive, fixed charges (ions), *N* is the conducting electron density (number of electrons per unit volume), *e* is the electron charge and ε_0 is the permittivity of free space and $\hat{\varepsilon} = \hat{\varepsilon}_r \varepsilon_0$ is the dielectric constant. At near-infra-red frequencies, the damping term in metals is negligible compared to the frequency i.e. $\omega >> 1/\tau$, and using equation C.46, the frequency dependent relative dielectric constant, according to the Drude model, becomes

$$\varepsilon_r' \approx 1 - \frac{\varpi_p^2}{\varpi^2} = n^2 - \kappa^2 \quad \text{and} \quad \varepsilon_r'' \approx \frac{\varpi_p^2}{\varpi^3\tau} = 2n\kappa \qquad \text{(C.47)}$$

At the plasma frequency, when $\varpi = \varpi_p$, $\varepsilon_r' = 0$ and $\varepsilon_r'' << 1$, or $n = \kappa$ and $\kappa < 1$. When $\varpi < \varpi_p$ then $\varepsilon_r' < 0$ and $\kappa > n$, and the incident field is quickly attenuated within the metal (large κ) and transmission tends to zero. According to conservation of energy, the light must be reflected. The reflectivity approaches unity for low frequencies $\omega < \omega_p$. Physically, free electrons inside the metal follow the incident field fast enough, inducing an electric field with a 180° phase shift that cancels out the incident field within the metal, resulting in large attenuation inside the metal and high reflectivity. In contrast, when $\varpi > \varpi_p$, $\varepsilon_r' > 0$ and $\kappa < n$, the real (oscillatory) part dominates, and transmission increases i.e. the metal becomes transparent, behaving more like a dielectric. Physically, the free electrons cannot move fast enough to shield the incoming field. Most metals have plasma frequencies in the ultra-violet, making most metals reflective in the visible.

C.7.3 Surface Plasmons and Surface Plasmon Polaritons

In the Drude model, free (conducting) electrons in a metal can respond to an incident electric field, which causes oscillations in the free electron density. A quantum of plasma oscillation is called a *plasmon*. At the interface between a metal and a dielectric, the charge- density oscillations are called surface plasmons (SP), which can couple to electro-magnetic waves, forming *surface plasmon polaritons*. Thus, a Surface Plasmon polariton (SPP) is a coupled state between an electro-magnetic wave and a surface plasmon, and are propagate along a metal-dielectric interface. A SPP propagates has an evanescent field that decays exponentially with perpendicular distance from the interface. Now the SPP dispersion relation can be derived.

C.7.3.1 Surface-Plasmon-Polariton Dispersion Relation

Consider a metal-dielectric interface at $z = 0$. The dielectric is in the region $z > 0$, while the metal is in the region of $z < 0$. The permittivity is assumed to only vary along the z direction i.e. $\hat{\varepsilon} = \hat{\varepsilon}(z)$, with dielectric constant of ε_d and $\hat{\varepsilon}_m$ of the dielectric and metal, respectively. The mediums are assumed to be non-magnetic, i.e. magnetic permeability is equal to that of free space μ_0. Considering a propagating wave propagating in the x-direction of the form $E(r,t) = E(z)e^{i(k_x x - \varpi t)}$, it can be shown (appendix C.7.6) that the solution to the wave-equation are propagating waves with different polarisation states (a) s-polarisation with non-zero field components B_x , B_z, E_y, where E_y is parallel to the interface (transverse electric, TE mode) , and (b) p-polarisation with non-zero field components E_x, E_z, B_y, where B_y is parallel to the interface (transverse magnetic TM mode). As the electric field of waves propagating along a metal-dielectric interface (x-direction) is perpendicular to that interface, i.e. $E_z \neq 0$, only p-polarised light, which has a non-zero electric field component perpendicular to the interface, can form such waves. Hence, here only TM modes are considered. The TM mode equations (appendix C.7.6) are given by

$$-\frac{i}{\varpi\mu\hat{\varepsilon}}\frac{\partial B_y}{\partial z}=E_x \tag{C.48a}$$

$$-\frac{k_x}{\varpi\mu\hat{\varepsilon}}B_y=E_z \tag{C.48b}$$

$$\frac{\partial^2 B_y}{\partial z^2}+(\varpi^2\mu\hat{\varepsilon}-k_x^2)B_y=0 \tag{C.48c}$$

From the solution of equation C.48c inside a metal and dielectric, respectively, it can be shown that (appendix C.7.7)

$$(\hat{k}_{z,d})^2=\hat{k}_{x,d}{}^2-\varepsilon_d k_0^2 \tag{C.49}$$

and

$$(\hat{k}_{z,m})^2=\hat{k}_{x,m}{}^2-\varepsilon_m k_0^2 \tag{C.50}$$

where $\hat{k}_{z,d}$ / $\hat{k}_{z,m}$ is the component of the wavevector perpendicular to the dielectric-metal interface inside the dielectric/metal, and $k_0=\varpi/c$. Applying the boundary conditions of continuous tangential fields at the interface i.e. $B_{y,m}(z=0)=B_{y,d}(z=0)$ and $E_{x,m}(z=0)=E_{x,d}(z=0)$, it can be shown that (appendix C.7.7)

$$\hat{k}_{x,m}=\hat{k}_{x,d}=\hat{k}_x \qquad \text{at } z=0 \tag{C.51}$$

and

$$\frac{\hat{k}_{z,d}}{\varepsilon_d}=-\frac{\hat{k}_{z,m}}{\hat{\varepsilon}_m} \tag{C.52}$$

Substituting equation C.49 and C.50 into C.51, the surface-plasmon-polariton dispersion relation is obtained

$$\hat{k}_x=\frac{\varpi}{c}\sqrt{\frac{\hat{\varepsilon}_m\varepsilon_d}{\hat{\varepsilon}_m+\varepsilon_d}} \tag{C.53}$$

Since $\hat{k}_x=k_x'+ik_x''$ is complex, it represents an attenuated wave, and has real and imaginary parts, respectively, equal to[361]

$$k_x'=\frac{\varpi}{c}\sqrt{\frac{\varepsilon_m'\varepsilon_d}{\varepsilon_m'+\varepsilon_d}} \qquad \text{and} \qquad k_x''=\frac{\varpi}{c}\left(\frac{\varepsilon_m'\varepsilon_d}{\varepsilon_m'+\varepsilon_d}\right)^{\frac{3}{2}}\frac{\varepsilon_m''}{2(\varepsilon_m')^2} \tag{C.54}$$

Thus, for a wave pinned to and propagating along the metal-dielectric interface (a SPP wave) to exist, k_x' must be real, which is satisfied if $\sqrt{\frac{\varepsilon_m' \varepsilon_d}{\varepsilon_m' + \varepsilon_d}} > 0$, i.e. if $\varepsilon_m < 0$ and $|\varepsilon_m| > \varepsilon_d$. As $\varepsilon_d > 0$ and at below the plasmon frequency $\varepsilon_m' < 0$, this is satisfied for a dielectric-metal interface below the plasmon frequency and SPP can exist.

K_x and k_z are both complex (equation C.54, C.49), and represent attenuation with distance along the interface and perpendicular from the interface, respectively. As k_x is complex, SPP will attenuate/decay with propagation, due to absorption in the metal. The propagation length of a SPP, *L*, is the distance a SPP travels along the interface before its electric field intensity has dropped by 1/e its original value, and (from equation C.54) is equal to

$$L_{SPP} = \frac{1}{2k_{SPP}''} = \lambda_0 \frac{(\varepsilon_m')^2}{2\pi\varepsilon_m''} \left(\frac{\varepsilon_m' + \varepsilon_d}{\varepsilon_m' \varepsilon_d} \right)^{\frac{3}{2}} \quad \text{(C.55)}$$

where λ_0 is the wavelength in vacuum. Thus, the SPP propagation length depends on the imaginary part of the metal dielectric constant i.e. $L_{SPP}(\varepsilon'')$. Metals with low losses, i.e. small ε_m'', and large negative real part ε_m', yield large L_{SPP}. As both ε_m'' and ε_m' are frequency dependent (equation C.47), $L_{SPP}(\varpi)$. L_{SPP} is long at low frequencies, and decreases as ω approaches the plasmon resonance frequency ω_p.

As k_z is complex, the electric field amplitude decays exponentially with distance from the interface (*z*-direction). The skin depth quantifies the extent of field penetration, and inside the dielectric and metal, respectively, is equal to

$$\delta_d = \frac{\lambda}{2\pi} \sqrt{\left(\frac{\varepsilon_m' + \varepsilon_d}{\varepsilon_d^2} \right)} \text{ and } \delta_m = \frac{\lambda}{2\pi} \sqrt{\left(\frac{\varepsilon_m' + \varepsilon_d}{\varepsilon_m'^2} \right)} \quad \text{(C.56)}$$

Strong concentration of the SPP electromagnetic field near the interface (small skin depth) occurs at large SPP wavevectors (equation C.47 and C.56). For small *k*, the SPP dispersion tends towards that of the lightline,

while for large *k*, the SPP frequency tends towards the surface plasmon frequency (appendix C.7.8)

$$\varpi_{SPP} = \frac{\varpi_p}{\sqrt{1+\varepsilon_d}} \tag{C.57}$$

At large *k*, the group velocity $\varpi_g = \frac{\partial \varpi}{\partial k} \to 0$ (zero gradient), i.e. the frequency becomes less dependent on the wavevector, resembling a classical non-dispersive surface plasmon.

C.7.4 Derivation of the Refractive Index and Attenuation Coefficient as a Function of the Dielectric Constant

According to the Drude model, the dielectric constant is equal to (equation C.40 in appendix C.7.1)

$$\varepsilon' = n^2 - \kappa^2 \tag{C.58a}$$

$$\varepsilon'' = 2n\kappa \tag{C.58b}$$

Squaring of (C.58) yields:

$$\varepsilon'^2(n,k) = n^4 + \kappa^4 - 2n^2\kappa^2 \tag{C.59a}$$

$$\varepsilon''^2(n,k) = 4n^2\kappa^2 \tag{C.59b}$$

Addition of (C.59a) to (C.59b) gives

$$\varepsilon'^2 + \varepsilon''^2 = n^4 + \kappa^4 + 2n^2\kappa^2 = (n^2+\kappa^2)^2 \tag{C.60}$$

Rearranging (C.60) gives

$$n^2 = \sqrt{\varepsilon'^2 + \varepsilon''^2} - \kappa^2 \tag{C.61a}$$

$$\kappa^2 = \sqrt{\varepsilon'^2 + \varepsilon''^2} - n^2 \tag{C.61b}$$

but $\varepsilon' = n^2 - \kappa^2$ (equation C.58a), so that

$$2n^2 = \sqrt{\varepsilon'^2 + \varepsilon''^2} - \varepsilon' \tag{C.62a}$$

$$2\kappa^2 = \sqrt{\varepsilon'^2 + \varepsilon''^2} + \varepsilon' \tag{C.62b}$$

C.7.5 Derivation of the Frequency Dependent Dielectric Constant

To find dielectric constant as a function of incident frequency equation C.35 in appendix C.7.1 is solved:

$$\rho = \rho_0 e^{-\frac{t}{\tau}} \quad \text{where } \tau = \frac{\varepsilon}{\sigma} \tag{C.63}$$

Assuming the incident field equals $E(t) = E_0 e^{-i\omega t}$, then the solution of (C.63) is of the form $v(t) = v_0 e^{-i\omega t}$, i.e. the free electrons will follow the optical field. Substituting this into $m\ddot{x} + bm\dot{x} = -eE$ yields a mean velocity of

$$\dot{x}(t) = -\frac{e\tau}{m(1 - i\omega\tau)} E(t) \tag{C.64}$$

where it is assumed that $b = \frac{1}{\tau}$. The current density, *J*, is related to the mean velocity via $J = -eN\dot{x}$, where *N* is the electron density (number of electrons per unit volume). According to Ohm's law, $J = \sigma E$, so that

$$\sigma = -\frac{en\dot{x}}{E} = \frac{e^2 N\tau}{m(1 - i\varpi\tau)} \tag{C.65}$$

but the complex dielectric constant equals $\hat{\varepsilon} = \varepsilon' + i\varepsilon'' = \varepsilon + \frac{i\sigma}{\omega}$, so that

$$\hat{\varepsilon} = \varepsilon - \frac{\varpi_p^2 \varepsilon_0}{\varpi^2 + i\varpi/\tau} \tag{C.66}$$

where $\varpi_p^2 = \frac{Ne^2}{m\varepsilon_0}$ is the plasma frequency, due to collective oscillation of free electrons against a background of positive, fixed charges (ions), and ε_0 is the permittivity of free space. The first term is due to bound electrons, while the second term is due to free electrons. Assuming the contribution from bound electrons can be neglected, the complex relative permittivity, $\hat{\varepsilon}_r = \hat{\varepsilon} / \varepsilon_0$, is then equal to

$$\hat{\varepsilon}_r = 1 - \frac{\varpi_p^2}{\varpi^2 + i\varpi/\tau} \tag{C.67}$$

Separating $\hat{\varepsilon}_r = \varepsilon' + i\varepsilon''$ into real (ε') and imaginary (ε'') parts, it is obtained

$$\varepsilon' = 1 - \frac{\varpi_p^2}{\varpi^2 + 1/\tau^2} \quad \text{and} \quad \varepsilon'' = \frac{\varpi_p^2 1/\tau}{\varpi(\varpi^2 + 1/\tau^2)} \tag{C.68}$$

C.7.6 Derivation of TE and TM Modes at a Metal-Dielectric Interface

Considering a propagating wave propagating in the x-direction, of the form $E(r,t) = E(z)e^{i(k_x x - \varpi t)}$. The wave-equation (equation C.36 in appendix C.7.1) can then be re-written as

$$\begin{aligned} &\nabla^2 E + \varpi^2 \mu\hat{\varepsilon} E = 0 \\ &\frac{\partial^2}{\partial z^2} E(z) + (\varpi^2 \mu\hat{\varepsilon} - k_x^2) E(z) = 0 \end{aligned} \tag{C.69}$$

Assuming a time dependence of $e^{-i\omega t}$ of the electric and magnetic fields of the wave, Maxwell`s equations ((C.29) and (C.30) appendix C.7.1) can be re-written as

$$\nabla \times B = \varepsilon\mu \frac{\partial E}{\partial t} + \mu\sigma E \quad \rightarrow \nabla \times B = -i\varpi\hat{\varepsilon}\mu E(z) e^{i(k_x x - \varpi t)} \tag{C.70a}$$

$$\nabla \times E = -\frac{\partial B}{\partial t} \quad \rightarrow \nabla \times E = i\varpi B \tag{C.70b}$$

Noting that the curl of a is equal to $\nabla \times a = \left(\frac{\partial a_x}{\partial z} - \frac{\partial a_z}{\partial x}\right) j + \left(\frac{\partial a_y}{\partial x} - \frac{\partial a_x}{\partial y}\right) k + \left(\frac{\partial a_z}{\partial y} - \frac{\partial a_y}{\partial z}\right) i$, where *i*, *j*, *k* are unit vectors in the *x*, *y*, *z* direction, respectively, and that there is no spatial variation in the *y*-direction i.e. $\frac{\partial}{\partial y} = 0$ and that $\frac{\partial}{\partial x} = ik_x$, $\frac{\partial}{\partial t} = i\varpi$, equation C.70a can be simplified to

$$\text{x-component} \rightarrow \frac{\partial B_y}{\partial z} = i\varpi\mu\hat{\varepsilon} E_x \tag{C.71a}$$

$$\text{y-component} \rightarrow \frac{\partial B_x}{\partial z} - ik_x B_z = -i\varpi\mu\hat{\varepsilon} E_y \tag{C.71b}$$

$$\text{z-component} \rightarrow ik_x B_y = -i\varpi\mu\hat{\varepsilon} E_z \tag{C.71c}$$

and equation C.70b $\nabla \times E = i\varpi B$ can be simplified to

$$\text{x-component} \rightarrow \frac{\partial E_y}{\partial z} = -i\varpi B_x \qquad \text{(C.72a)}$$

$$\text{y-component} \rightarrow \frac{\partial E_x}{\partial z} - ik_x E_z = i\varpi B_y \qquad \text{(C.72b)}$$

$$\text{z-component} \rightarrow ik_x E_y = i\varpi B_z \qquad \text{(C.72c)}$$

The solutions to these equations correspond to different polarisations of the propagating wave: transverse magnetic (TM) modes, where the only non-zero field components are E_x, E_z, and B_y and B_y is parallel to the interface (p-polarised) (equations C.71a, C.71c, C.72b), and transverse electric (TE) modes (s-polarised), with non-zero field components B_x , B_z and E_y, and E_y is parallel to the interface (equations C.71b, C.72a, C.72c).

C.7.7 Detailed Derivation of the SPP Dispersion

Consider the solutions to the TM equations in the dielectric and the metal, respectively (equations C.71 in appendix C.7.6). In the dielectric, where *z>0*, the permittivity/permeability equals $\hat{\varepsilon}_d / \mu_d$, and the solution the TM mode equation $\frac{\partial^2 B_y}{\partial z^2} + (\varpi^2 \mu \hat{\varepsilon} - k_x^2) B_y = 0$ equals $B_y = Ae^{-k_{z,d} z}$, where B is the amplitude pre-factor in the dielectric and k_z^d is the component of the wavevector perpendicular to the dielectric-metal interface, and by substituting back into the TM mode equation $\frac{\partial^2 B_y}{\partial z^2} + (\varpi^2 \mu \hat{\varepsilon} - k_x^2) B_y = 0$, can be seen to equal

$$(k_{z,d})^2 = k_x^{\ 2} - \varpi^2 \mu_d \hat{\varepsilon}_d \qquad \text{(C.73)}$$

Including the propagation factor in the x-direction of $e^{ik_{x,m}x}$, B_y can be written as

$$B_y = Ae^{-k_z^d z} e^{ik_x^d x} \qquad \text{(C.74a)}$$

The TM mode equations $-\frac{i}{\varpi\mu\hat{\varepsilon}}\frac{\partial B_y}{\partial z} = E_x$ (equation C.71) and $-\frac{k_x}{\varpi\mu\hat{\varepsilon}}B_y = E_z$ (equation C.71c) inside the dielectric, respectively, then become

$$i\frac{k_{z,d}}{\varpi\mu_d\hat{\varepsilon}_d}Ae^{-k_{z,d}z}e^{ik_{x,d}x} = E_x \tag{C.74b}$$

$$-\frac{k_{x,d}}{\varpi\mu_d\hat{\varepsilon}_d}Ae^{-k_{z,d}z}e^{ik_{x,d}x} = E_z \tag{C.74c}$$

In the metal, *z<0*, and permittivity/permeability equals $\hat{\varepsilon}_m/\mu_m$. The equations in the metal therefore become

$$B_y = Ce^{k_{z,m}z}e^{ik_{x,m}x} \tag{C.75a}$$

$$i\frac{k_{z,m}}{\varpi\mu_m\hat{\varepsilon}_m}Ce^{-k_{z,m}z}e^{ik_{x,m}x} = E_x \tag{C.75b}$$

$$-\frac{k_{x,m}}{\varpi\mu_m\hat{\varepsilon}_m}Ce^{-k_{z,m}z}e^{ik_{x,m}x} = E_z \tag{C.75c}$$

where

$$(k_{z,m})^2 = (k_{x,m})^2 - \varpi^2\mu_m\hat{\varepsilon}_m \tag{C.75d}$$

and *C* is the amplitude pre-factor in the metal. Assuming a non-magnetic dielectric and metal, $\mu_d = \mu_m = \mu_0$. Assuming continuous tangential field components B_y and E_x at the interface (*z=0*), i.e. $B_{y,m}(z=0) = B_{y,d}(z=0)$ and $E_{x,m}(z=0) = E_{x,d}(z=0)$, equations C.74 and C.75 yield $k_{x,d} = k_{x,m} = k_x$, and *A=C* and also

$$\frac{k_{z,d}}{\hat{\varepsilon}_d} = -\frac{k_{z,m}}{\hat{\varepsilon}_m} \tag{C.76}$$

From equation C.76, it can be seen that to obtain surface wave pinned to the interface propagating along the interface, i.e. a surface-plasmon-polariton SPP, the real part of $k_{z,d}$ and $k_{z,m}$ must be positive, i.e. the real parts of the complex permittivities $\hat{\varepsilon}_1$ and $\hat{\varepsilon}_2$ must be opposite in sign. While for dielectrics the real part of $\hat{\varepsilon}$ is positive, for most metals it is

negative for energies below the plasmon frequency (which is in the visible or lower energies) (appendix C.7.2). Thus, an interface between a metal and dielectric can support SPP. Substituting $(k_{z,d})^2 = (k_{x,d})^2 - \varpi^2 \mu_0 \hat{\varepsilon}_d$ and $(k_{z,m})^2 = (k_{x,m})^2 - \varpi^2 \mu_0 \hat{\varepsilon}_m$ into (C.76), and assuming the dielectric constant of the dielectric is real i.e. $\hat{\varepsilon}_d = \varepsilon_d$, the surface-plasmon-polariton dispersion relation is obtained

$$k_x = \frac{\varpi}{c} \sqrt{\frac{\varepsilon_d \hat{\varepsilon}_m}{\varepsilon_d + \hat{\varepsilon}_m}} \tag{C.77}$$

Since $\hat{\varepsilon}_m$ is complex, k_x is also complex. The real and imaginary parts $k_x = k' + k''$ can be separated by assuming $\varepsilon_m'' < |\varepsilon_m'|$ (i.e. ε_m'' can be neglected), where $\hat{\varepsilon}_m = \varepsilon_m' + i\varepsilon_m''$, and $\varepsilon_d < |\varepsilon_m'|$ and multiplying both the nominator and denominator by $(\varepsilon_d + \varepsilon_m') - i\varepsilon_m''$ to obtain a real denominator[361]

$$k' = \frac{\varpi}{c} \sqrt{\frac{\varepsilon_d \varepsilon_m'}{\varepsilon_d + \varepsilon_m'}} \text{ and } k'' = \frac{\varpi}{c} \left(\frac{\varepsilon_d \varepsilon_m'}{\varepsilon_d + \varepsilon_m'} \right)^{\frac{3}{2}} \frac{\varepsilon_m''}{2(\varepsilon_m')^2} \tag{C.78}$$

C.7.8 SPP Frequency at Large Wavevector k

It is assumed the metal relative dielectric constant ε_m' follows the Drude model of a free electron gas:

$$\varepsilon_m' = 1 - \frac{\varpi_p^2}{\varpi^2} \tag{C.79}$$

The SPP dispersion is equal to

$$k' = \frac{\varpi}{c} \sqrt{\frac{\varepsilon_m' \varepsilon_d}{\varepsilon_m' + \varepsilon_d}} \tag{C.80}$$

Eliminating ε_m' by substituting equation C.79 into equation C.80, and rearranging, yields

$$\frac{(\varpi^2 \varepsilon_d - \varpi_p^2 \varepsilon_d)\varpi^2}{k'c} = (1 + \varepsilon_d)\varpi^2 - \varpi_p^2 \tag{C.81}$$

At large k' the left hand term tends to zero, so that ϖ tends to

$$\varpi_{SPP} = \frac{\varpi_p}{\sqrt{1+\varepsilon_d}} \tag{C.82}$$

C.7.9 SPP-Far-Field Radiation Coupling via Prism Coupling

In the Otto configuration, a dielectric of dielectric constant ε_d and thickness d separates a prism, of dielectric constant ε_p, from a metal surface (Figure C.4(a)). For light of wavevector k_L, incident at an angle θ to the normal onto a prism-dielectric interface, the in-plane wavevector equals $k_{x,L} = k_L \sqrt{\varepsilon_d} \sin\theta$. A high refractive index prism, where $\sqrt{\varepsilon_p} > \sqrt{\varepsilon_d}$, has two effects, it (a) increases the in-plane wavevector to $k_{x,L} = k_L \sqrt{\varepsilon_p} \sin\theta$, allowing the dispersion curve of light inside the prism to cross that of SPP at the dielectric-metal interface (Figure C.4(c)); at resonance $k_{x,L} = \frac{\varpi_L \sqrt{\varepsilon_p}}{c} \sin\theta = k_{SPP}$, and (b) creates and an evanescent field at the prism-dielectric interface via total internal reflection (TIR), when $\theta > \theta_C$, where θ_C is the critical angle and according to Snell`s law of refraction equals $\theta_C = \arcsin\left(\sqrt{\frac{\varepsilon_d}{\varepsilon_p}}\right)$. As a result, the incident wave inside the prism, via the evanescent field, can excite a SPP at the metal-dielectric boundary a distance d away (Figure C.4(a)). However, for coupling to occur requires d to be less than the evanescent decay length inside the dielectric, which is about 200 nm.

The alternative Kretschman-Reather configuration avoids the problem of having to control d, by depositing a thin metal layer directly onto the prism base (Figure C.4(b)). The evanescent field is created at the prism-metal interface, and SPP can be excited at the opposite metal surface, the metal-dielectric interface, given that the metal-thickness is less than the skin-depth (a few nanometers). Note that only SPP at the metal-dielectric, not the metal-prism, interface can be excited in both the Otto

and Kretschman-Reather configuration, as the dispersion curves of light inside the prism and SPP at the prism-metal interface do not cross (Figure C.4(c)).

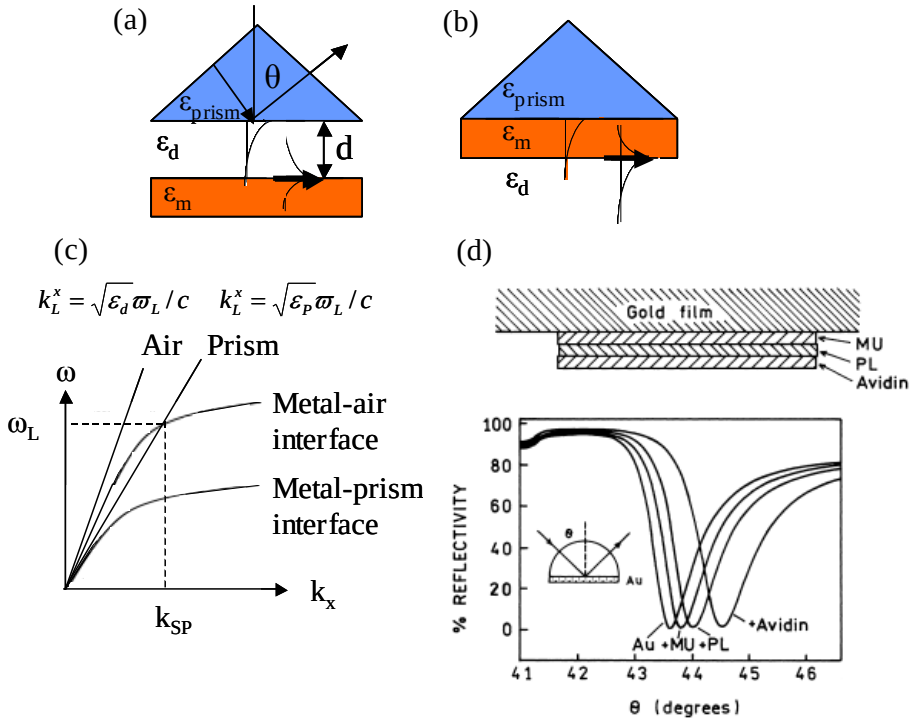

Figure C.4: SPP-optical field prism coupling configurations (a) Otto configuration (b) Kretschman-Reather configuration (c) dispersion curves of light in a dielectric (air) of dielectric constant ε_d, inside a prism of dielectric constant $\varepsilon_p > \varepsilon_d$, and the dispersion curve of a surface plasmon polariton at a metal-dielectric (air) and metal-prism interface (d) Kretschman configuration for sensitive detection of avidin, 11-mercaptoundecanoic acid (MU) and poly-lysine (PL) on a 47 nm thick gold film. Illumination was at 633 nm.[257]

The prism configuration has been used before in sensitive detection applications: a change in the dielectric refractive index due to deposition of macromolecules, for instance, will slightly change the effective dielectric refractive index, resulting in a small change in the angle at which surface plasmon resonance occurs. For incidence angles exceeding the critical angle, the reflectivity is high. However, at the angle that satisfies the resonance condition, a dip in the reflectivity occurs, as incident light excites SPP (Figure C.4(d)). Also, because the metal dielectric constant is frequency dependent, a change in the illumination light frequency will change the resonance angle. However, prism-coupling requires very precise geometry.

C.8 Mie Modes in Fully Enclosed Gold Nanovoids

To obtain the electromagnetic modes of a single dielectric sphere surrounded by an infinite expanse of gold, Maxwell`s equations in spherical coordinates are solved by applying the boundary conditions that the tangential components of ***E*** and ***H*** must be continues at the sphere surface.[21, 22] The resulting set of solutions take the form of spherical Bessel, J_l, and Henkel, H_l, functions[21]

$$\varepsilon_d H_i(k_m R)[k_d R J_l(k_d R)]' = \varepsilon_m(E) J_l(k_d R)[k_m R H_l(k_m R)]' \quad \text{(C.83)}$$

where R is the void radius, l and m is the angular momentum and azimuthal quantum number, respectively, $k_m = \sqrt{\varepsilon_m}k_0$ and $k_d = \sqrt{\varepsilon_d}k_0$ is the wavevector in the metal and dielectric void, respectively and ` donates differentiation with respect to ka. According to the Drude model $\varepsilon_m(\varpi) = 1 - \varpi_p^2/\varpi^2$, where ω_p is the 3D plasmon frequency. The solutions to equation C.83 give the resonant mode frequencies, which depend on the void radius R and angular momentum quantum number l. Modes with different values of m are energy degenerate due to spherical symmetry.[289]

The electromagnetic field distribution within a single dielectric cavity can also be calculated, the lowest two modes solutions ($l = 1, 2$) of which are shown in figure C.5(i)(a-c). It can be seen from Figure C.5(i)(a-c) that with increasing l, the Mie modes become increasingly confined to the metal surface.

An expression for the Mie plasmon wavevector k as a function of l and R can be obtained from the angular and linear momentum equations

$$\left|\vec{L}\right| = \hbar l = R\vec{p} \quad \text{(angular momentum)} \quad \text{(C.84a)}$$

$$\vec{p} = \hbar\vec{k} \quad \text{(linear momentum)} \quad \text{(C.84b)}$$

where $\vec{p}$ is the linear momentum. Rearranging equations C.84 for k leads to[362]

$$k = \frac{l}{R} \quad \text{(C.85)}$$

Combining this with the Mie plasmon energies *E(l, R)* (equation C.83), the dispersion relation can be constructed (Figure 4.9(ii) in section 4.2.2.2.1).

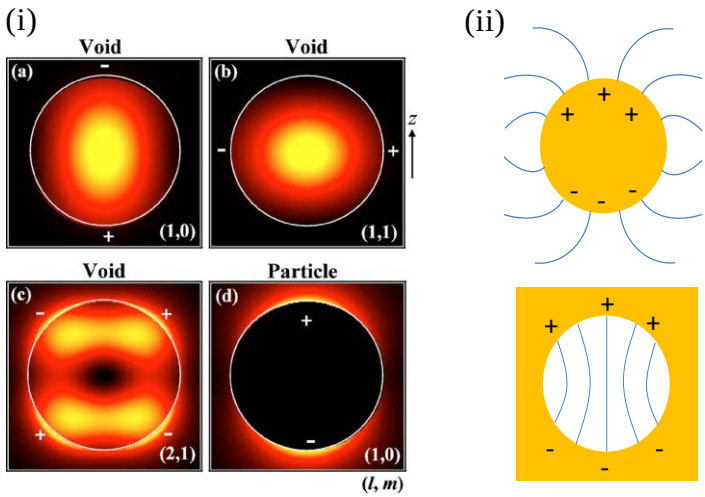

Figure C.5: Mie plasmon modes, as modelled by Mie theory (i) theoretical (Mie plasmon) electric field distribution for (a-c)spherical air void within an infinite expanse of gold (d) gold article surrounded by air for different (l, m) modes[21] (ii) electric field lines around gold sphere in a dielectric expanse (top) and inside dielectric void inside expanse of gold (bottom).[287]

The dispersion curve of Mie plasmons inside a dielectric metal nanovoid are blue-shifted compared to SPP on a flat metal surface (Figure 4.9(ii) section 4.2.2.2.1). The shift to higher energies can be rationalised by considering the electric field lines, which are perpendicular to the sphere surface.[287] In the case of a metal sphere, these field lines can expand into free space, while in a dielectric void, the electric field lines are confined within the nanovoid volume (Figure C.5(ii)). The increased concentration of the electric field lines inside the void volume relative to that on a particles causes the blue-shift.[289]

C.9 Assigning the angular Momentum Quantum Number to Mie Modes in Fully Enclosed Voids

(a) (b)

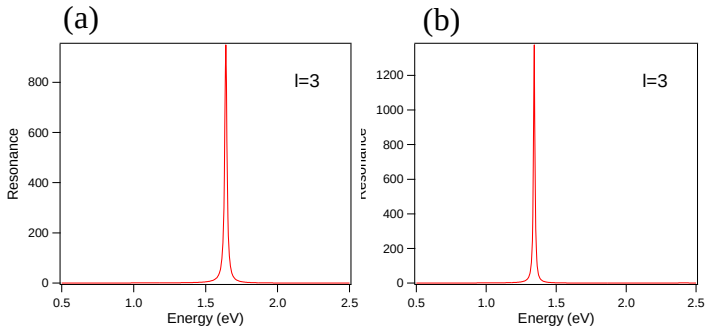

(c)

	D (nm)			
	780		989	
	Energy (eV)			
l	Mie theory	BEM	Mie theory	BEM
1	0.96	0.92	0.77	
2	1.32	1.24, 1.46	1.07	0.92,1.16
3	1.64	1.62	1.34	1.32
4	1.92	1.84, 2.00	1.60	1.62, 1.72
5	2.13	2.14	1.83	1.86
6	2.26		2.02	2.04
7	2.31		2.17	2.16

Figure C.6: Mie modes for water-filled, fully enclosed gold voids as predicted by Mie theory, the void diameter is equal to (a) 780 nm and (b) 989 nm and the angular momentum index l equal to 3; (c) energy values predicted by Mie theory (normalised thickness =1) and BEM (at normalised thickness = 0.99), for Mie modes of different values of l, D is the void diameter.

C.10 Standing Wave Model for Modelling Mie Plasmons in Truncated Voids

The one-dimensional standing wave model describes Mie plasmon modes supported by a truncated metal nanovoid in terms of plasmon standing waves.[21] According to the standing wave model, plasmons propagate within the rim but are reflected from the upper void edge, forming a plasmon standing wave within the void that is pinned at the upper void edge (Figure C.7). Only modes that have a half-wavelength that equal a multiple (p) of the curved rim-to-rim distance (y) can form a standing wave inside the void, i.e. $p\frac{\lambda_M}{2} = y$, where p is an integer. The Mie energy equals

$$E = \hbar c k_M \sqrt{\varepsilon_d^{-1} + \varepsilon_m^{-1}(E)} \tag{C.86}$$

where $k_M = p\frac{2\pi}{y} = \frac{\pi p}{D_{void} ac \cos(1-2\bar{t})}$ is the standing wave plasmon wavevector and ε_d and ε_m are the dielectric functions of the dielectric and metal, respectively, and the normalised void thickness equals $\bar{t} = t_{void} / D_{void}$. Thus, the energy of localised Mie plasmons is solely dependent on void geometry i.e. void diameter D_{void} and void thickness t_{void}. For normalised thickness above 0.8, theoretical predications are inconsistent with experimental data.

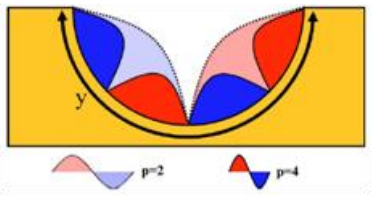

Figure C.7: 1D Standing wave model for Mie plasmon energies in truncated voids[21].

C.11 Boltzmann Statistics

Consider a system containing $N = \sum_i n_i$ molecules each occupying a quantised energy state of energy E_i and in thermal equilibrium at temperature *T (K)*. The total internal (thermal) energy of the system is equal to[363]

$$U = \sum_i n_i E_i \tag{C.87}$$

The number of molecules occupying energy level *j* is given by

$$\frac{n_j}{N} = \frac{\exp(-E_j/kT)}{\sum_i \exp(-E_i/kT)} \tag{C.88}$$

where *k* is Boltzmann`s constant. To simplify, only a two energy levels system is considered here. In thermal equilibrium, the number of molecules occupying the upper energy state E_2, where $E_2 > E_1$, is given by

$$\frac{n_2}{n_1+n_2} = \frac{\exp(-E_2/kT)}{\exp\left(-\frac{E_1}{kT}\right)+\exp(-E_2/kT)} \tag{C.89}$$

which can be simplified to

$$\frac{n_2}{n_1} = \frac{\exp(-E_2/kT)}{\exp(-E_1/kT)} = \exp(-\Delta E/kT) \tag{C.90}$$

where $\Delta E = E_2 - E_1$.The energy difference and hence population distribution of electronic and vibrational energy levels in an atom can be calculated using the hydrogen atom as an example. For one mole $R = N_A k$, where *R* is the gas constant *R=8.31 J/(mol*K)* and *NA=6.022*1023 mol*$^{-1}$ is Avogadro`s constant. The energy separation between the electronic ground state 1s and the first electronic state 2s of a hydrogen atom in a gas phase is equal to 1000 kJmol^{-1}, so that at room temperature *T=25 °C=298.15 °K* the population in each s-state given by[363]

$$\frac{n_{2s}}{n_{1s}} = = \exp\left(-\Delta E * \frac{NA}{RT}\right) = \exp(-1000/2.48) = \exp(-403) \tag{C.91}$$

i.e. practically all molecules occupy the lowest electronic state at room temperature.[363] The energy separation between two vibrational levels in a CO_2 molecule is equal to 25 KJmol^{-1}, so that[363]

$$\frac{n_{v=1}}{n_{v=0}} = = \exp\left(-\Delta E * \frac{NA}{RT}\right) = \exp(-25/2.48) = \exp(-10) \tag{C.92}$$

so that about 1 in 2,000 molecules occupies the higher vibrational state.[363]

C.12 Derivation of the Total Charge Q Required to Grow a Film Height h for a Close-Packed 2D Hexagonal Lattice of Spheres

Consider an area of dimensions *a*b* of a hexagonally close 2D packed lattice of spheres of radius *R*.

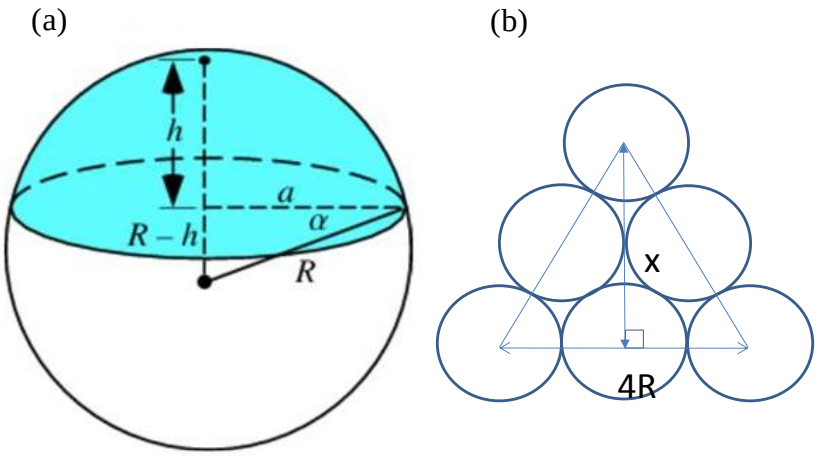

Figure C.8: Calculation of volume of space between spheres in a hexagonal close packed lattice (a) Volume of cap height h, sphere radius R, z-axis to sphere perimeter distance a[364] (b) one unit cell.

In a single sphere, a cap of height *h* (Figure C.8(a)) occupies a volume equal to

$$V_{cap} = \frac{1}{6}\pi h(3a^2 + h^2) \qquad \text{(C.93)}$$

According to Pythagoras,

$$(R-h)^2 + a^2 = R^2 \qquad \text{(C.94)}$$

Substituting for a (equation C.94) into equation C.93, gives

$$V_{cap} = \frac{1}{3}\pi h^2(3R-h) \qquad \text{(C.95)}$$

Now consider a unit cell (Figure C.8(b)), which is an equilateral triangle, of base width *4R* and length $x = 2*2R\cos 30\circ = 2\sqrt{3}R$. The triangle contains 2 spheres. Assuming a height h, the triangle volume is equal to

$$V_{triangle} = area * height = x * 4Rh/2 = 4\sqrt{3}R^2h \qquad \text{(C.96)}$$

The volume of space between spheres inside a single triangle volume is equal to the triangle volume minus the volume of 2 caps (as the triangle contains 2 caps), i.e.

$$V_{space} = 4\sqrt{3}R^2 h - 2\left[\frac{1}{3}\pi h^2 3R - h\right] \tag{C.97}$$

In a 2D lattice, a volume *a*b*t*, where *t<2R*, contains *N* number of triangles, where *N* is equal to

$$N = \frac{a*b*h}{V_{triangle}} = \frac{a*b*h}{4\sqrt{3}R^2 h} = \frac{a*b}{4\sqrt{3}R^2} \tag{C.98}$$

Thus, in a volume *a*b*h* the total volume of free space ($V_{totalspace}$) is proportional to the number of triangles in that volume and the volume of free space in a single triangle, i.e. equal to

$$V_{totalspace} = N*V_{space} = \frac{a*b}{4\sqrt{3}R^2}\left[4\sqrt{3}R^2 h - 2\left[\frac{1}{3}\pi h^2(3R-h)\right]\right]$$

$$= a*b*\left[h - \frac{1}{2\sqrt{3}R^2}\frac{1}{3}\pi h^2(3R-h)\right]$$

$$V_{totalspace} = a*b*\left[h - \frac{1}{2\sqrt{3}R^2}V_{cap}\right] \tag{C.99}$$

Faraday`s constant, *F*, is the quantity of charge carried by one mole of electrons. Letting N_A be Avogadro's number, the quantity of entities in 1 mole, and *e* the electronic charge, *F* can be written as

$$F = eN_A = 1.602*10^{-19}*6.022*10^{23}$$
$$F = 9.65*10^4 Cmol^{-1} \tag{C.100}$$

The total charge required to deposit a certain amount of material is equal to

$$Q(C) = nF \tag{C.101}$$

where *n* is the number of moles of electrons, but *n* is equal to the (total mass) divided by the (mass per unit mole) (atomic weight *W*), and the total mass is equal to (total volume)*(mass per unit volume) (density ρ), so that

$$n = \frac{V*\rho}{W} \tag{C.102}$$

Assuming an efficiency factor of 0.8, and a close packed hexagonal lattice of spheres, where the volume between the spheres is give by equation C.99, *Q* is equal to

$$Q(C) = \frac{a*b*\rho*F}{0.8W}\left[h - \frac{1}{2\sqrt{3}R^2}\frac{1}{3}\pi h^2(3R-h)\right] \qquad \text{(C.103)}$$

C.13 Derivation of the Void Thickness from SEM Images

Consider a void of thickness *t*, grown around a sphere of radius *R=494.5 nm* (Figure C.9). On the SEM images, the void length, *l*, can be measured (*l=722 nm*), from which *t* can be derived as follows. Consider the right-angled triangle a-b-c. According to Pythagoras

$$R^2 = (R-t)^2 + (l/2)^2 \qquad \text{(C.104)}$$

Rearranging gives

$$t = R - \sqrt{R^2 - (l/2)^2}$$

$$= 494.5nm - \sqrt{(494.5nm)^2 - (722nm/2)^2}$$

$$t \approx 157nm$$

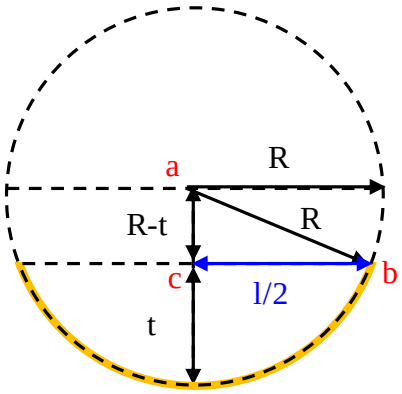

Figure C.9: Side view of a truncated void (yellow line) of thickness t and top void length, l, as grown from a sphere (dashed circle) of radius R.

C.14 Fluorescence Images of TOTO-1 within DNA Strands Stretched over Gold Nanovoids

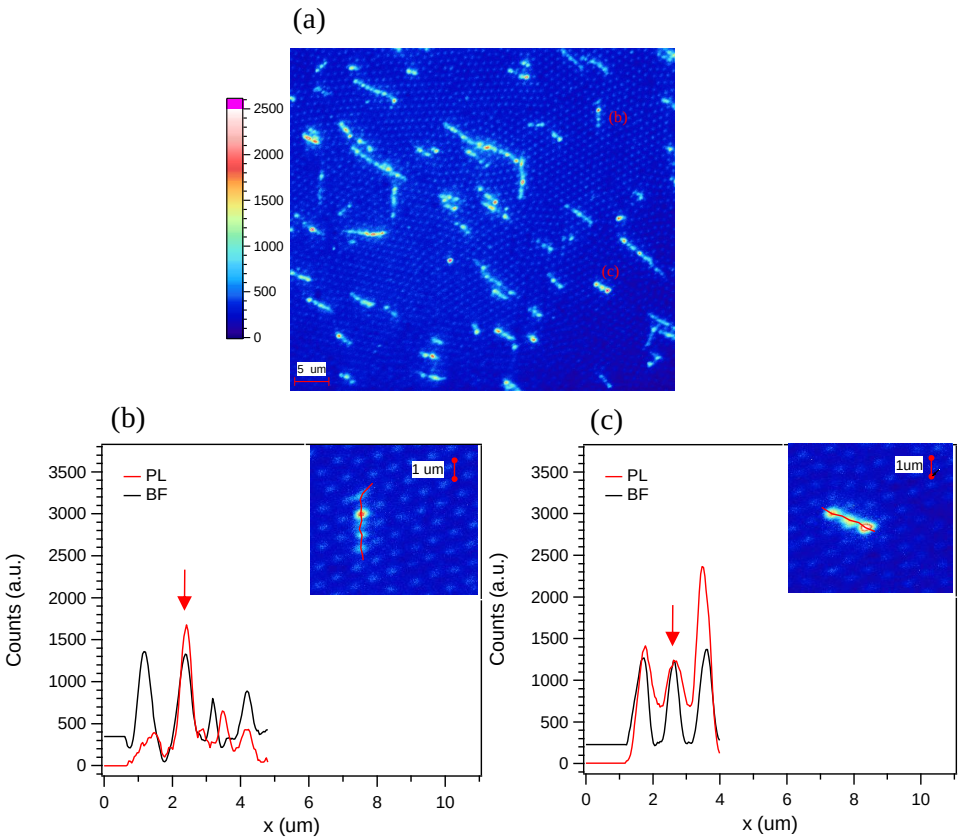

Figure C.10: Fluorescence of DNA-TOTO-1 stretched over a rough gold nanovoid substrate (a) 2D fluorescence image at two different sample locations (b, c) intensity profiles in fluorescence (red line) and bright field (black line) along individual DNA strands (drawn by hand), inset: path of maximum fluorescence intensity in the fluorescence image (PL, red line). Indicated are locations along the DNA profile where fluorescence and bright field peaks coincide (red arrows). The fluorescence images were obtained with 100x oil immersion, 1.6 optovar, integration time equals 28.652 s. The fluorescence image and intensity profiles were normalised to 30s integration time and fluorescence background level due to the top rough gold surface was subtracted. DNA concentration is equal to 25 pM, bp: TOTO-1 is equal to 1:0.16 coverslip dimension is 20x10 mm^2, drop- cast volume is 1.6µL.

C.15 Full Bright Field and Fluorescence Image of TOTO-1-DNA Strands Stretched Over a Gold Nanovoid Substrate

(a) (b)

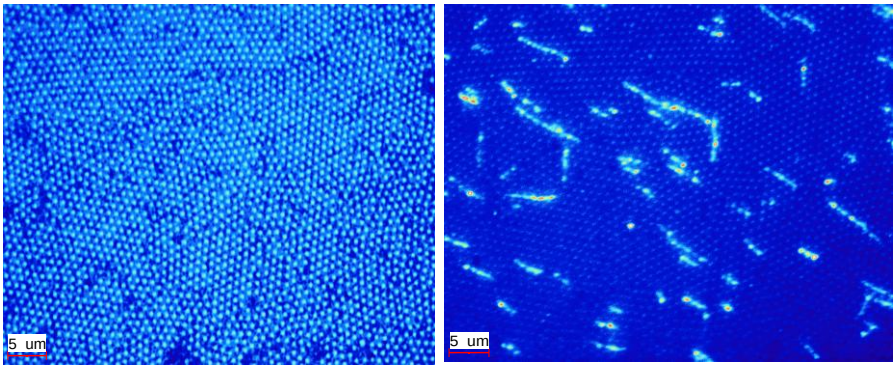

Figure C.11: Typical (a)Bright field and (b) fluorescence images of TOTO-1-DNA stretched over the nanovoid substrate with void diameter D_{void}=989 nm and void thickness d=157 nm.

C.16 Bright Field and Fluorescence Images of Individual TOTO-1-DNA Strands Stretched Over a Gold Nanovoid Substrate

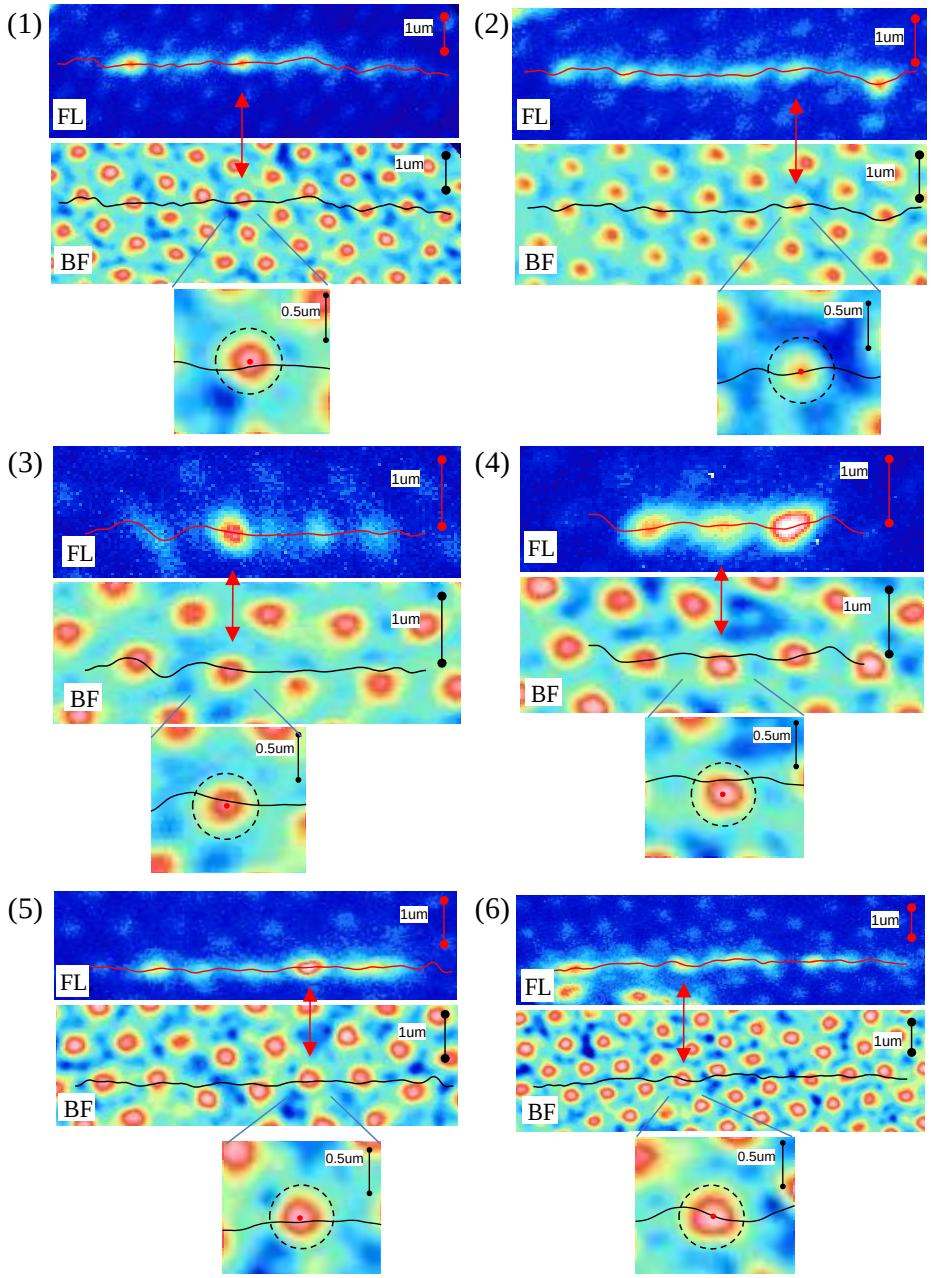

Figure C.12: Fluorescence (top)(FL) and bright field images (middle)(BF) of the individual stretched DNA strands, line in red (top) and black (middle) indicate line of maximum fluorescence intensity signal along stretched TOTO-1-DNA strand (drawn using a macro), close-up of the bright field-image (bottom) indicate the estimated location of the void rim (dashed circle) and the void centre (red dot) relative to the DNA strand (black line), DNA strands are from (1)Figure 4.35(b)(ii), (2) Figure 4.35(b)(iii), (3) Figure 4.35(b)(i), (4) C.10 in appendix C.14 (5) Figure 4.35(d)(ii), (6) Figure 4.35(d)(iii) in section 4.5.3.

C.17 TCSPC

Time –Correlated-Single-Photon-Counting (TCSPC) is a technique that measures the delay time between a single fluorescent photon and excitation pulse, and builds up a histogram of delay times by binning into delay time slots.[365] The TCSPC setup is shown in figure C.10.

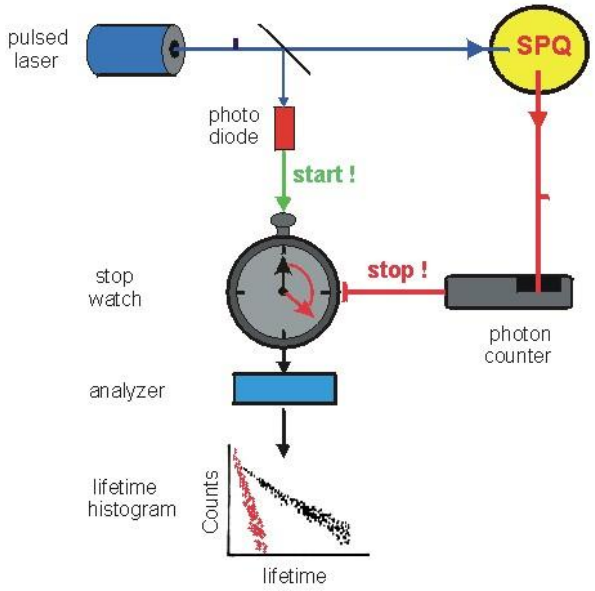

Figure C.13: Typical TCSPC setup[366]

A semitransparent mirror splits the optical path of the excitation pulse into two different directions (1) one excites a fluorescent sample, which emits a photon time t after excitation, which is detected by a photon counter (2) the other part passes a photodiode, which upon arrival of the excitation pulse, starts a time-to-amplitude converter. The time-to-amplitude converter counts time until a signal from the photon counter arrives. The time between arrival of the excitation pulse and the arrival of the florescent photon is equal to the time the sample spends in the excited state. After the measurement of one lifetime, the time-to-amplitude converter is reset to 0, and the delay times associated with the following pulse is measured, etc. Each measured delay time is stored in a memory address that is

proportional to the delay time, building up a histogram of number of photons versus delay time. It is assumed that the intensity of the excitation pulse is low enough to result in detection of a single photon per excitation pulse.

C.18 Summary of Fluorescence Lifetime Measurement Results

substrate	I (counts)	ti (ns)	ai (%)	av t (ns)	error av t (ns)
glass					
a		3.21	100	3.21	0.12
b		3.30	100	3.3	0.11
c		3.58	100	3.58	0.13
nanovoids	18	2.68	85.1	3.41	0.22
		7.60	14.9		
	22	1.76	73.7	2.68	0.39
		5.26	26.3		
	27	2.74	85.9	3.34	
		6.97	14.1		
	31	1.55	71.3	2.52	0.48
		4.93	28.7		
	31	2.52	96.1	2.68	0.90
		6.52	3.9		
	33	2.52	96.1	2.66	1.09
		6.07	3.9		
	37	2.42	79.9	3.25	0.35
		6.37	21.1		
	37	2.43	77.2	3.24	0.64
		5.99	22.8		
	38	2.59	94	2.77	1.09
		5.65	6		
	38	2.45	97.3	2.56	0.99
		6.66	2.7		
	41	2.84	93.4	3.03	0.22
		5.68	6.6		

Table C.1: Summary of multi-exponential fit parameters of the intensity decay curve of DNA-TOTO1 stretched over glass and gold nanovoid substrate.

C.19 Derivation of the Non-Radiative Decay Lifetime of TOTO-1.

The measured average fluorescence (or excited state) lifetime and quantum yield is equal to

$$\tau_0 = \frac{1}{k_r + k_{nr}} \text{ and } Q_0 = \frac{k_r}{k_r + k_{nr}} = \frac{\tau_0}{\tau_r} \quad \text{(C.105}$$

where the radiative lifetime, τ_r is equal to

$$\tau_r = \frac{1}{k_r} \quad \text{(C.106)}$$

The quantum yield and average fluorescence lifetime of TOTO-1 intercalated into Calf-thymus (CT) DNA is equal to [316] $Q_0^{DNA} = 0.34$ and $\tau_0^{DNA} = 1.96ns$, respectively, so that the radiative lifetime is equal to

$$\tau_r = \frac{\tau_0^{DNA}}{Q_0^{DNA}} = \frac{1.96ns}{0.34} = 5.76ns \quad \text{(C.107)}$$

Assuming that the radiative lifetime of TOTO-1 is unchanged upon intercalation into DNA, we have

$$\tau_r^{free} = \tau_r^{DNA} = \tau_r \quad \text{(C.108)}$$

The enhancement in quantum yield for DNA-bound TOTO-1 relative to TOTO-1 free in solution is equal to 1,400 [316]. We can define the enhancement in TOTO-1 quantum yield upon binding to DNA as

$$Q_{enh} = \frac{Q_0^{DNA}}{Q_0^{free}} \quad \text{(C.109)}$$

so that

$$Q_0^{free} = \frac{Q_0^{DNA}}{Q_{enh}} = \frac{0.34}{1{,}400} = 2.42 * 10^{-4} \quad \text{(C.110)}$$

Rearranging equation (C.105, Q_0) for the non-radiative decay rate k_{nr}, and using equations C.107 and C.110 yields for TOTO-1 free in solution

$$k_{nr}^{free} = \frac{(1 - Q_0^{free})}{\tau_r Q_0^{free}} = \frac{(1 - 2.42 * 10^{-4})}{5.76 * 10^{-9} * 2.42 * 10^{-4}} = 7.2 * 10^{11} s^{-1} \quad \text{(C.111)}$$

Assuming that

$$\tau_{nr}^{free} = \frac{1}{k_{nr}^{free}} \tag{C.112}$$

Then the non-radiative decay rate of TOTO-1 free in solution is equal to

$$\tau_{nr}^{free} = \frac{1}{k_{nr}^{free}} = \frac{1}{7.2*10^{11}} s = 1.4 ps \tag{C.113}$$

Applying equation C.111 for TOTO-1 intercalated into DNA, we find

$$k_{nr}^{DNA} = \frac{(1-Q_0^{DNA})}{\tau_r Q_0^{DNA}} = \frac{(1-0.34)}{5.76*10^{-9}*0.34} = 0.34*10^9 s^{-1} \tag{C.114}$$

so that equation C.112 for TOTO-1 bound to DNA yields

$$\tau_{nr}^{DNA} = \frac{1}{k_{nr}^{DNA}} = \frac{1}{0.34*10^9} s = 2.9 ns \tag{C.115}$$

Thus, from equations C.111 and C114 it can be seen that $k_{nr}^{DNA} << k_{nr}^{free}$.

Publications

1) Katrin Pechstedt, Tracy Whittle, Jeremy Baumberg, and Tracy Melvin, *Photoluminescence of Colloidal CdSe/ZnS Quantum Dots: The Critical Effect of Water Molecules*. J.Phys.Chem.C (2010), **114**: p. 12069-12077

2) Fabrice Birembaut, Nicolas Perney, Katrin Pechstedt, Philip N. Bartlett, Andrea E. Russell, Jeremy J. Baumberg, *Sharp-Cornered Liquid Drops by Wetting of Nanoscale Features.* Small (2008), **4**(12): p.2140-2142

References

1. X.Michalet, R.Ekong, F.Fougerousse, S.Rousseaux, C.Schurra, N.Hornigold, M.vanSlegtenhorst, J.Wolfe, S.Povey, J.S.Beckmann, A.Bensimon, *Dynamic Molecular Combing:Stretching the Whole Human Genome for High-Resolution Studies.* Science, 1997. **277**: p. 1518-1523.

2. J. Herrick, X.Michalet, C.Conti, C.Schurra, and A.Bensimon, *Quantifying single gene copy number by measuring fluorescent probe lengths on combed genomic DNA.* PNAS, 2000. **97**: p. 222-227.

3. E.Bailo, V.Deckert, *Tip-Enhanced Raman Spectroscopy of Single RNA Strands: Towards a Novel Direct-Sequencing Method.* Angew.Chem.Int.Ed., 2008. **47**: p. 1658-1661.

4. M.Stroun, P.Anker, P.Maurice, J.Lyautey, C.Lederrey, M.Beljanski, *Neoplastic Characteristics of the DNA Found in the Plasma of Cancer Patient.* Oncology, 1989. **46**: p. 318-322.

5. K.Yamashita, Y.Yamaguchi, M.Miyazaki, H.Nakamura, H.Shimizu, H.Maeda, *Direct observation of long-strand DNA conformational changing in microchannel flow and microfluidic hybridization assay*. Anal.Biochem., 2004. **332**: p. 274-279.

6. E.Y.Chan, N.M.Goncalves, R.A.Haeusler, A.J.Hatch, J.W.Larson, A.M.Maletta, G.R.Yantz, E.D.Carstea, M.Fuchs, G.G.Wong, S.R.Gullans, R.Gilmanshin, *DNA Mapping Using Microfluidic Stretching and Single-Molecule Detection of Fluorescent Site-Specific Tags.* Gen.Res., 2004. **14**: p. 1137-1146.

7. B.R.Cipriany, R.Zhao, X.P.J.Murphy, S.L.Levy, C.P.Tan, H.G.Craighead, and P.D.Soloway, *Single Molecule Epigenetic Analysis in a Nanofluidic Channel.* Anal.Chem., 2010. **82**: p. 2480-2487.

8. D.Branton, D.W.Dreamer, A.Marziali, H.Bayley, S.A.Benner, T.Butler, M.Di Ventra, S.Garaj, A.Hibbs, X.Huang, S.B.Jovanovich, P.S.Krstic,S.Lindsay, X.S.Ling, C.H.Mastrangelo, A.Meller, J.S.Oliver, Y.V.Pershin,J.M.Ramsey, R.Riehn, G.V.Soni, V.Tabard-Cossa, M.Wanunu, M.Wiggin, J.A.Schloss, *The potential and challenges of nanopore sequencing.* Nature Biotechnol., 2008. **26**(10): p. 1146-1153.

9. A. E. P.Schibel, T.Edwards, R.Kawano, W.Lan, and H. S.White, *Quartz Nanopore Membranes for Suspended Bilayer Ion Channel Recordings.* Anal.Chem., 2010. **82**: p. 7259-7266.

10. A.F.E.Hezinger, J.K.Tessmar, A.M.Göpferich. *Surface modified Quantum dots for the development of new drug delivery systems*. in *Partec 2007*. 2007.

11. X.Wu, H.Liu, J.Liu, K.N.Haley, J.A.Treadway, J.P.Larson, N.Ge, F.Peale, and M.P.Bruchez, *Immunofluorescent labeling of cancer marker Her2 and other cellular targets with semiconductor quantum dots.* Nature Biotech., 2003. **21**: p. 41-46.

12. W.C.W.Chan, D.J.Maxwell, X.Gao, R.E.Bailey, M.Han and S.Nie, *Luminescent quantum dots for multiplexed biological detection and imaging.* Curr.Opin.Biotechnol., 2002. **13**(1): p. 40-46.

13. T.Jamieson, R.Bakshi, D.Petrova, R.Pocock, M.Imani, A.M.Seifalian, *Biological applications of quantum dots.* Biomaterials, 2007. **28**: p. 4717-4732.

14. P.Alivisatos, *Colloidal quantum dots. From scaling laws to biological applications.* Pure Appl.Chem. , 2000. **72**(1-2): p. 3-9.

15. I.L.Mednitz, H.Mattoussi, A.R.Clapp, *Potential Clinical Applications of quantum dots.* Intern.J.Nanomedicine, 2008. **3**(2): p. 151-167.

16. U.Resch-Genger, M.Grabolle, S.Cavaliere-Jaricot, R.Nitschke, and T.Nann, *Quantum dots versus organic dyes as fluorescent labels.* Nature Meth., 2008. **5**(9): p. 763-775.

17. B.O.Dabbousi, J.Rodriguez-Viejo, F.V.Mikulec, J.R.Heine, H.Mattoussi, R.Ober, K.F.Jensen, M.G.Bawendi, *(CdSe)ZnS Core-Shell Quantum Dots: Synthesis and Characterization of a Size Series of Highly Luminescent Nanocrystallites.* J.Phys.Chem.B, 1997. **101**: p. 9463-9475.

18. J.Zhang, J.R.Lakowicz, *Metal-enhanced fluorescence of an organic fluorophore using gold particles.* Opt.Express, 2007. **5**(15): p. 2598-2606.

19. Y.Fu, J.Zhang, J.R.Lakowicz, *Metal-Enhanced Fluorescence of Single Green Fluorescent Protein (GFP).* Biochem.Biophys.Res.Commun., 2008. **376**(4): p. 712-717.

20. E.M.Goldys, A.Barnett, F.Xie, K.Drozdowicz-Tomsia, I.Gryczynski, E.G.Matveeva, Z.Gryczynski, T.Shtoyko, *Plasmon-enhanced fluorescence near metallic nanostructures: biochemical applications.* Appl.Phys.A, 2007. **89**: p. 265-271.

21. T.A.Kelf, Y.Suguwara, R.M.Cole, J.J.Baumberg, *Localised and delocalised plasmons in metallic nanovoids.* Phys.Rev.B, 2006. **74**: p. 245415.

22. R.M.Cole, J.J.Baumberg, F.J.Garcia deAbajo, S.Mahajan, M.Abdelsalam, and P.N.Bartlett, *Understanding Plasmons in Nanoscale Voids.* Nano Lett., 2007. **7**(7): p. 2094-2100.

23. M.E.Abdelsalam, P.N.Barlett, J.J.Baumberg, S.Coyle, *Preparation of Arrays of Isolated Spherical Cavities by Self-Assembly of Polystyrene Spheres on Self Assembled Pre-patterned Macroporous Films.* Adv.Mater., 2004. **16**(1): p. 90-93.

24. N.Douville, D.Huh, S.Takayama, *DNA linearization through confinement in nanofluidic channels.* Anal.Bioanal.Chem., 2008. **391**: p. 2395-2409.

25. A.H.Beggs, M.Koenig, F.M.Boyce and L.M.Kunkel, *Detection of 98% of DMD/BMD gene deletions by polymerase chain reaction* Hum.Gen., 1990. **86**(1): p. 45-48.

26. C.D.Bottema, S.S.Sommer, *PCR amplification of specific alleles: Rapid detection of known mutations and polymorphisms* Mutat.Res./Fundam.Molec.Mechan.Mutagen., 1993. **288**(1): p. 93-102.

27. S.Cheng, C.Fockler, W.M.Barnes, R.Higuchi, *Effective amplification of long targets from cloned inserts and human genomic DNA.* PNAS USA, 1994. **91**(12): p. 5695-5699.

28. K.S.Lundberg, D.D.Shoemaker, M.W.W.Adams, J.M.Short, J.A.Sorge and E.J.Mathur, *High-fidelity amplification using a thermostable DNA polymerase isolated from Pyrococcus furiosus.* Gene, 1991. **108**(1): p. 1-6.

29. A.E.Men, P.Wilson, K.Siemering, S.Forrest, *Next-Generation Genome Sequencing: Towards Personalized Medicine*, 2008, Wiley-VCH Verlag GmbH and Co. KGaA.

30. I.Pruysen, *Massive parallel ultra deep sequencing of Influenza/Herpes antiviral resistance with the Solexa Genome Analyzer*. in *Erasmus Medical Centre* , 2010, Graduation Report Bachelor Study, Rotterdam.

31. M.R.Schweiger, M.Kerick, B.Timmermann, M.Isau, *The power of NGS technologies to delineate the genome organization in cancer: from mutations to structural variations and epigenetic alterations.* Cancer Metastasis Rev., 2011. **30**: p. 199-210.

32. R.J.Roberts, *Restriction and modification enzymes and their recognition sequences.* Nucl.Ac.Res., 1980. **8**(1): p. r63-r80.

33. T.A.Brown, *Genomes*. 2002, Oxford: Wiley-Liss.

34. C.E.Browne, E.Hatchwell, A.Protopapos, J.Ramos, *Duplication of medial 15q confirmed by FISH.* J.Med.Genet., 2000. **37**: p. 1-2.

35. V.Shashi, D.Pallos, M.J.Pettenati, J.R.Cortelli, J.P.Fryns, C.vonKap-Herr, T.C.Hart, *Genetic heterogenity of gingival fibromatosis on chromosome 2p.* J.Med.Genet., 1999. **36**: p. 683-686.

36. C.Bendavid, B.R.Haddad, A.Griffin, M.Huizing, C.Dubourg, I.Gicquel, L.R.Cavalli, L.Pasquier, A.L.Shanske, R.Long, M.Ouspenskaia, S.Odent, F.Lacbawan, V.David, M.Muenke, *Multicolour FISH and quantitative PCR can detect submicroscopic deletions in holoprosencephaly patients with a normal karyotype.* J.Med.Genet., 2006. **43**: p. 496-500.

37. S.N.Bhatia, V.Suri, A.Bundy, C.M.Krauss, *Prenatal Detection and Mapping of a Distal 8p Deletion Associated with Congenital Heart Disease.* Prenat.Diagn., 1999. **19**: p. 863-867.

38. S.D.Pack, R.Boni, A.O.Vortmeyer, E.Pak, Z.Zhuang, *Detection of Gene Deletion in Single Metastatic Tumor Cells in the Excision Margin of a Primary Cutaneous Melanoma.* J.Nat.Cancer Institute, 1998. **90**(10): p. 782-783.

39. M.Nakano, Y.Kodama, K.Ohtaki, M.Itoh, R.Delongchamp, A.A.Awa, N.Nakamura *Detection of stable chromosome aberrations by FISH in A-bomb survivors: comparison with previous solid Giemsa staining data on the same 230 individuals.* Int.J.Radiat.Biol., 2001. **77**(9): p. 971-977.

40. Helmholtz-Gemeinschaft, Deutsches Krebsforschungszentrum in der Helmholz Gemeinschaft. *Molekulare Genetik: Tumor-Genomforschung*. 2008 [last accessed in December2010] http://www.dkfz.de/de/genetics/pages/projekte/tumor_genomforschung.html.

41. I.Parra, B.Windle, *High resolution visual mapping of stretched DNA by fluorescent hybridization.* Nature Genetics, 1993. **5**: p. 17-21.

42. R.J.FIorijn, L.A.J.Bonden, H.Vrolijk, J.Wiegant, J.W.Vaandrager, F.Baas, J.T.denDunnen, H.J.Tanke, G.J.B.vanOmmen, A.K.Raap, *High-resolution DNA Fiber-FISH for genomic DNA mapping and colour bar-coding of large genes.* Hum.Molec.Genet., 1995. **4**(5): p. 831-836.

43. D.Tsuchiya, M.Taga, *Application of fibre-FISH (fluorescence in situ hybridization) to filamentous fungi: visualization of the rRNA gene cluster of the ascomycete Cochliobolus heterostrophus.* Microbiology, 2001. **147**: p. 1183-1187.

44. R.Winkler, B.Perner, A.Rapp, M.Durm, C.Cremer, K.O.Greulich, M.Hausmann, *Labelling quality and chromosome morphology after low temperature FISH analysed by scanning far-field and near-field optical microscopy.* J.Microscopy, 2003. **2009**: p. 23-33.

45. H.Muramatsu, K.Homma, N.Yamamoto, J.Wang, K.Sakata-Sogawa, N.Shimamoto, *Imaging of DNA molecules by scanning near-field microscope.* Mater.Sci.Engin.C, 2000. **12**: p. 29-32.

46. C.O`Connor, *Fluorescence In Situ Hybridization (FISH).* Nature Education, 2008. **1**(1).

47. Invitrogen.com. *bioprobes.* [last accessed in March2010] www.invitrogen.com/etc/medialib/en/filelibrary/pdf/bioprobes/bioprobes42.Par.20920.File.tmp/5.pdf.

48. R.J.Florijn, F.M.van deRijke, H.Vrolijk, L.A.J.Blonde, M.H.Hofker, J.T.denDunnen, H.J.Tanke, G.J.B.vanOmmen, A.K.Raap, *Exon Mapping by Fiber-FISH or LR-PCR.* Genomics, 1996. **38**: p. 277-282.

49. F.M.van deRijke, R.J.Florijn, H.J.Tanke, and A.K.Raap, *DNA Fiber-FISH Staining Mechanism.* J.Histochem.Cytochem., 2000. **48**(6): p. 743-745.

50. J.H.Kim, W.X.Shi, and R.G.Larson, *Methods of Stretching DNA Molecules Using Flow Fields.* Langmuir, 2007. **23**: p. 755-764.

51. E.T.Dimalanta, A.Lim, R.Runnheim, C.Lamers, C.Churas, D.K.Forrest, J.J.de Pablo, M.D.Graham, S.N.Coppersmith, S.Goldstein, D.C.Schwartz, *A Microfluidic System for Large DNA Molecule Arrays.* Anal.Chem., 2004. **76**: p. 5293-5301.

52. K.Jo, Y.L.Chen, J.J.dePablo, and D.C.Schwartz, *Elongation and Migration of Single DNA Molecules in Microchannels Using Oscillatory Shear Flows.* Lab Chip., 2009. **9**(16): p. 2348-2355.

53. E.J.White, S.V.Fridrikh, N.Chennagiri, D.B.Cameron, G.P.Gauvin, R.Gilmanshin, *Staphylococcus aureus Strain Typing by Single Molecule DNA Mapping in Fluidic Microchips with Fluorescent Tags.* Clin.Chem., 2009. **55**(12): p. 2121-2129.

54. L.H.Thamdrup, A.Klukowska, A.Kristensen, *Stretching DNA in polymer nanochannels fabricated by thermal imprint in PMMA.* Nanotechnology, 2008. **19**: p. 125301.

55. P.G.deGennes, *Scaling concepts in polymer physics*. 1979, NY: Cornell University Press.

56. J.O.Tegenfeldt, C.Prinz, H.Cao, S.Chou, W.W.Reisner, R.Riehn, Y.M.Wang, E.C.Cox, J.C.Sturm, P.Silberzan, and R.H.Austin, *The dynamics of genomic-length DNA molecules in 100-nm channels.* PNAS, 2004. **101**(30): p. 10979-10983.

57. L.J.Guo, X.Cheng, C.F.Chou, *Fabrication of Size-Controllable Nanofluidic Channels by Nanoimprinting and Its Application for DNA Stretching.* Nano Lett., 2004. **4**(1): p. 69-73.

58. A.J.Storm, J.H.Chen, H.W.Zandbergen, C.Dekker, *Translocation of double-strand DNA through a silicon oxide nanopore.* Phys.Rev.E, 2005. **71**: p. 10.

59. R.M.Stöckle, Y.D.Suh, V.Deckert, R.Zenobi, *Nanoscale chemical analysis by tip-enhanced Raman spectroscopy.* Chem.Phys.Lett., 2000. **318**: p. 131-136.

60. W.G.J.H.M.vanSark, P.L.T.M.Frederix, D.J.Van denHeuvel, and H.C.Gerritsen, A. A.Bol, J.N.J.vanLingen, C.de Mello Donega, and A.Meijerink, *Photooxidation and Photobleaching of Single CdSe/ZnS Quantum Dots Probed by Room-Temperature Time-Resolved Spectroscopy.* J.Phys.Chem., 2001. **105**: p. 8281-8284.

61. W.G.J.H.M.vanSark, P.L.T.M.Frederix, A.A.Bol, H.C.Gerritsen, A.Meijerink, *Blueing, Bleaching, and Blinking of Single CdSe/ZnS Quantum Dots.* Chem.Phys.Chem., 2002. **3**(10): p. 871-879.

62. G.W.Shu, W.Z.Lee, I.J.Shu, J.L.Shen, J.C.A.Lin, W.H.Chang, R.C.Ruaan,and W.C.Chou, *Photoluminescence of Colloidal CdSe/ZnS Quantum Dots Under Oxygen Atmosphere.* IEEE Trans.Nanotechn., 2005. **4**(5): p. 632-636.

63. Y.Wang, Z.Tang, M.A.Correa-Duarte, I.Pastoriza-Santos, M.Giersig, N.A.Kotov, and L.M.Liz-Marzán, *Mechanism of Strong Luminescence Photoactivation of Citrate-Stabilized Water-Soluble Nanoparticles with CdSe Cores.* J.Phys.Chem.B, 2004. **108**(40): p. 15461-15469.

64. J.Müller, J.M.Lupton, A.L.Rogach, and J.Feldmann, D.V.Talapin and H.Weller, *Air-induced fluorescence bursts from single semiconductor nanocrystals.* Appl.Phys.Lett., 2004. **85**(3): p. 381-383.

65. F.Koberling, A.Mews, T.Basche, *Oxygen-Induced Blinking of Single CdSe Nanocrystals.* J.Adv.Mater., 2001. **13**(9): p. 672-676.

66. M.Jones, J.Nedeljkovic, R.J.Ellingson, A. J.Nozik, and G.Rumbles, *Photoenhancement of Luminescence in Colloidal CdSe Quantum Dot Solutions.* J.Phys.Chem.B, 2003. **107**: p. 11346-11352.

67. M.Oda, J.T., A.Hasegawa, N.Iwami, K.Nishiura, I.Hagiwara, N.Ando, H.Horiuchi, T.Tani, *Photobrightening of CdSe/ZnS/TOPO nanocrystals.* J.Luminescence, 2007. **122-123**: p. 762-765.

68. M.Oda, A.Hasegawa, N.Iwami, K.Nishiura, N.Ando, A.Nishiyama, H.Horiuchi, T.Tani, *Reversible photobluing of CdSe/ZnS/TOPO nanocrystals.* Coll.Surf.B:Biointerf., 2007. **56**(1-2): p. 241-245.

69. L.Jdira, *Electronic properties of semoconductor quantum dots-a scanning tunneing microscopy study*, in *Institute for Molecules and Materials*. 2008, Radboud University Nijmengen: Nijmengen. p. 1-113.

70. H.Mao, J.Chen, J.Wang, Z.Li, N.Dai, Z.Zhu, *Photoluminescence investigation of CdSe quantum dots and the surface state effect.* Physica E, 2005. **27**: p. 124-128.

71. V.I.Klimov, *Spectral and Dynamical Properties of Multiexcitons in Semiconductor Nanocrystals.* Annu.Rev.Phys.Chem. , 2007. **58**: p. 635-673.

72. L.Brus, *Electronic Wave Functions in Semiconductor Clusters: Experiment and Theory*. J.Phys.Chem., 1986. **90**: p. 2555-2560.

73. G.W.Hanson, *Fundamentals of Nanoelectronics*, 2008, Prentice Hall

74. G.T.Einevoll, *Confinement of excitons on quantum dots.* Phys.Rev.B, 1992. **45**(7): p. 3410-3417.

75. L.Besombes, L.Marsal, K.Kheng, and H.Mariette, *Exciton–Acoustic Phonon Coupling in Single CdTe Quantum Dots.* Phys.Stat.Sol.(B), 2001. **224**(3): p. 621-627.

76. D.Valerini, A.C., M.Lomascolo, L.Manna, R.Cingolani, M.Anni, *Temperature dependence of the photoluminescence properties of colloidal CdSe/ZnS core/shell quantum dots embedded in a polystyrene matrix.* Phys.Rev.B, 2005. **71**: p. 235409

77. S.A.Empedocles and G.Bawendi, *Quantum-Confined Stark Effect in Single CdSe Nanocrystallite Quantum Dots.* Science, 1997. **278**: p. 2114-2117.

78. A.Franceschetti and A.Zunger, *Optical transitions in charged CdSe quantum dots.* Phys.Rev.B, 2000. **62**(24): p. 287-290.

79. Al.L.Efros and M.Rosen, M.K., M.Nirmal, and M.Bawendi, *Band-edge exciton in quantum dots of semiconductors with a degenerate valence band: Dark and bright exciton states.* Phys.Rev.B, 1996. **54**(7): p. 4843-4856.

80. C.de Mello Donegá, M.Bode, and A.Meijerink, *Size- and temperature-dependence of exciton lifetimes in CdSe quantum dots.* Phys.Rev.B, 2006. **74**: p. 085320

81. D.F.Underwood, T.Kippeny, and S.J.Rosenthal, *Ultrafast Carrier Dynamics in CdSe Nanocrystals Determined by Femtosecond Fluorescence Upconversion Spectroscopy*. J.Phys.Chem.B, 2001. **105**: p. 436-446.

82. S.Pokrant and K.B.Whaley, *Tight-binding studies of surface effects on electronic structure of CdSe nanocrystals: the role of organic ligands, surface reconstruction, and inorganic capping shells.* Europ.Phys.J.D, 1999. **6**: p. 255-267.

83. E.Rabani, B.Hetenyi, and B.J.Berne, L.E.Brus, *Electronic properties of CdSe nanocrystals in the absence and presence of a dielectric medium.* J.Chem.Phys., 1999. **110**(11): p. 5355-5369.

84. L.Qu, X.Peng, *Control of Photoluminescence Properties of CdSe Nanocrystals in Growth.* JACS, 2002. **124**(9): p. 2049-2055.

85. F.Pinaud, X.Michalet, L.A.Bentolila, J.M.Tsay, S.Doose, J.J.Li, G.Iyer, S.Weiss, *Advances in fluorescence imaging with quantum dot bio-probes.* Biomater., 2006. **27**: p. 1679-1687.

86. T.Pons, I.L.Medintz, X.Wang, D.S.English, H.Mattoussi, *Solution-Phase Single Quantum Dot Fluorescence Resonance Energy Transfer.* JACS, 2006. **128**: p. 15324-15331.

87. R.Sarkar, S.S.Narayanan, L.O.Palsson, F.Dias, A.Monkman, and S.K.Pal, *Direct Conjugation of Semiconductor Nanocrystals to a Globular Protein to Study Protein-Folding Intermediates.* J.Phys.Chem.B, 2007. **111**: p. 12294-12298.

88. W.C.W.Chan and S.Nie, *Quantum Dot Bioconjugates for Ultrasensitive Nonisotopic Detection.* Science, 1998. **281**: p. 2016-2018.

89. H.Montón, C.Nogues, E.Rossinyol, O.Castell, M.Roldán, *QDs versus Alexa: reality of promising tools for immunocytochemistry.* J.Nanobiotechnology, 2009. **7**(4): p. 10.

90. B.L.Wehrenberg, C.Wang, P.Guyot-Sionnest, *Interband and Intraband Optical Studies of PbSe Colloidal Quantum Dots.* J.Phys.Chem.B, 2002. **106**: p. 10634-10640.

91. M.Bruchez Jr., M.Moronne, P.Gin, S.Weiss, A.P.Alivisatos, *Semiconductor Nanocrystals as Fluorescent Biological Labels.* Science, 1998. **281**: p. 2013-2016.

92. A.C.S.Samia, X.Chen, and C.Burda, *Semiconductor Quantum Dots for Photodynamic Therapy.* JACS, 2003. **125**: p. 15736-15717.

93. S.Hohng and T.Ha, *Near-Complete Suppression of Quantum Dot Blinking in Ambient Conditions.* JACS, 2004. **126**: p. 1324-1325.

94. C.R.Bagshaw and D.Cherny, *Blinking fluorophores: what do they tell us about protein dynamics?* Biomed.Soc.Trans., 2006. **34**(5): p. 979-982.

95. M.Nirmal, B.O.Dabbousi, M.G.Bawendi, J.J.Macklin, J.K.Trautman, T.D.Harris and L.E.Brus, *Fluorescence Intermittency in single cadmium selenide nanocrystals.* Nature, 1996. **383**: p. 802-804.

96. T.D.Krauss and L.E.Brus, *Charge, Polarizability, and Photoionization of Single Semiconductor Nanocrystals.* Phys.Rev.Lett., 1999. **83**: p. 4840-4843.

97. A.K.Gooding, D.E.Gomez, and P.Mulvaney, *The Effects of Electron and Hole Injection on the Photoluminescence of CdSe/CdS/ZnS Nanocrystal Monolayers.* ACS Nano, 2008. **2**(4): p. 669-676.

98. Al.L.Efros and M.Rosen, *Random Telegraph Signal in the Photoluminescence Intensity of a Single Quantum Dot.* Phys.Rev.Lett., 1997. **78**(6): p. 1110-1113.

99. X.Brokmann, G.Messin, P.Desbiolles, E.Giacobino, M.Dahan and J.P.Hermier, *Colloidal CdSe/ZnS quantum dots as single-photon sources.* New J.Physics, 2004. **6**: p. 1-8.

100. Y.Fu, J.Zhang, J.R.Lakowicz, *Suppressed blinking in single quantum dots (QDs) immobilized near silver island films (SIFs).* Chem.Phys.Lett., 2007. **447**: p. 96-100.

101. R.J.Cook, H.J.Kimble, *Possibility of Direct Observation of Quantum Jumps.* Phys.Rev.Lett., 1985. **54**(10): p. 1023-1026.

102. B.Lounis, H.A.Bechtel, D.Gerion, P.Alivisatos, W.E.Moerner, *Photon antibunching in single CdSe/ZnS quantum dot fuorescence.* Chem.Phys.Lett., 2000. **329**: p. 399-404.

103. R.M.Kraus, P.G.Lagoudakis, J.Müller, A.L.Rogach, J.M.Lupton, and J.Feldmann, D.V.Talapin and H.Weller, *Interplay between Auger and Ionization Processes in Nanocrystal Quantum Dots.* J.Phys.Chem.B, 2005. **109**: p. 18214-18217.

104. N.I.Hammer, K.T.Early, K.Sill, M.Y.Odoi, T.Emrick, M.D.Barnes, *Coverage-Mediated Suppression of Blinking in Solid State Quantum Dot Conjugated Organic Composite Nanostructures.* J.Phys.Chem.B, 2006. **110**: p. 14167-14171.

105. S.Jin, N.Song, T.Lian, *Suppressed Blinking Dynamics of Single QDs on ITO.* ACS Nano, 2010. **4**(3): p. 1545-1552.

106. R.G.Neuhauser, K.T.Shimizu, W.K.Woo, S.A.Empedocles, and M.G.Bawendi, *Correlation between Fluorescence Intermittency and Spectral Diffusion in Single Semiconductor Quantum Dots.* Phys.Rev.Lett., 2000. **85**(15): p. 3301-3304.

107. M.Shim and P.Guyot-Sionnest, *Permanent dipole moment and charges in colloidal semiconductorquantum dots.* J.Chem.Phys., 1999. **111**(15): p. 6955-6964.

108. M.Kuno, D.P.Fromm, S.T.Johnson, A.Gallagher, D.J.Nesbitt, *Modeling distributed kinetics in isolated semiconductor quantum dots.* Phys.Rev.B, 2003. **67**(12): p. 125304.

109. M.Kuno, D.P.Fromm, H.F.Hamann, A.Gallagher, and D.J.Nesbitt, *"On"/"off" fluorescence intermittency of single semiconductor quantum dots.* J.Chem.Phys., 2001. **115**(2): p. 1028-1040.

110. T.Uematsu, S.Maenosono, and Y.Yamaguchi, *Photoinduced Fluorescence Enhancement in Mono- and Multilayer Films of CdSe/ZnS Quantum Dots: Dependence on Intensity and Wavelength of Excitation Light.* J.Phys.Chem.B, 2005. **109**(18): p. 8613-8618.

111. M.Wijtmans, S.J.Rosenthal, B.Zwanenburg,and N.A.Porter, *Visible Light Excitation of CdSe Nanocrystals Triggers the Release of Coumarin from Cinnamate Surface Ligands.* JACS, 2006. **128**: p. 11720-11726.

112. S.Maenosono, E.Ozaki, K.Yoshie and Y.Yamaguchi, *Nonlinear Photoluminescence Behavior in Closely Packed CdSe Nanocrystal Thin Films.* Jap.J.Appl.Phys., 2001. **40**: p. L638-L641.

113. S.Maenosono, *Modeling photoinduced fluorescence enhancement in semiconductor nanocrystal arrays.* Chem.Phys.Lett., 2003. **376**: p. 666-670.

114. J.Kimura, T.Uematsu, S.Maenosono, and Y.Yamaguchi, *Photoinduced Fluorescence Enhancement in CdSe/ZnS Quantum Dot Submonolayers Sandwiched between Insulating Layers: Influence of Dot Proximity.* J.Phys.Chem.B, 2004. **108**(35): p. 13258-13264.

115. T.Uematsu, J.Kimura and Y.Yamaguchi, *The reversible photoluminescence enhancement of a CdSe/ZnS nanocrystal thin film.* Nanotechnology, 2004. **15**(7): p. 822-827.

116. H.P.Chen, H.E.Gai, E.S.Yeung, *Inhibition of photobleaching and blue shift in quantum dots.* Chem.Commun., 2009: p. 1676-1678.

117. S.N.Sharma, Z.S.Pillai, P.V.Kamat, *Photoinduced Charge Transfer between CdSe Quantum Dots and p Phenylenediamine.* J.Phys.Chem.B, 2003. **107**: p. 10088-10093.

118. M.Shim, C.J.Wang, P.Guyot-Sionnest, *Charge-tunable optical properties in colloidal semiconductor nanocrystals.* J.Phys.Chem.B 2001. **105**: p. 2369-2373.

119. C.Burda, S.Link, M.Mohamed, and M.El-Sayed, *The Relaxation Pathways of CdSe Nanoparticles Monitored with Femtosecond Time-Resolution from the Visible to the IR: Assignment of the Transient Features by Carrier Quenching.* J.Phys.Chem.B, 2001. **105**(49): p. 12286–12292.

120. Y.Ito, K.Matsuda, Y.Kanemitsu, *Mechanism of photoluminescence enhancement in single semiconductor nanocrystals on metal surfaces.* Phys.Rev.B, 2007. **75**: p. 033309.

121. I.S.Liu, H.H.Lo, C.T.Chien, Y.Y.Lin, C.W. Chen,Y.F.Chen, W.F.Su and S.C.Liou, *Enhancing photoluminescence quenching and photoelectric properties of CdSe quantum dots with hole accepting ligands.* J.Mater.Chem., 2008. **18**: p. 675-682.

122. S.R.Cordero, P.J.Carson, R.A.Estabrook, G.F.Strouse, and S.K.Buratto, *Photo-Activated Luminescence of CdSe Quantum Dot Monolayers.* J.Phys.Chem.B, 2000. **104**(51): p. 12137-12142.

123. M.Oda, J.Tsukamoto, A.Hasegawa, N.Iwami, K.Nishiura, I.Hagiwara, N.Ando, H.Horiuchi, T.Tani, *Photoluminescence of CdSe/ZnS/TOPO nanocrystals expanded on silica glass substrates: Adsorption and desorption effects of polar molecules on nanocrystal surfaces.* J.Luminescence, 2006. **119-120** p. 570-575.

124. S.Dembski, C.Graf, T.Kruger, U.Gbureck, A.Ewald, A.Bock, E.Rühl, *Photoactivation of CdSe/ZnS Quantum Dots Embedded in Silica Colloids.* Small, 2008. **4**(9): p. 1516-1526.

125. Y.Wang, Z.T., M.A.Correa-Duarte, I.Pastoriza-Santos, M.Giersig, N.A.Kotov, and L.M.Liz-Marza, *Mechanism of Strong Luminescence Photoactivation of Citrate-Stabilized Water Soluble Nanoparticles with CdSe Cores.* J.Phys.Chem.B, 2004. **108**: p. 15461-15469.

126. W.G.J.H.M.vanSark, P.L.T.M.Frederix, D.J.Van denHeuvel, and H.C.Gerritsen, A.A.Bol, J.N.J.vanLingen, C.de Mello Donegá, and A.Meijerink, *Photooxidation and Photobleaching of Single CdSe/ZnS Quantum Dots Probed by Room-Temperature Time-Resolved Spectroscopy*. J.Phys.Chem.B, 2001. **105**(35): p. 8281-8284.

127. J. E.Bowen Katari, V.L.Colvin, A.P.Alivisatos, *X-ray Photoelectron Spectroscopy of CdSe Nanocrystals with Applications to Studies of the Nanocrystal Surface.* J.Phys.Chem., 1994. **98**: p. 4109-4117.

128. Y.Zhang, J.He, P.N.Wang, J.Y.Chen, Z.J.Lu, D.R.Lu, J.Guo, C.C.Wang,and W.L.Yang, *Time-Dependent Photoluminescence Blue Shift of the Quantum Dots*

in Living Cells: Effect of Oxidation by Singlet Oxygen. JACS, 2008. **128**: p. 13396-13401.

129. J.Kim, M.E.Rodriguez, M.Guo, M.E.Kenney, N.L.Oleinick, V.E.Anderson, *Oxidative modification of cytochrome c by singlet oxygen.* Free Radical Biology and Medicine 2008. **44**: p. 1700-1711.

130. R.Schmidt, *Photosensitized Generation of Singlet Oxygen.* Photochem.Photobiol., 2006. **82**: p. 1161-1177.

131. M.Niedre, M.S.Patterson and B.C.Wilson, *Direct Near-Infrares Luminescence Detection of Singlet Oxygen Generated by Photodynamic Therapy in Cells In Vitro and Tissues In Vivo.* Photochem. and Photobiol., 2001. **75**(4): p. 382-391.

132. B.A.Lindig, M.A.J.Rodgers and A.P.Schaap, *Determination of the Lifetime of Singlet Oxygen in D20 Using 9,lO-Anthracenedipropionic Acid, a Water-Soluble Probe.* JACS, 1980. **102**: p. 5590-5593.

133. P.B.Merkel and D.R.Kearns, *Radiationless Decay of Singlet Molecular Oxygen in Solution. An Experimental and Theoretical Study of Electronic-to-Vibrational Energy Transfer.* JACS, 1972. **94**: p. 7244-7253.

134. M.Sc.K.Chen, *Photophysical characterization and optimization of novel polymer based photosensitizer carrier systems for PDT*, in *Mathematisch-Naturwissenschaftlichen Fakultät I*. 2010, D.Phil. thesis, Humboldt-Universität zu Berlin.

135. B.I.Ipe, M.Lehnig, and C.M.Niemeyer, *On the Generation of Free Radical Species from Quantum Dots.* Small, 2005. **1**(7): p. 706-709.

136. A.C.Carter, C.E.Bouldin, K.M.Kemner, M.I.Bell, J.C.Woicik, S.A. Majetich, *Surface structure of cadmium selenide nanocrystallites.* Phys.Rev.B, 1997. **55**(20): p. 13822-13828.

137. J.E.Bowen Katari, V.L.Colvin, A.P.Alivisatos, *X-ray Photoelectron Spectroscopy of CdSe Nanocrystals with Applications to Studies of the Nanocrystal Surface.* J.Phys.Chem., 1994. **98**(15): p. 4109-4117.

138. P.Juzenas, W.Chen, Y.P.Sun, M.A.N.Coelho, R.Generalov, N.Generalova, I.L.Christensen, *Quantum dots and nanoparticles for photodynamic and radiation therapies of cancer.* Adv.Drug Delivery Rev., 2008. **60**: p. 1600-1614.

139. T.Dalon and Y.Nosaka, *Formation and Behavior of Singlet Molecular Oxygen in TiO2 Photocatalysis Studied by Detection of Near-Infrared Phosphorescence.* J.Phys.Chem.C, 2007. **111**: p. 4420-4424.

140. J.M.Tsay, M.Trzoss, L.Shi, X.Kong, M.Selke, M.E.Jung, and S.Weiss, *Singlet Oxygen Production by Peptide-Coated Quantum Dot-Photosensitizer Conjugates.* JACS, 2007. **129**: p. 6865-6871.

141. M.Green and E.Howma, *Semiconductor quantum dots and free radical induced DNA nicking.* Chem.Commun., 2005: p. 121-123.

142. A.E.Aust, J.F.Eveleigh, *Mechanisms of DNA Oxidation.* P.S.E.B.B., 1999. **222**: p. 246-252.

143. J.Y. Chen, Y.M.Lee, D.Zhao, N.K.Mak, R.N.S.Wong, W.H.Chan and N.H.Cheung, *Quantum Dot-mediated Photoproduction of Reactive Oxygen*

Species for Cancer Cell Annihilation. Photochem.Photobiol., 2010. **86**: p. 431-437.

144. V.I.Bruskov, Z.K.Masalimov, and A.V.Chernikov, *Heat-Induced Generation of Reactive Oxygen Species in Water.* Doklady Biochem. and Biophys., 2002. **384**: p. 181-184.

145. V.I.Bruskov, L.V.Malakhova, Z.K.Masalimov, A.V.Chernikov, *Heat-induced formation of reactove oxygen species and 8-oxoguanine, a biomarher of damage to DNA.* Nucl.Ac.Res., 2002. **30**(6): p. 1354-1363.

146. A.P.Greeff, H.C.Swart, *Quantifying the cathodoluminescence generated in ZnS-based phosphor powders* Surf.Interf.Anal., 2002. **34**(1): p. 593-596.

147. H.C.Swart, *A review on ZnS phosphor degradation* Phys.Stat.Sol.C, 2004. **1**(9): p. 2354-2359.

148. K.X.Hay, V.Y.Waisundara, Y.Zong, M.Y.Han, and D.Huang, *CdSe Nanocrystals as Hydroperoxide Scavengers: A New Approach to Highly Sensitive Quantification of Lipid Hydroperoxides.* Small, 2007. **3**(2): p. 290-293.

149. J.Aldana, Y.A.Wang, and X.Peng, *Photochemical Instability of CdSe Nanocrystals Coated by Hydrophilic Thiols.* JACS, 2001. **123**: p. 8844-8850.

150. B.J.Fischer, *Particle Convection in an Evaporating Colloidal Droplet.* Langmuir, 2002. **18**: p. 60-67.

151. V.N.Truskett, K.J.Stebe, *Influence of Surfactants on an Evaporating Drop: Fluorescence Images and Particle Deposition Patterns.* Langmuir, 2003. **19**: p. 8271-8279.

152. C.R.Kagan, C.B.Murray, and M.G.Bawendi *Long-range resonance transfer of electronic excitations in close-packed CdSe quantum-dot solids.* Phys.Rev.B, 1996. **54**(12): p. 8633-8643.

153. O.I.Micic, S.P.Ahrenkiel, A.J.Nozik, *Synthesis of extremely small InP quantum dots and electronic coupling in their disordered solid films.* Appl.Phys.Lett., 2001. **78**(25): p. 4022-4024.

154. M.V.Artemyev, U.Woggon, H.Jaschinski, L.I.Gurinovich, S.V.Gaponenko, *Spectroscopic Study of Electronic States in an Ensemble of Close-Packed CdSe Nanocrystals.* J.Phys.Chem.B, 2000. **104**: p. 11617-11621.

155. H.Döllefeld, H.Weller, and A.Eychmüller, *Semiconductor Nanocrystal Assemblies: Experimental Pitfalls and a Simple Model of Particle-Particle Interaction.* J.Phys.Chem.B, 2002. **106**: p. 5604-5608.

156. T.Uematsu, S.Maenosono, and Y.Yamaguchi, *Photoinduced fluorescence enhancement in CdSe/ZnS quantum dot monolayers: Influence of substrate.* Appl.Phys.Lett., 2006. **89**(3): p. 031910

157. L.Lehr, M.T.Zanni, C.Frischkorn, R.Weinkauf, D.M.Neumark, *Electron Solvation in Finite Systems: Femtosecond Dynamics of Iodide·(Water) n Anion Clusters.* Science, 1999. **284**: p. 635-638.

158. A.Calhoun and G.A.Voth, *Isotope Effects in Electron Transfer across the Electrode-Electrolyte Interface: A Measure of Solvent Mode Quantization.* J.Phys.Chem.B, 1998. **102**: p. 8563-8568.

159. G.Nemethy, H.A.Scheraga, *Structure of Water and Hydrophobic Bonding in Proteins. IV. The Thermodynamic Properties of Liquid Deuterium Oxide.* J.Chem.Phys., 1964. **41**(3): p. 680-689.

160. J.Lee, G.W.Robinson, *Solvent Isotope Effect on Electron-Transfer Processes.* J.Phys.Chem., 1985. **89**(10): p. 1872-1875.

161. C.D.Wagner, A.V.Naumkin, A.Kraut-Vass, J.W. Allison, C.J.Powell, and J.R.Rumble, Jr. *NIST X-ray Photoelectron Spectroscopy Database, NIST Standard Reference Database 20, Version 3.5* 2007 [last accessed in March2010] http://srdata.nist.gov/xps/Default.aspx

162. J.S.Hammond, S.W.Gaarenstroom, N.Winograd, *X-Ray Photoelectron Spectroscopic Studies of Cadmium- and Silver -Oxygen Surfaces.* Anal.Chem., 1975. **47**(13): p. 2193-2199.

163. B.Canava, J.Vigneron, A.Etcheberry, J.F.Guillemoles, D.Lincot, *High resolution XPS studies of Se chemistry of a Cu(In, Ga)Se2 surface.* Appl.Surf.Science, 2002. **202**(1-2): p. 8-14.

164. M.Zheng, J.Wu, *One-step synthesis of nitrogen-doped ZnO nanocrystallites and their properties.* Appl.Surf.Science, 2009. **255**: p. 5656-5661.

165. J.D.G.Duran, M.C.Guindo, A.V.Delgado, *Electrophoretic Properties of Colloidal Dispersions of Monodisperse Zinc Sulfide: Effects of Potential-Determining Ions and Surface Oxidation.* J.Coll.Interf.Sci., 1995. **173**(2): p. 436-442.

166. J.Y.Chen, Y.M.Lee, D.Zhao, N.K.Mak, R.N.S.Wong, W.H.Chan and N.H.Cheung, *Quantum Dot-mediated Photoproduction of Reactive Oxygen Species for Cancer Cell Annihilation.* Photochem.Photobiol., 2010. **86**: p. 431-437.

167. P.Oudet, M.Gross-Bellard, and P.Chambon, *Electron Microscopic and Biochemical Evidence that Chromatin Structure Is a Repeating Unit.* Cell, 1975. **4**: p. 281-300.

168. K.Luger, A.W.Maeder, R.K.Richmond, D.F.Sargent and T.J.Richmond, *Crystal structure of the nucleosome core particle at 2.8A resolution.* Nature, 1997. **389**: p. 251-260.

169. R.D.Kornberg, *Chromatin Structure: A Repeating Unit of Histones and DNA.* Science, 1974. **184**(4139): p. 868-871.

170. G.Felsenfeld, *Chromatin.* Nature, 1978. **271**: p. 115-122.

171. J.Widom, *Toward a Unified Model of Chromatin Folding.* Ann.Rev.Biophys.Biophys.Chem., 1989. **18**: p. 365-395.

172. G.Thoma, T.Koller and A.Klug, *Involvelemnt of Histone H1 in the Organization of the Nucleosome and of the Salt-dependent Superstructures of Chromatin.* J.Cell Biol., 1979. **83**: p. 403-427.

173. R.D.Kornberg and Y.Lorch, *Twenty-Five Years of the Nucleosome, Fundamental Particle of the Eukaryote Chromosome.* Cell, 1999. **98**: p. 285-294.

174. R.D.Kornberg, *Structure of Chromatin.* Ann.Rev.Biochem., 1977. **46**: p. 931-954.

175. J.D.McPhee and G.Felsenfeld, *Nucleosome Structure.* Ann.Rev.Biochem., 1980. **49**: p. 1115-1156.

176. A.T.Annunziato, *DNA Packaging: Nucleosomes and Chromatin.* Nature Educ., 2008. **1**.

177. H.W.Zhu, C.L.Xu, D.H.Wu, B.Q.Wei, R.Vajtai, P.M.Ajayan, *Direct Synthesis of Long Single-Walled Carbon Nanotube Strands.* Science, 2002. **296**: p. 884-886.

178. Z.Guo, P.J.Sadler, S.C.Tsang, *Immobilization and Visualization of DNA and Proteins on Carbon Nanotubes.* Adv.Mater., 1998. **10**(9): p. 701-703.

179. M.Zheng, A.Jagota, E.D.Semke, B.A.Diner, R.S.McLean, S.R.Lustig, R.E.Richardson, N.G.Tassi, *DNA-assisted dispersion and separation of carbon nanotubes.* Nature Mater., 2003. **2**: p. 338-342.

180. G.I.Dovbeshko, O.P.Repnytska, E.D.Obraztsova , Y.V.Shtogun, *DNA interaction with single-walled carbon nanotubes: a SEIRA study.* Chem.Phys.Lett., 2003. **372**: p. 432-437.

181. D.Nepal, J.I.Sohn, W.K.Aicher, S.Lee, K.E.Geckeler, *Supramolecular Conjugates of Carbon Nanotubes and DNA by a Solid-State Reaction.* Biomacromolecules, 2005. **6**: p. 2919-2922.

182. M.Zheng, A.Jagota, M.S.Strano, A.P.Santos, P.Barone, S.G.Chou, B.A.Diner, M.S.Dresselhaus, R.S.Mclean, G.B.Onoa, G.G.Samsonidze, E.D.Semke, M.Usrey, D.J.Walls, *Structure-Based Carbon Nanotube Sorting by Sequence-Dependent DNA Assembly.* Science, 2003. **302**: p. 1545-1548.

183. J.Rajendra and A.Rodger, *The Binding of Single-Stranded DNA and PNA to Single-Walled Carbon Nanotubes Probed by Flow Linear Dichroism.* Chem.Eur.J., 2005. **11**: p. 4841-4847.

184. R.Bakalova, Z.Zhelev, H.Ohba,and Y.Baba, *Quantum Dot-Conjugated Hybridization Probes for Preliminary Screening of siRNA Sequences.* JACS, 2005. **127**: p. 11328-11335.

185. R.Mahtab, J.P.Rogers, C.P.Singleton, and C.J.Murphy, *Preferential Adsorption of a "Kinked" DNA to a Neutral Curved Surface: Comparisons to and Implications for Nonspecific DNA-Protein Interactions.* JACS, 1996. **118**: p. 7028-7032.

186. D.Zhou, L.Ying, X.Hong, E.A.Hall, C.Abell, and D.Klenerman, *A Compact Functional Quantum Dot-DNA Conjugate: Preparation, Hybridization, and Specific Label-Free DNA Detection.* Langmuir, 2008. **24**: p. 1659-1664.

187. J.Montgomery, C.T.Wittwer, J.O.Kent, L.Zhou, *Scanning the Cystic Fibrosis Transmembrane Conductance Regulator Gene Using High-Resolution DNA Melting Analysis.* Clin.Chem., 2007. **53**(11): p. 1891-1898.

188. W.R.Algar and U.J.Krull, *Adsorption and Hybridization of Oligonucleotides on Mercaptoacetic Acid-Capped CdSe/ZnS Quantum Dots and Quantum Dot-Oligonucleotide Conjugates.* Langmuir, 2006. **22**: p. 11346-11352.

189. D.Zhou, L.Ying, X.Hong, E.A.Hall, C.Abell, D.Klenerman, *A Compact Functional Quantum Dot-DNA Conjugate: Preparation, Hybridization, and Specific Label-Free DNA Detection.* Langmuir, 2008. **24**: p. 1659-1664.

190. D.Zhou, J.D.Piper, C.Abell, D.Klenerman, D.J.Kang, and L.Ying, *Fluorescence resonance energy transfer between a quantum dot donor and a dye acceptor attached to DNA.* Chem.Commun., 2005: p. 4807-4809.

191. R.Gill, I.Willner, I.Shweky, and U.Banin, *Fluorescence Resonance Energy Transfer in CdSe/ZnS-DNA Conjugates: Probing Hybridization and DNA Cleavage.* J.Phys.Chem.B, 2005. **109**: p. 23715-23719.

192. R.Mahtab, S.M.Sheldon, S.E.Hunyadi, B.Kinard, T.Ray, C.J.Murphy, *Influence of the nature of quantum dot surface cations on interactions with DNA.* J.Inorg.Biochem., 2007. **101**: p. 559-564.

193. I.L.Medintz, L.Berti, T.Pons, A.F.Grimes, D.S.English, A.Alessandrini, P.Facci, and H.Mattoussi, *A Reactive Peptidic Linker for Self-Assembling Hybrid Quantum Dot-DNA Bioconjugates.* Nano Lett., 2007. **7**(6): p. 1741-1748.

194. Q.Wang, Y.Liu, Y.Ke, and H.Yan, *Quantum Dot Bioconjugation during Core–Shell Synthesis.* Angew.Chem.Int.Ed., 2008. **47**: p. 316-319.

195. A.Fu, C.Micheel, J.Cha, H.Chang, H.Yang, and A.Alivisatos, *Discrete Nanostructures of Quantum Dots/Au with DNA.* JACS, 2004. **126**: p. 10832-10833.

196. R.Mahtab, H.H.Harden, and C.J.Murphy, *Temperature- and Salt-Dependent Binding of Long DNA to Protein-Sized Quantum Dots:Thermodynamics of "Inorganic Protein"−DNA Interactions.* JACS, 2000. **122**: p. 14-17.

197. L.Spanhel, M.Haase, H.Weller, and A.Henglein, *Photochemistry of Colloidal Semiconductors. 20. Surface Modification and Stability of Strong Luminescing CdS Particles.* JACS, 1987. **109**: p. 5649-5655.

198. N.V.Hud, J.Plavec, *A Unified Model for the Origin of DNA Sequence- Directed Curvature.* Biopolymers, 2003. **69**: p. 144-159.

199. W.Han, M.Dlakic, Y.J.Zhu, S.M.Lindsay, R.E.Harrington, *Strained DNA is kinked by low concentrations of Zinc.* PNAS, 1997. **94**: p. 10565-10570.

200. W.Han, S.M.Lindsay, M.Dlakic, R.E.Harrington, *Kinked DNA.* Nature, 1997. **386**: p. 563-563.

201. V.Tchernaenko, H.R.Halvorson, L.C.Lutter, *Topological Measurement of an A-tract Bend Angle: Effect of Magnesium.* J.Molec.Biol., 2004. **341**: p. 55-63.

202. I.Rouzina and V.A.Bloomfield, *DNA Bending by Small, Mobile Multivalent Cations.* Biophys.J., 1998. **74**: p. 3152-3164.

203. B.Jerkovic and P.H.Bolton, *Magnesium Increases the Curvature of Duplex DNA That Contains dA Tracts.* Biochemistry, 2001. **40**: p. 9406-9411.

204. D.M.Crothers, T.E.Haran, J.G.Nadeau, *Intrinsically Bent DNA.* J.Biol.Chem., 1990. **265**: p. 7093-7096.

205. D.S.Goodsell, M.L.Kopka, D.Cascio, R.E.Dickerson, *Crystal structure of CATGGCCATG and its implications for A-tract bending models.* PNAS, 1990. **90**: p. 2930-2934.

206. K.A.Sharp, A.Nicholls, R.F.Fine, B.Honig, *Reconciling the magnitude of the microscopic and macroscopic hydrophobic effects.* Science, 1991. **252**: p. 106-109.

207. Y.Nosaka, N.Ohta, T.Fukuyama, N.Fujii, *Size Control of Ultrasmall CdS Particles in Aqueous Solution by Using Various Thiols* J.Coll.Interf.Sci., 1993. **155**(1): p. 23-29.

208. R.S.Spolar, M.T.Record, Jr, *Coupling of local folding to site-specific binding of proteins to DNA* Science, 1994. **263**: p. 777-784.

209. J.Ghabboun, M.Sowwan, H.Cohen, T.Molotsky, N.Borovok, B.Dwir, E.Kapon, A.Kotlyar, D.Porath, *Specific and efficient adsorption of phosphorothioated DNA on Au-based surfaces and electrodes.* Appl.Phys.Lett., 2007. **91**: p. 173101.

210. A.R.Herdt, S.M.Drawz, Y.Kang, T.A.Taton, *DNA dissociation and degradation at gold nanoparticle surfaces.* Coll.Surf.B:Biointerf., 2006. **51**: p. 130-139.

211. B.Beermann, E.Carillo-Nava, A.Scheffer, W.Buscher, A.M.Jawalekar, F.Seela, H.J.Hinz, *Association temperature governs structure and apparent thermodynamics of DNA–gold nanoparticles.* Biophys.Chem., 2007. **126**: p. 124-131.

212. E.Y.Kim, J.Stanton, R.A.Vega, K.J.Kunstman, C.A.Mirkin, S.M.Wolinsky, *A real-time PCR-based method for determining the surface coverage of thiol-capped oligonucleotides bound onto gold nanoparticles.* Nucl.Ac.Res., 2006. **34**(7): p. e54.

213. T.M.Herne and M.J.Tarlov, *Characterization of DNA Probes Immobilized on Gold Surfaces.* JACS, 1997. **119**: p. 8916-8920.

214. R.Levicky, T.M.Herne, M.J.Tarlov, and S.K.Satija, *Using Self-Assembly To Control the Structure of DNA Monolayers on Gold: A Neutron Reflectivity Study.* JACS, 1998. **120**: p. 9787-9792.

215. L.M.Demers, C.A.Mirkin, R.C.Mucic, R.A.Reynolds, R.L.Letsinger, R.Elghanian, and G.Viswanadham, *A Fluorescence-Based Method for Determining the Surface Coverage and Hybridization Efficiency of Thiol-Capped Oligonucleotides Bound to Gold Thin Films and Nanoparticles.* Anal.Chem., 2000. **72**: p. 5535-5541.

216. C.Y.Lee, P.C.T.Nguyen, D.W.Grainger, L.J.Gamble, D.G.Castner, *Structure and DNA Hybridization Properties of Mixed Nucleic Acid/Maleimide-Ethylene Glycol Monolayers.* Anal.Chem., 2007. **79**: p. 4390-4400.

217. M.Sam, E.M.Boon, J.K.Barton, M.G.Hill, and E.M.Spain, *Morphology of 15-mer Duplexes Tethered to Au(111) Probed Using Scanning Probe Microscopy.* Langmuir, 2001. **17**: p. 5727-5730.

218. L.A.Gearheart, H.J.Ploehn, and C.J.Murphy, *Oligonucleotide Adsorption to GoldNanoparticles: A Surface-Enhanced Raman Spectroscopy Study of Intrinsically Bent DNA.* J.Phys.Chem.B, 2001. **105**: p. 12609-12615.

219. S.Lecomte, M.H.Baron, *Surface-Enhanced Raman Spectroscopy Investigation of Fluoroquinolones–DNA–DNA Gyrase–Mg2+ Interactions. II. Interaction of Pefloxacin with Mg2+ and DNA.* Biospectroscopy, 1997. **1**: p. 31-45.

220. M.Sam, E.M.Boon, J.K.Barton, M.G.Hill, and E.M.Spain, *Morphology of 15-mer Duplexes Tethered to Au(111) Probed Using Scanning Probe Microscopy.* Langmuir, 20001. **17**: p. 5727-5730.

221. M.Zheng, Z.Li, and X.Huang, *Ethylene Glycol Monolayer Protected Nanoparticles: Synthesis, Characterization, and Interactions with Biological Molecules.* Langmuir, 2004. **20**: p. 4226-4235.

222. P.Day, P.S.Flora, J.Fox, and M.Walker, *Immobilization of polynucleotides on magnetic particles.* Biochem.J., 1991. **278**: p. 735-740.

223. X.He, K.Wang, W.Tan, B.Liu, X.Lin, C.He, D.Li, S.Huang, and J.Li, *Bioconjugated Nanoparticles for DNA Protection from Cleavage.* JACS, 2003. **125**: p. 7168-7169.

224. I.Roy, T.Y.Ohulchanskyy, D.J.Bharali, H.E.Pudavar, R.A.Mistretta, N.Kaur, and P.N.Prasad, *Optical tracking of organically modified silica nanoparticles as DNA carriers: A nonviral, nanomedicine approach for gene delivery.* PNAS, 2005. **102**(2): p. 279-284.

225. W.Tan, K.Wang, X.He, X.J.Zhao,T.Drake, L.Wang, R.P.Bagwe, *Bionanotechnology Based on Silica Nanoparticles.* Medic.Res.Rev., 2004. **24**(5): p. 621-638.

226. J.G.Vandersteen, P.Bayrak-Toydemir, R.A.Palais, C.T.Wittwer, *Identifying Common Genetic Variants by High-Resolution Melting*. Clin.Chem., 2007. **53**(7), p. 1191-1198.

227. J.A.Richardson, *Novel DNA probes for sensitive DNA detection*, in *School of Chemistry*. 2010, D.Phil. thesis, University of Southampton.

228. Wikipedia. *Amino Acid*. [last accessed in March2010] http://en.wikipedia.org/wiki/Amino_acid.

229. *Tutorial on Fluorescence and Fluorescent Instrumentation*. [last accessed in March 2010] http://fmrc.pulmcc.washington.edu/DOCUMENTS/FMRC299.pdf.

230. K.Okamoto, I.Niki, A.Scherer, Y.Narukawa, T.Mukai, Y.Kawakami, *Surface plasmon enhanced spontaneous emission rate of InGaN/GaN quantum wells probed by time-resolved photoluminescence spectroscopy.* Appl.Phys.Lett., 2005. **87**: p. 071102.

231. C.T.Yuan, W.C.Chou, D.S.Chuu, W.H.Chang, H.S.Lin, R.C.Ruaan, *Fluorescence Properties of Colloidal CdSe/ZnS Quantum Dots with Various Surface Modifications.* J.Medic.Biol.Engin., 2006. **26**(3): p. 131-135.

232. Z.Chunyang, M.Hui, N.Shuming, D.Yao, J.Lei, C.Dieyan, *Quantum dot-labeled trichosanthin.* Analyst Commun., 2000. **125**: p. 1029-1031.

233. D.F.Eaton, *Reference materials for fluorescence measurements.* Pure and Appl.Chem., 1988. **80**(7): p. 1107-1114.

234. S.K.Sarkar, G.Hodes, *Charge Overlap Interaction in Quantum Dot Films: Time Dependence and Suppression by Cyanide Adsorption.* J.Phys.Chem.B, 2005. **109**: p. 7214-7219.

235. A.Higuchi, K.Kato, M.Hara, T.S.G.Ishikawa, H.Nakano, S.Satoh, S.Manabe, *Rejection of single stranded and double stranded DNA by porous hollow fiber membranes.* J.Membr.Sci., 1996. **116**: p. 191-196.

236. R.Shusterman, S.Alon, T.Gavrinyov, O.Krichevsky, *Monomer Dynamics in Double- and Single Stranded DNA Polymers.* Phys.Rev.Lett., 2004. **92**(4): p. 048303.

237. Y.Lin, X.C.Shen, J.J.Wang, L.Bao, Z.L.Zhang and D.W.Pang *Measuring radial Young's modulus of DNA by tapping mode AFM.* Chin.Sci.Bull., 2007. **52**(23): p. 3189-3192.

238. M.Antognozzi, M.D.Szczelkun, A.N.Round, M.J.Miles, *Comparison Between Shear Force and Tapping Mode AFM - High Resolution Imaging of DNA.* Single Mol., 2002. **3**(2-3): p. 105-110.

239. J.D.Watson, F.H.C.Crick, *Molecular Structure of Nucleic Acids-A structure for Deoxyribose Nucleic Acid.* Nature, 1953. **171**: p. 737-738.

240. C.Bustamante, C.Rivetti and D.J.Keller, *Scanning force microscopy under aqueous solutions.* Curr.Opin.Struct.Biol., 1997. **7**: p. 709-716.

241. Y.L.Lyubchenko, P.I.Oden, D.Lampner, S.M.Lindsay and K.A.Dunker, *Atomic force microscopy of DNA and bacteriophage in air, water and propanol: the role of adhesion forces.* Nucl.Ac.Res., 1993. **21**: p. 1117-1123.

242. W.L.Shaiu, D.D.Larson, J.Vesenka and E.Henderson, *Atomic force microscopy of oriented linear DNA molecules labeled with 5nm gold spheres.* Nucl.Ac.Res., 1993. **21**: p. 99-103.

243. C.Bustamante, J.Vesenka, C.L.Tang, W.Rees, M.Guthold and R.Keller, *Circular DNA Molecules Imaged in Air by Scanning Force Microscopy.* Biochem., 1992. **31**: p. 22-26.

244. Y.L.Lyubchenko, L.Shlyakhtenko, R.Harrington, P.I.Oden and S.M.Lindsay, *Atomic force microscopy of long DNA: Imaging in air and under water.* PNAS USA, 1993. **90**: p. 2137-2140.

245. Y.Ebenstein, E.Nahum, U.Banin, *Tapping Mode Atomic Force Microscopy for Nanoparticle Sizing: Tip-Sample Interaction Effects.* Nano Lett., 2002. **2**(9): p. 945-950.

246. V.A.Bloomfield, *DNA condensation.* Curr.Opin.Struct.Biol., 1996. **6**: p. 334-341.

247. J.Adamcik, D.V.Klinov, G.Witz, S.K.Sekatskii, G.Dietler, *Observation of single-stranded DNA on mica and highly oriented pyrolytic graphite by atomic force microscopy.* FEBS Lett., 2006. **580**: p. 5671-5675.

248. D.Pastre, L.Hamon, F.Landousy, I.Sorel, M.O.David, A.Zozime, E.LeCam, O.Pietrement, *Anionic Polyelectrolyte Adsorption on Mica Mediated by Multivalent Cations: A Solution to DNA Imaging by Atomic Force.* Langmuir, 2006. **22**: p. 6651-6660.

249. D.Pastre, O.Pietrement, S.Fusil, F.Landousy, J.Jeusset, M.O.David, L.Hamon, E.LeCam, A.Zozime, *Adsorption of DNA to Mica Mediated by Divalent Counterions: A Theoretical and Experimental Study.* Biophys.J., 2003. **85**: p. 2507-2518.

250. Y.Burak, G.Ariel, D.Andelman, *Onset of DNA Aggregation in Presence of Monovalent and Multivalent Counterions.* Biophys.J., 2003. **85**: p. 2100-2110.

251. J.Malicka, I.Gryczynski, J.R.Lakowicz, *DNA hybridization assays using metal-enhanced fluorescence.* BBRC, 2003. **306**: p. 213-218.

252. J.R.Lakowicz, *Radiative decay engineering 3. Surface plasmon coupled directional emission.* Anal.Biochem., 2004. **324**: p. 153-169.

253. S.Kühn, U.Hakanson, L.Rogobete, V.Sandoghdar, *Enhancement of single-molecule fluorescence using a gold nanoparticle as an optical nanoantenna.* Phys.Rev.Lett., 2006. **97**: p. 017402.

254. S.Praharaj, S.K.Ghosh, S.Nath, S.Kundu, S.Panigrahi, S.Basu, T.Pal, *Size-selective synthesis and stabilization of gold organosol in C(n)TAC: enhanced molecular fluorescence from gold-bound fluorophores.* J.Phys.Chem.B, 2005. **109**(27): p. 13166-13174.

255. P.Bharadwaj, P.Anger, L.Novotny, *Nanoplasmonic enhancement of single-molecule fluorescence.* Nanotechnology, 2007. **18**(4): p. 044017.

256. J.R.Lakowicz, *Radiative decay engineering 5: metal-enhanced fluorescence and plasmon emission.* Anal.Biochem., 2005. **337**: p. 171-194.

257. J.R.Lakowicz, *Radiative decay engineering 3. Surface plasmon-coupleddirectional emission.* Anal.Biochem., 2004. **324**: p. 153-169.

258. N.N.Horimotoa, K.Imura, H.Okamoto, *Dye fluorescence enhancement and quenching by gold nanoparticles: Direct near-field microscopic observation of shape dependence* Chem.Phys.Lett., 2008. **467**(1-3): p. 105-109.

259. J.B.Khurgin, G.Sun, R.A.Soref, *Enhancement of luminescence efficiency using surface plasmon polaritons: figures of merit.* J.Opt.Soc.Am.B, 2007. **24**(8): p. 1968-1980.

260. G.Sun, J.B.Khurgin, R.A.Soref, *Practicable enhancement of spontaneous emission using surface plasmons.* Appl.Phys.Lett., 2007. **90**: p. 111107.

261. J.B.Khurgin, G.Sun, *Enhancement of light absorption in a quantum well by surface plasmon polariton.* Appl.Phys.Lett., 2009. **94**: p. 191106.

262. B.Wardle, *Principles and Applications of Photochemsitry*. 2009: Wiley.

263. J.Simons, Department of Chemistry, University of Utah. *Index of Papers, Book2_C6.pdf, chapter 6, Internal Conversion and Intersystem Crossing*. [last accessed in June2010] http://simons.hec.utah.edu/papers/BOOK2_C6.PDF.

264. Wikipedia. *Franck-Condon principle*. [last accessed in March2010] http://www.thefullwiki.org/Franck-Condon_principle.

265. Invitrogen.com. *Product Spectra-TOTO-1/DNA*. [last accessed in March2010] http://www.invitrogen.com/site/us/en/home/support/Product-Technical-Resources/Product-Spectra.3600dna.html.

266. E.Fort and S.Gresillon, *Topical Review: Surface enhanced fluorescence.* J.Phys.D:Appl.Phys., 2008. **41**: p. 0130017.

267. W.L.Barnes, *Topical review: Fluorescence near interfaces: the role of photonic mode density.* J.Mod.Opt., 1998. **45**(4): p. 661-699.

268. D.Toptygin, *Effects of the Solvent Refractive Index and Its Dispersion on the Radiative Decay Rate and Extinction Coefficient of a Fluorescent Solute.* J.Fluorescence, 2003. **13**(3): p. 201-219.

269. E.P.Petrov, V.N.Bogomolov, I.I.Kalosha, and S.V.Gaponenko, *Spontaneous Emission of Organic Molecules Embedded in a Photonic Crystal.* Phys.Rev.Lett., 1998. **81**(1): p. 77-80.

270. R.K.Lee, Y.Xu, and A.Yariv *Modified spontaneous emission from a two-dimensional photonic bandgap crystal slab.* J.Opt.Soc.Am., 2000. **17**(8): p. 1438-1442.

271. A.M.Adawi, D.G.Lidzey, *Enhancing the radiative decay rate of fluorescent organic molecules using micropillar microcavities and optical nanocavities.* Mater.Sci.Engin.B, 2008. **149**: p. 266-269.

272. W.Fang, J.Y.Xu, A.Yamilov, H.Cao, Y.Ma, S.T.Ho, G.S.Solomon, *Large enhancement of spontaneous emission rates of InAs quantum dots in GaAs microdisks.* Opt.Lett., 2002. **27**(11): p. 948.

273. A.M.Adawi, A.Cadby, L.G.Connolly, W.C.Hung, R.Dean, A.Tahraoui, A.M.Fox, A.G.Cullis, D.Sanvitto, M.S.Skolnick, and D.G.Lidzey, *Spontaneous Emission Control in Micropillar Cavities Containing a Fluorescent Molecular Dye.* Adv.Mater., 2006. **18**: p. 742-747.

274. R.M.Amos and W.L.Barnes, *Modification of the spontaneous emission rate of Eu 3+ ions close to a thin metal mirror.* Phys.Rev.B, 1997. **55**(11): p. 7249-7254.

275. K.H.Drexhage, M.Fleck, H.Kuhn, F.P.Schäfer, W.Sperling, Ber.Bunsenges.Phys.Chem., 1966. **70**: p. 1179.

276. K.H.Drexhage, *Influence of a dielectric interface on fluorescence decay time.* J.Luminescence, 1970. **1**(2): p. 693-701.

277. K.Okamoto, Y.Kawakami, *Enhancements of emission rates and efficiencies by surface plasmon coupling.* Phys.Stat.Sol.C, 2010. **7**(10): p. 2582-2585.

278. M.Ambati, D.A.Genov, R.F.Oulton, and X.Zhang, *Active Plasmonics: Surface Plasmon Interaction With Optical Emitters.* IEEE J.Sel.Top.Quant.Electron., 2008. **14**(6): p. 1395-1403.

279. R.Paschotta, *Encyclopedia of Laser Physis and Technology*. 2008, Wiley-VCH.

280. E.F.Schubert, Department of Electrical, Computer and Systems Engineering, Rensselaer Polytechnic Institute. *Optical modes*. [last accessed in April2010] http://www.ecse.rpi.edu/~schubert/Light-Emitting-Diodes-dot-org/chap14/F14-01%20Optical%20modes.jpg.

281. Y.C.Tsai, C.F.L., J.W.Chang, *Controlling Spontaneous Emission with the Local Density of States of Honeycomb Photonic Crystals.* Opt.Rev., 2009. **16**(3): p. 347-350.

282. M.Fox, *Quantum Optics: An Introdiction*. 2006: Oxford University Press.

283. R.C.Pennington, *Spectral Properties and Modes of Surface Microcavities*, in *School of Physics and Astronomy*. 2009, D.Phil. thesis, Universty of Southampton

284. M.Wu, J.R.Lakowicz, C.D.Geddes, *Enhanced Lanthanide Luminescence Using Silver Nanostructures: Opportunities for a New Class of Probes with Exceptional Spectral Characteristics.* J.Fluorescence, 2005. **15**(1): p. 53-59.

285. K.Okamoto, S.Vyawahare, A.Scherer, *Surface-plasmon enhanced bright emission from CdSe quantum-dot nanocrystals.* J.Opt.Soc.Am.B, 2006. **23**(8): p. 1674-1678.

286. Y.J.Hung, I.I.Smolyaninov, C.C.Davis, H.C.Wu, *Fluorescence enhancement by surface gratings.* Opt.Express, 2006. **14**(22): p. 10825-10830.

287. T.A.Kelf, *Light-Matter Interactions on Nano-Structured Metallic Films*, in *School of Physics and Astronomy*. 2006, D.Phil. thesis, University of Southampton.

288. T.V.Teperik, V.V.Popov, F.J.Garcia deAbajo, and J.J.Baumberg, *Tuneable coupling of surface plasmon-polaritons and Mie plasmons on a planar surface of nanoporous metal.* Phys.Stat.Sol.C, 2005. **2**(11): p. 3912-3915.

289. S.Coyle, M.C.Netti, J.J.Baumberg, M.A.Ghanem, P.R.Birkin, P.N.Bartlett, and D.M.Whittaker, *Confined Plasmons in Metallic Nanocavities.* Phys.Rev.Lett., 2001. **87**: p. 176801.

290. F.J.Garcia deAbajo, A.Howie, *Relativistic Electron Energy Loss and Electron-Induced Photon Emission in Inhomogeneous Dielectrics.* Phys.Rev.Lett., 1998. **80**(23): p. 5180-5183.

291. P.B.Johnson and R.W.Christy, *Optical Constants of Noble Metals.* Phys.Rev.B, 1972. **6**(12): p. 4370-4379.

292. Robin M. Cole, J.J.Baumberg, F. J. Garcia de Abajo, and M.A. Sumeet Mahajan, and Philip N. Bartlett, *Understanding Plasmons in Nanoscale Voids.* Nanoletters, 2007. **7**(7): p. 2094-2100.

293. A.Politano, V.Formoso, G.Chiarello, *Dispersion and Damping of Gold Surface Plasmon.* Plasmonics, 2008. **3**: p. 165-170.

294. S. Coyle, M.C.Netti, J. J. Baumberg, M. A. Ghanem, P. R. Birkin, P. N. Bartlett, and D. M. Whittaker, *Confined Plasmons in Metallic Nanocavities.* Physical Review Letters, 2001. **87**(176801-1): p. 176801.

295. J. B. Khurgin, G.Sun, *Enhancement of light absorption in a quantum well by surface plasmon polariton.* Applied Physics Letters, 2009. **94**: p. 191106.

296. F.J.Garcia deAbajo, *BEMAX-Boundary Element Method for Axial-symmetric electromagnetism*. BEMAX-Boundary Element Method for Axial-symmetric electromagnetism 2006, 8.5.1998 to 5.4.2006; Explanation of programming codes for simulations of Mie plamsmon modes using the Boundary Element Model.

297. S.M.Weekes, F.Y.Ogrin, W.A.Murray, P.S.Keatley, *Macroscopic Arrays of Magnetic Nanostructures from Self-Assembled Nanosphere Templates.* Langmuir, 2007. **23**: p. 1057-1060.

298. C.F.Chau, *A Nanostructured Porous Silicon Based Drug Delivery Device*, in *School of Electronics and Computer Science*. 2009, D.Phil. thesis, University of Southampton

299. E.Koukharenko, Z.Moktadir, M.Kraft, M.E.Abdelsalam, and C.V. D.M.Bagnall, M.P.A.Jones, E.A.Hinds, *Microfabrication of gold wires for atom guides.* Sensors and Actuators A, 2004. **115**: p. 600-607.

300. M.Schlesinger, M.Paunovic, *Modern Electroplating, 4th edition*. 2000: Wiley Interscience.

301. N.Milanovich, M.Suh, R.Jankowiak, G.J.Small, and J.M.Hayes, *Binding of TO-PRO-3 and TOTO-3 to DNA: Fluorescence and Hole-Burning Studies.* J.Phys.Chem., 1996. **100**: p. 9181-9186.

302. Zeiss.com. *Fluorescence Dyes Database*. [last accessed in June2010] https://www.micro-shop.zeiss.com/us/us_en/spektral.php?f=fa.

303. S.Laib and S.Seeger, *FRET Studies of the Interaction of Dimeric Cyanine Dyes with DNA.* J.Fluorescence, 2004. **14**(2): p. 187-191.

304. K.M.Sovenyhazy, J.A.Bordelon and J.T.Petty, *Spectroscopic studies of the multiple binding modes of a trimethine-bridged cyanine dye with DNA.* Nucl.Ac.Res., 2003. **31**(10): p. 2561-2569.

305. J.Bunkenborg, M.M.Stidsen, J.P.Jacobsen, *On the sequence selective bis-intercalation of a homodimeric thiazole orange dye in DNA.* Bioconjug.Chem., 1999. **10**(5): p. 824-831.

306. M.E.Macey, *Flow Cytometry: Principles and Applications*, 2007, Totowa, New Jersey: Humana Press.

307. Invitrogen.com. *Nucleic Acid Stains-Section 8.1*. [last accessed in December2010] http://www.invitrogen.com/site/us/en/home/References/Molecular-Probes-The-Handbook/Nucleic-Acid-Detection-and-Genomics-Technology/Nucleic-Acid-Stains.html.

308. H.P.Spielmann, D.E.Wemmer, and J.Peter, *Solution Structure of a DNA Complex with the Fluorescent- Bis-Intercalator TOTO Determined by NMR Spectroscopy.* Biochemistry, 1995. **34**: p. 8542-8553.

309. J.P.Jacobsen, J.B.Pedersen, L.F.Hansen and D.E.Wemmer, *Site selective bis-intercalation of a homodimeric thiazole orange dye in DNA oligonucleotides.* Nucl.Ac.Res., 1995. **23**(5): p. 753-760.

310. L.J.Kricka, P.Fortina, *Analytical Ancestry:"Firsts" in Fluorescent Labeling of Nucleosides, Nucleotides, and Nucleic Acids.* Clin.Chem., 2009. **55**(4): p. 670-683

311. H.P.Spielmann, University of Kentucky, Center for Structural Biology. *Ligand*. [last accessed in April 2010] http://www.mc.uky.edu/biochemistry/dept_personnel/faculty/spielmann/ligand.html.

312. H.S.Rye, S.Yue, D.E.Wemmer, M.A.Quesada, R.P.Haugland, R.A.Mathies, A.N.GIazer, *Stable fluorescent complexes of double-stranded DNA with bis-*

intercalating asymmetric cyanine dyes: properties and applications. Nucl.Ac.Res., 1992. **20**(11): p. 2803-2812.

313. R.R. Gupta, L.Strekowski, *Topics in Heterocyclic Chemistry*, in *Heterocyclic Polymethine Dyes-Synthesis, Properties and Applications*, 2008, Springer.

314. R.O.Dempcy, I.A.Afinova, N.M.J.Vermeulen, *Hybridization-Triggered Fluorescent Detection of Nucleic Acids*, 2005: U.S. Patent, Patent No.:US 6.951,930 B2

315. M.E.Cullum, L.G.Simonson, S.Z.Schade, L.A.Lininger, A.L.McArthur, *Fluorescence polarization instruments and methods for detection of exposure to biological materials by fluorescence polarization immunoassay of saliva, oral or bodily fluids*, 2008, U.S. Patent, Patent No.: US 7,408,640 B2

316. T.L.Netzel, K.Nafisi, M.Zhao, J.R.Lenhard, I.Johnson, *Base-Content Dependence of Emission Enhancements, Quantum Yields, and Lifetimes for Cyanine Dyes Bound to Double-Strand DNA: Photophysical Properties of Monomeric and Bichromophoric DNA Stains.* J.Phys.Chem., 1995. **99**: p. 17936-17947.

317. A.Castro, F.R.Fairfield, and E.B.Shera, *Fluorescence Detection and Size Measurement of Single DNA Molecules.* Anal.Chem., 1993. **65**: p. 849-852.

318. Zeiss.com. *Dye TOTO-1-DNA, Excitation, Emission*. [last accessed in December2010] https://www.micro-shop.zeiss.com/us/us_en/spektral-info.php?i=Objekt-0000-272.

319. T.F.Chan, C.Ha, A.Phong, D.Cai, E.Wan, L.Leung, P.Y.Kwok, M.Xiao, *A simple DNA stretching method for fluorescence imaging of single DNA molecules.* Nucl.Ac.Res., 2006. **34**(17): p. e113.

320. V.Stsiapura, A.Sukhanova, A.Baranov, M.Artemyev, O.Kulakovich, V.Oleinikov, M.Pluot, J.H.M.Cohen, I.Nabiev, *DNA-assisted formation of quasi-nanowires from fluorescent CdSe/ZnS nanocrystals.* Nanotechnology, 2006. **17**: p. 581-587.

321. CE.Lyon and C.T.Wittwer, *Award Lecture: LightCycler Technology in Molecular Diagnostics.* J.Molec.Diagnostics, 2009. **11**(2): p. 93-101.

322. C.H.Reccius, S.M.S., J.T.Mannion, L.P.Walker, and H.G.Craighead, *Conformation, Length, and Speed Measurements of Electrodynamically Stretched DNA in Nanochannels.* Biophys.J., 2008. **95**: p. 273-286.

323. S.S.Shankar, L.Rizello, R.Cingolani, R.Rinaldi, and P.Paolo Pompa, *Micro/Nanoscale Patterning of Nanostructured Metal Substrates for Plasmonic Applications.* ACS Nano, 2009. **3**(4): p. 893-900.

324. K.Ray, M.H.Chowdhury, and J.R.Lakowicz, *Aluminum Nanostructured Films as Substrates for Enhanced Fluorescence in the Ultraviolet-Blue Spectral Region.* Anal.Chem., 2007. **79**(17): p. 6480-6487.

325. R.M.P.Doornbos, B.G.deGrooth, and J.Greve, *Experimental and Model Investigations of Bleaching and Saturation of Fluorescence in Flow Cytometry.* Cytometry, 1997. **29**: p. 204-214.

326. M.Winter, Department of Chemistry, University of Sheffield, *University of Sheffield, Chemistry, Mark winter, Orbitron, Introduction*. [last accessed in December2010] http://winter.group.shef.ac.uk/orbitron/AOs/3d/index.html.

327. E.H.K.Stelzer, *Constrast, resolution, pixelation, dynamic range and signal-to-noise ratio: fundamental limits to resolution in fluorescence microscopy.* J.Microscopy, 1997. **189**: p. 15-24.

328. K.Kemnitz, K.Yoshihara, T.J.Tani, *Short and excitation-independent fluorescence lifetimes of J-aggregates adsorbed on silver(I) bromide and silica.* J.Phys.Chem 1990. **94**(7): p. 3099-3104.

329. P.Bharadwaj and L.Novotny, *Spectral dependence of single molecule fluorescence enhancement.* Opt.Express, 2007. **15**(21): p. 14266-14274.

330. L.Dyadyusha, H.Yin, S.Jaiswal, T.Brown, J.J.Baumberg, F.P.Booy and T.Melvin, *Quenching of CdSe quantum dot emission, a new approach for biosensing.* Chem.Commun., 2005: p. 3201-3203.

331. R.A.Floyd, *Role dof oxygen free radicals in carcinogenesis and brain ischemia.* The FASEB Journal, 1990. **4**: p. 2587-2597.

332. M.S.Cooke, M.D.Evans, M.Dizdaroglu, and J.Lunec, *Oxidative DNA damage: mechanisms, mutation, and disease.* The FASEB Journal, 2003. **17**: p. 1195-1214.

333. J.P.Shelby and D.T.Chiu, *Mapping Fast Flows over Micrometer-Length Scales Using Flow-Tagging Velocimetry and Single-Molecule Detection.* Anal.Chem., 2003. **75**: p. 1387-1392.

334. M.Zimmermann, E.Delamarche, M.Wolf, and P.Hunziker, *Modeling and Optimization of High-Sensitivity, Low Volume Microfluidic-Based Surface Immunoassays.* Biomed.Microdevices, 2005. **7**(2): p. 99-110.

335. M.Gösch, H.Blom, J.Holm,T.Heino, and R.Rigler, *Hydrodynamic Flow Profiling in Microchannel Structures by Single Molecule Fluorescence Correlation Spectroscopy.* Anal.Chem., 2000. **72**: p. 3260-3265.

336. R.F.Ismagilov, A.D.S., P.J.A.Kenis, and G.Whitesides, H.A.Stone, *Experimental and theoretical scaling laws for transverse diffusive broadening in two-phase laminar flows in microchannels.* Appl.Phys.Lett., 2000. **76**(17): p. 2376-2378.

337. N.Stokes, A.M.McDonagh, M.B.Cortie, *Preparation of Nanoscale Gold Structures by Nanolithography.* Gold Bulletin, 2007. **40**(4): p. 310-320.

338. R.C.Pennington, G.D`Alessandro., J.J.Baumberg, and M.Kaczmarek, *Tracking spatial modes in nearly hemispherical microcavities.* Opt.Lett., 2007. **32**(21): p. 3131-3133.

339. G.V.Prakash, L.Besombes, T.Kelf, and J.J.Baumberg, P.N.Bartlett and M.E.Abdelsalam, *Tunable resonant optical microcavities by self assembled templating.* Opt.Lett., 2004. **29**(13): p. 1500-1502.

340. G.Stefani, *Photoemission Spectrocopy: Fundamental Aspects*. 2009, Dipartimento di Fisca "E. Amaldi",Universita' Roma TreCNISM Unita' di Ricerca di Roma 3: X SILS School on Synchrotron Radiation: Fundamental, Methologies and Applications. Duino (Trieste).

341. Stanford Linear Accelerator Center, Menlo Park., CA. *X-Ray Photoelectron Spectroscopy*. [last accessed in March2010] http://www.group.slac.stanford.edu/sms/xrayspectroscopy.html.

342. Leibniz-Institut fuer Festkoerper und Werkstoffforschung Dresden. *X-Ray Photoelectron Spectroscopy (XPS)*. 2007 [last accessed March 2010]; Available from: http://www.ifw-dresden.de/institutes/ikm/organisation/dep-31/methods/x-ray-photoelectron-spectroscopy-xps.

343. K.Fleming. *Spectroscopy Lecture 08: Finishing Fluorescence Spectroscopy Introduction to Circular Dichroism*. 2008 [last accessed in March2010] http://freedom.bph.jhu.edu/Teaching/Techniques2008/lecture_notes/k8.pdf.

344. Zeiss.com. *Fluorescence Dye and Filter Database*. [last accessed in December2010] https://www.micro-shop.zeiss.com/us/us_en/spektral.php?f=fi.

345. Department of Biochemistry and Molecular Biophysics, The University of Arizona. *The Biology Project, Biochemistry, Acids and Bases Problem Set*. 1999 [last accessed in December2010] http://www.biology.arizona.edu/biochemistry/problem_sets/ph/10t.html.

346. M.Gregory, Clinto Community College., State University of New York, Plattsburgh, New York. *Organic Chemistry, Biochemistry*. [last accessed in April2010] http://faculty.clintoncc.suny.edu/faculty/michael.gregory/files/bio%20101/bio%20101%20lectures/biochemistry/biochemi.htm#Condensation.

347. EvidentTechnologies. *EviDots and Evicomposites, Quantum dot nanomaterials for research*. [last accessed in December 2010] http://www.getters.kr/data/goodsImages/GOODS1_1273643228.pdf.

348. EvidentTechnologies. personal corresondencem, 2010

349. Y.S.Kim, S.J.Yun, *Studies on polycrystalline ZnS thin films grown by atomic layer deposition for electroluminescent applications.* Appl.Surf.Science, 2004. **229**: p. 105-111.

350. Y.Ooshika, *Absorption Spectra of Dyes in Solution.* J.Phys.Soc.Japan, 1954. **9**(4): p. 594-602.

351. P.O.Lowedin, *Advances in Quantum Chemistry*. 1964, Academic Press

352. Wikipedia.com. *Atomic force microscopy*. [last accessed in November2010] http://en.wikipedia.org/wiki/Atomic_force_microscopy.

353. Wikipedia.com. *Atomic force microscopy*. [last accessed in March2010] http://en.wikipedia.org/wiki/Atomic_force_microscopy.

354. Cnx.org. *Sugar-Phospahte-Backbone*. [last accessed in December2010] http://cnx.org/content/m11411/latest/sugar-phosphate_backbone.jpg.

355. W.T.Johnson, Agilent Technologies (2008) *Imaging DNA in Solution with the AFM*.

356. A.Krylov. *University of Southaern California, Department of Chemistry: Research Focus: Open-shell species: A challenge to electronic structure theory*. 2010 [last accessed December 2010]; Available from: http://chem.usc.edu/faculty/Krylov.html.

357. H.L.Ng, M.L.Kopka, and R.E.Dickerson, *The structure of a stable intermediate in the A to B DNA helix transition.* PNAS, 2000. **97**(5): p. 2035-2039.

358. A.V.Kavokin, J.J.Baumberg, G.Malpuech, F.P.Laussy, *Microcavities*. Series on Semiconductor Science and Technology, 2007: Oxford University Press.

359. T.Numai, *Electromagnetic Wave Scattering on Nonspherical Particles*. Springer Series in Optical Sciences, 2004: Springer

360. N.M.B.Perney, *Light propagation and localisation on periodic dieletric and metallic nanostructures*, in *School of Physics and Astronomy*. 2007, D.Phil. thesis, University of Southampton

361. H.Reather, *Surface plasmons on smooth and rough surfaces and on gratings*. Springer tracts in modern physics, 1988: Springer.

362. T.A.Kelf, *Light-Matter Interactions on Nano-Structured Metallic Films*, in *School of Physics and Astronomy*. 2006, D.Phil. thesis, University of Southampton

363. T.Turanyi. *Physical Chemistry I.for SOTE Students of Pharmacy-The Boltzmann Distribution*. 2010 [last accessed in March2010] http://garfield.chem.elte.hu/Turanyi/oktatas/PhysChem_Pharmacy.html.

364. E.W.Weisstein. *Spherical Cap, MathWorld-A Wolfram Web Resource*. [last accessed June2010] http://mathworld.wolfram.com/SphericalCap.html.

365. Becker&Hickl GmbH. *Time-Correlated Single Photon Counting*. 2002 [last accessed in April2010] http://www.becker-hickl.de/pdf/tcspc1l.pdf.

366. Sinnesphysiologie.de. *Moderne Methoden der Zellbiologie:IV: Fluoreszenztechniken II:Time-correlated single-photon counting*. [last accessed in June2010] http://www.sinnesphysiologie.de/methoden/fluo/tcspch.htm.